A HEMILABILE LIGAND APPROACH TO RUTHENIUM-BASED LUMINESCENT MOLECULAR SENSORS

by

CERRIE WENLYN ROGERS

Hon. B. Sc., McMaster University, 1996

A THESIS SUBMITTED IN PARTIAL FULFILLMENT OF
THE REQUIREMENTS FOR THE DEGREE OF

DOCTOR OF PHILOSOPHY

in

THE FACULTY OF GRADUATE STUDIES

(Department of Chemistry)

We accept this thesis as conforming
to the required standard

THE UNIVERSITY OF BRITISH COLUMBIA

December 2001

In presenting this thesis in partial fulfilment of the requirements for an advanced degree at the University of British Columbia, I agree that the Library shall make it freely available for reference and study. I further agree that permission for extensive copying of this thesis for scholarly purposes may be granted by the head of my department or by his or her representatives. It is understood that copying or publication of this thesis for financial gain shall not be allowed without my written permission.

Department of Chemistry

The University of British Columbia
Vancouver, Canada

Date Dec. 10, 2001

Abstract

In this thesis, luminescent Ru(II) complexes that contain a metal-based receptor site for nucleophilic small molecules were studied, with emphasis on their potential utility as luminescent chemosensors. Two approaches to achieving small-molecule dependent luminescence were investigated: one exploited a metal-based lumophore (Part 1) and the other an organic-based lumophore (Part 2).

In Part 1 of this thesis, molecular sensors based on the well-known $[cis\text{-Ru(bpy)}_2\text{(L-L')}]^{2+}$ lumophore were investigated. Complexes in which L'-L' is a hemilabile phosphine-ether ligand (POR) were shown to bind small-molecule analytes (*e.g.*, water, acetonitrile, thiols, dimethylsulfoxide) via displacement of the labile ether moiety, which was readily monitored via ^{1}H and $^{31}P\{^{1}H\}$ NMR spectroscopy. The resulting changes in the coordination sphere of the metal caused the metal-to-ligand charge-transfer derived absorption and emission spectra to be shifted. For example, complex **1**, $[cis\text{-Ru(bpy)}_2\text{(POMe-}P,O\text{)}]^{2+}$ (POMe = 2-methoxyphenyl-diphenylphosphine), yields orange luminescence at low temperatures when the ether is metal-bound. In response to analytes, the emission of **1** changes colour as follows: yellow for acetonitrile, cherry red for triethylamine, poppy red for dimethylsulfoxide, brownish yellow for thiols. Thus, $[cis\text{-Ru(bpy)}_2\text{(POR)}]^{2+}$ complexes are potential candidates for development into sensory materials in multianalyte sensor applications, although their luminescence is limited to low temperatures.

A side reaction encountered during the preparation of **1** was also studied. Specifically, the metal-bound ether in **1** was found to be prone to dealkylation by free phosphine-ether ligands to form phosphino-phenoxide complex **4**, $[cis\text{-Ru(bpy)}_2\text{(Ph}_2\text{PPhO-}P,O\text{)}]^{+}$. Similar *P,O*-complexes with the ligands POEt (POEt = 2-ethoxyphenyldiphenylphosphine) and PC2OMe (2-methoxyethyldiphenylphosphine) showed lower propensities toward ether dealkylation. The trend in reactivity was determined to be related to the electrophilicity of the ether's C_α as well as resonance stabilization of **4**.

Changes in the ether substituent in the P,O-ligands were found to influence the reactivity of the $[cis\text{-Ru(bpy)}_2\text{(POR)}]^{2+}$ complexes. The POEt complex, **2**, showed reactivity

and photophysical properties very similar to those of **1** but had slightly higher affinities for most analytes. Isopropyl- and trifluoromethyl-substituted ligands yielded complexes with such enhanced ether lability that their *P,O*-chelate complexes (**6** and **7**) were not isolated free from coordinated solvents. These types of modifications may be useful in future studies on tuning the selectivity and specificity of hemilabile molecular sensors.

An unsuccessful attempt to introduce room temperature luminescence into a small-molecule reactive $[cis\text{-}Ru(bpy)_2(L\text{-}L')]^{2+}$ lumophore involved replacement of the phosphine in the hemilabile ligand with a nitrogen-based donor. The pyridine-ether ligands PyC1OMe (PyC1OMe = 2-(methoxymethyl)pyridine) and PyC2OMe (PyC2OMe = 2-(2-methoxyethyl)pyridine) led to complexes **8** and **9**, which were shown to be luminescent only at low temperature. Furthermore, the pyridine-ether ligands in these complexes did not exhibit the hemilabile behaviour desired for chemosensory applications.

In Part 2 of this thesis, the hemilabile approach was used to effect analyte-induced displacement of an organic lumophore away from a metal-based analyte receptor. Specifically, a pyrene lumophore was incorporated into a phosphine-ether ligand (POC4Pyr = 4-(2-(diphenylphosphino)phenoxy)butylpyrene) and used to prepare *trans,cis,cis*-$RuCl_2$(POC4Pyr-*P,O*)$_2$, **10**. Complex **10** was shown to exhibit a rapid, dramatic luminescence response to carbon monoxide at room temperature. The resulting dicarbonyl complex *trans,trans,trans*-$RuCl_2(CO)_2$(POC4Pyr-*P*)$_2$, **11**, was observed to slowly convert into the *cis,cis,trans*-isomer **12**, which showed very strong blue-green pyrene excimer-based emission.

Table of Contents

List of Tables

List of Figures

List of Schemes

List of Symbols and Abbreviations

Abbreviation	Description
Å	Ångstrom
A	pre-exponential factor
α	proportionality constant describing effective concentration
A	small-molecule analyte
ACD	NMR spectral prediction software from Advanced Chemistry Development Inc.
A.C.S.	American Chemical Society
AEP	3-(2-aminoethyl)pyridine
APT	attached proton test
AQ	acquisition time (NMR spectroscopy)
atm	atmosphere
BDMPP	bis(2,6-dimethoxyphenyl)phenylphosphine
biq	biquinoline
b.p.	boiling point (°C)
bpy	2,2'-bipyridine
bpy'	substituted 2,2'-bipyridine
br	broad
Bu	butyl
C_α	carbon atom bound to oxygen
Calcd.	calculated
CalTech	California Institute of Technology
ccc	*cis, cis, cis*
CCDC	Cambridge Crystallographic Data Centre
cct	*cis, cis, trans*
cf.	*confer*
CIF	crystallographic information file
COSY	^{1}H NMR correlation spectroscopy

18-crown-6	$(CH_2CH_2CH_2O)_6$, cyclic polyether for solubilizing K^+
CV	cyclic voltammogram
cyclam	macrocyclic amine ligand: 1,4,8,11-tetraazacyclotetradecane
Δ	difference (general usage); or, refers to reaction carried out in boiling solvent (as used in synthetic schemes)
δ	chemical shift (ppm)
d	doublet (spectroscopy), or day
D1	dead time; delay used between acquisitions in NMR spectroscopy
dd	metal-centred excited state; or, doublet of doublets (NMR)
dmb	4,4'-dimethyl-2,2'-bipyridine
DMSO, dmso	dimethylsulfoxide
dppe	bis(diphenylphosphino)ethane
dppm	bis(diphenylphosphino)methane
ε	extinction coefficient ($M^{-1}cm^{-1}$)
$E^{o'}$	reduction potential of electronically excited state
$E_{1/2}$	half wave reduction potential (V)
E_a	activation barrier
E_{abs}	absorption energy
e.g.	*exempli gratia*
E_{em}	emission energy
E_{ox}	peak potential, oxidation process (V)
equiv	stoichiometric equivalent
E_{red}	peak potential, reduction process (V)
Et	ethyl
et al.	*et aliae*
etc.	*et cetera*
ether	diethyl ether
EtOH	ethanol
eV	electron Volt
excimer	excited state dimer

Fc	ferrocene
FTIR	Fourier transform infrared spectroscopy
GOF	goodness-of-fit indicator (X-ray crystallography)
h	hour
hν	photon
HOMO	highest occupied molecular orbital
ICT	internal charge transfer
I.D.	inner diameter
i.e.	*id est*
^{i}Pr	isopropyl, IUPAC 2-propyl
ipso	in a ring substituent, describes the carbon atom that sits at the point of attachment to the rest of the molecule
IR	infrared
irrev	irreversible
IUPAC	International Union of Pure and Applied Chemistry
J	scalar coupling constant (Hz)
K	degrees Kelvin
k_B	Boltzmann's constant: 1.38066×10^{-23} JK^{-1}
K	equilibrium constant
K_{eff}	effective equilibrium constant (defined on p. 48)
k_{nr}	rate constant for nonradiative excited state deactivation
k_{obs}	observed rate constant for excited state deactivation
k_r	rate constant for radiative excited state deactivation
KO^{t}Bu	potassium *t*-butoxide
λ_{em}	emission wavelength (nm)
λ_{ex}	excitation wavelength (nm)
λ_{max}	wavelength at band maximum (nm)
LC	ligand-centred
L, L'	ligands
L-L'	heterotopic bidentate ligand

LMCT	ligand-to-metal charge transfer
LUMO	lowest occupied molecular orbital
M	molecular mass (g mol^{-1})
M	molarity
m	multiplet
MC	metal-centred
MDMPP	(2,6-dimethoxyphenyl)diphenylphosphine
Me	methyl
MeCN	acetonitrile
$Me_{10}Fc$	decamethylferrocene
MeO	methoxy
MeOH	methanol
MePy	3-methylpyridine
MeX	methyl halide
MLCT	metal-to-ligand charge transfer
m.p.	melting point (°C)
mult	multiplet
ν	IR absorption frequency (cm^{-1})
ν_M	vibrational spacing (cm^{-1}) in emission spectrum
n-	normal
^{n}Bu	*n*-butyl
$^{n}BuLi$	*n*-butyllithium
ND	not determined
NMR	nuclear magnetic resonance
NOE	nuclear Overhauser enhancement
O.D.	outer diameter
ORTEP	Oak Ridge Thermal Ellipsoid Plot
OTf	trifluoromethylsulfonate, $CF_3SO_3^-$, common name triflate
PC2OMe	2-methoxyethyldiphenylphosphine
PE	Perkin Elmer
PET	photoinduced electron transfer

Ph	phenyl
$PhOCH_3$	methoxy-substituted phenyl ring
PhOR	ether-substituted phenyl ring
pK_a	negative logarithm of acid dissociation constant
ppb	parts per billion
ppm	parts per million
ppt	parts per trillion
POC4Pyr	4-(2-(diphenylphosphino)phenoxy)butylpyrene
$POCF_3$	2-trifluoromethoxyphenyldiphenylphosphine
POEt	2-ethoxyphenyldiphenylphosphine
PO^iPr	2-(2-propoxy)phenyldiphenylphosphine
POMe	2-methoxyphenyldiphenylphosphine
PO, POR	phosphine-ether ligand
PR_3	tertiary phosphine
PTFE	poly(tetrafluoroethylene)
py	pyridine
PyC1OMe	2-(methoxymethyl)pyridine
PyC2OMe	2-(2-methoxyethyl)pyridine
PyOMe	2-methoxypyridine
Pyr	pyrene
q	quartet
Φ	luminescence quantum yield
ρ	density (g cm^{-1})
R	alkyl substituent
R_1	agreement factor (residuals determined using observed data)
Refl.	reflections
rev	reversible
R_f	retention factor (chromatography)
RSH	alkyl thiol
RT	room temperature
σ	standard deviation

s	singlet
S_0	singlet ground electronic state
S_1	singlet excited electronic state
sat.	saturated
SCE	saturated Calomel electrode
sh	shoulder
sept	septet
SOMO	singly occupied molecular orbital
SUNY Binghamton	State University of New York, at Binghamton
τ	luminescence lifetime
t	triplet
t-	tertiary
T	temperature
T_1	triplet excited electronic state
T_1	longitudinal relaxation time (NMR spectroscopy)
THF	tertahydrofuran
TLC	thin layer chromatography
TMPP	tris(2,4,6-trimethoxyphenyl)phosphine
TMS	tetramethylsilane
tren	tripodal tetradentate ligand: tris(2-aminoethyl)amine
tt	*trans, trans*
ttt	*trans, trans, trans*
UV	ultraviolet
μ	energy of X-rays used for crystallographic determination (cm^{-1})
V	volume of unit cell ($Å^3$)
V	Volts
Vis, vis	visible
vs.	*versus*
v/v	volume to volume ratio
wR_2	weighted agreement factor (residuals determined using all data)
Z	number of molecules in crystallographic unit cell

Acknowledgments

I would like to thank foremost my supervisor, Mike Wolf, for his undying support. His enthusiasm and encouragement kept me motivated throughout this project. Mike, your patience, understanding and friendship, and your amazing ability to coach each person in their own way, made all the difference to my experience here. Thank you so much for everything.

I also would like to thank the members of the Wolf group, past and present. The intellectual and emotional support provided by each of you made an enormous difference to the quality of my life through these past five years (although I could have managed without Olivier's music!). I admire and thank you all for surviving the wrath of Safety Chick with good cheer.

My thanks also go out to so many people that provided technical assistance and general wisdom. The Chemistry Department support staff were always very helpful. In particular, I'd like to thank Dr. Nick Burlinson, Ms. Marietta Austria and Ms. Liane Darge for sharing their NMR wisdom and supplying so much experimental assistance. As well, I'd like to thank the X-ray crystallographers, Dr. Brian Patrick and the late Dr. Steve Rettig, who solved the structures of my complexes, as well as Mr. Peter Borda for his careful elemental analyses. I also would like to acknowledge Prof. Les Burnick and Prof. Ian Clark-Lewis for allowing me to use their luminescence spectrometers, and my collaborators at SUNY Binghamton, Prof. Wayne E. Jones, Jr., and Ms. Yan Zhang, for their help with photophysical experiments. Many people also provided me with much-appreciated intellectual discussions and synthetic advice; in particular, much wisdom was gleaned over the years from the members of the Fryzuk group and the Piers group.

I would also like to thank my family and wonderful friends for their love and support over these emotionally (and financially) demanding years. I especially thank Sam Johnson, who convinced me to stick it out when it was so tempting to do otherwise. It is truly the belief of others in me that has propelled me through this journey. My heartfelt thanks go out to all of you who helped me survive this degree.

"Those who wander are not always lost."

--T.S. Eliot

To the people who believed in me...

Chapter One

Luminescent molecular sensors based on the coordination of analyte to a metal centre

1.1 Luminescent molecule-based chemosensors: an introduction

Molecule-based chemosensors are, in essence, molecules designed to change their properties in response to the presence of other molecules. Conventionally, chemical sensor applications have exploited the bulk properties of solid-state materials such as metal oxides, which can exhibit, for example, changes in conductivity in response to the adsorption of oxidizing or reducing gases to the surface of the material. The appeal of using molecules in sensing applications derives from several attractive features of molecules in general. First, the power and versatility of chemical synthesis enables chemists to prepare a huge variety of molecules. Molecules can be designed to interact specifically with other molecules. Analyte-binding receptors can be carefully assembled using combinations of hydrogen bonding, electrostatics, covalent and coordinative bonding. Furthermore, the factors that influence

References begin on page 26.

molecule-based electronic properties are understood to the extent that molecule-analyte interactions can be engineered to produce changes in readily monitored properties such as colour, photoluminescence and reduction potential. These changes can, in turn, be interpreted in terms of sensor-analyte response. A major driving force behind the field of molecule-based chemosensors is the potential for miniaturization of sensor technology down to the nanometer scale, where a single molecule could act as an individual sensor element.[1]

Molecular recognition is a well-developed field unto its own, studied largely out of interest in understanding the recognition processes in biological molecules such as enzymes. It is the combination of molecule-molecule interactions with changes in measurable properties that distinguishes molecular recognition from molecule-based chemosensing. Thus, molecule-based sensors combine analyte-binding or *receptor* function and analyte-response or *reporter* function, and the architecture of such sensors is often, but not necessarily, modular in nature. In this thesis, molecules that perform these types of functions are referred to as sensors or chemosensors. However, it should be noted that the more generally accepted usage of these terms is in reference to operational devices comprised of sensing and response elements, detectors and output devices, as well as the electronics required to support the function of these interacting components. Thus, the molecule-based sensors discussed in this thesis would be considered as potential candidates for sensing elements in sensory devices.

The purpose of receptors is to provide fast and reversible binding of the analyte of interest, and molecular receptors for sensing purposes are designed with this function in mind. A few common themes deserve introduction. Cations are typically coordinated by crown ethers, cyclams and other arrays of lone-pair donors. Specificity is determined based on ion size and charge; for example, the receptors shown in Scheme 1.1 are specific for the ions shown and have been tethered to luminescent moieties to act as receptor modules in molecule-based sensors for these ions.[2-5]

References begin on page 26.

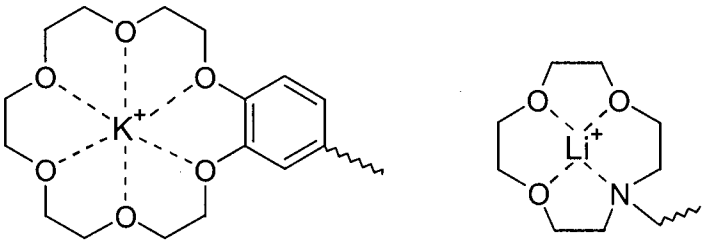

Scheme 1.1.

Anions are typically bound using sets of hydrogen-bond donors and acceptors that are complementary to the acceptors/donors in the anion of interest.[6,7] For example, the receptor depicted in Scheme 1.2 complexes phosphodiesters and has been successfully incorporated into a luminescent ruthenium 2,2'-bipyridine complex that responds to these anions.[8]

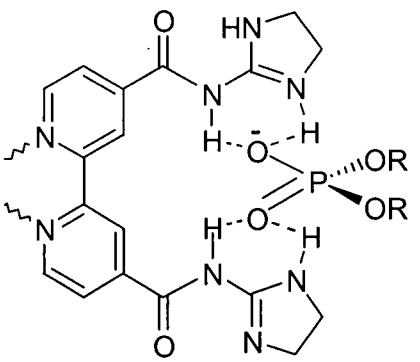

Scheme 1.2.

Finally, small-molecule analytes such as CO, O_2, NH_3, H_2O and organic compounds that contain donor atoms can be coordinated by transition metals. Thus, the metal-ligand interaction has been utilized to develop transition-metal based small-molecule receptors, which will be elaborated upon later in this chapter (section 1.3) as it is the foundation of the work presented in this thesis.

References begin on page 26.

In response to analyte-receptor binding, molecule-based sensors must undergo changes in readily monitored properties. While there is a variety of potentially variable properties to choose from, photoluminescence is particularly attractive for a number of reasons, which have been summarized well in a recent review by de Silva *et al.*[2] From the standpoint of miniaturization, the advantage of luminescence is that it avoids the problem of making electrical connections to extremely small sensors (*i.e.*, individual molecules). Moreover, luminescence offers both high spatial and temporal resolution, as well as inherently large signal-to-noise ratios that can be further improved by designing the analyte-binding event to switch the sensor molecule between luminescent and nonluminescent forms. The most striking advantage of luminescence, however, is the high degree of sensitivity that can be achieved; in fact, luminescence arising from a single molecule can be detected via single photon counting. In addition to these advantages, the structural and environmental factors that influence molecular luminescence are well understood. This provides a rational basis for the design of molecule-based chemosensors that respond to analytes via changes in photoluminescence.

1.2 An introduction to photoluminescence

1.2.1 The basics of photoluminescence theory

Luminescence is the general term for the emission of light from electronically excited atoms or molecules. Depending on the source of the excitation energy, luminescence is divided into several subtypes: photoluminescence (from light absorption), electroluminescence (from electrical excitation), chemiluminescence (from chemical reaction), thermoluminescence (from thermal excitation), triboluminescence (from mechanical stress). The most common of these subtypes is by far photoluminescence, and excellent discussions of the underlying theory are presented in general texts[9] and in a number of specialized texts available on the subject.[10-12] The discussion in this chapter will be limited to a brief overview of photoluminescence theory.

Just as a chemical moiety that absorbs light is called a chromophore, a molecule or chemical subunit that emits light is called a *lumophore* or *luminophore*; the term lumophore

References begin on page 26.

will be used throughout this work. When a chromophore absorbs a photon from the UV or visible region of the spectrum, the energy induces a transition to an electronically excited state, as illustrated schematically in the energy-level diagram in Figure 1.1. Electronic transitions are extremely rapid and therefore most probable between vibrational states with similar nuclear positions (*Frank-Condon principle*); thus, photoexcitation produces molecules that are both electronically and vibrationally excited. The vibrational levels are omitted in Figure 1.1 for the sake of simplicity. The extra vibrational energy is rapidly dissipated as heat, while conversion between excited and ground electronic states can occur via both radiative and nonradiative processes. In most cases, rapid nonradiative processes (such as vibrations, internal conversion between electronic states with overlapping vibrational states, and intermolecular collisions) efficiently dissipate the energy, and the molecule returns to the ground state without the emission of light. However, molecules with rigid structures due to extended π-systems or fixed coordination geometries have restricted vibrational freedom, and therefore they show decreased rates of nonradiative relaxation. This allows the slower radiative processes to compete, which accounts for the empirical observation that lumophores often contain aromatic systems.

Light emission due to spin-allowed transitions (*i.e.*, between states with the same multiplicity, *e.g.*, $S_1 \rightarrow S_0$) is called *fluorescence*, while emission that involves an electronic spin-flip (*e.g.*, $T_1 \rightarrow S_0$) is called *phosphorescence*. Phosphorescence is formally a forbidden process and is considerably slower than fluorescence; in fact, for most organic molecules, phosphorescence can only be observed at extremely low temperatures at which nonradiative relaxation processes are minimized. In molecules that contain heavy atoms, however, spin-forbidden processes become increasingly probable because of enhanced spin-orbit coupling (the *heavy-atom effect*). Thus, the presence of heavy atoms in a lumophore is often correlated with relatively weak luminescence, as the longer lived triplet states are more prone to nonradiative deactivation. However, conformationally rigid transition-metal complexes such as $[Ru(bpy)_3]^{2+}$ (bpy = 2,2'-bipyridine) yield strong luminescence at room temperature from an emissive excited state that is predominantly triplet in character.[13]

References begin on page 26.

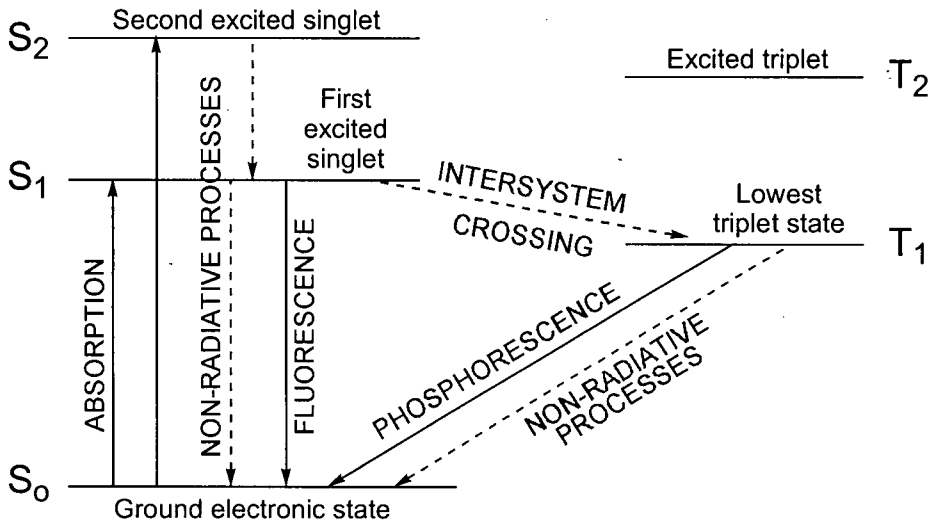

Figure 1.1. Schematic energy level diagram illustrating radiative and nonradiative transitions between ground and excited electronic states. Vibrational states are omitted for simplicity. Adapted from ref 9 with permission (© Wadsworth Publishing Company, 1988).

1.2.2 Factors that influence luminescence properties and the link to chemosensing

An understanding of the ways in which the emissive properties of lumophores can be manipulated is essential in order to design molecular sensors with analyte-dependent luminescence.[14] The structural factors that determine whether a molecule acts as a lumophore are well understood; a thorough explanation of the molecular basis of photoluminescence is beyond the scope of this chapter and can be found in numerous texts.[9-13] In this section, a brief discussion of some of the environmental and chemical factors that can influence a lumophore's emissive properties will be presented. Factors that can perturb the energetics of excited states are presented first, followed by a discussion of chemical processes that lead to the quenching of excited states. These are placed into the context of chemosensing through the

References begin on page 26.

inclusion of general examples of sensor motifs based on each manner of manipulating the emissive properties of lumophores, and references are provided to reviews on the topic.

1.2.2.1 Stabilization and destabilization of the excited state

The ways in which an emissive excited state can become energetically stabilized or destabilized depend on the nature of the excited state. Excited states are classified according to the orbitals involved in the excitation. Common excited states are those derived from n-π^*, π-π^*, metal-centred and charge-transfer (internal charge-transfer (ICT), metal-to-ligand charge transfer (MLCT), ligand-to-metal charge transfer (LMCT), *etc.*) transitions. In the following paragraphs, several examples of energetic perturbations of excited states that lead to shifted emission spectra or changes in emission intensity are presented.

Excited states that involve a large degree of charge separation, such as ICT and other charge-transfer states, are stabilized by polar solvents and, therefore, yield lower energy emission in polar solvents than in nonpolar solvents. Emission efficiencies from these polar excited states are also often affected by solvent. An implication of solvent-dependent luminescence is that certain types of lumophores are quite sensitive to the polarity of the environment in which they exist. For this reason, luminescent tags are often employed in protein and synthetic receptor studies to report on conformational changes involved in, for example, substrate binding.

Bonding interactions between lumophores and other molecules or ions can alter the ordering of energy levels, which can result in switching of the lumophore between luminescent and nonluminescent forms. For example, molecules whose lowest energy excited states are n-π^* in character, such as azaaromatics (*e.g.*, phenanthroline), are typically nonemissive. However, the nitrogen lone pairs can coordinate cations such as H^+ and metal ions. The formation of Lewis acid-base adducts destabilizes the n-π^* state such that the order of the energy levels is reversed, and the lowest excited state becomes an emissive π-π^* state. This type of OFF-ON luminescence switching has been used as the foundation of many luminescent molecule-based sensors for pH and metal cations.[2]

References begin on page 26.

Metal-centred, MLCT and LMCT excited states are susceptible to stabilization or destabilization through interactions that perturb the energetics of either the metal-based or ligand-based orbitals. Changes in the coordination environment of a metal centre affect the energetics of the metal-based orbitals, which in turn can alter the energy of metal-based, MLCT or LMCT transitions involving these orbitals. The result can range from subtle shifts in emission energies to switching between emissive and nonemissive forms, depending on the complexity of the excited-state manifold of the complex. For example, luminescent Re, Ru and Os diimine complexes show strongly ligand-dependent luminescence properties, with both the colour of the emitted light and the sensitivity of the emission to temperature influenced by the nature of the ligands on the metal.[13] The sensitivity of MLCT excited states in particular to changes in the nonchromophoric ligands is the basis of much of the work in this thesis, and a detailed discussion of this topic is presented in Chapter Two. Moreover, the binding of molecules or ions to receptors built into the ligands involved in MCLT and LMCT transitions can alter the energetics of the ligand-based orbitals, and therefore induce changes in luminescence properties.[2,7] Numerous systems containing transition-metal diimine complexes with pendant anion receptors have been shown to display analyte-dependent luminescence because of electrostatic stabilization or destabilization of the emissive MLCT states.

1.2.2.2 Deactivation of the excited state

While the preceding section focused on the perturbation of the energetics of emissive excited states, the following section deals with ways in which the excited state can be deactivated. In the context of chemical sensing, lumophores that can be switched between emissive and nonemissive forms are attractive because they offer the potential for extremely high signal-to-noise ratios. Excited-state deactivation can occur through typical nonradiative deactivation pathways, and the interaction of analyte species with the lumophore can sometimes alter these processes. For example, hydrated lanthanide complexes are weakly luminescent, but replacement of the coordinated waters by nonhydroxylic ligands results in dramatically increased luminescence intensities because the efficient nonradiative deactivation pathway provided by O-H stretching modes is removed.[2,15] For chemosensory applications, however, a more commonly utilized approach to excited-state deactivation is via the interaction of the lumophore with other moieties that have the ability to deactivate, or *quench*,

References begin on page 26.

the excited state. The two major quenching pathways, energy transfer and electron transfer, are introduced below.

(i) Energy-transfer quenching

Energy-transfer quenching occurs when the excited state's excitation energy is passed to another species in its ground state. This process can occur if the energy acceptor has an excited state of lower energy than that of the donor, as long as the rules of spin conservation are obeyed. Energy transfer occurs through one of two distinct mechanisms:

(a) through collisions, via an electron-exchange mechanism that requires orbital overlap and is therefore strongly distance dependent (≤ 10 Å between donor and acceptor); or,

(b) through long-range resonance transfer, via dipole-dipole interactions that can take place over distances of up to 100 Å between the donor and acceptor.

Detailed explanations of the theories underlying energy-transfer processes are provided in the texts recommended earlier in this chapter.[11,13] Many luminescent sensors for oxygen gas are based on energy-transfer quenching of lumophores with triplet excited states; the presence of oxygen is signaled by a decrease in luminescence intensity.[14,16] More elaborate molecular sensor designs incorporate an energy donor and acceptor into the same molecule and function on the premise that the analyte-binding event modulates the distance between the donor and acceptor components.[2]

(ii) Electron-transfer quenching

The other principal type of quenching process involves deactivation of the excited state by removal or addition of an electron from or to one of the excited state's singly occupied frontier orbitals. This *photoinduced electron transfer* (*PET*) leaves the lumophore in an oxidized or reduced state that is no longer emissive. As illustrated in Figure 1.2, PET processes can occur if the electron donor's highest occupied molecular orbital (HOMO) is higher in energy than the excited electron acceptor's singly occupied molecular orbital (SOMO). Alternatively, PET can occur if the acceptor's lowest unoccupied molecular orbital (LUMO) is lower in energy than the excited donor's singly occupied orbital (not shown in

References begin on page 26.

Figure 1.2). In either case, if the acceptor and donor are tethered together, subsequent back electron transfer returns both the acceptor radical anion and the donor radical cation to their original neutral states, which makes the PET process nondestructive. Again, detailed discussions of the theory underlying PET processes can be found in texts[13] and the primary references listed in pertinent review articles.[2,4] One aspect of PET of particular importance, however, is the strong distance dependence of electron-transfer processes; the rates of electron-transfer processes show inverse exponential dependence on the distance between the electron donor and acceptor moieties.

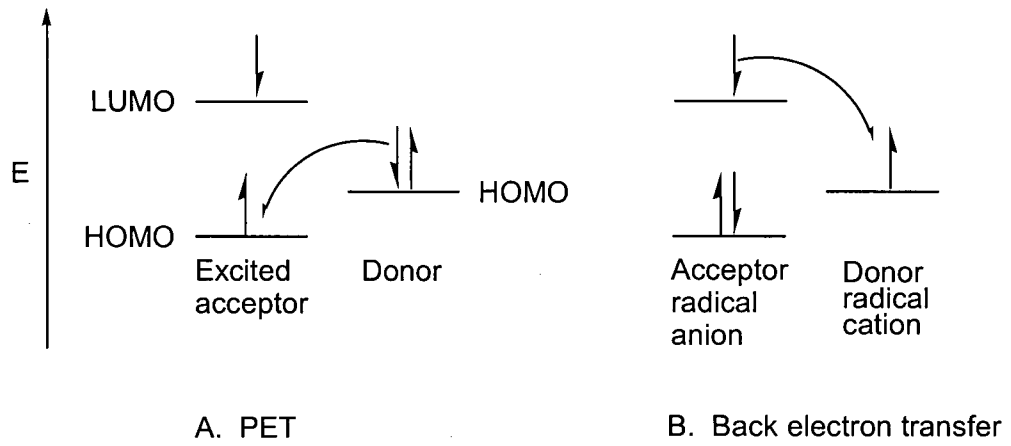

Figure 1.2. Depictions of the frontier orbital energy levels to illustrate the thermodynamics involved in the photoinduced electron transfer process (A) and the ensuing back electron transfer (B) for an excited molecule that undergoes reductive electron-transfer quenching. Adapted from ref 2 with permission (© American Chemical Society, 1997).

Molecular sensors based on PET are built with a modular design; that is, the lumophore and receptor components are typically separated by a spacer unit of well-defined length that allows for efficient electron-transfer processes. Several reviews that provide comprehensive

References begin on page 26.

coverage of the important literature in this well-developed field have been written.[2-6,17] In typical PET-based chemosensors with the lumophore-spacer-receptor design, the analyte-binding event modifies the relative energies of the donor and acceptor energy levels such that the PET mechanism is switched ON or OFF upon coordination of analyte. This type of energetic perturbation forms the basis of many metal sensors that switch to a highly luminescent form in the presence of metal ions. For example, the complexation of metal cations by macrocyclic receptors, such as crown ethers, can modify the reduction potential of the receptor such that it can no longer transfer an electron to the lumophore's excited state. In other cases, the analyte itself acts as the electron-transfer quencher, which results in luminescence being switched OFF in response to the presence of analyte. This approach has led to sensors for redox-active analytes ranging from open-shell metal ions to organic species such as quinones and nucleotides.

A less common approach to PET-based luminescence switching exploits the distance dependence of electron-transfer processes. In this approach, the binding of analyte to the receptor site causes a change in the distance between the lumophore and the quencher.[18-21] This distance modulation can result in analyte-induced ON-OFF or OFF-ON luminescence switching, depending on the design of the system. An example of this type is presented in detail in section 1.3.2.2, in which analyte-induced displacement of a lumophore from the vicinity of an open-shell transition-metal ion results in a dramatic increase in luminescence intensity.[19,20]

1.3 Sensing based on analyte coordination to a metal centre

In order to design lumophores to respond to the presence of analyte species, it is important to establish an intimate link between the analyte-binding event and the luminescence properties of the lumophore. This can be achieved through careful consideration of the factors presented above and by selection of appropriate analyte-receptor moieties. As described in section 1.1, sensor-analyte interactions should be fast, reversible and accompanied by an energetic perturbation in order to report the presence of analyte via a change in measurable

References begin on page 26.

properties. Metal-ligand coordinative bonding, by its very nature, fulfils these criteria. There has been a variety of molecular sensors reported that are based on direct coordination of analytes to metal centres. To date, this aspect of the literature has not been reviewed in its own right, although several review articles include examples of sensors based on this premise.[6,15,22-25] Metal-based sensors that lack pendant receptors have been discussed briefly in a recent review[22] published in the special "Luminescent Sensors" issue of Coordination Chemistry Reviews (Issue 205, August 2000). As well, some examples of metals in both receptor and dual receptor-lumophore roles have been presented in an earlier review by de Silva *et al.*[23]

Part of the appeal of metal-based luminescent sensors is their photophysical versatility. Luminescent metal complexes that have the ability to coordinate analytes are natural candidates for molecule-based chemosensors because they can perform dual roles, as both the receptor and the lumophore in an all-in-one design. Metal-based lumophores are common and range from metalloporphyrins to late-metal diimine complexes to lanthanide complexes, which offer widely different luminescence characteristics and diverse coordination chemistry. The coordination of analyte to the metal can occur via occupation of a vacant coordination site or through displacement of weakly bound ligands. In either case, the resulting changes in the ligand environment around the metal influence the energetics of the metal-based molecular orbitals. These perturbations often lead to analyte-dependent changes in the absorption and luminescence properties of the complex, such as spectral shifts, but can also result in dramatic changes in luminescence intensity.

Alternatively, metal-based analyte receptors can be combined with organic lumophores to create coordination-based sensors with a modular design. By virtue of their ability to undergo electron-transfer processes, many open-shell transition metals are effective luminescence quenchers; this trait is often exploited to construct complexes with analyte-dependent luminescence properties. In some cases, the analyte-binding event simply modulates the distance between the organic lumophore and an intramolecular quencher, such as the metal centre. In other cases, the analyte itself is capable of either quenching the luminescence or switching off a quenching mechanism. Both approaches result in analyte-

References begin on page 26.

dependent changes in luminescence intensity that can be used to monitor the presence of analytes.

In the following sections, the recent literature on molecule-based chemosensors whose photophysical response to analytes arises from direct metal-analyte coordination will be briefly reviewed. The literature is presented here according to the nature of the analyte binding event, *i.e.*, coordination of analyte to a vacant site on the metal *vs.* coordination via displacement of weakly bound ligands. The literature is further subdivided based on the role that the metal plays, either as a dual purpose receptor-lumophore or as a receptor that influences a lumophore to which it is tethered.

1.3.1 Analyte coordination to a vacant coordination site

The simplest receptor design involves straightforward binding of the analyte species to a coordinatively unsaturated metal centre. Molecule-based chemosensors based on metal complexes with vacant coordination sites are common; many of these consist of complexes with polydentate ligands such as tren derivatives or macrocycles such as porphyrins and cyclams. In many cases, the metal plays a dual role as both receptor and lumophore, but the more common approach involves modular designs in which a metal acts as the receptor and the analyte binding event influences an organic lumophore.

1.3.1.1 Metals as both receptor and lumophore

Complexes of macrocyclic ligands, such as porphyrins and phthalocyanines, are widely used as the basis of synthetic small-molecule receptors in studies on molecular recognition and chemosensing; only a cursory overview of these complexes is presented here since reviews are available on this subject.[25,26] The planar nature of the ligand framework leaves the metal with empty coordination sites to which Lewis basic small molecules and anions can bind. Porphyrins and phthalocyanines are often used as synthetic small-molecule receptors in sensors based on nonphotophysical response,[27] such as those that use quartz microbalances[28,29] and surface acoustic wave devices;[30] metalloporphyrins have also been used as surface-tethered

References begin on page 26.

analyte receptors on luminescent CdSe films.[31-33] However, applications of metalloporphyrins are typically linked to their interesting photophysical and photochemical properties;[13,34] the complexes are intensely coloured, usually luminescent, and undergo a variety of energy- and electron-transfer processes. Many examples of sensing using metalloporphyrin receptors rely largely on the colour changes that occur when the empty coordination sites on the metal are occupied by analytes. For example, a cobalt(II) porphyrin complex coordinated to an imidazole-functionalized polymer reversibly binds oxygen to produce a large colour change.[35] Molecular imprinting techniques have been used to prepare Zn(II) porphyrin-doped polymers that show colour changes specifically in response to nucleobases.[36] Colorimetric sensor arrays based on metalloporphyrin dyes reported by Rakow and Suslick permit a wide range of coordinating organic solvents to be distinguished upon exposure of the sensor array to solvent vapours;[37] these arrays function without interference from water vapour and yield low detection limits (< 100 ppb). Recent literature on porphyrin-based chemosensors with luminescence response has been predominantly focused on sensing oxygen gas.[38-46] Furthermore, a recent review[26] presents a variety of luminescent metalloporphyrins that bind analytes via cooperation of the metal and elaborate binding pockets built around the open coordination sites.

Cluster complexes with coordinatively unsaturated metal atoms have also been studied in light of their potential to act as luminescent chemosensors. In a recent example, a luminescent tetrametallic silver (I) bipyridyl phosphine cluster complex[47] shows luminescence that is sensitive to oxygen, coordinating solvents and certain other ligating species. Addition of DMSO or MeCN to the cluster complex leads to an enormous decrease in luminescence intensity; the complex also reversibly responds to CO gas, but irreversibly to NO. The luminescence response arises from reorganization of the cluster's core because of the addition of extra ligands to the coordination spheres of the metals.

Luminescent gold complexes have also been presented as candidates for chemosensory applications. In a recent report,[48] a nonluminescent two-coordinate gold(I) bis(phosphine) loop complex was described that switches to a highly luminescent form (yellow emission) upon coordination of triphenylphosphine to the unsaturated Au centre. Three-coordinate Au(I)

References begin on page 26.

phosphine complexes are generally luminescent,[49] which suggests that this complex might be used to report the presence of a variety of different analyte species. The improved chemical stability of the loop complex over other two-coordinate Au(I) complexes may make this complex particularly attractive for sensor applications.

Finally, the laboratory of van Koten has reported extensive work on organoplatinum(II) halide complexes with a monoanionic bis(amino)aryl "NCN" pincer ligand. These coordinatively unsaturated metal complexes are not luminescent, but their simple design and reversible colorimetric response to analyte in both solution and the solid state demand attention. As shown in Scheme 1.3, the four-coordinate metal centre rapidly and reversibly binds SO_2 via the sulfur atom to form a five-coordinate species, and the increase in coordination number is accompanied by a dramatic colour change from colourless to orange.[50,51] These Pt complexes have been incorporated into dendrimeric structures[52-54] and polymers[55] and show great promise as SO_2 sensors.[53]

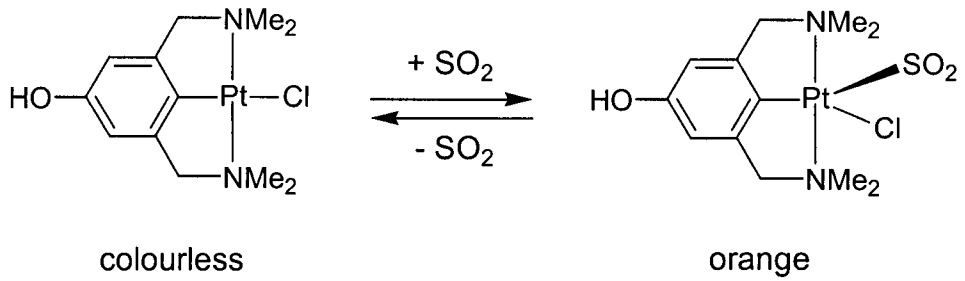

Scheme 1.3.

1.3.1.2 Metal-based receptors with organic lumophores

In the somewhat more complicated modular design, the metal functions as the receptor while the luminescence response arises from a (typically organic) lumophore that is covalently attached to the metal-based receptor. The metals involved are generally late transition metals with unfilled d-shells, such as Cu(II) and Co(II), and their ability to quench excited states via electron-transfer processes is exploited to achieve analyte-dependent luminescence

References begin on page 26.

response.[2,17] Organic lumophores abound, but those most commonly encountered in the molecular sensor literature[2,17] are based on polyaromatic hydrocarbons (pyrene, anthracene, naphthalene), acridine, coumarin and dansyl units, all of which are susceptible to luminescence quenching via electron transfer to appropriate electron acceptors. Closed-shell metal ions such as Zn(II) are also commonly used in conjunction with lumophores such as azaaromatics, whose emission is switched on upon formation of Lewis acid-base adducts. In these cases, the lumophore's response to the coordination of analyte to the metal centre arises from quenching mechanisms other than electron transfer.

In one approach, organic lumophores capable of coordinating to metal ions are employed, and analyte binding is accomplished through interaction with the coordinatively unsaturated metal centre and an additional receptor moiety tethered to the lumophoric ligand. (It should be noted that these experiments are typically performed in aqueous solution, and it is likely that the 'vacant' coordination sites on the metal are occupied by water molecules. However, since these ligands have not been intentionally included as part of the chemosensor design, this approach has been included in this section on analyte coordination to vacant sites on the metal.) For example, a combination of the carboxylate-binding ability of Zn(II) and the reactivity of boronic acids toward hydroxyl groups has been utilized to create a receptor for sugar derivatives.[56] In this chemosensor, a boronic acid group is pendant to a phenanthroline unit, which serves a dual role as the ligand that anchors the boronic acids to a Zn(II) centre and as the lumophore. The binding of uronic acids, in particular, to the complex (via coordination to both the boronic acids and the metal centre) disrupts a luminescence quenching mechanism; the presence of uronic acids is, therefore, signaled by a significant increase in phenanthroline-based emission. In a similar approach, a copper(II) phenanthroline complex has been designed with a citrate binding site that contains two guanidinium groups plus the Cu(II) centre, as shown in Scheme 1.4.[57] Again, the lumophore is the phenanthroline unit, and the binding of citrate to the guanidinium groups and the Cu(II) centre disrupts the quenching of the phenanthroline emission by the metal. The luminescence response of this complex has been successfully used to determine the amount of citrate in sports drinks.

References begin on page 26.

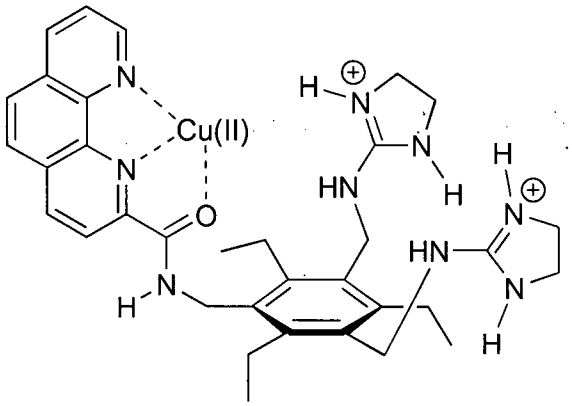

Scheme 1.4.

Fabbrizzi and coworkers have contributed several examples of Zn(II)-based small-molecule receptors that influence the emission of an intramolecular lumophore. In one example, a luminescent anthracene unit with pendant amines that can encapsulate a Zn(II) centre shows decreased luminescence in response to the binding of aromatic carboxylate ions to the coordinatively unsaturated Zn(II) centre.[58,59] The luminescence response arises from electron-transfer quenching between the aromatic groups and the anthracene when they are held close together in space by the metal centre. In another example, an anthracene unit with eight amino groups forms a dizinc(II) complex that binds imidazolates as a bridging ligand between the metal centres, such that the imidazolate ring is π-stacked with the anthracene.[60] In this case, the anthracene luminescence is quenched by the imidazolate via electron transfer from the imidazolate anion to the photoexcited anthracene.

In a similar approach, an acridine lumophore with a pendant cyclam unit that binds Zn(II) has been used as a luminescent nucleoside receptor.[61,62] The open coordination site on the metal allows nucleosides to bind in such a way that the nucleoside and acridine interact with one another. The luminescence is significantly quenched in the presence of thymidine, whereas other nucleosides do not result in a large luminescence response. Thus, this sensor provides a selective response even without specific binding.

References begin on page 26.

1.3.2 Analyte coordination through displacement of weakly bound ligands

1.3.2.1 Metals as both receptor and lumophore

A considerable amount of effort has been focused on the use of luminescent lanthanide complexes in chemosensing applications. The metal-centred excited states of lanthanide complexes give rise to long-lived emission, particularly in the absence of hydroxylic ligands. In lanthanide-based chemosensor complexes, analytes typically bind to the metal by displacing weakly bound water molecules; this gives rise to a strong enhancement of luminescence because O-H stretching modes provide a powerful nonradiative deactivation pathway for lanthanide excited states. Because the f electrons involved in the photophysics are shielded by the d-shell electrons, lanthanide emission is relatively insensitive to environmental effects and changes in ligands. This tolerance to changes in ligands enables complexes to be prepared with a wide range of ligands, to provide high chemical stability and other desirable properties, without compromising the desired luminescence properties. Excellent reviews are available that discuss lanthanide-based sensors,[2,15] so no effort is made here to summarize the literature on this topic. One example of particular note, however, involves a europium(III) complex with polymerizable ligands that was polymerized to form a molecularly imprinted polymer matrix specific for the detection of organofluorophosphorus nerve agents.[63] The luminescence response of prototype sensor devices containing this lanthanide-derivatized polymer permits quantitative detection of the hydrolysis product of chemical warfare agents at levels as low as 125 ppt.

1.3.2.2 Metal-based receptors with organic lumophores

Structural motifs such as cyclodextrins and calixarenes, commonly studied for their interesting host-guest chemistry, have also been adapted for application to luminescent chemosensing. Incorporation of lumophores and metal-coordination sites pendant to these guest-binding pockets has led to a number of complexes that show analyte-responsive photophysical behaviour. For example, the cyclodextrin depicted schematically in Scheme 1.5 contains a pendant dansyl-terminated diethylenetriamine group, which binds to Cu(II) via the three nitrogen atoms to form a complex that exhibits only weak dansyl-based luminescence because of electron-transfer quenching by the open-shell metal ion.[21] Addition of amino acids

References begin on page 26.

to the complex results in a significant increase in luminescence intensity due to displacement of the dansyl's amido group from the metal centre, which shuts off the quenching mechanism by increasing the distance between the lumophore and quencher. The cyclodextrin cavity appears to be involved in the binding process because L-alanine and L-tryptophan give rise to luminescence responses of different magnitude.

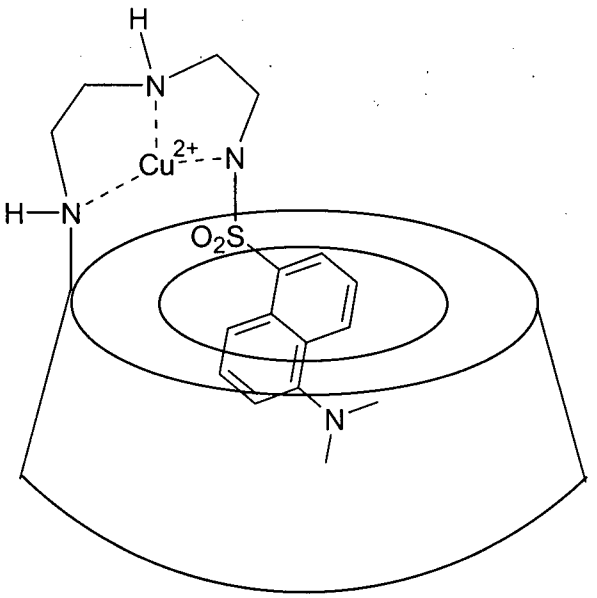

Scheme 1.5.

More recently, a metal-based small-molecule receptor with luminescent response to nitric oxide gas was reported by Lippard and co-workers.[19,20] In this complex, depicted below in Scheme 1.6, two dansyl groups are held in close proximity to a Co(II) centre by virtue of the fact that the lumophores are covalently attached to chelating amido-imine ligands. In this arrangement, the dansyl groups are only weakly luminescent because of efficient electron transfer from the dansyl excited state to the open-shell metal. Exposure of the complex to NO results in replacement of one of the amido-imine chelates with two coordinated NO molecules. Thus, one of the dansyl moieties is displaced to a site distant from the metal such that the distant-dependent electron-transfer quenching mechanism is disrupted, and strong

References begin on page 26.

luminescence is observed from the dansyl group. Although this reaction is irreversible, the system does show great potential as an NO sensor.

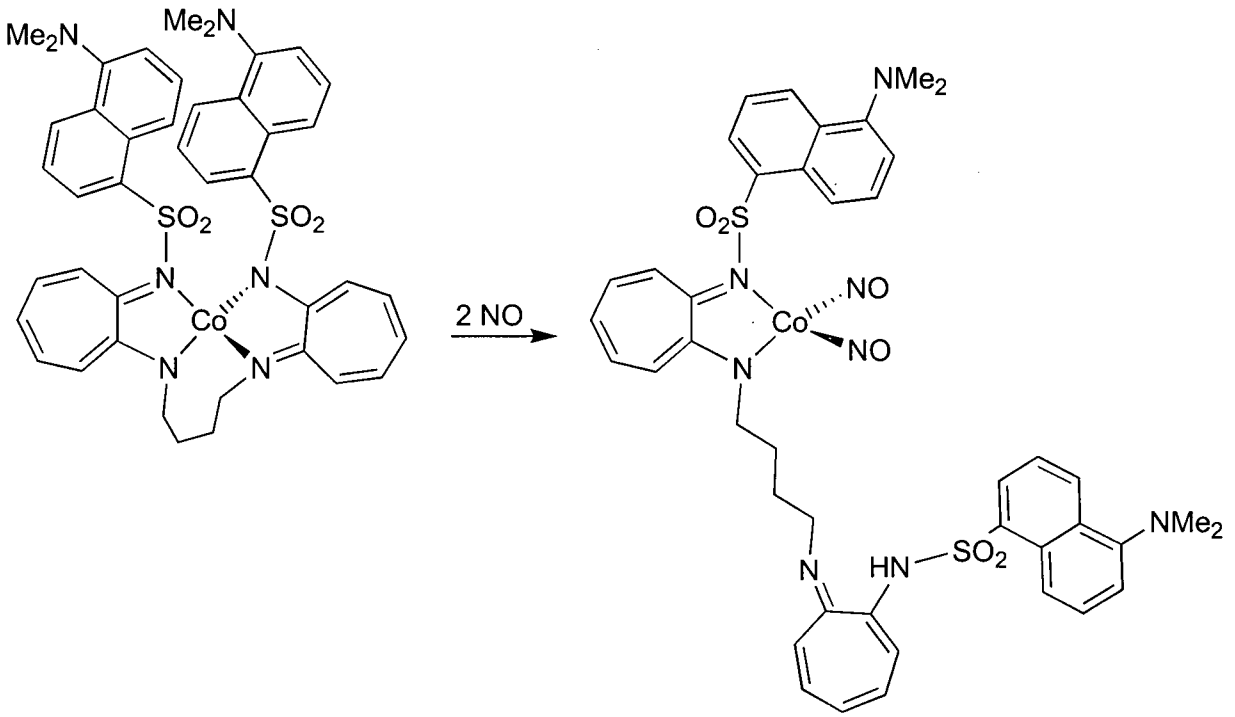

Scheme 1.6.

1.4 The hemilabile approach to analyte coordination

In this thesis, a similar approach to molecular sensing to the last discussed above is taken, wherein the coordination of analytes to a metal centre is accomplished via dissociation of a relatively weakly bound ligand. In the Lippard chemosensor described above, the tether between the two amido-imine units is sufficiently long that, even if the coordinated NO molecules were to dissociate from the metal, recoordination of the second amido-imine unit is entropically disfavoured. Thus, in its present design, the complex is limited to irreversible sensing of analyte. In the present approach, however, special emphasis has been placed on creating complexes that are predisposed to reversible analyte coordination. In short, this

References begin on page 26.

problem has been addressed here via the use of hemilabile ligands. An introduction to hemilability and its applicability to chemical sensing are presented in the following sections.

1.4.1 An introduction to hemilability

As has been described in section 1.3, the coordination of ions or small molecules to transition metals is typically achieved by using either:

(a) coordinatively unsaturated metal complexes with vacant sites that can bind additional ligands; or,

(b) coordinatively saturated complexes that contain displaceable ligands.

In the context of chemical sensing, interactions between the analyte and metal should ideally be reversible. Case (a) is amenable to reversible interactions with analytes since dissociation of analyte regenerates the vacant coordination site. In contrast, case (b) generally leads to irreversible metal-analyte interactions because the displaced ligand can diffuse away from the metal after the analyte binds. However, it is possible to covalently tether the displaceable ligand to the metal to prevent this departure, and it is this modification of case (b) which has been the focus of the present work.

Covalent tethering of a displaceable ligand to a metal centre necessitates the use of multifunctional ligands that can bind to a transition metal via two (or more) donor atoms. The simplest case involves a bidentate ligand with two different donors, one that binds strongly to the metal and one that binds weakly and therefore can be displaced by other coordinating species. Such ligands are described as *hemilabile* because half the ligand can undergo displacement from the metal while the other half remains firmly bound to the metal.[64] A generalized substitution reaction in which a hemilabile ligand competes for a coordination site with a small molecule donor, A, is shown in Scheme 1.7. The labile donor is displaced yet remains in the vicinity of the metal centre. Thus, an equilibrium is established in which recoordination of the labile moiety is entropically favoured due to the chelate effect; the position of equilibrium, however, will naturally depend on the relative metal-ligand affinities.

References begin on page 26.

Ideally, the chelate complex can be regenerated if the concentration of competing small molecule A is decreased, and it is this promise of reversibility that is attractive for chemical sensing applications.

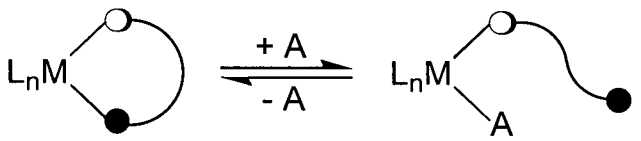

Scheme 1.7.

The selection of potentially hemilabile ligands for a given transition metal requires consideration of hard/soft acid/base theory.[65] In this description of Lewis acids and bases, species that are highly polarizable are named 'soft' while those that are not are labeled 'hard'. The hard/soft classification of a variety of Lewis acids and bases is listed in Table 1.1. In general, soft acids (such as 2nd and 3rd row late transition-metal cations) bind strongly to soft bases (such as PR_3, R_2S, CN^-, CO, I^-), in a largely covalent manner due to their high polarizability. Conversely, hard acids (such as alkali metal cations) bind strongly in a predominantly electrostatic manner to hard bases (such as OH^-, F^-, H_2O, NH_3). While factors other than polarizability certainly influence bonding, the hard/soft acid/base classification assists in understanding metal-ligand interactions. In the present context, a bifunctional ligand is likely to be hemilabile if it consists of a donor that is matched in terms of hardness to the metal linked to another donor that is hardness-mismatched to the metal.

For the most part, hemilabile ligands have been developed for homogeneous catalysis applications, where 'pseudo-vacant coordination sites' or easily displaceable 'intramolecular solvent molecules' are desirable in order to facilitate the binding of small-molecule substrates to transition metal-based catalysts. Studies of hemilabile ligands have also been motivated by interest in small-molecule activation and stabilization of reactive transition-metal complexes. There are a number of reviews available on the subject of hemilabile ligands[66-68] that outline the motivations and provide detailed summaries of the diverse literature on this topic.

References begin on page 26.

Table 1.1. Classification[65] of Lewis acids and bases[a]

	Hard	Borderline	Soft
Acids	H^+, Li^+, Na^+, K^+	Fe^{2+}, Co^{2+}, Ni^{2+}	Cu^+, Ag^+, Au^+, Tl^+, Hg^+
	Be^{2+}, Mg^{2+}, Ca^{2+}	Cu^{2+}, Zn^{2+}, Pb^{2+}	Ru^{2+}, Pd^{2+}, Cd^{2+}, Pt^{2+}, Hg^{2+}
	Cr^{2+}, Cr^{3+}, Al^{3+}	SO_2, BBr_3	BH_3
	SO_3, BF_3		
Bases	F^-, OH^-, H_2O, ROH	NO_2^-, SO_3^{2-}, Br^-	H^-, R^-, $\underline{C}N^-$, $\underline{C}O$
	R_2O, CO_3^{2-} NO_3^-, O^{2-}	N_3^-, N_2	I^-, $\underline{S}CN^-$, PR_3
	SO_4^{2-}, PO_4^{3-}, ClO_4^-	Py, $SC\underline{N}^-$	C_6H_6, R_2S, S^{2-}, $DM\underline{S}O$
	$DMS\underline{O}$, NH_3, CH_3CN		

[a]The underlined atom is the donor site being classified.

1.4.2 The natural connection between hemilability and chemical sensing

Transition-metal complexes of hemilabile ligands are attractive candidates for molecule-based chemosensors because of their intrinsic capacity for reversible reaction with a variety of small molecules. Given that changes in a metal's coordination sphere often cause changes in readily monitored properties, such as colour, luminescence or reduction potential, one can envision a host of possible designs for chemosensors based on hemilability. While examples of this sort in the literature are few, interest in this direction has recently increased.[68]

The first study of hemilability described in terms of chemical sensing was reported by Dunbar and co-workers in 1992.[69] They have extensively studied the reactions of carbon monoxide with cationic Rh(I) and Rh(II) complexes[70,71] that contain the hemilabile phosphine-ether ligand tris(2,4,6-trimethoxyphenyl)phosphine (TMPP). The Rh(I) monocarbonyl complex shown in Scheme 1.8 reacts with CO, a process that is accompanied by absorption changes in both the visible and IR regions of the spectrum as well as a change in the metal's reduction potential. The reaction is reversible and the response is selective for CO in the presence of O_2, CO_2, N_2 and H_2 under ambient conditions. Furthermore, the reversible response to CO is maintained when the CO-sensing complex is incorporated[69] into solid-phase

References begin on page 26.

thin films of zirconia glass prepared via the sol-gel process (chemical sensing using sol-gels has been recently reviewed[72-74]). Thus, this complex is a very promising molecule-based CO sensor.

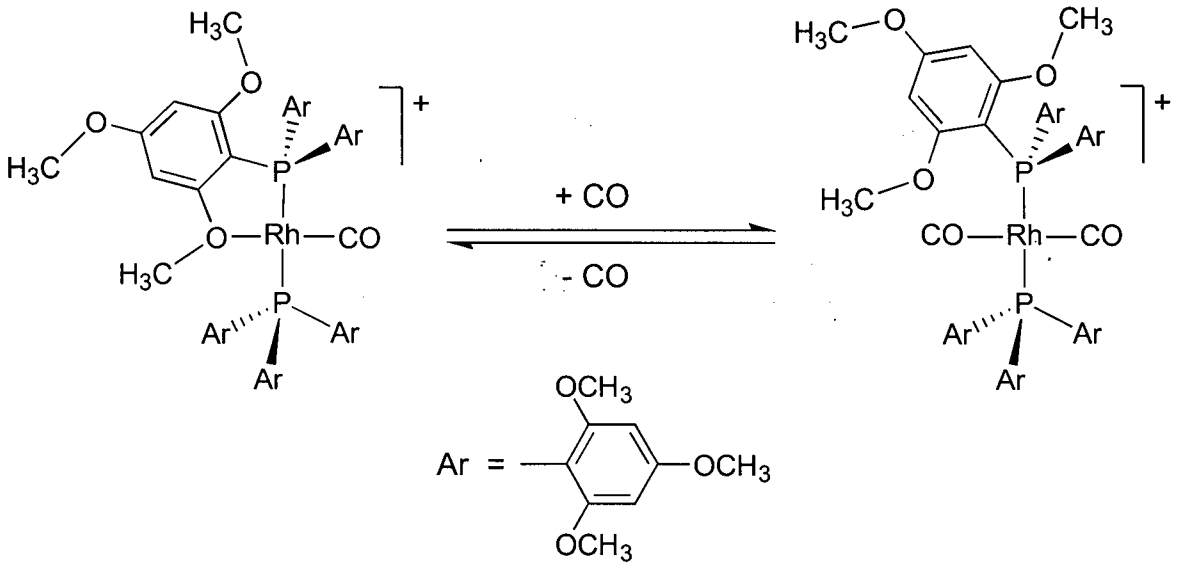

Scheme 1.8.

1.5 The scope of this thesis

The motivation behind the work presented in this thesis has been an interest in investigating the chemical sensing capability of transition-metal complexes designed to have luminescence properties that are influenced by the coordination of small molecules to the metal centre. Two distinct routes to coordination-dependent luminescence have been investigated; one exploits a metal-based lumophore and the other an organic-based lumophore. The unifying theme of this thesis, however, is the use of hemilabile phosphine-ether ligands on Ru(II) to provide a receptor site for small molecules. The suitability of hemilabile ligands for this role has been clearly established by the work described above from the Dunbar laboratory.

In Part 1 of this thesis (Chapters Two to Six), the hemilabile approach to molecular sensing is used wherein small-molecule analytes coordinate directly to a transition metal-based

References begin on page 26.

lumophore. In this work, a MLCT lumophore based on Ru bis(2,2'-bipyridine) was used. Changes in the coordination sphere of the metal upon binding of small-molecule analytes influence the energetics of the metal-based orbitals and therefore change the MLCT-derived emission spectra. An introduction to the Ru-bipyridyl lumophore is provided in Chapter Two, followed by studies of the reactivity of a Ru bipyridyl phosphine-ether complex; the luminescence response of this complex to small-molecule coordination is discussed in Chapter Three. Chapter Four deals with a side reaction encountered during the preparation of Ru(II) bis(bipyridyl) phosphine-ether complexes, specifically the dealkylation of the coordinated ether moiety by free phosphine-ether ligand. Chapter Five deals with the effects of changes in the hemilabile ligands on the lability of the ether moiety. In Chapter Six, an attempt to improve the room temperature luminescence of the MLCT lumophore is described, which involved replacement of the phosphine donor in the hemilabile ligand with a nitrogen-based donor. In light of the goals of this work, the most promising MLCT-based luminescent small-molecule receptor presented in this thesis is that described in Chapters Two and Three. The practical applicability of this chemosensor, however, is limited by its requirement for low temperatures.

In Part 2 of this thesis (Chapter Seven), the hemilabile approach is used to effect analyte-induced displacement of an organic lumophore away from a transition metal centre. Specifically, a pyrene lumophore was incorporated into a hemilabile phosphine-ether ligand and utilized to prepare a Ru(II) complex that exhibits a dramatic luminescence response to carbon monoxide that occurs at room temperature. The work presented in this chapter forms the basis of a promising new family of small-molecule chemosensors that will be pursued by future workers in the Wolf laboratory.

References begin on page 26.

1.6 References

(1) Mirkin, C. A.; Ratner, M. A. *Annu. Rev. Phys. Chem.* **1992**, *43*, 719.

(2) de Silva, A. P.; Gunaratne, H. Q. N.; Gunnlaugsson, T.; Huxley, A. J. M.; McCoy, C. P.; Rademacher, J. T.; Rice, T. E. *Chem. Rev.* **1997**, *97*, 1515.

(3) Valeur, B.; Leray, I. *Coord. Chem. Rev.* **2000**, *205*, 3.

(4) de Silva, A. P.; Fox, D. B.; Huxley, A. J. M.; Moody, T. S. *Coord. Chem. Rev.* **2000**, *205*, 41.

(5) Prodi, L.; Bolletta, F.; Montalti, M.; Zaccheroni, N. *Coord. Chem. Rev.* **2000**, *205*, 59.

(6) Fabbrizzi, L.; Licchelli, M.; Rabaioli, G.; Taglietti, A. *Coord. Chem. Rev.* **2000**, *205*, 85.

(7) Beer, P. D.; Cadman, J. *Coord. Chem. Rev.* **2000**, *205*, 131.

(8) Watanabe, S.; Onogawa, O.; Komatsu, Y.; Yoshida, K. *J. Am. Chem. Soc.* **1998**, *120*, 229.

(9) Willard, H. H.; Merritt, L. L.; Dean, J. A.; Settle, F. A. *Instrumental Methods of Analysis*; 7th ed.; Wadsworth Publishing Company: Belmont, 1988.

(10) Becker, R. S. *Theory and Interpretation of Fluorescence and Phosphorescence*; Wiley Interscience: Toronto, 1969.

(11) Birks, J. B. *Photophysics of Aromatic Molecules*; Wiley-Interscience: Toronto, 1970.

(12) Turro, N. J. *Modern Molecular Photochemistry*; The Benjamin/Cummings Publishing Co., Inc.: Don Mills, 1978.

(13) Kalyanasundaram, K. *Photochemistry of Polypyridine and Porphyrin Complexes*; Academic Press: Toronto, 1992.

(14) Demas, J. N.; DeGraff, B. A. *Coord. Chem. Rev.* **2001**, *211*, 317.

References begin on page 26.

(15) Parker, D. *Coord. Chem. Rev.* **2000**, *205*, 109.

(16) Wolfbeis, O. S. in *Fiber Optic Chemical Sensors and Biosensors*; Wolfbeis, O. S., Ed.; CRC Press: Boca Raton, FL, 1991; Vol. 2, p. 19.

(17) Bergonzi, R.; Fabbrizzi, L.; Licchelli, M.; Mangano, C. *Coord. Chem. Rev.* **1998**, *170*, 31.

(18) Fabbrizzi, L.; Licchelli, M.; Pallavicini, P.; Parodi, L. *Angew. Chem., Int. Ed. Engl.* **1998**, *37*, 800.

(19) Franz, K. J.; Singh, N.; Spingler, B.; Lippard, S. J. *Inorg. Chem.* **2000**, *39*, 4081.

(20) Franz, K. J.; Singh, N.; Lippard, S. J. *Angew. Chem., Int. Ed. Engl.* **2000**, *39*, 2120.

(21) Corradini, R.; Dossena, A.; Galaverna, G.; Marchelli, R.; Panagia, A.; Sartor, G. *J. Org. Chem.* **1997**, *62*, 6283.

(22) Keefe, M. H.; Benkstein, K. D.; Hupp, J. T. *Coord. Chem. Rev.* **2000**, *205*, 201.

(23) de Silva, A. P.; Fox, D. B.; Huxley, A. J. M.; McClenaghan, N. D.; Roiron, J. *Coord. Chem. Rev.* **1999**, *185*, 297.

(24) Canary, J. W.; Gibb, B. C. *Prog. Inorg. Chem.* **1997**, *45*, 1.

(25) Wright, J. D. *Inst. Phys. Conf. Ser. No 111: Int. Conf. on New Materials and their Applications*, Univ. of Warwick, **1990**, 333.

(26) Robertson, A.; Shinkai, S. *Coord. Chem. Rev.* **2000**, *205*, 157.

(27) Zhou, R.; Josse, F.; Gopel, W.; Ozturk, Z. Z.; Bekaroglu, O. *Appl. Organomet. Chem.* **1996**, *10*, 557.

(28) Brunink, J. A. J.; Di Natale, C.; Bungaro, F.; Davide, F. A. M.; D'Amico, A.; Paolesse, R.; Boschi, T.; Faccio, M.; Ferri, G. *Anal. Chim. Acta* **1996**, *325*, 53.

References begin on page 26.

(29) Di Natale, C.; Paolesse, R.; Macagnano, A.; Troitsky, V. I.; Berzina, T. S.; D'Amico, A. *Anal. Chim. Acta* **1999**, *384*, 249.

(30) Hierlemann, A.; Ricco, A. J.; Bodenhofer, K.; Gopel, W. *Anal. Chem.* **1999**, *71*, 3022.

(31) Ashkenasy, G.; Ivanisevic, A.; Cohen, R.; Felder, C. E.; Cahen, D.; Ellis, A. B.; Shanzer, A. *J. Am. Chem. Soc.* **2000**, *122*, 1116.

(32) Ivanisevic, A.; Reynolds, M. F.; Burstyn, J. N.; Ellis, A. B. *J. Am. Chem. Soc.* **2000**, *122*, 3731.

(33) Ivanisevic, A.; Ellis, A. B.; Ashkenasy, G.; Shanzer, A.; Rosenwaks, Y. *Langmuir* **2000**, *16*, 7852.

(34) Dolphin, D., Ed. *The Porphyrins*; Vols. 1-7, Academic Press: New York, 1977.

(35) Roosli, S.; Pretsch, E.; Morf, W. E.; Tsuchida, E.; Nishide, H. *Anal. Chim. Acta* **1997**, *338*, 119.

(36) Matsui, J.; Tachibana, Y.; Takeuchi, T. *Anal. Commun.* **1998**, *35*, 225.

(37) Rakow, N. A.; Suslick, K. S. *Nature* **2000**, *406*, 710.

(38) Amao, Y.; Asai, K.; Okura, I. *J. Porphyrins Phthalocyanines* **2000**, *4*, 292.

(39) Amao, Y.; Asai, K.; Miyashita, T.; Okura, I. *Polym. Adv. Technol.* **2000**, *11*, 705.

(40) Amao, Y.; Okura, I. *Analyst* **2000**, *125*, 1601.

(41) Bedlek-Anslow, J.; Hubner, J.; Carroll, B.; Schanze, K. *Langmuir* **2000**, *16*, 9137.

(42) Holmes-Smith, A.; Hamill, A.; Campbell, M.; Uttamlal, M. *Analyst* **1999**, *124*, 1463.

(43) Ji, H.; Shen, Y.; Hubner, J.; Carroll, B.; Schmehl, R.; Simon, J.; Schanze, K. *Appl. Spec.* **2000**, *54*, 856.

(44) Lee, S.; Okura, I. *Anal. Chim. Acta* **1997**, *342*, 181.

References begin on page 26.

(45) Lee, S.; Okura, I. *Spectrochim. Acta, Part A* **1998**, 91.

(46) Mills, A.; Lepre, A. *Anal. Chem.* **1997**, *69*, 4653.

(47) Catalano, V. J.; Kar, H. M.; Garnas, J. *Angew. Chem., Int. Ed. Engl.* **1999**, *38*, 1979.

(48) Chan, W.-H.; Mak, T. C. W.; Che, C.-M. *J. Chem. Soc., Dalton Trans.* **1998**, 2275.

(49) Forward, J. M.; Fackler, J. P., Jr.; Assefa, A. in *Photophysical and Photochemical Properties of Gold(I) Complexes* in *Optoelectronic Properties of Inorganic Compounds*; Roundhill, D. M. and Fackler, J. P., Jr., Eds.; Plenum Press: New York, 1999, pp. 195-229.

(50) Terheijden, J.; van Koten, G.; Mul, W. P.; Stufkens, D. J. *Organometallics* **1986**, 519.

(51) Albrecht, M.; Gossage, R. A.; Frey, U.; Ehlers, A. W.; Baerends, E. J.; Merbach, A. E.; van Koten, G. *Inorg. Chem.* **2001**, *40*, 850.

(52) Albrecht, M.; Hovestad, N. J.; Boersma, J.; van Koten, G. *Chem. Eur. J.* **2001**, *7*, 1289.

(53) Albrecht, M.; van Koten, G. *Adv. Mater.* **1999**, *11*, 171.

(54) Albrecht, M.; Gossage, R. A.; Lutz, M.; Spek, A. L.; van Koten, G. *Chem. Eur. J.* **2000**, *6*, 1431.

(55) Albrecht, M.; Rodriguez, G.; Schoenmaker, J.; van Koten, G. *Org. Lett.* **2000**, *2*, 3461.

(56) Takeuchi, M.; Yamamoto, M.; Shinkai, S. *Chem. Commun.* **1997**, 1731.

(57) Cabell, L. A.; Best, M. D.; Lavigne, J. J.; Schneider, S. E.; Perreault, D. M.; Monahan, M. K.; Anslyn, E. V. *J. Chem. Soc., Perkin Trans. II* **2001**, 315.

(58) De Santis, G.; Fabbrizzi, L.; Licchelli, M.; Poggi, A.; Taglietti, A. *Angew. Chem. Int. Ed. Engl.* **1996**, *35*, 202.

(59) Fabbrizzi, L.; Licchelli, M.; Parodi, L.; Poggi, A.; Taglietti, A. *Eur. J. Inorg. Chem.* **1999**, 35.

References begin on page 26.

(60) Fabbrizzi, L.; Francese, G.; Licchelli, M.; Perotti, A.; Taglietti, A. *Chem. Commun.* **1997**, *6*, 581.

(61) Shionoya, M.; Ikeda, T.; Kimura, E.; Shiro, M. *J. Am. Chem. Soc.* **1994**, *116*, 3848.

(62) Kimura, E.; Ikeda, T.; Shionoya, M. *Pure & Appl. Chem.* **1997**, *69*, 2187.

(63) Jenkins, A. L.; Uy, O. M.; Murray, G. M. *Anal. Commun.* **1997**, *34*, 221.

(64) Jeffrey, J. C.; Rauchfuss, T. B. *Inorg. Chem.* **1979**, *18*, 2658.

(65) Shriver, D. F.; Atkins, P. W. *Inorganic Chemistry*; 3rd ed.; W. H. Freeman and Company: New York, 1999; pp. 167-169.

(66) Bader, A.; Lindner, E. *Coord. Chem. Rev.* **1991**, *108*, 27.

(67) Slone, C. S.; Weinberger, D. A.; Mirkin, C. A. *Prog. Inorg. Chem.* **1999**, *48*, 233.

(68) Braunstein, P.; Naud, F. *Angew. Chem., Int. Ed. Engl.* **2001**, *40*, 680.

(69) Dulebohn, J. I.; Haefner, S. C.; Berglund, K. A.; Dunbar, K. R. *Chem. Mater.* **1992**, *4*, 506.

(70) Dunbar, K. R.; Haefner, S. C.; Swepston, P. N. *J. Chem. Soc., Chem. Commun.* **1991**, 460.

(71) Haefner, S. C.; Dunbar, K. R.; Bender, C. *J. Am. Chem. Soc.* **1991**, *113*, 9540.

(72) Ingersoll, C. M.; Bright, F. V. *Chemtech* **1997**, 26.

(73) Wolfbeis, O. S.; Reisfeld, R.; Oehme, I. *Struct. Bonding* **1996**, *85*, 51.

(74) Lev, O.; Tsionsky, M.; Rabinovich, L.; Glezer, V.; Sampath, S.; Pankratov, I.; Gun, J. *Anal. Chem.* **1995**, *67*, 22A.

References begin on page 26.

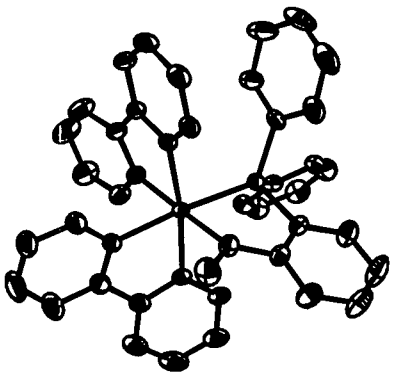

Chapter Two

A Ru(II) bis(bipyridyl) complex containing a hemilabile phosphine-ether ligand and its ability to coordinate small molecules

2.1 Introduction to Ru bipyridyl-based lumophores

Tris-chelate complexes of Ru(II) with bidentate diimine ligands, such as 2,2'-bipyridyl and 1,10-phenanthroline, are low-spin d^6 octahedral complexes that have several remarkable characteristics. The most striking among these is their strong, long-lived photoluminescence in solution at room temperature. In addition, they reversibly undergo electron- and energy-transfer processes, which has led to extensive study of these complexes as potential photocatalysts for the decomposition of water into H_2 and O_2, and in light-harvesting photoelectrochemical cells. To add to the appeal of these intriguing properties, the complexes tend to exhibit remarkably high chemical and photochemical stability. Numerous reviews[1-4] and books[5,6] are available that describe the fascinating photochemistry and photophysics of polyimine complexes of Ru(II) and their applications.

References begin on page 69.

The first class of molecule-based sensors presented in this thesis is based on analyte-induced modulation of the photoluminescence from a metal-to-ligand charge transfer (MLCT) lumophore with the general structure: [*cis*-Ru(bpy)$_2$LL']$^{2+}$. As an introduction, the well-known MLCT lumophore [Ru(bpy)$_3$]$^{2+}$ will be discussed in some detail, followed by a brief description of the effect of nonchromophoric ligands on the lumophore.

2.1.1 The [Ru(bpy)$_3$]$^{2+}$ lumophore

The best-known MLCT lumophore[5] is [Ru(bpy)$_3$]$^{2+}$, an orange complex that emits orange light when photoexcited. Figure 2.1 shows the absorption and emission spectra for this complex at room temperature. The UV absorptions correspond mainly to bpy-based π-π^* transitions, while the visible band ($\lambda_{max} \approx 452$ nm) that accounts for the orange colour of the complex arises from metal-to-ligand charge transfer (Ru dπ to bpy π^*). The MLCT transition is a spin-allowed process. Because of the presence of the heavy Ru atom, the excited state manifold is of mixed singlet-triplet character, but the emissive MLCT excited state has been assigned as a predominantly triplet state. Thus, the ligand-to-metal charge transfer (LMCT) emission process from this excited state is largely spin-forbidden and, therefore, relatively long lived ($\tau = 0.6$ μs at 25 °C). The quantum yield for emission from the MLCT state is quite high ($\Phi = 0.042$) even at room temperature.

The emission spectrum of [Ru(bpy)$_3$]$^{2+}$ contains one broad band with maximum intensity at ~ 602 nm. The spectrum is relatively insensitive to the excitation wavelength because of rapid internal conversion of the higher excited states and intersystem crossing to the low-lying triplet MLCT state. The emission is, however, very sensitive to the medium: solvent polarity affects the spectral energy; oxygen quenches the emission; and finally, the emission shows a strong temperature dependence ($\tau \approx 5$ μs, $\Phi \approx 0.4$ at 77 K),[5] a phenomenon that will be elaborated upon in section 2.1.3.

References begin on page 69.

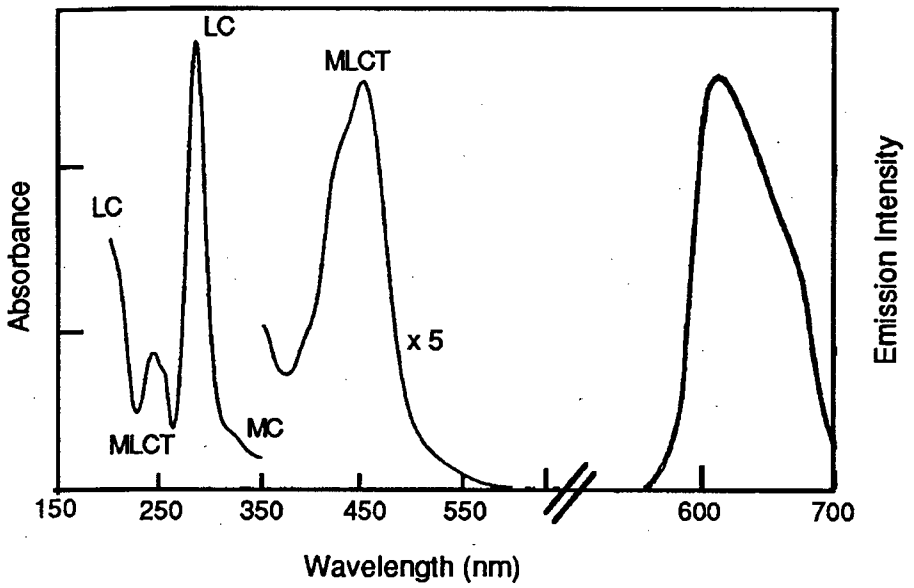

Figure 2.1. Absorption and emission spectra for $[Ru(bpy)_3]^{2+}$ in aqueous solution at 25 °C. Bands are labeled according to the origin of the transitions: MC = metal-centred; LC = ligand-centred; MLCT = metal-to-ligand charge transfer. Reproduced with permission from the book by Kalyanasundaram (© Academic Press, 1992).[5]

2.1.2 The effects of nonchromophoric ancillary ligands: [*cis*-Ru(bpy)$_2$LL']$^{2+}$

Replacement of one of the bipyridyl ligands in $[Ru(bpy)_3]^{2+}$ by nonchromophoric ancillary ligands (herein abbreviated as L, L') leads to significant changes in the photophysical properties of the lumophore, which depend upon the nature of the ancillary ligand. Provided that L and L' are less easily reduced than the bpy ligands, the lowest-energy electronic transition is still an MLCT process. A series of complexes of the type $[cis\text{-}Ru(bpy)_2LL']^{2+}$ has been studied by Caspar and Meyer,[7] with a range of ancillary ligands that includes pyridine, an amino-substituted pyridine, and aryl-substituted phosphines and arsines. In general, complexes with nitrogen-donor ancillary ligands show similar or lower energy MLCT absorption and emission than $[Ru(bpy)_3]^{2+}$. Phosphines and arsines lead to higher energy MLCT absorption and emission. As will be discussed in section 2.1.3, the nonchromophoric ligands can also have a profound effect on the temperature dependence of the luminescence.

References begin on page 69.

The MLCT excited state arises from promotion of an electron from a metal-based dπ orbital to a bpy π* orbital; the excited electron is delocalized over the bpy rings in the excited complex.[8] The nonchromophoric ligands have been shown to predominantly influence the energetics of the metal-based orbitals, and they affect the degree of stabilization of the Ru(II) state over the Ru(III) state according to the ligand-induced variations in the $Ru^{III/II}$ reduction potential. The reduction of the bpy ligands is affected to a lesser degree by changes in the nonchromophoric ligands since they are somewhat removed from the Ru-L coordination site. Thus, variations in the nonchromophoric ligands are known to perturb the energetics of the MLCT transition and the emission from the resulting excited state.

2.1.3 The temperature dependence of luminescence from the MLCT state

The long-lived triplet MLCT states of Ru(II) bipyridyl complexes are typically highly emissive, especially at low temperatures. Because the excited state lifetime is long, nonradiative deactivation processes may occur before emission takes place, but at low temperatures, the rates of these competing processes are slow. As the temperature increases, nonradiative processes become increasingly competitive, which results both in decreased luminescence quantum yields and decreased excited-state lifetimes. To illustrate, the emission lifetime of deaerated solutions of $[Ru(bpy)_3]^{2+}$ decreases from 5.21 μs at 77 K ($\Phi = 0.38$)[9] in immobilized glass to 0.49 μs at 25 °C ($\Phi = 0.029$)[7] in fluid solution, largely (but not entirely) because of increased nonradiative deactivation. $[Ru(bpy)_3]^{2+}$ is, however, still highly luminescent in solution at room temperature.

Although $[Ru(bpy)_3]^{2+}$ is luminescent over a wide range of temperatures, replacement of one of the bpy ligands by other nonchromophoric ligands often leads to complexes that exhibit markedly temperature-dependent luminescence. This temperature dependence arises because of the existence of a nonluminescent metal-centred excited state (denoted dd) that is accessible from the long-lived MLCT state via a small activation barrier, E_a, as schematically depicted in Figure 2.2. As the temperature increases, the electronically excited molecules have

References begin on page 69.

sufficient thermal energy to overcome E_a; above a certain temperature, MLCT emission is switched off completely.

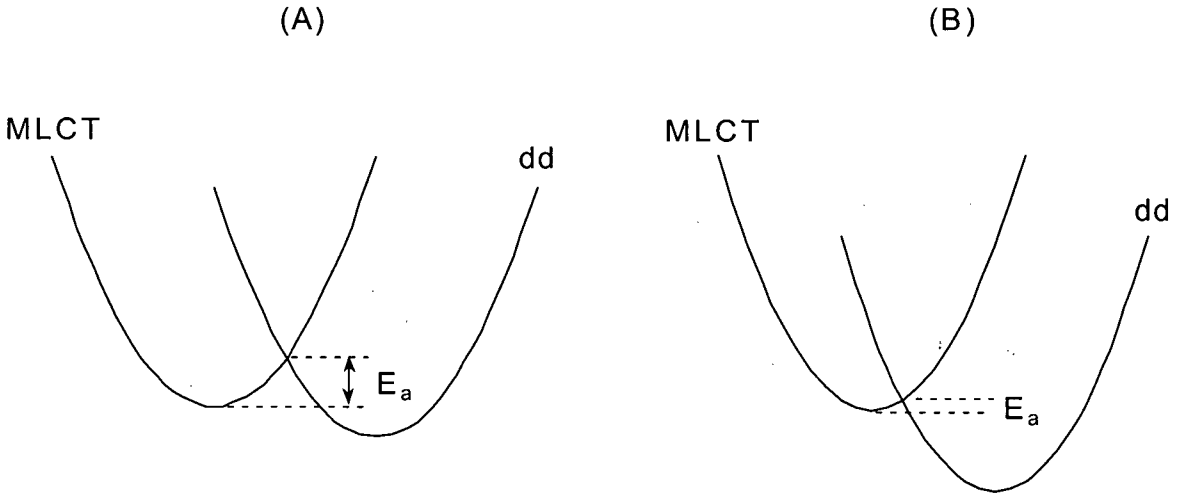

Figure 2.2. Schematic energy diagrams to illustrate the effect of ligand variation in [*cis*-Ru(bpy)$_2$LL']$^{2+}$ complexes on the thermal accessibility of nonemissive metal-centred (dd) excited states. (A) L = nitrogen-donor ligand (E_a = 2700 – 3600 cm^{-1}); (B) L = tertiary phosphine or arsine (E_a < 850 cm^{-1}). Adapted from ref 7 with permission, © A.C.S., 1983).

The relative energies of the MLCT and dd states depend on the nature of the nonchromophoric ancillary ligands (L, L').[7] For complexes with nitrogen-based nonchromophoric ligands (*e.g.*, pyridine), the thermal barrier is relatively large and emission can be measured at room temperature. With phosphine and arsine ligands, however, the barrier is small, which leads to complete thermal deactivation of the emissive excited state well below room temperature (T < 200 K). In some cases the thermal barrier is entirely absent; for example, there is no detectable emission at 77 K for the complex [*cis*-Ru(bpy)$_2$(CO)Cl]$^+$.

In theory, by measuring the temperature dependence of the emission lifetime, it is possible to determine the magnitude of the activation barrier to the dd state. Based on

References begin on page 69.

Equation 2.1,[7] a plot of -ln(τ) *vs.* 1/T should yield a straight line with negative slope ($-E_a/k_B$) from which the activation barrier can be calculated.

$$\frac{1}{\tau} = k_{obs} + A\exp(-E_a/k_B T) \qquad [2.1]$$

The rate constant k_{obs} is the sum of the rate constants for radiative (k_r) and nonradiative (k_{nr}) decay processes for the MLCT excited states. In combination with quantum yield measurements, it is possible to determine a value for k_r and therefore k_{nr}; however, quantum yields were not measured in the present work.

2.2 Small-molecule sensing based on changes in nonchromophoric ligands

It is upon the premise of ligand-dependent photophysics that the first generation of luminescent molecule-based sensors described in this thesis was constructed. A [*cis*-Ru(bpy)$_2$LL']$^{2+}$ lumophore was conceived in which the nonchromophoric ligands L and L' are covalently linked to one another, and they each bind to the metal centre with different affinities. This differential binding strength permits one of the coordination sites to be substitutionally labile such that, together, L and L' comprise a hemilabile bidentate ligand, which enables other Lewis basic small molecules to coordinate to the metal centre. Such a reaction results in a change in the nonchromophoric ligands of the lumophore, which should then lead to measurable changes in its photophysical properties.

In this scenario, the binding event occurs directly at the metal centre rather than in the ligand periphery, and thus, the lumophore itself acts as the analyte receptor. Molecular sensors based on this approach are amenable to multianalyte sensing, because the Ru(II) centre is capable of coordinating a variety of Lewis bases. The metal-analyte interaction may be relatively nonspecific, but the sensitivity of the [*cis*-Ru(bpy)$_2$LL']$^{2+}$ lumophore to changes in its nonchromophoric ligand permits different types of Lewis basic small molecules to be distinguished. Furthermore, the hemilabile nature of the nonchromophoric ligand encourages reversible binding of analytes.

References begin on page 69.

2.2.1 Choice of hemilabile ligands

Based on the selection of the [*cis*-Ru(bpy)$_2$LL']$^{2+}$ lumophore, the hemilabile ligands of choice for this work are necessarily those that coordinate to Ru(II). Phosphines, which are soft bases, bind strongly to Ru(II), which is a soft acid, and therefore can function to anchor a hemilabile ligand to the metal centre. Conversely, hard bases such as ethers bind weakly to Ru(II) and can therefore be displaced by donor molecules that are better suited to interaction with the soft metal. Indeed, there is a large body of work that concerns the hemilabile coordination chemistry of phosphine-ether ligands (denoted POR) on Ru(II),[10-13] in particular with respect to complexes of the type $RuCl_2(POR)_2$.[14-18] In these complexes, the phosphine is typically a diphenylphosphine derivative, and the third substituent on the phosphorus is either an ether-substituted aryl or alkyl group. For this work, simple triphenylphosphine derivatives with a single ether substituent positioned *ortho* to the phosphorus, such as 2-methoxyphenyldiphenylphosphine (abbreviated as POMe), were selected because they display the desired hemilability on Ru(II).[10,15] Conveniently, they are easy to synthesize and are relatively air-stable.

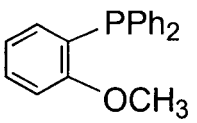

POMe

2.2.2 The scope of this chapter

The parent luminescent small-molecule receptor of this work is [*cis*-Ru(bpy)$_2$(POMe-*P,O*)](PF$_6$)$_2$, **1**, which contains the hemilabile phosphine-ether ligand POMe. This chapter begins with a description of the preparation and structural characterization of this complex. A discussion of the reactivity of **1** toward several Lewis basic small molecules and its natural ability to act as a receptor follows. The redox and photophysical properties of **1** and its response to small-molecule coordination are presented in Chapter Three, along with an evaluation of **1** with respect to its applicability to small-molecule sensing.

References begin on page 69.

2.3 Synthesis and structural characterization of 1

2.3.1 Preparation of complex 1

Ruthenium bis(bipyridyl) complexes are generally accessed from the easily prepared Ru(II) dichloro complex, Ru(bpy)$_2$Cl$_2$•2H$_2$O.[19] Replacement of the chlorides by neutral ligands such as phosphines to yield dicationic complexes is typically achieved in one of two ways:

(a) via direct displacement of the chlorides by treatment of Ru(bpy)$_2$Cl$_2$•2H$_2$O with excess ligand in boiling aqueous ethanol;[20] or,

(b) via a two-step reaction in which Cl^- is first removed by Ag^+ in a coordinating solvent to form a complex such as [*cis*-Ru(bpy)$_2$(acetone)$_2$](BF$_4$)$_2$,[20,21] followed by displacement of the weakly coordinated solvent molecules by other neutral ligands.

These routes have both been successfully used for the preparation of bis(phosphine) complexes, although substitution by way of the acetone complex is more efficient in some cases.[20]

The synthesis of complex **1** was first attempted using the direct substitution route, via the treatment of Ru(bpy)$_2$Cl$_2$•2H$_2$O with the phosphine-ether ligand POMe in boiling aqueous ethanol. Although this route did lead to the desired complex, there were difficulties that arose from a side reaction in which free ligand nucleophilically attacks the *P,O*-complex (see Chapter Four).[22] The synthesis was also attempted in boiling ethylene glycol solution,[23] but the side reaction dominated under those conditions. The best results were obtained using the labile acetone complex; this route to complex **1** is shown in Scheme 2.1.[24]

Phosphine-ether complex **1** was prepared by reaction of Ru(bpy)$_2$Cl$_2$•2H$_2$O with Ag^+ in acetone solution at room temperature, followed by removal of the precipitated AgCl and treatment of the resulting [*cis*-Ru(bpy)$_2$(acetone)$_2$](BF$_4$)$_2$ solution with one equivalent of POMe in boiling acetone solution for several hours. The wine-red bis(acetone) complex oxidizes to a green solution if exposed to air, so it was prepared as needed and used *in situ*

References begin on page 69.

rather than isolated. Displacement of the coordinated acetone by the phosphine-ether ligand was accompanied by a colour change, from deep wine-red to clear orange, at which point the phosphine-ether complex was isolated. It is important to use accurate 1:1 metal-ligand stoichiometry in this reaction, because free phosphine-ether present in the reaction mixture can react with the desired bidentate phosphine-ether complex. This nucleophilic attack of free phosphine on the ruthenium-bound ether moiety is the topic of Chapter Four.

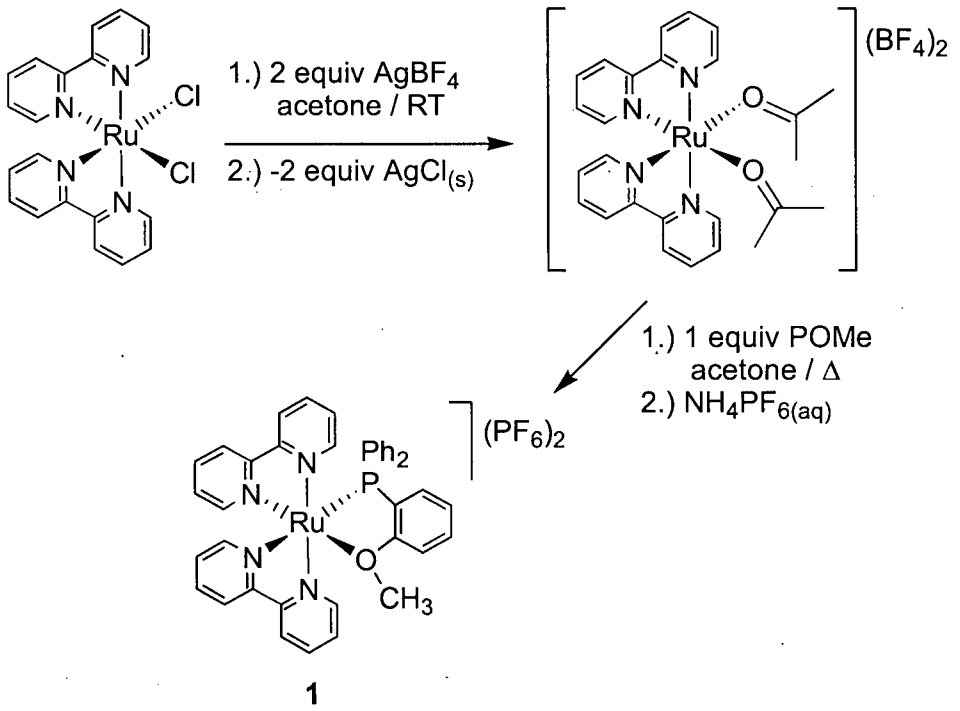

1

Scheme 2.1.

Complex **1** was purified based on its solubility properties. Chromatography was in general unsuccessful. Chromatographic purification of related complexes of the type [*cis*-Ru(bpy)$_2$(PR$_3$)$_2$](PF$_6$)$_2$ typically requires the use of coordinating solvents (*e.g.*, acetonitrile)[20] that react with complex **1**, as will be discussed later in this chapter. Thus, the complex was purified as follows. First, the crude tetrafluoroborate salt was converted into the hexafluorophosphate salt by salt metathesis via precipitation of an acetone solution of the BF_4^- salt by addition of aqueous NH_4PF_6. The precipitated yellow-orange PF_6^- salt was collected by filtration, and any unreacted solvate complex remained in the filtrate. Additional purification

References begin on page 69.

was achieved by repeated precipitation of the PF_6^- salt from acetone solution by the addition of diethyl ether, or from dichloromethane solution by the addition of hexanes. Finally, the complex was recrystallized from hot methanol. Samples of analytical purity were typically obtained after one precipitation from organic solvent mixtures. Complex **1** is a yellow-orange powder that is soluble in polar organic solvents and shows no sign of decomposition after 10 days in air-saturated solution.

2.3.2 Crystallographic characterization of 1

Red block-shaped crystals of **1** suitable for X-ray crystallographic analysis were obtained by crystallization from hot methanol solution. An ORTEP depiction of the solid-state molecular structure of **1** is depicted in Figure 2.3. The crystallographic data, collection and refinement details are presented in Appendix 2.1.

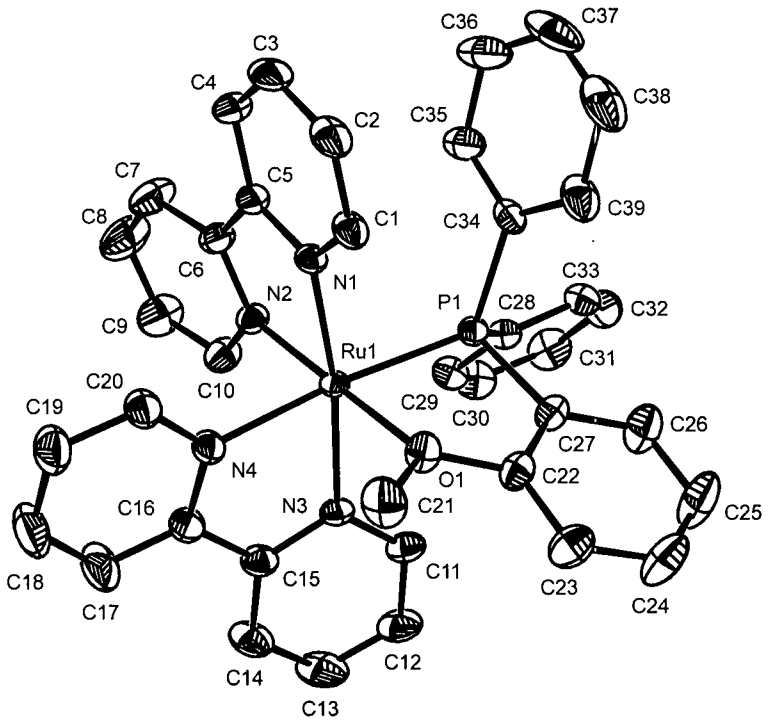

Figure 2.3. ORTEP representation of the solid-state molecular structure of **1**, [*cis*-Ru(bpy)$_2$(POMe-*P,O*)](PF$_6$)$_2$. Thermal ellipsoids are drawn at the 50% probability level. Hydrogen atoms and hexafluorophosphate counterions are omitted for clarity.

References begin on page 69.

The POMe ligand is bound to the metal in a bidentate fashion via both the phosphine and ether, and the geometry of the complex is distorted octahedral. Relevant bond lengths and angles are listed in Table 2.1. The Ru-P bond length of 2.2908(6) Å in **1** is somewhat longer than those in *trans,cis,cis*-RuCl$_2$(POMe-*P,O*)$_2$ (2.219(1) and 2.217(1) Å), an octahedral Ru(II) complex that contains the same phosphine-ether ligand.[15] The longer bond is not surprising since the phosphine in **1** is *trans* to a π-accepting bipyridyl ligand and therefore must compete for backbonding to the metal, whereas in RuCl$_2$(POMe-*P,O*)$_2$ the phosphines are *trans* to σ- and π-donating ether ligands. The Ru-O bond length of 2.172(2) Å is shorter than those in RuCl$_2$(POMe-*P,O*)$_2$ (2.299(3) and 2.257(3) Å),[10,15]; in fact, it is closer to the Ru-O distance (2.143 Å) observed in a Ru(III) ester complex.[25]

Table 2.1. Selected bond distances and angles for **1**.

	Distances (Å)		
Ru(1)-O(1)	2.171(2)	Ru(1)-P(1)	2.2908(6)
Ru(1)-N(1)	2.050(2)	Ru(1)-N(2)	2.030(2)
Ru(1)-N(3)	2.095(2)	Ru(1)-N(4)	2.112(2)
O(1)-C(21)	1.441(3)	O(1)-C(22)	1.395(3)
	Angles (°)		
P(1)-Ru(1)-O(1)	80.14(4)	P(1)-Ru(1)-N(1)	89.85(5)
P(1)-Ru(1)-N(2)	101.89(6)	P(1)-Ru(1)-N(3)	98.76(5)
O(1)-Ru(1)-N(1)	96.68(7)	O(1)-Ru(1)-N(3)	85.70(6)
O(1)-Ru(1)-N(4)	95.23(7)	N(1)-Ru(1)-N(2)	79.04(7)
N(1)-Ru(1)-N(4)	93.84(7)	N(2)-Ru(1)-N(3)	98.21(7)
N(2)-Ru(1)-N(4)	82.97(8)	N(4)-Ru(1)-N(3)	77.63(7)

References begin on page 69.

2.3.3 Solution structure of 1

In the solid-state molecular structure of **1**, the methoxy hydrogens are predicted to be in close proximity (< 3 Å on average) to both the neighbouring phenyl H (*ortho* to oxygen) and a hydrogen at the 6-position of one of the bipyridine rings. Thus, if the ligand's coordination mode in solution is bidentate as it is in the solid state, a nuclear Overhauser enhancement (NOE) should be observed between the methoxy protons and one 6-position bipyridyl proton. Table 2.2 lists the predicted distances between relevant hydrogen atoms in **1** and the expected strength of NOE. Regardless of the coordination mode, a NOE should be observed between the methoxy protons and the phenyl proton that is *ortho* to oxygen.

Irradiation at the methoxy protons' resonance (δ3.71) leads to enhancement of only two resonances in the aromatic region at δ 8.30 (d) and δ7.33 (dd, coupled to ^{31}P). Using ^{1}H{^{31}P} NMR spectroscopy and two-dimensional ^{1}H correlation spectroscopy (COSY), these signals were assigned to a bpy 6-H and the $PhOCH_3$ hydrogen *ortho* to oxygen. The absence of a NOE to other phenyl hydrogens suggests that the methoxy group does not spend an appreciable amount of time oriented away from the metal, as it presumably would if the ligand was bound in a monodentate fashion via only the phosphorus.

Furthermore, the ^{1}H NMR spectrum of **1** obtained at -80 °C (CD_2Cl_2) is unchanged from the spectrum at 25 °C. Thus, either the opening-and-closing of the phosphine-ether chelate ring does not occur on the NMR timescale or the opening-and-closing process is still fast at low temperature (-80 °C). Overall, these NMR spectral data are consistent with the hypothesis that the solution structure of **1** is predominantly the same as that in the solid state but are not conclusive. It should be noted, however, that a small amount of monodentate phosphine-bound complex, either 5-coordinate or with a bound solvent molecule, may be present but is below the detection limit of the NMR experiment.

References begin on page 69.

Table 2.2. H-H distances[a] from solid-state structure of **1** and expected strength of NOE

Type	Atom Label	Description	Atom Label	Distance (Å)	Expected strength of NOE
CH_3		Ph H *ortho* to Me	H20	1.712[b]	strong
CH_3		bpy H on C1	H1	2.488[b]	medium
CH_3		bpy H on C20	H16	2.897[b]	weak
bpy H on C1	H1	Ph H on C39	H33	3.389	weak
	H1	bpy H on C2	H2	2.351	medium
bpy H on C20	H16	bpy H on C19	H15	2.353	medium

[a]Distances calculated based on estimated hydrogen positions from the solid-state structural data using ORTEP-32 for Windows. [b]Distance to circle defined by methyl hydrogens calculated assuming free rotation of the methyl group. All CH_3-H distances were measured but only those expected to cause NOE were included in this table.

2.4 Reactivity of 1 toward small molecules

The reactivity of **1** toward a variety of small molecules known to coordinate to transition metals has been explored. Based on Lewis acid/base theory[27] (Chapter One, section 1.4.1), the soft Ru(II) in **1** was predicted to show the following preferences for binding small-molecules: R_3P > CO, R_2S, R_3N, MeCN > R_2O. It must be emphasized, however, that other factors, such as σ-donor and π-acceptor strengths, play important roles in determining the strength of the metal-ligand interaction.

Small molecules with a range of donor properties were selected in order to investigate the coordinative competition between the incoming donor and the metal-tethered ether moiety. Potential analytes tested include small molecules containing sulfur, nitrogen and oxygen. Phosphorus-containing small molecules were not pursued due to the observation of

References begin on page 69.

nucleophilic dealkylation of **1** by phosphines, mentioned previously and discussed in detail in Chapter Four. Furthermore, in the context of the goals of this work, potential analytes were also chosen with the aim of perturbing the metal-based photophysics; small molecules that induced visible colour changes were given priority. Thus, the similarity in photophysical characteristics between **1** and the known complex [*cis*-Ru(bpy)$_2$(PPh$_2$Me)$_2$]$^{2+}$ (discussed in section 3.3.1) provided little incentive to study phosphine-based analytes.

It was anticipated that the ether would be less easily displaced from the metal in **1** than in the well studied complex *trans,cis,cis*-RuCl$_2$(POMe-*P,O*)$_2$[15,18] because the Ru-O bond in **1** is significantly shorter. This prediction was based on the assumption that a smaller proportion of the complex would exist in a 'receptive' 5-coordinate form if indeed the shorter Ru-O bond indicates that the ether is more strongly bound to the metal. The ether-displacement likely occurs through a largely dissociative mechanism, as is generally accepted for substitution reactions at Ru(II) complexes;[26] detailed kinetic studies with each analyte would be required to establish whether reaction occurs via a dissociative or associative mechanism (presented in more detail in section 2.4.2.1), and such studies were not included in the present work. Qualitatively, however, different analytes were found to react with **1** at different rates. Importantly, because rapid equilibration between sensor and analyte is critical for chemical sensing applications, small molecules found to react slowly with **1** were not pursued further as analytes.

For the purpose of monitoring the reactions, it was convenient to survey the reactivity of **1** by adding prospective small-molecule analytes to solution NMR samples ([**1**] = ~ 10^{-3} M). The bidentate *P,O*-complex **1** gives rise to a simple $^{31}P\{^1H\}$ NMR spectrum that contains one singlet resonance for the ligand phosphorus (δ 50.9 in CD_2Cl_2; δ 52.8 in acetone-d_6) and one septet resonance for the PF_6^- counterions. As well, the ^1H NMR spectrum of **1** contains a peak from the methoxy group (CD_2Cl_2: δ 3.71, s) that is well-resolved from the phenyl and bipyridine ^1H signals (δ6.4 – 8.6). Both the ligand phosphorus atom and the methoxy protons experience different electronic environments when the ether moiety is displaced from the metal centre by an analyte A, as shown in Scheme 2.2. Thus, reactions are accompanied by significant changes in chemical shift for these resonances and are easily monitored by NMR spectroscopy.

References begin on page 69.

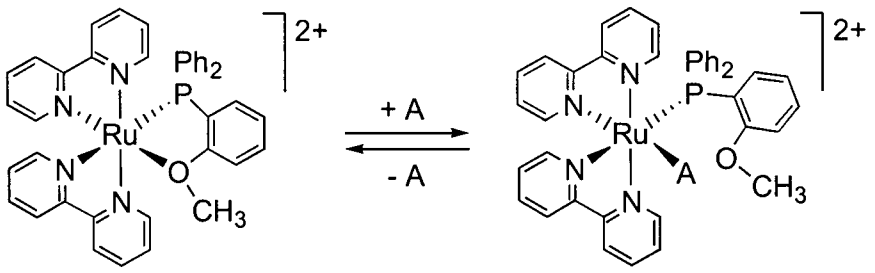

Scheme 2.2.

2.4.1 Reaction with carbon monoxide

As described in Chapter One, transition metal complexes containing hemilabile phosphine-ether ligands have been shown to exhibit reversible reactivity toward CO, and this small molecule was the first potential analyte tested for reactivity in the present work with complex **1**. Solutions of **1** in both CD_2Cl_2 and acetone-d_6 were sparged with CO and sealed under 1 atm of CO, then monitored by ^1H and $^{31}P\{^1H\}$ NMR spectroscopy. However, no immediate visible changes were observed, and no reaction between **1** and CO was detected by NMR spectroscopy after a few hours. After the samples stood for 2 days at 25 °C under 1 atmosphere of CO, NMR spectroscopy revealed approximately 30 % conversion to a new species (in acetone-d_6 solution, $^{31}P\{^1H\}$: δ37.3; ^1H: δ3.47 (s, OCH_3)).

Thermodynamically, coordination of CO is certainly favourable; related carbonyl complexes such as [*cis*-Ru(bpy)$_2$(CO)Cl]$^+$ exist.[7] Under the same conditions as above, the neutral phosphine-ether complex *trans,cis,cis*-RuCl$_2$(POMe-*P,O*)$_2$ reacts immediately with carbon monoxide.[15] When the reduction potential of **1** is considered (section 3.2.1), its relative inertness to CO is not surprising. The Ru centre in **1** is considerably more electron deficient ($E_{ox}(Ru^{III/II})$ = 1.56 V *vs.* SCE) than in RuCl$_2$(POMe-*P,O*)$_2$ ($E_{1/2}(Ru^{III/II})$ = 0.56 V *vs.* SCE).[15] When competition with the π-accepting bpy ligands for backbonding to the metal is also considered, the poor σ-donating ability of CO likely accounts for the sluggish reaction; thus, formation of the carbonyl complex **1•CO** is kinetically rather than thermodynamically

References begin on page 69.

impeded. In the context of chemical sensing, **1** is a poor receptor for CO, and the slow reaction of **1** with carbon monoxide was not investigated in further detail.

2.4.2 Reaction with oxygen donors

The synthesis of **1** involves the use of several oxygen-donor solvents, such as acetone, water and diethyl ether. There was no significant difference between the NMR spectra of **1** determined in the relatively noncoordinating solvent CD_2Cl_2 and in the coordinating solvent acetone-d_6. As well, there was no evidence for reaction of **1** with added water or diethyl ether at concentrations of **1** typically used for NMR spectroscopy (10^{-2} M) in either solvent. Other oxygen-based donors, THF, 1,4-dioxane, methanol and ethanol, were also tested and did not detectably react with **1**. It was not until photophysical experiments were performed at considerably more dilute concentrations that any reaction with oxygen donors was suspected.

2.4.2.1 Reaction with water

Absorption and emission studies of **1** conducted over a range of concentrations (10^{-3} – 10^{-5} M) showed that the spectra are sensitive to the dryness of the solvent used. The discussion of the photophysical studies will be elaborated in Chapter Three (section 3.4.1); however, evidence will be provided here for the reaction of **1** with water in dilute solution. The solvent mixture used for the photophysical measurements was 2:1 ethanol/acetone. $^{31}P\{^1H\}$ NMR spectra of **1** measured in this solvent mixture at concentrations of 10^{-2} M and 10^{-3} M were comparable and did not suggest reaction with either acetone or ethanol. Addition of 5 % v/v water (~ 2.7 M) to the solutions, however, produced different results at the two concentrations. Consistent with previous experiments, no changes were observed for the sample with [**1**] = 10^{-2} M. However, in ~10-fold more dilute solution, the addition of water clearly led to formation of a new complex, as evidenced by the appearance of a new ^{31}P resonance (δ 40.4), as shown in Figure 2.4. This new complex is proposed to be a simple aquo complex, **1•OH$_2$**, as depicted in Scheme 2.3.

References begin on page 69.

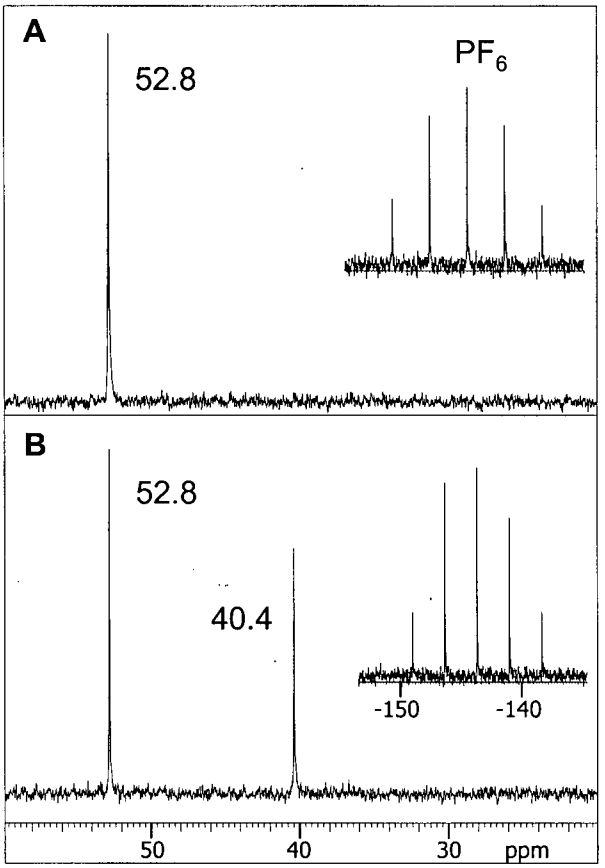

Figure 2.4. $^{31}P\{^1H\}$ NMR spectrum of **1** in 2:1 ethanol/acetone solution, [**1**] = 2×10^{-3} M (panel A), and after addition of 5 % v/v H_2O (panel B).

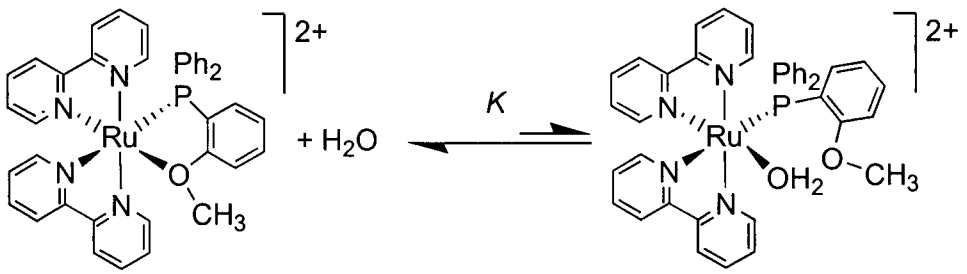

Scheme 2.3.

References begin on page 69.

Complexes **1** and **1•OH$_2$** exist in equilibrium in the presence of water, as depicted in Scheme 2.3. Two mechanisms are possible for the reaction of **1** with water:

(a) a concerted/interchange mechanism in which the ether competes with water for the labile coordination site, and the reaction proceeds via a 7-coordinate transition state; or,

(b) a step-wise/dissociative-associative mechanism in which the ether and water compete for binding to a 5-coordinate intermediate.

Both mechanisms require consideration of the effective concentration of the displaced ether moiety, and lead to an equilibrium expression of the form:

$$K = \frac{[\mathbf{1 \cdot OH_2}](\alpha \cdot [\text{"OMe"}])}{[\mathbf{1}][\mathbf{H_2O}]}$$

where the concentration of displaced ether ["OMe"] = [**1•OH$_2$**] because the ether is a component of the aquo complex. The proportionality constant α accounts for the fact that the ether is tethered in close proximity to the metal centre and therefore has a higher effective concentration than it would have if it was free in solution. Thus, the equilibrium expression becomes:

$$K_{eff} = \frac{K}{\alpha} = \frac{[\mathbf{1 \cdot OH_2}]^2}{[\mathbf{1}][\mathbf{H_2O}]}$$

and a plot of [**1•OH$_2$**]^2/[**1**] *vs.* [H_2O] should be linear. Indeed, the ratio of aquo complex to *P,O*-complex determined by monitoring a titration of **1** with H_2O via $^{31}P\{^1H\}$ NMR spectroscopy was found to scale nonlinearly with [H_2O]. As shown in Figure 2.5, a linear relationship is observed for the data when [**1•OH$_2$**]^2/[**1**] is plotted *vs.* [H_2O]. It should be noted that the true equilibrium constant K cannot be determined without knowledge of the effective ether concentration, which requires determination of the proportionality constant α. However, the effective equilibrium constant K_{eff} does provide a means to compare the affinity of various small molecules for **1** if the effective ether concentration is assumed to be constant regardless of the nature of the donor that occupies the labile coordination site.

References begin on page 69.

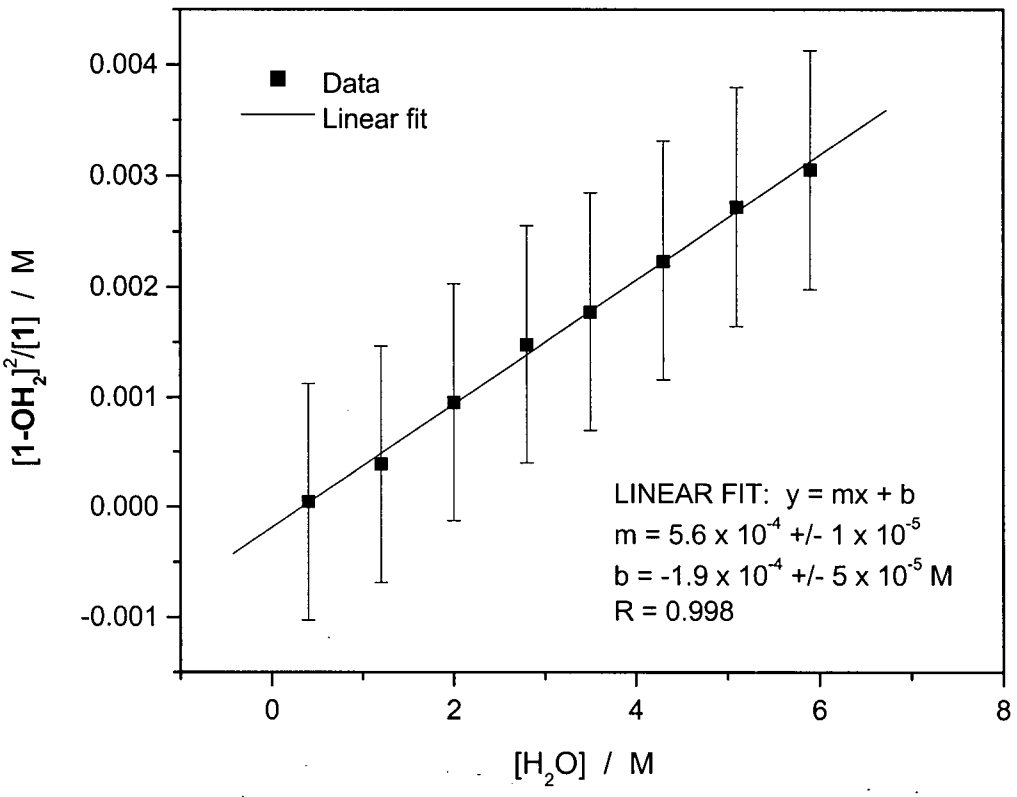

Figure 2.5. Plot of $[\mathbf{1{\cdot}OH_2}]^2/[\mathbf{1}]$ *vs.* $[H_2O]$ as determined from integration of $^{31}P\{^1H\}$ NMR spectra of **1** in 2:1 ethanol/acetone-d_6 solution, [**1**] = 3.3×10^{-3} M, with increasing water content. Error bars are ± 1 σ from the data.

The data shown in Figure 2.5 yield an effective equilibrium constant for the reaction depicted in Scheme 2.3 of $K_{eff} = (6 \pm 3) \times 10^{-4}$. With such a small formation constant, the aquo complex **1·OH$_2$** is observable by NMR spectroscopy only when the concentration of water is quite large (> 0.2 M) and the total metal concentration is relatively low. This situation arises as described above by deliberately adding water to a sample. Residual water contained in commercially available 'anhydrous' organic solvents (~ 0.5 % v/v ≈ 0.3 M H_2O) is insufficient to produce an amount of aquo complex detectable by $^{31}P\{^1H\}$ NMR spectroscopy.

References begin on page 69.

2.4.3 Reaction of 1 with nitrogen donors

2.4.3.1 Reaction with acetonitrile

Unlike the strong π-acceptor CO, acetonitrile is a strong σ-donor with weaker π-acceptor character. Given this and the intermediate hardness of the nitrogen donor, acetonitrile was expected to readily displace the weakly coordinated ether from the electron-poor Ru in **1**. Indeed, complex **1** reacted rapidly with acetonitrile to form a new complex **1•MeCN**. The reaction was evidenced both by a change in colour from orange to yellow and by upfield shifts of the methoxy ^{1}H and phosphine ^{31}P{^{1}H} NMR resonances of the hemilabile ligand (CD_2Cl_2: ^{31}P δ 39.6; ^{1}H δ 3.14 (s, OC*H*$_3$)). Complete disappearance of **1** (^{31}P δ 50.9; ^{1}H δ 3.71 (s, OC*H*$_3$)) occurred when one equiv of MeCN (or more) was used. The observed changes in the ^{1}H and ^{31}P chemical shifts are consistent with the reaction proceeding via displacement of the ether moiety from the metal by MeCN, as shown in Scheme 2.4. The reaction proceeded to completion as long as there was a stoichiometric excess of MeCN present. It was therefore concluded that the effective equilibrium constant for the reaction of **1** with acetonitrile is large, $K_{eff} > 360$.

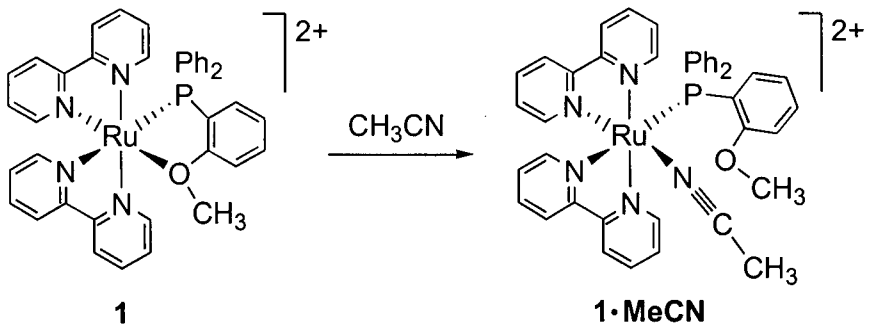

1 **1•MeCN**

Scheme 2.4.

The large formation constant for **1•MeCN** permitted this analyte-bound complex to be isolated and fully characterized. Complex **1•MeCN** was prepared via reaction of **1** with excess acetonitrile at room temperature and isolated as a brown-orange powder. The C-N stretching frequency of the metal-bound MeCN measured by IR spectroscopy (ν_{CN} = 2276 cm^{-1}, KBr

References begin on page 69.

pellet) was comparable to that of other Ru(II) complexes containing similar phosphine-ether ligands (*e.g.*, ν_{CN} = 2277 cm^{-1} for $RuCl_2$(PC2OMe-*P,O*)(PC2OMe-*P*)(MeCN), where PC2OMe = 2-(2-methoxyethyl)diphenylphosphine);[28] these are both higher energy than free MeCN (ν_{CN} = 2254 cm^{-1}), which implies that acetonitrile does not act as a π-acceptor when bound to Ru(II) in these systems. The complete NMR spectra for **1•MeCN** are given in the experimental section (section 2.6.3.2). A NOE difference ^{1}H NMR spectrum showed enhancement of only the adjacent phenyl H's resonance (δ6.63) upon irradiation of the methoxy resonance (δ3.07), which suggests that the MeO-substituted phenyl ring sits with the methoxy group aimed away from the metal once the ether has been displaced.

The coordinated MeCN in **1•MeCN** could not be removed from the metal under mild conditions; drying **1•MeCN** under vacuum (0.1 mm Hg) overnight resulted in no detectable regeneration of complex **1**. Furthermore, there was no evidence for dissociation of the MeCN ligand when **1•MeCN** was dissolved in organic solvents (10^{-2} M) for analysis by NMR spectroscopy, which had been observed for the above mentioned PC2OMe complex and others.[17,28] At extremely low concentration (10^{-5} M) in 2:1 ethanol/acetone solution, however, a concentration-dependent red shift of the absorption spectrum was again observed, as for **1**, although this has not been studied in detail. Thus, it appears that the reaction with acetonitrile is truly an equilibrium, but the acetonitrile is relatively difficult to remove from the metal.

2.4.3.2 Reactions with other nitrogen donors

The reactions of **1** with two other nitrogen donors, a pyridine derivative and an amine, were investigated at a cursory level. The *para*-substituted pyridine 4-picoline (*i.e.*, 4-methylpyridine) was investigated because of the additional ^{1}H NMR spectroscopic handle provided by the methyl group (CD_2Cl_2: δ2.37 (s, C*H*$_3$)). Addition of one equiv of 4-picoline to a solution of **1** in CD_2Cl_2 (2 × 10^{-2} M) led to immediate formation of a new product (^{31}P δ 40.4; ^{1}H δ 2.92 (s, OC*H*$_3$), 2.25 (s, C*H*$_3$)) and nearly complete disappearance of **1**. The effective equilibrium constant was estimated to be K_{eff} = 31 ± 9 from the NMR spectral data. An attempt to isolate the picoline complex was unsuccessful because of dissociation of the ligand from the metal during purification.

References begin on page 69.

The reaction of **1** with triethylamine was of greater interest due to the accompanying colour change from orange to red. Addition of approximately one equiv of NEt_3 to a solution of **1** (6×10^{-2} M in CD_2Cl_2) led to partial conversion of **1** into a new product, according to ^1H and $^{31}P\{^1H\}$ NMR spectroscopy (^{31}P δ 47.8; ^1H δ 3.28 (q, Ru-N(CH_2CH_3)$_3$), 2.92 (s, OCH_3), 1.33 (m, Ru-N(CH_2CH_3)$_3$)). The effective equilibrium constant was K_{eff} = 5 ± 1 from integration of the ^1H resonances. The ratios of **1**:**1**•**NEt$_3$** determined from integration of the ^1H (1:2.2) versus ^{31}P (1:1.8) resonances were reasonably similar considering that the longitudinal relaxation times (T_1) of the phosphorus nuclei were found to be different (T_1 = 3.2 s for **1**, 4.2 s for **1**:**1**•**NEt$_3$**). After standing for a period of one day, the sample had turned brownish in colour, and analysis of the reaction mixture by $^{31}P\{^1H\}$ NMR spectroscopy revealed the presence of multiple products. No attempts were made to isolate any of the products on a preparative scale.

2.4.4 Reactions with sulfur donors

Odiferous sulfur-containing compounds, such as H_2S, thiols and sulfides, are interesting small-molecule analytes for several reasons, including their potential contribution to unpleasant breath odours. In fact, an 'artificial nose' developed at CalTech and Cyrano Sciences has been used by health-care researchers in their studies on remedies for chronic oral malodour.[29] SO_2 is an industrially and environmentally relevant gas that is an attractive analyte because of its widespread use in treatment of food products and its contribution to atmospheric pollution and acid rain. Sulfoxides are widely used in the pharmaceutical industry, particularly dimethylsulfoxide (abbreviated DMSO), which has led to some interest in sensors specific for these compounds as well.

Sulfur is a soft donor atom that is well-matched for bonding to soft acids such as Ru(II). Accordingly, complex **1** was found to react with a variety of neutral sulfur compounds, including sulfur dioxide, hydrogen sulfide, ethanethiol, dodecanethiol, dimethylsulfide and dimethylsulfoxide. As with the nitrogen donors, reactions with sulfur donors caused the methoxy ^1H and phosphine $^{31}P\{^1H\}$ NMR resonances for the analyte-bound complexes to be shifted upfield relative to **1**, and the reactions were easily monitored by NMR spectroscopy.

References begin on page 69.

The complexes were characterized *in situ* by $^{31}P\{^1H\}$ and ^1H NMR spectroscopy and were not isolated.

2.4.4.1 Reaction with SO_2

Treatment of a solution of **1** in CD_2Cl_2 with 1 atm of SO_2 did not lead to reaction even after 1 day at 25 °C. A sample that was saturated with SO_2 via sparging did, however, indicate slow reaction of **1** with SO_2 by a gradual reddening of the solution's colour. After 2 hours reaction time, the $^{31}P\{^1H\}$ NMR spectrum contained a small product resonance (δ38.3, s) plus two small triplet resonances at considerably lower chemical shift (δ-13.2, t, J = 964 Hz; and δ -18.4, broad t, J = 964 Hz); over the course of a day, these signals increased and another singlet resonance grew in at δ20.8, but **1** remained the major species present in the sample. The two singlet resonances may be due to two analyte-bound complexes differing in their SO_2-coordination mode (*S*- versus *O*-bound), although this has not been confirmed; it may be that sparging with SO_2 led to the accumulation of significant amounts of unidentified coordinating impurities in the solution. The growth of the triplet ^{31}P resonances was accompanied by diminishing intensity of the PF_6^- resonance, indicative of a possible chemical reaction between the analyte and the counterion; the triplet multiplicity and magnitude of the coupling constant suggest that the resonances correspond to substituted -PF_2 groups (*cf.* $^1J_{PF}$ = 711 Hz for PF_6^-). Further study of the reaction of **1** with SO_2 was hindered by this unexpected incompatibility. Alternative counterions were not investigated in the present thesis but should certainly be considered for further study of this interesting analyte by subsequent researchers.

2.4.4.2 Reaction with H_2S

The reaction of **1** with the poisonous gas H_2S was also examined. Two hours after sparging a solution of **1** in CD_2Cl_2 for 1 min with the gas, small amounts of several products were evident from the $^{31}P\{^1H\}$ NMR spectrum. The sample appeared to undergo decomposition over the next several hours and a dark solid precipitated from the greenish-brown solution. The reaction was not investigated in further detail.

References begin on page 69.

2.4.4.3 Reactions with RSH

Ethanethiol and dodecanethiol each led to partial conversion to one stable product according to NMR spectroscopy. These reactions each required a few hours to reach a steady state, during which time the initially orange solutions gradually acquired a deep olive colour. The proposed reaction with thiols is shown in Scheme 2.5. Coordination of thiols by **1** caused shifting of both ligand and thiol resonances as expected (*cf.* free EtSH in CD_2Cl_2: ^{1}H δ2.54 (m, C*H*$_2$), 1.42 (t, S*H*), 1.30 (t, C*H*$_3$)). For example, treatment of **1** (5×10^{-2} M, in CD_2Cl_2) with approximately 2 equiv of EtSH led to ~ 30 % conversion to a new product with the following well-resolved NMR resonances: ^{31}P δ 37.1; ^{1}H δ 3.23 (s, OC*H*$_3$), 1.12 (triplet-like dd, SCH$_2$C*H*$_3$). The coordinated thiol's CH_2 resonances are obscured by the SH and CH_2 resonances from free EtSH as well as a somewhat broad water peak (δ~ 1.62), but they occur at δ1.25 – 1.68 according to the coupling to the methyl resonance observed in the ^{1}H COSY spectrum. A small, broad resonance (δ 3.13) partially obscured by the methoxy peak is assigned to the SH in **1•EtSH**, although the expected coupling to the methylene resonances was not resolved in the COSY spectrum. The lack of coupling may be the result of exchange processes (free H_2O peak is also broad) or the limited resolution of the COSY experiment when the CH_2 peaks cover such a large chemical shift range.

These spectroscopic assignments were further substantiated upon addition of a drop of D_2O to the sample. Exchange of D for H resulted in the disappearance of both the broadened water peak and the SH resonance of free EtSH (δ1.42, t); thus, the metal-bound thiol's CH_2 resonances became nearly entirely unobscured in the ^{1}H spectrum (δ1.35 – 1.68; small region from δ1.25 – 1.35 remained obscured by EtSH's CH_3 resonance). Furthermore, the broad resonance at δ3.13 shifted downfield to δ4.75, which supports assignment of this resonance as due to an exchangeable, acidic metal-bound SH. The relatively small downfield shift implies only partial conversion of **1•EtSH** to **1•EtSD**, which suggests that either (a) at equilibrium, there is considerably more EtSH than EtSD bound to the metal, or (b) the system was not yet at equilibrium, which implies that the H/D exchange process is slow (not at equilibrium after the ~ 15 minutes reaction time).

References begin on page 69.

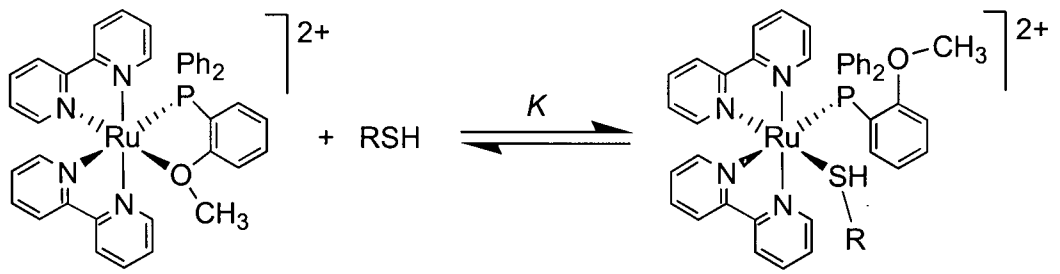

1 **1•RSH**

Scheme 2.5.

The effective equilibrium constant for the reaction with EtSH was $K_{eff} = 0.11 \pm 0.02$; similarly, for dodecanethiol, $K_{eff} = 0.12 \pm 0.03$. The reversibility of the reaction of thiols with **1** was established by varying the concentration of analyte in solution and observing changes in the ratios of **1•RSH** to **1** as an equilibrium was reestablished that fit the previously determined value for K_{eff}. It should be noted that although the resonances due to the thiol hydrogens in **1•RSH** (RSH = ethanethiol, dodecanethiol) were not conclusively identified, the reactions with thiols were found to be reversible, which suggests that coordination of thiols to **1** was not accompanied by conversion to the thiolate.

2.4.4.4 Reaction with SMe_2

Dimethylsulfide showed a higher affinity for **1** than any of the other sulfur donors studied. Addition of 2 equiv of SMe_2 to a solution of **1** (5×10^{-2} M in CD_2Cl_2) led to an equilibrium in which over 80 % of the sensor complex **1** was bound to SMe_2 (selected resonances for **1•SMe$_2$**: ^{31}P δ 32.6; ^1H δ 2.69 (s, OC*H*$_3$), 1.08 (s, S(C*H*$_3$)$_2$); compare to free SMe_2 in CD_2Cl_2: ^1H δ 2.09 (s). The effective equilibrium constant for this reaction, shown in Scheme 2.6, was determined to be $K_{eff} = 1.7 \pm 0.3$.

References begin on page 69.

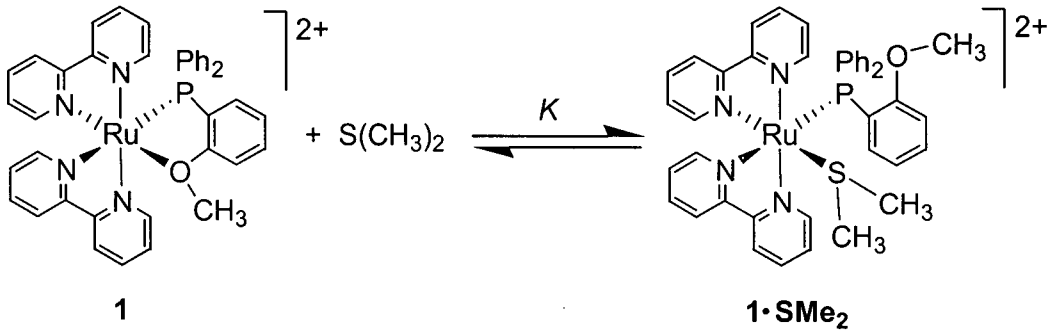

Scheme 2.6.

2.4.4.5 Reactions with dimethylsulfoxide

(i) Bonding of sulfoxides to metals

Sulfoxides are ambidentate ligands; they can coordinate to metals via the lone pairs on either the soft sulfur atom or the hard oxygen atom, depending on the hardness of the metal involved. In rare cases, sulfoxides act as bridging ligands.[30,31] In general, Ru(II) shows a preference to coordinate sulfoxides via the soft sulfur atom,[32] although *O*-bound complexes are known, and in some cases both bonding modes are present within the same complex (*e.g.*, *cis*-$RuCl_2$(DMSO-*S*)$_3$(DMSO-*O*)).[33] *O*-bonding is preferred in Ru(II) complexes in which the sulfoxide is coordinated *trans* to a π-acceptor ligand, such as CO, NO or *S*-bonded DMSO.[32]

The coordination mode of sulfoxides can be determined via a number of techniques,[34] including IR and ^{1}H NMR spectroscopy. Upon coordination of a sulfoxide to a metal, the strong absorption due to a S=O stretching mode observed by IR spectroscopy is shifted relative to the free sulfoxide (ν_{SO} = 1055 cm^{-1} for uncoordinated DMSO). This shift typically occurs to lower frequencies for *O*-bonded complexes and to higher frequencies for *S*-bonded complexes. ^{1}H NMR spectra reveal shifts in the resonances for protons α to sulfur relative to the free sulfoxide resonance, as well as differences in the chemical shift of diastereotopic protons α to sulfur (not relevant to DMSO), that are also useful in assigning the coordination mode. *O*-bonded sulfoxides show only slight downfield shifts (< 0.5 ppm) of the α-proton resonances, while *S*-bonded sulfoxides show large downfield shifts (~ 1 ppm).

References begin on page 69.

(ii) Reaction of 1 with DMSO

Complex **1** equilibrated in less than 5 minutes with one equiv of DMSO in acetone or dichloromethane solutions ([DMSO] = [**1**] ≈ 4 × 10^{-2} M) to yield a small fraction (~ 8%) of a new species (in CD_2Cl_2: ^{31}P δ 37.7; ^1H δ2.97 (s, OCH_3), 2.38, 2.24 (s, inequivalent OS(CH_3)$_2$). Addition of more DMSO (8 equiv; 0.3 M) resulted in the formation of more of this species (total ~ 38%) plus a small amount (< 5%) of a second product (in CD_2Cl_2: ^{31}P δ 29.7; ^1H δ3.11 (s, OCH_3), coordinated DMSO methyl signals buried under broad free DMSO peak: δ2.54, s). As introduced above, these two products likely differ only in the coordination mode of the sulfoxide ligand, as depicted in Scheme 2.7.

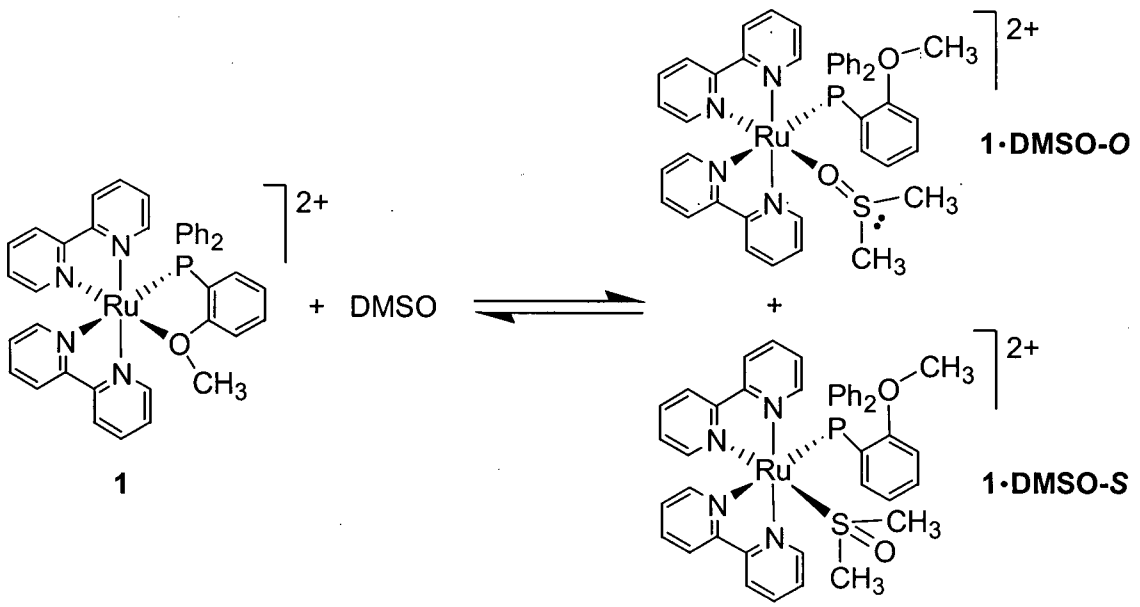

Scheme 2.7.

Complexes **1•DMSO-*S*** and **1•DMSO-*O*** exist in equilibrium with **1**; variation of the relative concentrations of **1** and DMSO yielded identical pseudo-equilibrium constants (0.016 ± 0.002 for major product; 0.0006 ± 0.0001 for minor product). True effective equilibrium constants K_{eff} were not determined because of the interrelationship between the three

References begin on page 69.

complexes. However, the equilibrium constants are small enough that in neat DMSO-d_6 solution ([**1**] = 4×10^{-2} M, [DMSO] ≈ 14 M), a detectable amount (~ 5 %) of **1** remains.

Neither DMSO complex was isolated, although several attempts were made. Precipitation of the complexes from DMSO solution was unsuccessful because the solvents in which [*cis*-Ru(bpy)$_2$L$_2$](PF$_6$)$_2$ complexes are generally insoluble (diethyl ether, hexanes) are immiscible with DMSO. Attempts to crystallize the complexes from DMSO, benzene/DMSO, and CH_2Cl_2/DMSO solutions also failed. It is important to stress at this point that the reactions of **1** with DMSO are reversible. Evaporation of DMSO-containing solutions of **1** did not lead to isolation of the DMSO complexes because at the high temperatures required to remove the excess high-boiling solvent *in vacuo*, the coordinated DMSO was also removed and **1** was regenerated. Although the reversibility of these reactions was a hindrance to characterization of the DMSO complexes, it must be emphasized that reversibility is an attractive feature for chemical sensing purposes. Thus, DMSO was considered a promising analyte.

Without isolation of the complexes, efforts to conclusively assign the structures of the two **1•DMSO** complexes were unsuccessful because signals from free DMSO masked the critical spectroscopic features. IR spectroscopy was unhelpful because the ν_{SO} peak from residual uncoordinated DMSO was so strong that it overwhelmed the spectral region of interest. Furthermore, the ^{1}H NMR spectra did not provide assistance in the assignment of bonding mode. In the major product, both DMSO methyl groups (δ 2.38, 2.24) appeared upfield of free DMSO (δ 2.54) in the ^{1}H spectrum, contrary to the trend for known DMSO complexes in which metal-bound DMSO methyl groups tend to resonate downfield of free DMSO.[34] This is, however, consistent with the metal-bound DMSO methyl groups experiencing strong shielding from the π-systems in the nearby bpy and Ph groups; solid-state molecular structures of RuPOR-*P* complexes with bound analyte molecules presented in Chapter Five (**6•OH$_2$**: Figure 5.1, p. 162; **7•MeCN-d_3**: Figure 5.2, p. 167) show that the metal-bound analyte species lie within the shielding cones of both bpy and phenyl rings. No comments can be made regarding the minor product, because at the high DMSO concentrations required to observe this species by ^{31}P{^{1}H} NMR spectroscopy, the resonance from free DMSO overwhelmed the ^{1}H spectrum and the bound-DMSO methyl resonances could not be located. Furthermore, although the equilibria should shift towards products at lower

References begin on page 69.

temperatures based on entropic arguments, the ^{1}H NMR spectra acquired at lower temperatures did not reveal a substantial enough increase in the amount of **1•DMSO** to assist in characterization ([**1•DMSO** (major product)]:[**1**] ≈ 1:5 at 25 °C *cf.* 2.5:1 at - 30 °C).

With the hope of assigning the DMSO bonding modes in the **1•DMSO** complexes by comparison to the spectral features of a similar DMSO complex, [*cis*-Ru(bpy)$_2$(PPh$_3$)(DMSO)](PF$_6$)$_2$ was targeted. It was hoped that this complex would be more easily isolated and characterized, although no references to this compound were found in the literature. Several attempts to synthesize this complex were made, but none were successful. Reaction of [*cis*-Ru(bpy)$_2$(acetone)$_2$](BF$_4$)$_2$ with DMSO at 25 °C led to a green solution that slowly turned orange after treatment with PPh$_3$; however, the product of this reaction was extremely insoluble and could not be characterized by NMR spectroscopy, so it was not likely the desired complex. Treatment of [*cis*-Ru(bpy)$_2$(acetone)$_2$](BF$_4$)$_2$ with 1 equiv of PPh$_3$ followed by an excess of DMSO also did not lead to the desired complex. Reaction of the complex [*cis*-Ru(bpy)$_2$(PPh$_3$)Cl]PF$_6$[20] with AgBF$_4$ in acetone solution to afford the solvate complex [*cis*-Ru(bpy)$_2$(PPh$_3$)(acetone)](PF$_6$)$_2$ followed by treatment with DMSO led to a complex mixture of products both at room temperature and after heating.

Given the difficulties with isolation of the **1•DMSO** complexes and the analogous complex [*cis*-Ru(bpy)$_2$(PPh$_3$)(DMSO)](PF$_6$)$_2$, data on other closely related complexes were sought from the literature. Two Ru(II) bipyridine complexes, [*cis*-Ru(bpy)$_2$(DMSO)Cl]PF$_6$[35] and [*trans*-Ru(bpy)$_2$(4-Etpy)(DMSO)](PF$_6$)$_2$[36] have been shown to contain *S*-bonded DMSO according to IR and ^{1}H NMR spectroscopy[35] and crystallographic analysis.[36] Although in general the DMSO methyl groups typically appear downfield of free DMSO when metal bound, this is not the case for [*cis*-Ru(bpy)$_2$(DMSO-*S*)Cl]PF$_6$ (δ 3.13, 2.06 (s, inequivalent OS(C*H*$_3$)$_2$) nor was it the case for the major **1•DMSO** (δ2.38, 2.24 (s, inequivalent OS(C*H*$_3$)$_2$)) product. Based on the similarity of the ligand environments in these complexes and in **1**, the major product likely contains *S*-bound DMSO, while the minor product likely contains *O*-bound DMSO.

References begin on page 69.

2.4.5 Summary and discussion of reactivity of 1

Small-molecule analytes covering a range of donor properties were surveyed to probe the competition between coordination of the ligand's ether moiety and the incoming donor. For comparison purposes, a summary of the NMR spectral data for the analyte-bound complexes and their formation constants is presented in Table 2.3. Overall, the small-molecule preferences for **1** predicted from Lewis acid/base theory ($R_3P > R_2S$, $R_3N > R_2O$)[27] are quite accurate. No evidence has been observed for displacement of the phosphine arm of the POMe ligand, and the ether moiety is most readily displaced by nitrogen- and sulfur-containing small molecules. In short, the phosphine-ether complex **1** can coordinate a number of types of small molecules, which illustrates the suitability of hemilabile ligand complexes for use as multianalyte receptors.

Oxygen-donor analytes, such as ethers, alcohols and water, are of similar hardness to the labile ligand donor; the chelate effect, therefore, favours binding of the metal-tethered ether over binding of analytes with similar affinity for the soft Ru(II) centre. Indeed, oxygen donors did not compete well with the ligand's ether at the typical concentration (10^{-2} M) used for $^{31}P\{^1H\}$ NMR spectroscopy, and no reactions were detected by NMR spectroscopy in the presence of 1- to 10-fold excesses of analyte. However, at very high relative analyte concentrations, reaction was observed between **1** and water. Accordingly, the effective equilibrium constant for reaction of **1** with water was determined to be small ($K_{eff} = (6 \pm 3) \times 10^{-4}$).

Small molecules containing nitrogen donors compete very well for coordination to the metal centre in **1**. Indeed, the largest of all the sensor-analyte binding affinities determined was observed for acetonitrile ($K_{eff} > 360$), a sterically undemanding, strong σ-donor. The other N-donors studied also show high affinities for **1** and have considerably different effects on the complex's colour, as discussed in Chapter Three (section 3.4.2). Complex **1** appears to be well suited to reporting the presence of nitrogen-based analytes.

Soft sulfur-containing small molecules, such as thiols, DMS and DMSO, are well matched with the soft Ru centre in **1** and effectively compete with the ligand's ether. Of the sulfur donors studied, dimethylsulfide shows the highest affinity for **1** ($K_{eff} \approx 1.7$); thiols also compete well for the metal ($K_{eff} \approx 0.1$), while DMSO is the most weakly coordinated. This

References begin on page 69.

trend in binding affinity is consistent with the decrease in electron density at the sulfur from dialkylsulfide to thiol to sulfoxide. Although not studied here in depth because of incompatibility with the PF_6^- counterion, the reaction of **1** with SO_2 is promising as well; investigation of **1**'s reactivity toward this analyte would certainly be worthwhile given its importance in the food processing industry and as an atmospheric pollutant.

Table 2.3. Summary of NMR spectral data for **1** and analyte-bound **1**

Analyte	^{1}H NMR, OC*H*$_3$ δ(ppm)[a]	^{31}P{^{1}H} NMR δ(ppm)[a]	K_{eff} [a,b]
—	3.71	50.9	—
MeCN	3.14	39.9	> 360[c]
4-MePy	2.92	40.4	31 ± 9
NEt_3	2.92	47.8	5 ± 1
SMe_2	2.70	32.8	1.7 ± 0.3
EtSH	3.23	37.4	0.11 ± 0.02
$C_{12}H_{25}SH$	3.23	37.4	0.12 ± 0.03
DMSO	2.97[d]	37.7[d]	0.016 ± 0.0002[d]
	3.11[e]	29.7[e]	0.0006 ± 0.0001[e]
H_2O	—	40.4	(6 ± 3) × 10^{-4}

[a]10^{-2} M in CD_2Cl_2 solution; [b]> 3 hour equilibration time; [c]No unreacted **1** remained; [d]Major product; [e]Minor product; [d,e]Pseudo-equilibrium constants were calculated by assuming the two products formed independently of each other.

References begin on page 69.

2.5 Summary and outlook

In this chapter, the synthesis and reactivity of the hemilabile phosphine-ether complex [*cis*-Ru(bpy)$_2$(POMe-*P,O*)]$^{2+}$, **1**, were described. The ether moiety in the POMe ligand is weakly bound to the metal and can be displaced by several classes of small molecules, including water, nitriles, amines, thiols, sulfides and sulfoxides. Many of these reactions are reversible, and in most cases equilibria are established in which a fraction of **1** remains unreacted in the presence of excess analyte. Small molecules containing soft Lewis bases tend to compete well for the Ru centre in **1**, although strongly π-acidic small molecules with poor σ-donor ability do not. The analyte with the highest affinity for **1** is acetonitrile. Thus, it is concluded that the hemilabile ligand in **1** provides the nonspecific binding site required for the metal complex to function as a multianalyte small-molecule receptor, and this site shows a preference for σ-donors.

With these results in mind, it was of interest to explore the effects of the ether substituents on its lability, with the aim of shifting the sensor-analyte equilibria toward more complete reaction. Indeed, the lability of the ether moiety can be tuned through substituent effects. The preparation and reactivity of [*cis*-Ru(bpy)$_2$(POR)]$^{2+}$ complexes that contain different phosphine-ether ligands are described in Chapter Five.

Although introduced at the beginning of this chapter, the discussion of complex **1** as an MLCT-based lumophore is resumed in Chapter Three. The redox properties of **1** and the effects of small-molecule analytes are presented first. The characterization of **1** in terms of its absorption and photoluminescence properties is described next, and a discussion of the analyte-induced colour and luminescence changes alluded to in this chapter follows. Chapter Three concludes with an evaluation of **1** as a luminescent molecule-based sensor.

References begin on page 69.

2.6 Experimental section

2.6.1 General procedures

NMR spectra were acquired on Bruker AC-200, Avance 300, Avance 400, AM-400, AMX-500 or Varian XL-300 instruments. Residual protiated solvent peaks were used as internal ^{1}H reference (*vs.* TMS at δ 0). ^{31}P{^{1}H} NMR spectra were referenced to 85 % H_3PO_4 (δ 0) by comparison to external reference samples of $P(OMe)_3$ or PPh_3 in the appropriate deuterated solvent. IR spectroscopic measurements were made using a BOMEM MB155S FTIR spectrometer. Elemental analyses were performed by Mr. Peter Borda of this department. X-ray crystallographic analyses were performed by Dr. Brian Patrick of this department.

2.6.2 Materials

Chemicals were used as received from the suppliers (Aldrich, Strem, Alfa Aesar) unless otherwise specified. Deuterated solvents were used as received from Cambridge Isotope Labs. *cis*-$Ru(bpy)_2Cl_2 \cdot 2H_2O$[19] and 2-methoxyphenyldiphenylphosphine (POMe)[14] were prepared by published procedures.

2.6.3 Preparation and characterization of complexes

2.6.3.1 Synthesis and characterization of [cis-Ru(bpy)$_2$(POMe-P,O)](PF$_6$)$_2$, 1

A suspension of $Ru(bpy)_2Cl_2 \cdot 2H_2O$ (0.874 g, 1.68 mmol) in nitrogen-sparged acetone (20 mL) was treated with solution of $AgBF_4$ (0.660 g, 3.39 mmol) in acetone (20 mL). The mixture was sparged thoroughly with nitrogen, stirred at room temperature for several hours to ensure complete precipitation of AgCl, then filtered through Celite to yield a deep wine-red solution of the solvate complex. To this solution was added 1 equiv of 2-methoxyphenyldiphenylphosphine (0.491 g, 1.68 mmol) as a solution in deaerated acetone (50

References begin on page 69.

mL), and the mixture was heated to reflux under nitrogen overnight to yield a clear reddish orange solution. The cooled reaction mixture was filtered, evaporated to dryness and the residue dissolved in a small volume of acetone and precipitated with aqueous NH_4PF_6. The flocculent orange solid was collected, washed with water and ether, and dried; it was then reprecipitated from acetone solution by the addition of diethyl ether, collected and dried. Yield: 1.47 g (88 %). Recrystallization from hot methanol yielded crystals suitable for X-ray crystallographic analysis. Elemental analysis calcd. for $C_{39}H_{33}F_{12}N_4OP_3Ru$ (%): C, 47.05; H, 3.34; N, 5.63; found: C, 47.30; H, 3.39; N, 5.70. Vis (CH_2Cl_2, λ_{max}, ε): 414 nm, 7200 $M^{-1}cm^{-1}$. CV (200 mV/s, 25 °C, CH_2Cl_2/$^nBu_4NPF_6$, V *vs.* SCE): $E_{ox}(Ru^{III/II})$ = 1.56 V; E_{red} = -1.27, -1.71 V.

^{1}H NMR (500 MHz, 25 °C, CD_2Cl_2): δ 8.55 (overlapping d, 2H, inequivalent), 8.30 (coincident d, $^3J_{HH}$ = 5.6 Hz, 2H, inequivalent), 8.13 (m, 2H), 8.01 (d, $^3J_{HH}$ = 7.7 Hz, 1H), 7.95 (d, $^3J_{HH}$ = 7.6 Hz, 1H), 7.92-7.52 (m, 11H), 7.50 (m, 1H), 7.43 (m, 1H), 7.38 (m, 2H), 7.33 (dd, $^3J_{HH}$ = 8.6 Hz, $^4J_{HP}$ = 4.9 Hz, 1H, *ortho* to O), 7.24 (m, 1H *para* to P, Ph_A), 7.17 (m, 1H), 6.97 (m, $^4J_{PH}$ = 2.4 Hz, 2H *meta* to P, Ph_A), 6.39 (ddd, $^3J_{PH}$ = 11.2 Hz, $^3J_{HH}$ = 7.3 Hz, $^4J_{HH}$ = 1.1 Hz, 2H *ortho* to P, Ph_A), 3.71 (s, 3H, CH_3O). Note: assignments and coupling constants determined based on additional information from 500 MHz $^1H\{^{31}P\}$ spectrum and 400 MHz ^{1}H COSY and NOE spectra.

$^{31}P\{^1H\}$ NMR (81.0 MHz, CD_2Cl_2): δ 50.9 (s; PO), -143.8 (septet, $^1J_{PF}$ = 711 Hz, PF_6).

^{1}H NMR NOE difference spectrum (400 MHz, 25 °C, CD_2Cl_2). Peaks enhanced from true through-space effects (*i.e.*, nuclei not scalar coupled) are noted in bold. Irradiation of methoxy proton resonance at δ 3.71 enhanced two aromatic resonances: δ **8.30** (d, bpy H 6-position), **7.33** (dd, $PhOCH_3$ H *ortho* to O). Selected aromatic resonances: irradiated δ 6.39 (dd), enhanced 6.97 (m); irradiated δ 7.18 (t), enhanced 8.14 (m), 8.30 (d); irradiated δ 8.30 (d, $^3J_{HH}$ = 7.2 Hz), enhanced **7.62** (m, weak), *7.37 (d, strong), *7.17 (d, strong), **6.39** (dd, weak), **3.71** (s). *Peaks observed as doublets in the NOE experiment that appeared as more complex multiplets under broad-band irradiation.

References begin on page 69.

^{1}H COSY spectrum (400 MHz, 25 °C, CD_2Cl_2). A complete set of correlations could not be determined because of poor resolution, although both COSY and COSY45 experiments were done. Ph_A: δ6.39 (2H, *ortho* to P) - 6.97 (2H, *meta* to P) - 7.24 (1H, *para* to P). Bpy_A: δ8.56 (d, 3-position) - 8.14 (m) - 7.18 (m) - 8.30*a* (d, 6-position). Bpy_B: δ8.55 (d) - 8.13 (m) - 7.50 (m) - 7.71. Bpy_C: 7.59 (buried, 3-position) - 7.88 (buried) - 7.37 (m) - 8.30*b* (d, 6-position). The remaining bpy fragment, Ph and ether-substituted Ph groups could not be assigned fully.

X-ray crystallographic structural determination of 1 (Dr. B. O. Patrick)

A brownish-red blocked-shaped crystal of **1** grown from methanol was selected and mounted on a thin glass fibre. Data were collected at 173 (± 1) K on a Rigaku/ADSC CCD area detector in two sets of scans (ϕ = 0.0 to 190.0°, χ = 0.0°; and ω = -19.0 to 23.0°, χ = 90.0°) using 0.50° oscillations with 19.0 second exposures. Data were collected and processed using the d*TREK program (Molecular Structure Corporation); the structure was solved using direct methods[37] and expanded using Fourier techniques.[38] The nonhydrogen atoms were refined anisotropically. Hydrogen atoms were included but not refined. All calculations were performed using the teXsan crystallographic software package (Molecular Structure Corporation). The ORTEP representation of the solid-state molecular structure of **1** was prepared using ORTEP-32 for Windows.[39] The complex crystallizes in the monoclinic space group $P2_1/n$ (No. 14); the crystallographic details are summarized in Table A.2.1.

2.6.3.2 Synthesis and characterization of [cis-Ru(bpy)$_2$(POMe-P)(MeCN)](PF$_6$)$_2$, 1•MeCN

Complex **1** (0.056 g; 0.056 mmol) was dissolved in acetonitrile (2 mL). After a few minutes, the solvent was removed *in vacuo*; the residue was suspended in diethyl ether then collected by filtration as an orange-brown powder, which was dried *in vacuo*. Yield: 100 %. ^{1}H NMR (400 MHz, 25 °C, CD_2Cl_2): δ 8.95 (d, $^3J_{HH}$ = 5.6 Hz, 1H), 8.91 (d, $^3J_{HH}$ = 5.3 Hz, 1H), 8.48 (d, $^3J_{HH}$ = 8.2 Hz, 1H), 8.40 (d, $^3J_{HH}$ = 8.1 Hz, 1H), 8.21 (m, 1H), 8.15 - 6.85 (m, 24H), 6.61 (dd, 1H, $PhOCH_3$ H *ortho* to O), 3.14 (s, 3H, CH_3O), 2.35 (s, 3H, CH_3CN-Ru). $^{31}P\{^1H\}$ NMR (81.0 MHz, CD_2Cl_2): δ 39.6 (s, PO), -144.2 (sept, $^1J_{PF}$ = 711 Hz, PF_6). Elemental analysis calcd. for $C_{41}H_{36}F_{12}N_5OP_3Ru$ (%): C, 47.50; H, 3.50; N, 6.76; found: C, 47.63; H, 3.68; N, 6.54. IR (KBr): ν_{CN} = 2276 cm^{-1}. Vis (CH_2Cl_2, λ_{max}, ε): 412 nm, 6900 M$^-$

References begin on page 69.

^{1}cm^{-1}. CV (200 mV/s, 25 °C, $CH_3CN/^nBu_4NPF_6$, V *vs.* SCE): $E_{1/2}(Ru^{III/II})$ = 1.53 V; E_{red} = -1.30 (sh, irrev), -1.42 (irrev), -1.54, -1.83 V.

^{1}H NMR NOE difference spectrum (400 MHz, 25 °C, CD_3CN). Irradiation of the methoxy proton resonance at δ 3.07 enhanced one aromatic resonance: δ 6.63 (dd, $PhOCH_3$ H *ortho* to O).

2.6.4 Reactivity trials

Reactivity trials were performed by addition of prospective small-molecule analytes to solution NMR samples of **1** (in CD_2Cl_2 or acetone-d_6 solution, [**1**] ≈ 4 × 10^{-2} M, at RT, under air). Solutions were prepared with known concentration in volumetric glassware. Liquid analytes were added in 1 – 10× stoichiometry in neat form via microlitre syringe; reactions with gases were investigated under 1 atm of analyte, either after purging the headspace of the tube with the gas or after saturation of the solution via sparging, as specified in the text. The progress of the reactions was monitored by ^{1}H and ^{31}P{^{1}H} NMR spectroscopy, both immediately after addition of analyte and again several hours later to determine whether the sample had been at equilibrium when probed at short reaction times. Most reactions were complete or had reached an equilibrium state after a period of seconds to minutes. Cl_3CCH_2Cl (δ 6.03, unobscured by peaks due to **1** or analytes) was used as an internal standard for concentration determinations. Reactions were tested for reversibility by adding another aliquot of the original solution of **1** to the sample and comparing the reaction quotients determined for the two analyte concentrations; equivalent reaction quotients were interpreted as evidence of reestablishment of equilibrium.

2.6.4.1 Determination of K_{eff} using ^{1}H NMR spectroscopy

Effective equilibrium constants, K_{eff}, were calculated from the ratio of the integrated methoxy ^{1}H resonances for product (denoted **1•L**) and unreacted **1** using the following equation:

References begin on page 69.

$$K_{eff} = \frac{K}{\alpha} = \frac{[\mathbf{1} \bullet \mathbf{L}]^2}{[\mathbf{1}][\mathbf{L}]}$$

where the concentrations [**1**•**L**] and [**1**] were calculated by solving the following two equations with two unknowns:

$$\text{Integration ratio} = \frac{[\mathbf{1} \bullet \mathbf{L}]}{[\mathbf{1}]}$$

$$[\mathbf{1}]_i = [\mathbf{1}] + [\mathbf{1} \bullet \mathbf{L}]$$

Then, substitution of [**1**•**L**] followed to solve for [**L**]:

$$[\mathbf{L}] = [\mathbf{L}]_i - [\mathbf{1} \bullet \mathbf{L}]$$

The determinations of effective equilibrium constants were estimated to be accurate within ± 10 – 20 %. The major sources of uncertainty were the measurement of analyte via microlitre syringe and the measurement of the integrals themselves, whose reliability varied with the resolution and width of peaks in the spectra. It was estimated that up to 5 % impurities can be difficult to observe by ^{1}H NMR spectroscopy; thus, reactions that appear to go to completion by NMR may contain up to 5 % unreacted **1**. Based on this estimation of sensitivity, the upper limit for effective equilibrium constants determined using this technique is $K_{eff} \approx 360$.

2.6.4.2 Determination of K_{eff} using $^{31}P\{^1H\}$ NMR spectroscopy

Integration of the corresponding $^{31}P\{^1H\}$ NMR spectra is less reliable than the ^{1}H spectra for quantitative analysis due to differences in longitudinal relaxation times (T_1) for phosphorus nuclei in different environments. The routine acquisition parameters used for $^{31}P\{^1H\}$ NMR spectra (AC-200 NMR spectrometer with autosampler) included a delay time (*D1*) of ~ 1 second; since the delay between pulses should be at least 5 × T_1 to yield accurate integration, these parameters would suffice for rapidly relaxing ^{31}P nuclei (T_1 < 0.2 s). However, T_1 values for phosphines typically range from 2 – 30 seconds, with metal-

References begin on page 69.

coordinated phosphines at the lower end of this range.[40] The longitudinal relaxation time of the ligand phosphorus in complex **1** was determined by Liane Darge of the NMR Facility (inversion recovery experiment performed on the Varian XL-300 NMR spectrometer) to be T_1 = 3.2 seconds. Thus, prohibitively long acquisition times (> 16 seconds between pulses; total time for 256 scans ~ 4 h, *cf.* 15 min) would have been required to obtain accurate integration. The relaxation time for one of the analyte-bound complexes, **1•NEt$_3$**, was determined to be even longer (T_1 = 4.2 seconds). Thus, although integration of routine $^{31}P\{^1H\}$ NMR spectra was useful in a qualitative sense, it was not trusted to yield accurate quantitative information for a given complex unless a direct comparison between the ^1H integration and ^{31}P integration was first performed.

Nonetheless, the aquo complex **1•OH$_2$** was studied in predominantly protiated solvent (2:1 ethanol-h_6/acetone-d_6), so all quantitative information was obtained solely from $^{31}P\{^1H\}$ NMR spectra. Because a low metal complex concentration was required to observe the aquo complex, $^{31}P\{^1H\}$ spectra were averaged over a large number of scans (NS > 1000). To overcome the problems introduced by long ^{31}P relaxation times, a paramagnetic complex, $Cr(acac)_3$, was added to the solutions because it is known to provide efficient dipolar relaxation pathways that substantially shorten the relaxation times of cosolutes.[41] In the presence of $Cr(acac)_3$, the ^{31}P T_1s of **1•OH$_2$** and **1** are sufficiently short that spectra acquired using a delay of 2 seconds yield integrals indistinguishable from those obtained from spectra acquired with a long delay ($D1$ = 20 s); a short acquisition time (AQ = 1 s) was sufficient to achieve complete decay of the magnetization. Furthermore, $^{31}P\{^1H\}$ NMR spectra were run with inverse-gated ^1H decoupling (*i.e.*, decoupler on only during FID acquisition) such that $^1H - ^{31}P$ NOE effects were minimized. A comparison of the **1•OH$_2$**:**1** integration ratio determined for a sample analyzed under broadband decoupling *vs.* inverse-gated decoupling conditions, however, showed that the the difference between the spectra was insignificant, which indicates that the ^{31}P nuclei in the two complexes experience NOEs of similar magnitude. Using these parameters (inverse-gated decoupling, $D1$ = 2 s, AQ = 1 s), $^{31}P\{^1H\}$ NMR experiments for samples containing mixtures of **1•OH$_2$** and **1** ($[\mathbf{1}]_i \approx 3 \times 10^{-3}$ M; $[H_2O] \approx 0.4 - 6$ M) required 1.5 – 3 h to achieve spectra with satisfactory signal-to-noise ratios.

References begin on page 69.

2.7 References

(1) Kalyanasundaram, K. *Coord. Chem. Rev.* **1982**, *46*, 159.

(2) Meyer, T. J. *Pure & Appl. Chem.* **1986**, *58*, 1193.

(3) Juris, A.; Balzani, V.; Barigelletti, F.; Campagna, S.; Belser, P.; Von Zelewsky, A. *Coord. Chem. Rev.* **1988**, *84*, 85.

(4) Barbara, P. F.; Meyer, T. J.; Ratner, M. A. *J. Phys. Chem.* **1996**, *100*, 13148.

(5) Kalyanasundaram, K. *Photochemistry of Polypyridine and Porphyrin Complexes*; Academic Press: London, 1992.

(6) Roundhill, D. M. *Photochemistry and Photophysics of Metal Complexes*; Plenum Press: New York, 1994.

(7) Caspar, J. V.; Meyer, T. J. *Inorg. Chem.* **1983**, *22*, 2444.

(8) Treadway, J. A.; Loeb, B.; Lopez, R.; Anderson, P. A.; Keene, F. R.; Meyer, T. J. *Inorg. Chem.* **1996**, *35*, 2242.

(9) Demas, J. N.; Crosby, G. A. *J. Am. Chem. Soc.* **1971**, *93*, 2841.

(10) Bader, A.; Lindner, E. *Coord. Chem. Rev.* **1991**, *108*, 27.

(11) Yamamoto, Y.; Sugawara, K.; Aiko, T.; Ma, J.-F. *J. Chem. Soc., Dalton Trans.* **1999**, 4003.

(12) Yamamoto, Y.; Sato, R.; Matsuo, F.; Sudoh, C.; Igoshi, T. *Inorg. Chem.* **1996**, *35*, 2329.

(13) Yamamoto, Y.; Sato, R.; Ohshima, M.; Matsuo, F.; Sudoh, C. *J. Organomet. Chem.* **1995**, *489*, C68.

(14) Rauchfuss, T. B.; Patino, F. T.; Roundhill, D. M. *Inorg. Chem.* **1975**, *14*, 652.

References begin on page 69.

(15) Jeffrey, J. C.; Rauchfuss, T. B. *Inorg. Chem.* **1979**, *18*, 2658.

(16) Lindner, E.; Pautz, S.; Haustein, M. *Coord. Chem. Rev.* **1996**, *155*, 145.

(17) Lindner, E.; Geprags, M.; Gierling, K.; Fawzi, R.; Steimann, M. *Inorg. Chem.* **1995**, *34*, 6106.

(18) Lindner, E.; Scheytt, C.; Wegner, P. *Chem. Ber.* **1987**, *120*, 1621.

(19) Lay, P. A.; Sargeson, A. M.; Taube, H. *Inorg. Synth.* **1986**, *24*, 292.

(20) Sullivan, B. P.; Salmon, D. J.; Meyer, T. J. *Inorg. Chem.* **1978**, *17*, 3334.

(21) Yam, V. W. W.; Lee, V. W. M.; Cheung, K. K. *J. Chem. Soc., Dalton Trans.* **1997**, 2335.

(22) Rogers, C. W.; Patrick, B. O.; Rettig, S. J.; Wolf, M. O. *J. Chem. Soc., Dalton Trans.* **2001**, 1278.

(23) Thompson, A. M. W. C.; Smailes, M. C. C.; Jeffery, J. C.; Ward, M. D. *J. Chem. Soc., Dalton Trans.* **1997**, 737.

(24) Rogers, C. W.; Wolf, M. O. *Chem. Commun.* **1999**, 2297.

(25) Braunstein, P.; Matt, D.; Nobel, D.; Bouaoud, S.-E.; Carluer, B.; Grandjean, D.; Lemoine, P. *J. Chem. Soc., Dalton Trans.* **1986**, 415.

(26) Miessler, G. L.; Tarr, D. A. *Inorganic Chemistry*; Prentice-Hall: Toronto, 1991.

(27) Shriver, D. F.; Atkins, P. W. *Inorganic Chemistry*; 3rd ed.; W. H. Freeman and Company: New York, 1999; pp. 167-169.

(28) Lindner, E.; Meyer, S.; Wegner, P.; Karle, B.; Sickinger, A.; Steger, B. *J. Organomet. Chem.* **1987**, *335*, 59.

(29) Greenberg, I., "A nose for business", *Technology Review* **1999**, *July/August*, p. 63.

References begin on page 69.

(30) Geremia, S.; Mestroni, S.; Calligaris, M.; Alessio, E. *J. Chem. Soc., Dalton Trans.* **1998**, 2447.

(31) Tanase, T.; Aiko, T.; Yamamoto, Y. *Chem. Commun.* **1996**, 2341.

(32) Calligaris, M.; Carugo, O. *Coord. Chem. Rev.* **1996**, *153*, 83.

(33) Evans, I. P.; Spencer, A.; Wilkinson, G. *J. Chem. Soc., Dalton Trans.* **1973**, 204.

(34) Davies, J. A. *Adv. Inorg. Chem. Radiochem.* **1981**, *24*, 115.

(35) Hesek, D.; Inoue, Y.; Everitt, S. R. L.; Ishida, H.; Kunieda, M.; Drew, M. G. B. *Chem. Commun.* **1999**, 403.

(36) Coe, B. J.; Meyer, T. J.; White, P. S. *Inorg. Chem.* **1993**, *32*, 4012.

(37) Altomare, A.; Burla, M. C.; Cammalli, G.; Cascarano, M.; Giacovazzo, C.; Guagliardi, A.; Moliterni, A. G. G.; Polidori, G.; Spagna, A. *J. Appl. Cryst.* **1999**, *32*, 115.

(38) Beurskens, P. T.; Admiraal, G.; Beurskens, G.; Bosman, W. P.; deGelder, R.; Israel, R.; Smits, J. M. M. "The DIRDIF-94 program system, Technical Report of the Crystallography Laboratory," University of Nijmegen, 1994.

(39) Farrugia, L. J. *J. Appl. Cryst.* **1997**, *30*, 565.

(40) Verkade, J. G.; Quin, L. D. *Phosphorus-31 NMR Spectroscopy in Stereochemical Analysis*; Marchand, A. P., Ed.; VCH Publishers: Deerfield Beach, FL, 1987; Vol. 8; pp. 12, 466-470.

(41) Kasler, F.; Tierney, M. *Anal. Chem.* **1979**, *51*, 1070.

References begin on page 69.

Appendix 2.1 Crystallographic details

The crystallographic data for complex **1** have been deposited into the Cambridge Crystallographic Data Centre (CCDC) archives (reference number: 153809). The data can be accessed in CIF and other electronic formats on the world wide web through the Royal Society of Chemistry website (supplement to ref 22): http://www.rsc.org/suppdata/dt/b0/b0089311.

Table A.2.1. Crystallographic data, collection and refinement details for complex **1**

	1
Formula	$C_{39}H_{33}F_{12}N_4OP_3Ru$
M	995.69
μ / cm^{-1}	6.00
T / K	173 ± 1
Colour, habit	brown-red, block
Crystal system	monoclinic
Space group	$P2_1/n$ (No. 14)
a / Å	12.0656(4)
b / Å	20.2301(5)
c / Å	16.9836(6)
β / deg	102.651(2)
V / Å^3	4044.9(2)
ρ / g·cm^{-3}	1.635
Z	4
Refl. collected / unique / R_{int}	33540/8759/0.038
R_1[a]	0.031
wR_2[b]	0.086
GOF	1.48

[a]$I > 3\sigma(I)$. [b]All data. $R_1 = \Sigma \big| |F_o| - |F_c| \big| / \Sigma |F_o|$ (observed data). $wR_2 = (\Sigma(F_o^2 - F_c^2)^2 / \Sigma w(F_o^2)^2)^{½}$ (all data).

References begin on page 69.

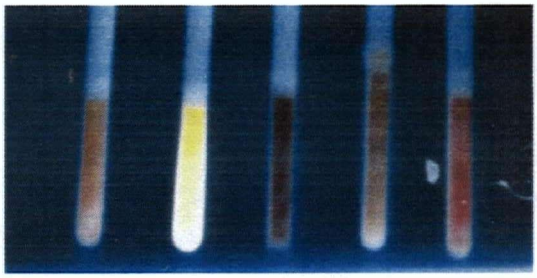

Chapter Three

The [*cis*-Ru(bpy)$_2$(POMe-*P,O*)]$^{2+}$ lumophore and its response to small-molecule coordination

3.1 The scope of this chapter

As introduced in Chapter Two (section 2.1), Ru(II) bis(bipyridyl) complexes are well-known to be photoluminescent, and variations in the ancillary ligand set tend to influence the energetics of the emissive MLCT excited state. Thus, the potential for ligand-dependent emission wavelength and intensity provides the incentive for investigating the hemilabile phosphine-ether complex **1** as a coordination-based luminescent sensor for Lewis basic small molecules. In Chapter Two, it was shown that complex **1** reacts with a variety of small-molecule analytes, and therefore satisfactorily performs the receptor function required of a molecule-based sensor. In this chapter, the redox, absorption and luminescence properties of **1** are presented. The changes in these properties that accompany the coordination of small molecules, which fulfill the requirement for a reporter function, are also presented. The

References begin on page 119.

chapter concludes with a discussion of complex **1** in the context of its intended function as a luminescent coordination-based multianalyte sensor.

3.2 Redox properties of 1 and the effect of analyte coordination

Determination of the reduction potential of a transition metal complex provides a measure of the electron density at the metal, which plays a role in defining its reactivity. It was of interest to probe the electron density of the metal in **1** in order to better understand its reactivity toward small molecules of different electron-donating abilities. Moreover, the redox chemistry of **1** was also of interest for reasons related to its lumophoric nature, as described below.

Ru(II) bipyridyl complexes typically undergo reversible oxidation and reduction in solution. The solution redox processes in these complexes normally involve the same molecular orbitals as the photoinduced metal-to-ligand charge transfer transition that gives rise to the luminescent MLCT excited state. Thus, information about the luminescent excited state can be gleaned from the ground-state reduction potentials.[1,2] The energy of the MLCT absorption, which corresponds to $Ru^{II}(bpy) \rightarrow Ru^{III}(bpy^{\bullet -})$, scales linearly with the difference between the $Ru^{III/II}$ and $bpy^{0/-}$ redox couples, $\Delta E_{(redox)}$;[3] the same holds true for the emission energies. These relationships have been used as confirmation that, within families of Ru(II) bpy complexes, the absorption and emission arise from analogous MLCT and LMCT processes. Excellent discussions of these relationships are available in reviews by Lever.[4,5] For compilations of hundreds of Ru(II) bpy complexes, the following relationship between absorption and redox energies has been determined:[3]

$$E_{abs}(MLCT) = 1.00\Delta E_{(redox)} + 0.21 \qquad [3.1]$$

where E_{abs}(MLCT) is the energy (in eV) of the MLCT band in the visible absorption spectrum; using Equation 3.1, the standard deviation between the observed and predicted energies is 0.11 eV. The light emitted from Ru diimine complexes is usually ~ 0.48 eV lower in energy than

References begin on page 119.

the difference in the $Ru^{III/II}$ and $bpy^{0/-}$ reduction potentials. The following relationship has been established[6] from a series of 23 emissive Ru(II) bpy complexes:

$$E_{em}(0–0) = 0.76(\pm0.06)\Delta E_{(redox)} + 0.14(\pm0.04) \qquad [3.2]$$

where $E_{em}(0–0)$ is the energy (in eV) of the first vibrational component of the low temperature emission spectrum. A series of seven [*cis*-Ru(bpy)(biq)LL]$^{2+}$ complexes (biq = biquinoline) yields different linear parameters, as shown in Equation 3.3:[4,7,8]

$$E_{em}(0–0) = 0.49(\pm0.03)\Delta E_{(redox)} + 1.06(\pm0.01) \qquad [3.3]$$

As will be seen later in this chapter, the complexes studied in this thesis are better described using Equation 3.3.

The redox processes of Ru(II) bpy complexes are typically examined by cyclic voltammetry in order to determine $\Delta E_{(redox)}$. In general, cyclic voltammograms of these complexes contain one reversible $Ru^{III/II}$ oxidation wave and a number of reversible reduction waves that correspond to one-electron reduction of each of the bpy ligands. For complexes of the type [*cis*-Ru(bpy)$_2$L$_2$]$^{2+}$, the metal-based oxidation occurs at 0.9 – 1.8 V, depending on the ancillary ligand L, while the bpy reductions (-1.3 – -1.5 V) are less sensitive to the nature of the ancillary ligands.[9] The effects of ligand variations on the electrochemical properties of Ru(II) bpy complexes are well understood, to the extent that this type of complex was used by Lever to establish a ligand electrochemical series[10] which is conceptually similar to the spectrochemical series used in electronic spectroscopy. Lever's ligand electrochemical parameters (E_L) are additive and permit prediction of both metal-based[10] and ligand-based[11] reduction potentials for a wide range of transition metal complexes. Lists of Lever parameters for hundreds of common ligands are available in the literature, derived from experimental electrochemical data[10] and also recently from computational studies;[12] Lever parameters used in this thesis are listed in Table 3.1.

References begin on page 119.

Table 3.1. Lever parameters (E_L)[10] for a variety of ligands.[b]

Ligand	E_L / V	Ligand	E_L / V
Cl^-	-0.24	MeCN	0.34
H_2O	0.04	Ph_3P	0.39
$^iPrNH_2$	0.05	Me_2O	0.45[a]
$BuNH_2$	0.13	DMSO	0.47
py	0.25	CO	0.99
bpy	0.259	POMe	0.63[c]
DMS	0.31	*o*-PhOMe	0.24[d]

[a]From ref 12; [b]Listed as potentials in Volts *vs.* NHE = -0.240 V *vs.* SCE; [c]Calculated from Eq. 3.4 using $RuCl_2$(POMe-*P,O*)$_2$, $E_{1/2}(Ru^{III/II})$ = 0.80 V *vs.* NHE; [d]Calculated from the E_L for POMe by removing the contribution from the PPh_3 moiety (E_L = 0.39).

For Ru(II) complexes, the metal reduction potential can be predicted from the sum of the Lever parameters for the ligands using Equation 3.4:[10]

$$E_{1/2}(Ru^{III/II})_{calc} = 0.97[\Sigma E_L] + 0.04 \qquad [3.4]$$

Similarly, the bpy reduction potential in Ru^{II}(bpy) complexes can be predicted using Equation 3.5:[11]

$$E_{1/2}(bpy^{0/-})_{calc} = 0.25(\pm 0.01)[\Sigma E_L(bpy)] - 1.40(\pm 0.03) \qquad [3.5]$$

where ΣE_L(L) is the sum of the Lever parameters minus the contribution from the bpy ligand being reduced (*i.e.*, ΣE_L(bpy) = ΣE_L - (2 × 0.259) V). It should be noted that Lever parameters were defined using data from complexes that exhibit reversible redox chemistry and do not undergo ligand exchange during electrochemical experiments; thus, application of Equations 3.4 and 3.5 to systems that are not similarly well-behaved[10] must be done with caution.

References begin on page 119.

3.2.1 Characterization of 1 by cyclic voltammetry

The cyclic voltammogram (CV) of complex **1**, shown in Figure 3.1, contains three main features. The metal-based oxidation occurs at +1.56 V *vs.* SCE and is not fully reversible, even at fast scan rates. There are two main ligand-based reductions at -1.27 V and -1.71 V, which are also irreversible. The shoulder at -1.19 V did not consistently appear resolved from the other reduction waves in all voltammograms, which may be related to the presence of water in the solution, even though precautions were taken to dry the solvent and electrolyte before use.

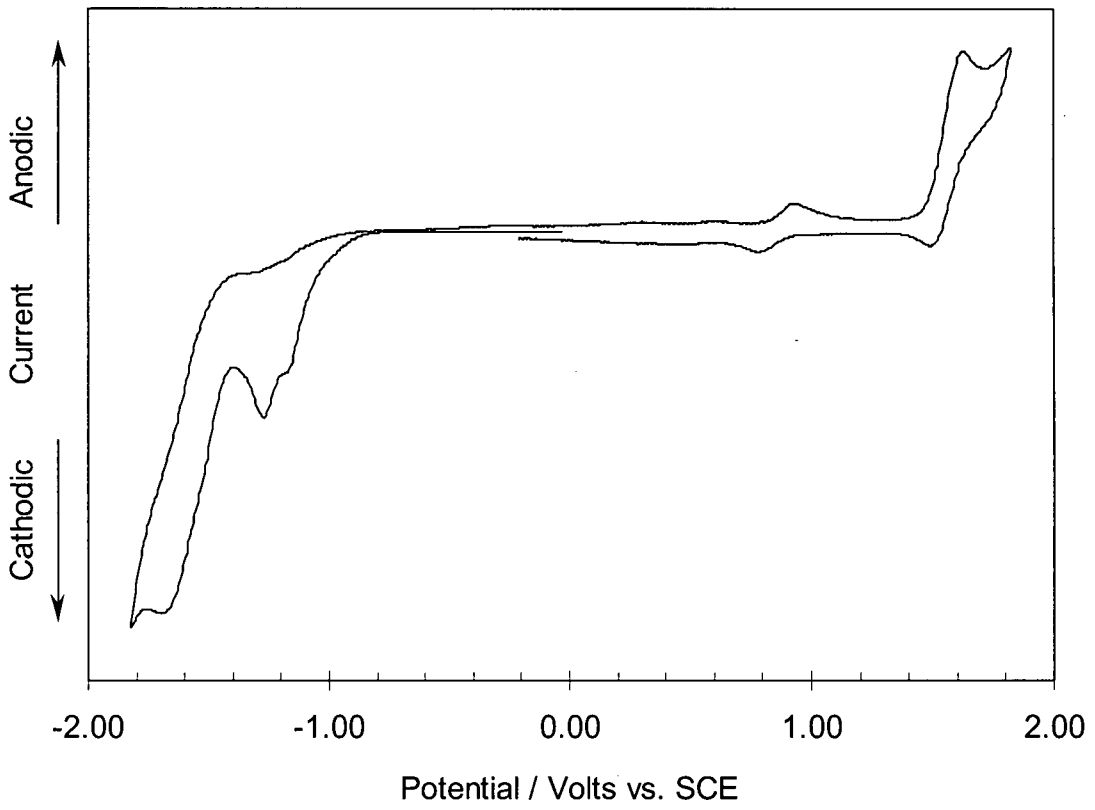

Figure 3.1. Cyclic voltammogram of **1** in CH_2Cl_2 solution containing 0.1 M $^nBu_4NPF_6$ as supporting electrolyte; [**1**] $\approx 10^{-3}$ M. The potential sweep program was: 0 $\rightarrow$ -1.80 $\rightarrow$ +1.80 $\rightarrow$ -0.20 V *vs.* SCE.

References begin on page 119.

Table 3.2 lists the experimentally derived reduction potentials in comparison to those predicted from Equations 3.4 and 3.5. Based on the values predicted using Lever parameters, the first reproducible reduction wave (E_{red} = -1.27 V) can be assigned to the bpy reduction. Thus, the difference between the metal and bpy redox couples ($\Delta E_{(redox)}$) is 2.83 V. This value is identical to the reported value[9] of $\Delta E_{(redox)}$ for [*cis*-Ru(bpy)$_2$(PPh$_2$Me)$_2$]$^{2+}$, and fits with the $\Delta E_{(redox)}$ *vs.* E_{em}(0–0) correlations reported in the literature.[4,6-9]

Table 3.2. Reduction potentials for **1** and model complex (V *vs.* SCE).

Complex	Observed		Predicted	
	E_{ox}	E_{red}	$E_{1/2}(Ru^{III/II})_{calc}$	$E_{1/2}(bpy^{0/-})_{calc}$
1	1.56	-1.19	1.42[a]	-1.35[a]
		-1.27		
		-1.71		
[Ru(bpy)$_2$(PPh$_3$)(Me$_2$O)]$^{2+}$	---	---	1.62	-1.30

[a]Calculated using E_L = 0.63 V for the POMe ligand.

It should be noted that the appearance of the CV of **1** depends on the direction of the potential scan because of the irreversibility of the reduction. Voltammograms obtained with an initial oxidative sweep (0 → +2 → -2 → 0 V) do not contain the additional small oxidation wave ($E_{1/2}$ = 0.86 V) that is observed when the initial sweep direction is reversed (as in Figure 3.1: 0 → -2 → +2 → 0 V). The extra oxidation wave corresponds to a stable product that forms rapidly when **1** is reduced; efforts to identify this compound were unsuccessful. However, it is not the demethylated complex ($E_{1/2}$ = 0.63 V; see Chapter Four), which is also unstable toward reduction to yield a different product that can be reversibly oxidized. The instability of the reduced species is unusual; similar complexes[9] such as [*cis*-Ru(bpy)$_2$(PPh$_2$Me)$_2$]$^{2+}$ show reversible redox chemistry, which suggests that the reductive reaction process involves the phosphine-ether ligand. Complexes in which the ether is not coordinated exhibit predominantly reversible electrochemistry (one wave remains irreversible;

References begin on page 119.

vide infra). Phosphine aquo complexes have relatively low metal-based reduction potentials (*e.g.*, for [*cis*-Ru(bpy)$_2$(PPh$_3$)(H$_2$O)]$^{2+}$, $E_{1/2}$ = 0.50 V, measured in aqueous solution);[13] it may be that some of the reduced complex reacts with trace water in the solvent to form an aquo complex.

In general, the reduction potentials observed for **1** are comparable to those of the related bis(phosphine) complex [*cis*-Ru(bpy)$_2$(PPh$_2$Me)$_2$]$^{2+}$ ($E_{1/2}(Ru^{III/II})$ = 1.56 V, $E_{1/2}$(bpy/bpy$^{\bullet-}$) = -1.27 V). Interestingly, both metal oxidation and ligand reduction occur at more positive potentials than in the similar chelating bis(phosphine) complex [*cis*-Ru(bpy)$_2$(dppe)]$^{2+}$ ($E_{1/2}(Ru^{III/II})$ = 1.41 V, $E_{1/2}$(bpy/bpy$^{\bullet-}$) = -1.37 V; dppe = Ph$_2$P(CH$_2$)$_2$PPh$_2$)[9], while the metal oxidation occurs at lower potential than in [*cis*-Ru(bpy)$_2$(dppm)]$^{2+}$ ($E_{1/2}(Ru^{III/II})$ = 1.64 V, $E_{1/2}$(bpy/bpy$^{\bullet-}$) = -1.29 V; dppm = Ph$_2$PCH$_2$PPh$_2$).[14] This appears to reflect differences in metal-phosphorus orbital overlap due to conformational restrictions imposed by the bridges (methylene *vs.* ethylene *vs. o*-phenylene) between the donor atoms. Of potentially greater significance to this work is the fact that the irreversibility of the redox chemistry of **1** is atypical of Ru(II) bipyridyl complexes. To compare, inspection of the CV of [*cis*-Ru(bpy)$_2$(dppm)]$^{2+}$ reveals a reversible metal oxidation (1.64 V) and two reversible bpy reductions (-1.28, -1.54 V) with no other reductive features.[14] In general, for Ru(II) (bis)bipyridyl bis(phosphine) complexes there are no redox processes (within the +2 to –2 V range) that involve the phosphine ligands, while for **1** there may be a third reductive process (although it may be an experimental artifact related to the presence of water). This is noteworthy because it lowers the certainty of the assignment of the reduction processes; it is possible that the lowest energy solution redox processes in complex **1** may not be strictly analogous to the MLCT transition as they are for other Ru(II) bipyridyl complexes.

3.2.2 Electrochemical response of 1 to small-molecule analytes

Changes in the coordination sphere of **1** brought about by displacement of the labile ether by small molecules were expected to impact upon the redox properties of **1**, particularly the potential at which the metal undergoes oxidation to Ru(III). In turn, these changes were expected to correlate with the differences in MLCT absorption and emission properties induced

References begin on page 119.

by the binding of analytes. Using Lever parameters to estimate the reduction potentials of the complexes (Equations 3.4 and 3.5), values of $\Delta E_{(redox)}$ were predicted for the various analyte-bound complexes described in Chapter Two. Where possible, the solution electrochemistry of the sensor-analyte complexes was examined via cyclic voltammetry to compare to these predicted values; details of these CV experiments are presented in the following sections. The experimentally observed and predicted values of $\Delta E_{(redox)}$ are listed below in Table 3.3. From these $\Delta E_{(redox)}$ values, the MLCT absorption and LMCT emission energies for **1** and the series of sensor-analyte complexes, **1•L**, were predicted using Equations 3.1, 3.2 and 3.3; these are presented later in the chapter (section 3.4.4) in Table 3.6.

Table 3.3. Reduction potentials for **1** and sensor-analyte complexes, **1•L** (V *vs.* SCE).

Complex	Observed			Predicted		
	E_{ox}	E_{red}	$\Delta E_{(redox)}$	$E_{1/2}(Ru^{III/II})_{calc}$	$E_{1/2}(bpy^{0/-})_{calc}$	$\Delta E_{(redox)calc}$
1	1.56	-1.27	2.83	1.42[a]	-1.35[a]	2.77
1•MeCN	1.53	-1.30	2.83	1.52	-1.33	2.85
1•NEt$_3$	---	---	---	1.28	-1.39	2.67
1•EtSH	---	---	---	1.48	-1.34	2.82
1•DMSO-*S*	---	---	---	1.64	-1.30	2.94
1•DMSO-*O*	1.17[b]	---	---	1.17	-1.41	2.58
1•Me$_2$S	---	---	---	1.49	-1.34	2.82
1•OH$_2$	---	---	---	1.23	-1.40	2.63

[a]Calculated using E_L = 0.63 V for the POMe ligand. [b]Used to estimate E_L = -0.02 V for *O*-bound DMSO. [c]Calculated using E_L = -0.02 V for *O*-bound DMSO.

3.2.2.1 Electrochemical effects of coordination of MeCN to 1

The CV shown in Figure 3.2 reveals several redox waves for **1•MeCN**, dramatically different from the irreversible voltammetry observed for **1** (Figure 3.1). With MeCN

References begin on page 119.

coordinated to the metal, the $Ru^{III/II}$ couple ($E_{1/2}(Ru^{III/II})$ = 1.53 V) is quasireversible. Several reduction waves are present: E_{red} = -1.30 (sh) and -1.42; $E_{1/2}$ = -1.54 and -1.83 V. Based on comparison to the predicted bpy reduction potential, the two lowest energy reduction waves observed for **1•MeCN** are likely bpy-based and the higher energy reductions may be localized on the POMe ligand.

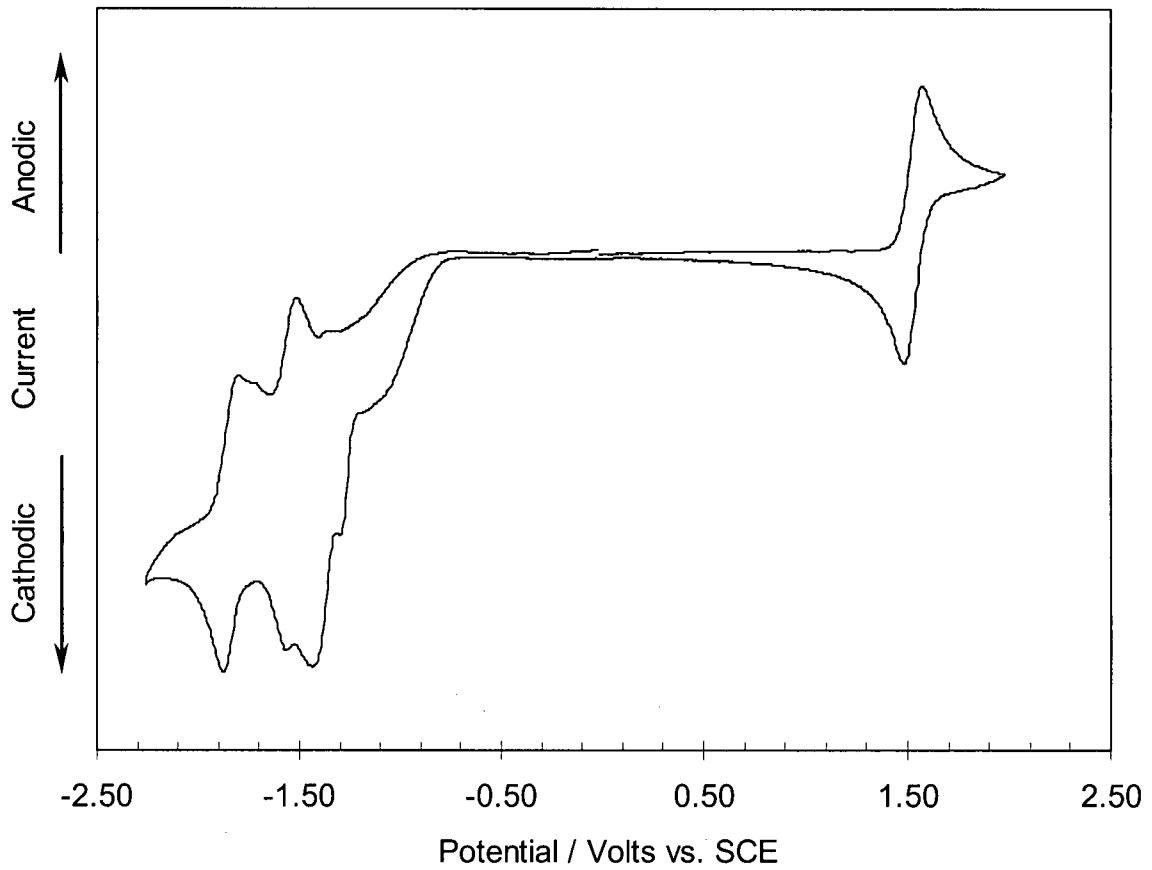

Figure 3.2. Cyclic voltammogram of **1•MeCN** in CH_3CN solution containing 0.1 M $^nBu_4NPF_6$ as supporting electrolyte, [**1•MeCN**] $\approx 2 \times 10^{-3}$ M. The potential sweep program was: $0 \rightarrow +2.0 \rightarrow -2.3 \rightarrow 0$ V *vs.* SCE.

As for **1**, a product resulting from reduction ($E_{1/2}$ = 0.45 V) is observed by CV if the potential is first swept past the irreversible reduction waves. Again, the identity of this

References begin on page 119.

reduction product has not been determined. However, it is with certainty not [*cis*-Ru(bpy)$_2$(MeCN)$_2$]$^{2+}$ ($E_{1/2}$ = 1.44 V),[15] and its low reduction potential suggests it might contain anionic ligands (*cf. cis*-Ru(bpy)$_2$Cl$_2$•2H$_2$O, $E_{1/2}$ = 0.31 V; *cis*-Ru(bpy)$_2$Br$_2$•2H$_2$O, $E_{1/2}$ = 0.37 V)[16] or coordinated water.

According to the potential of the $Ru^{III/II}$ couple, the electron density at the metal is not changed significantly upon coordination of MeCN. Moreover, the ligand reductions are not shifted significantly. Thus, $\Delta E_{(redox)}$ of **1•MeCN** (2.83 V) is equivalent to that of **1** (2.83 V), which implies that the MLCT absorption band should be similar in energy to that of **1**. Thus, the solution redox chemistry predicts a negligible colour change, although in reality a distinct yellowing of the solution is observed by eye when **1** is reacted with MeCN. The photophysical properties of this complex are discussed in further detail in section 3.4.2.1.

3.2.2.2 Electrochemical response to other analytes

The electrochemistry of the DMSO and dodecanethiol complexes was also investigated. The experiments were performed in CH_2Cl_2 solution ([**1**] ≈ 2 × 10^{-3} M) with analyte added in successive small aliquots (> 200 equiv at a time) so that changes in the CV could be followed. In cases where the $Ru^{III/II}$ oxidation wave was significantly shifted by coordination of analyte, $E_{1/2}(Ru^{III/II})$ could be measured; however, the corresponding reduction waves could not be located because of overlap with the ligand reduction waves of **1**. Thus, it was not possible to determine, from voltammetry, experimental values of $\Delta E_{(redox)}$ for analyte complexes other than **1•MeCN**.

In the presence of DMSO, a new reversible metal-based oxidation is observed in the voltammogram, with $E_{1/2}(Ru^{III/II})$ = 1.17 V (clearly observable for [DMSO] > 0.2 M ≈ 100 equiv), as shown in Figure 3.3. Oxidation of unreacted **1** and free DMSO obscured the CV beyond ~ 1.5 V. The **1•DMSO-*S*** oxidation is predicted using Lever parameters to occur at ~ 1.64 V. It should be noted that the Lever parameter for DMSO (E_L = 0.45) is reported to be uncertain relative to other Lever parameters,[10] which may explain the disagreement between experiment and prediction in this case. However, given that complex **1** also binds DMSO via the oxygen atom and that the complex **1•DMSO-*O*** is undoubtedly present when **1** is exposed

References begin on page 119.

to such a large excess of DMSO, the observed redox wave very likely corresponds to oxidation of **1•DMSO-*O***. A ligand electrochemical parameter has not been reported for *O*-bound DMSO before; from these data, a value of E_L = -0.02 is obtained, which is comparable to the accepted Lever parameter for water (E_L = 0.04). The bpy reduction potentials for the DMSO-bound complexes could not be determined from the CV because the waves are obscured by those of **1**. The MLCT transition energy for **1•DMSO-*O*** should be smaller than that of **1** based on its smaller predicted $\Delta E_{(redox)calc}$ of 2.58 V (*cf.* 2.83 V for **1**), while that of For **1•DMSO-*S*** should be larger ($\Delta E_{(redox)calc}$ = 2.94 V). Thus, it is difficult to predict the colour and emission changes that would be observed due to DMSO coordination, since they should depend on the speciation in the sample; the photophysical details are elaborated in section 3.4.3.3.

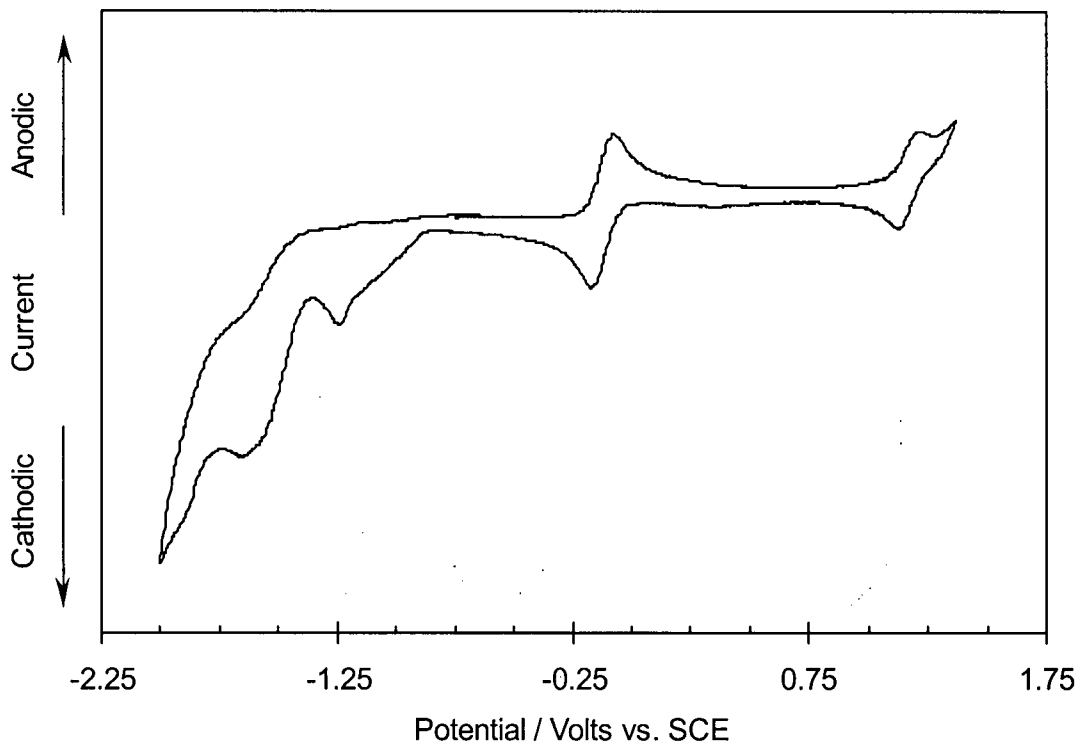

Figure 3.3. Cyclic voltammogram of a mixture of **1** and **1•DMSO** in CH_2Cl_2 solution containing 0.1 M $^nBu_4NPF_6$ as supporting electrolyte, [**1** + **1•DMSO**] ≈ 2 × 10^{-3} M, [DMSO] ≈ 2 × 10^{-2} M. The potential sweep program was: 0 → +1.5 → -2.0 → 0 V *vs.* SCE. The large wave at $E_{1/2}$ = -0.120 V is due to $Me_{10}Fc$.

References begin on page 119.

A similar experiment was performed with dodecanethiol. A sample of **1** was treated with 100 equiv of dodecanethiol; no immediate changes were evident in the CV aside from the appearance of a large irreversible wave due to oxidation of free thiol, which restricted the working potential range to < 1.42 V, well below the potential at which **1** is oxidized. The sample was left to equilibrate for ~ 1 h, during which time the usual colour change from orange to olive occurred, but there were no further changes observed in the CV. Thus, the coordination of dodecanethiol by **1** does not lead to easier oxidation of the metal, unless the colour change from orange to greenish is itself indicative of oxidation of the metal centre upon thiol coordination. Because the reaction was shown by NMR spectroscopy to be reversible, however, this suggestion is relatively unlikely. It is therefore concluded that thiol coordination does not significantly decrease the reduction potential of the metal, which is consistent with the photoluminescence response discussed in section 3.4.3.1.

3.3 Photophysical properties of 1

3.3.1 Absorption and luminescence spectra of 1

Complex **1** exhibits photophysical behaviour that is typical of [*cis*-Ru(bpy)$_2$L$_2$]$^{2+}$ complexes.[9] The visible absorption spectrum, shown in Figure 3.4, contains a broad structureless band (λ_{max} = 412 nm). Although not shown in Figure 3.4, strong ligand-based absorptions are observed in the UV region due to bipyridine and phenyl-based $\pi \rightarrow \pi^*$ processes. The visible band, responsible for the orange colour of the complex, is assigned to a spin-allowed metal-to-ligand charge transfer (MLCT) transition that leaves the excited electron on a bpy ring (*i.e.*, $d\pi \rightarrow \pi^*$), as is typical for [Ru(bpy)$_3$]$^{2+}$ and related bipyridyl complexes.[1] The intensity of this MLCT absorption (λ_{max} = 412 nm, ε = 7200 M^{-1}cm^{-1}) is similar to that of [*cis*-Ru(bpy)$_2$(PPh$_2$Me)$_2$]$^{2+}$ (λ_{max} = 427 nm, ε = 6920 M^{-1}cm^{-1}),[14] both of which are lower than for [Ru(bpy)$_3$]$^{2+}$ (λ_{max} = 452 nm, ε = 14450 M^{-1}cm^{-1})[17] because there are fewer bipyridyl ligands. The MLCT absorption energy (E_{abs}(MLCT)) is ~ 3.01 eV, approximately 0.2 eV larger than the measured difference in the solution redox potentials ($\Delta E_{(redox)}$ = 2.83 V), as is generally the case for Ru diimine complexes (Equation 3.1). The predicted MLCT transition

References begin on page 119.

energy based solely on Lever parameters ($E_{abs}(MLCT)_{calc}$ = 2.98 eV, using E_L = 0.63 for POMe) is in excellent agreement with experiment.

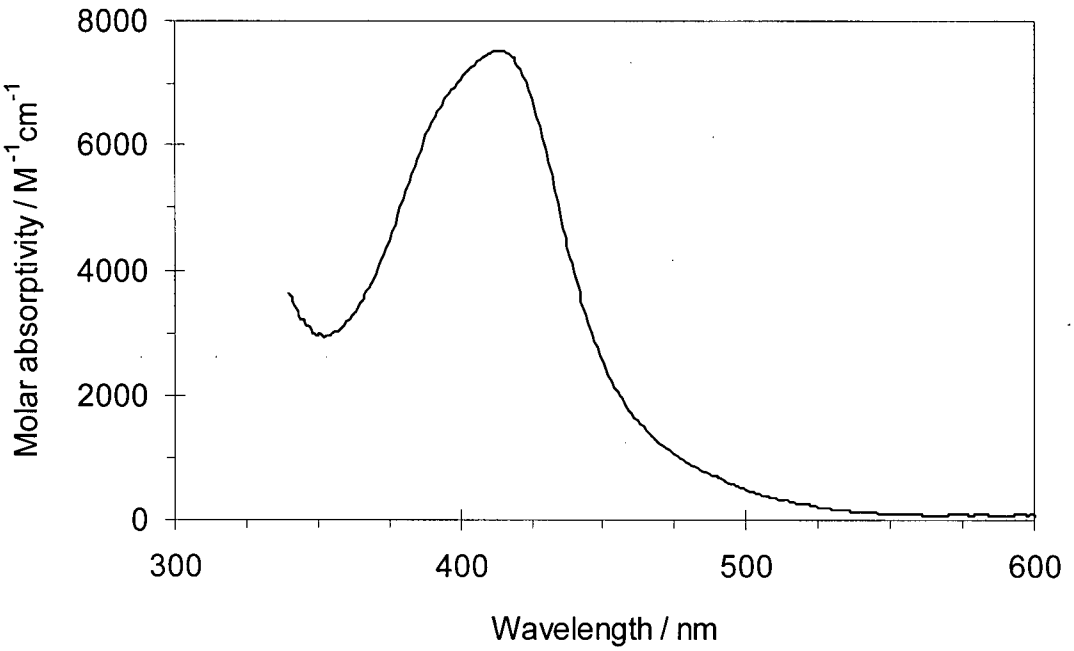

Figure 3.4. Visible absorption spectrum of **1** measured in CH_2Cl_2 solution at RT

Orange emission can be observed by eye if a solution of **1** is frozen in liquid nitrogen and illuminated by a handheld UV lamp (366 nm). The emission fades within a few seconds as the sample begins to warm up. At room temperature, no emission can be detected by eye or using a fluorometer. The sensitivity of the luminescence to temperature is related to the existence of both emissive MLCT and nonemissive dd excited states and will be elaborated upon in section 3.3.2.

References begin on page 119.

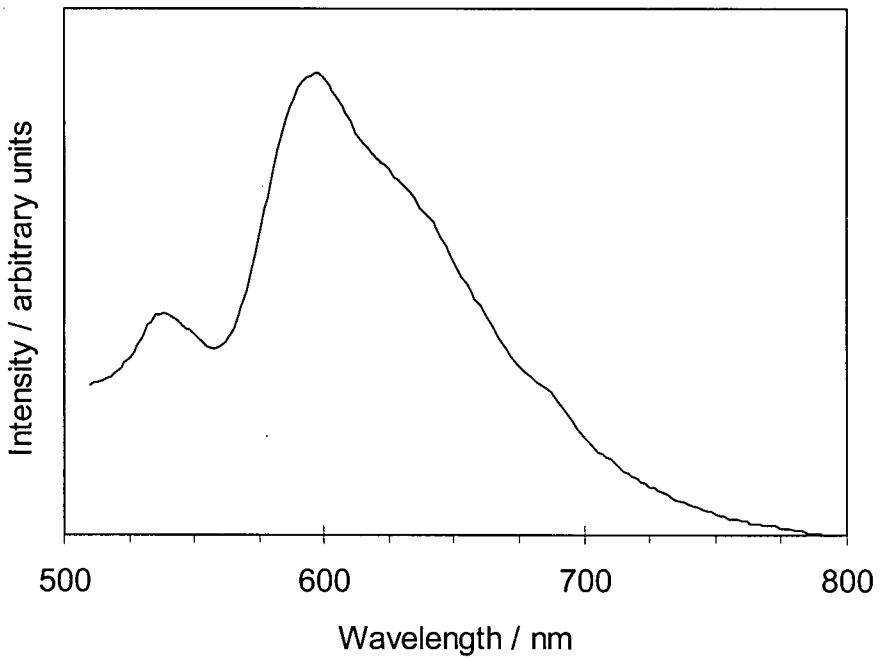

Figure 3.5. Photoluminescence spectrum of **1** measured at 77 K in solid 2:1 ethanol/acetone solution, [**1**] = 10^{-3} M, λ_{ex} = 455 nm.

The emission spectrum of **1** (Figure 3.5) measured at 77 K in frozen 2:1 ethanol/acetone solution (10^{-3} M) consists of a broad, slightly structured band centred at approximately 600 nm with a long tail to lower energy. Although not shown, the excitation spectrum is similar to the absorption spectrum of **1**, which supports assignment of this emission as due to complex **1** rather than an unidentified impurity. The highest energy emission band observed (λ_{em} = 542 nm; E_{em} = 2.29 eV) may correspond to the 0–0 transition, but it is significantly lower in energy than the value of $E_{em}(0–0)$ predicted from the electrochemical data and Lever parameters ($E_{em}(0–0)_{calc}$ = 2.42 eV; $\lambda_{em}(0–0)_{calc}$ = 512 nm). It is probable that the intensity of the 0–0 band is too low to be resolved. The highest energy observed emission band is considerably weaker in intensity than the subsequent band (λ_{em} = 588 nm), which dominates the spectrum and accounts for the orange colour of the emission. Emission spectra for [*cis*-Ru(bpy)$_2$L$_2$]$^{2+}$ complexes typically show a gradual decrease in band

References begin on page 119.

intensity with decreasing energy across the vibrational progression, and a pronounced low-energy tail.[9] The vibrational progression is generally attributed to vibrations within the bipyridine ligand framework. It should be noted that electronic transitions happen so quickly that nuclei generally do not have time to change their locations, 'vertical transitions' (*i.e.*, vertical on a potential energy diagram with E *vs.* internuclear separation) from the lowest vibrational level of the excited state are most probable. Normally for Ru(II) bpy complexes, the 0–0 transition dominates. This implies that the bond lengths in the MLCT excited state are similar to those in the ground state, even though the excited state is long-lived and therefore thermally equilibrated. The diminutive high-energy band observed for **1** implies that the bond lengths in the MLCT excited state of **1** are significantly different than those in the ground state. This difference may be related to geometrical constraints imposed by the 5-membered *P,O*-chelate ring. It is unlikely to be related to symmetry considerations since a complex containing a different asymmetric (6-membered) chelate with *N,N'*-coordinated 2-(2-aminoethyl)pyridine)[9] shows the typical vibrational progression in its emission spectrum.

As is clear from the data listed in Table 3.4, the emission spectrum of **1** is energetically similar to that of the complex [*cis*-Ru(bpy)$_2$(PPh$_2$Me)$_2$]$^{2+}$ ($E_{em}(0–0)$ = 18.5 × 10^3 cm^{-1} and $E_{em}(0–1)$ = 17.4 × 10^3 cm^{-1}),[9] although the emission from [*cis*-Ru(bpy)$_2$(PPh$_2$Me)$_2$]$^{2+}$ is more yellowish in colour because of its (typical) dominant 0–0 band. While the spectra of both complexes show poorly resolved vibrational structure at 77 K, the spacing (ν_M) between the 0–0 and 0–1 components in the spectrum of **1** is noticeably larger (~1500 cm^{-1} for **1** *vs.* ~1100 cm^{-1} for [*cis*-Ru(bpy)$_2$(PPh$_2$Me)$_2$]$^{2+}$). The vibrational spacing in Ru(II) bpy complexes is known to be influenced to some degree by the ancillary ligands. Values of ν_M range from 1100 cm^{-1} for [*cis*-Ru(bpy)$_2$(PPh$_2$Me)$_2$]$^{2+}$, to 1350 cm^{-1} for [Ru(bpy)$_3$]$^{2+}$, to 1450 cm^{-1} for [*cis*-Ru(bpy)$_2$(*o*-(AsMe$_2$)$_2$Ph]$^{2+}$,[9] but there is no obvious relationship between the nature of the ancillary ligand (*e.g.*, chelate *vs.* monodentate) and the magnitude of ν_M.

References begin on page 119.

Table 3.4. Photoluminescence data for **1** and related complexes at 77 K

Compound	$\lambda_{em}(0–0)$ / nm	$E_{em}(0–0) \times 10^{-3}$ / cm^{-1}	ν_M / cm^{-1}	$E_{em}(0–0)$ / eV	τ / μs
$[Ru(bpy)_3]^{2+}$ [a]	584	17.12	1350	2.12	5.21 ± 0.06[b]
$[Ru(bpy)_2(PPh_2Me)_2]^{2+}$ [a]	540	18.52	1100	2.30	---
1[c]	542	18.5	1500	2.29	2.04 ± 0.07

[a]Measured in 4:1 EtOH/MeOH glass.[9] [b]From ref [18]. [c]Measured in 2:1 EtOH/acetone solid solution, [**1**] ≈ 10^{-3} M; λ_{ex} = 455 nm for spectral data; λ_{ex} = 337 nm for lifetime determination.

3.3.2 Temperature-dependent emission from 1

Weak orange emission is observed from complex **1** when photoexcited at low temperature (77 K). The intensity of the emission diminishes rapidly as the temperature is increased, and no emission is detectable at temperatures above ~ 180 K. This behaviour matches that of other Ru(II) bipyridyl phosphine complexes and is consistent with the existence of a nonemissive metal-centred excited state that is thermally accessible via a small activation barrier from the MLCT excited state. Because the emission from **1** is limited to low temperatures like other Ru(II) bis(bipyridyl) bis(phosphine) complexes, a collaboration was initiated with Prof. Wayne Jones and doctoral student Yan Zhang at the State University of New York at Binghamton in order to study the temperature dependence of the photoluminescence of **1** (and its congeners) in more detail. Although much of the variable-temperature emission data reported in this chapter was gathered by our colleagues, some measurements were performed jointly during a recent visit to their facilities at SUNY Binghamton.

The lifetime of the emitting excited state for **1** was determined by monitoring the time-resolved decay of the emission after excitation by a pulsed N_2 laser (337 nm). At 77 K in deaerated 2:1 ethanol/acetone solution ([**1**] ≈ 10^{-3} M), the emission was found to arise from a single emitting species. As shown in Figure 3.6, the emission decayed exponentially with a

References begin on page 119.

lifetime of $\tau = 2.04 \pm 0.08$ μs. The emission lifetime is significantly shorter than those of both $[Ru(bpy)_3]^{2+}$ (τ = 5.21 μs)[18] and the related chelating phosphine complex [*cis*-$Ru(bpy)_2(dppe)]^{2+}$ ($\tau = 6.2$ μs)[9] at 77 K. This suggests that neither the phosphine moiety nor the chelating nature of the POMe ligand is responsible for the decreased longevity of the emissive excited state of **1** at low temperatures. Thus, the metal-bound ether moiety may provide alternative nonradiative deactivation pathways that depopulate the MLCT excited state rapidly even at 77 K, either due to an intrinsic effect of ether coordination or by virtue of the fact that this coordination is weak.

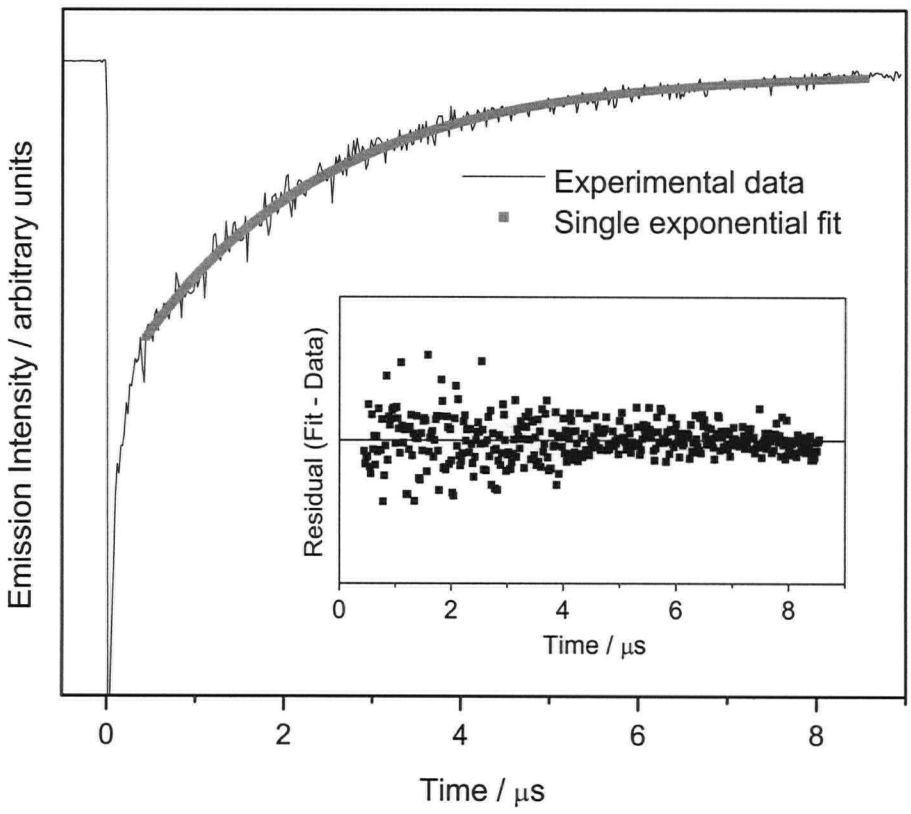

Figure 3.6. Emission (630 nm) decay trace for lifetime determination of **1** at 77 K in solid 2:1 ethanol/acetone solution containing residual water (~ 0.3 M); [**1**] = 1×10^{-3} M, $\tau = 2.13 \pm 0.02$ μs. Inset plot shows residuals (first order decay model - data).

References begin on page 119.

A full study of the temperature dependence of the emission from **1** was attempted, but the emission was too weak for reliable time-resolved emission data to be gathered over a meaningful temperature range. For this reason, it was not possible to calculate a value for the MLCT-dd activation barrier. Given the similarity in their other photophysical parameters, however, it is reasonable to estimate that the thermal barrier is of similar magnitude for **1** and [*cis*-Ru(bpy)$_2$(PPh$_2$Me)$_2$]$^{2+}$, *i.e.*, $E_a \leq 850$ cm^{-1}.

3.3.3 Summary of photophysical properties of 1 compared to related complexes

The coordinated ether moiety in **1** has relatively little impact on the photophysical properties of the [*cis*-Ru(bpy)$_2$LL']$^{2+}$ lumophore, even though it clearly diminished the reversibility of the solution redox processes discussed in section 3.2.1. The absorption and emission spectra of **1** are characteristic of phosphine complexes, as is the loss of luminescence at temperatures above ~ 180 K. The most significant photophysical differences between **1** and related bis(phosphine) complexes are the diminutive 0–0 emission band and the shorter emission lifetime for **1**, which likely arises from additional nonradiative deactivation pathways made available by the hemilabile ligand.

3.4 Photophysical effects of small-molecule coordination

As described in section 2.1.2, the nonchromophoric ligands in [*cis*-Ru(bpy)$_2$LL']$^{2+}$ complexes influence the MLCT absorption and emission spectra. The temperature dependence of the emission is also strongly dependent upon the nature of these ligands; in the case of complex **1**, the POMe ligand's phosphine moiety limits the emission to low temperatures. Changes in occupancy of the labile coordination site due to displacement of the ether moiety by other Lewis bases was expected to lead to energetic perturbations of the excited state manifold, and the emission from the lowest-energy MLCT excited state.

Indeed, the reaction of **1** with small molecules generally leads to visible colour changes, which were mentioned briefly in the previous sections as each reaction was described.

References begin on page 119.

In the following sections, the effect of each analyte is elaborated in terms of changes in the absorption and emission spectra of **1**. The interpretation of the spectroscopic data for the collection of analytes, as summarized in Tables 3.5 and 3.6, is discussed in section 3.4.4. Due to the infancy of our collaboration with Prof. Wayne Jones and Yan Zhang at SUNY Binghamton, only a limited selection of temperature-dependence studies is available for discussion at this time.

3.4.1 Photophysical response to water

As described in Chapter Two (section 2.4.2.1), NMR spectroscopic evidence shows that complex **1** reacts with water. Consistent with this finding, the absorption spectrum of **1** varies depending on the dryness of the solvent. Solutions of **1** (10^{-4} M) prepared in anhydrous CH_2Cl_2 show maximum MLCT absorption at 413 nm; in this solvent, no significant changes are observed if some water is added, presumably due to the low miscibility of water with CH_2Cl_2. However, the addition of 5 % v/v water (~ 3 M) to a solution of **1** in 2:1 ethanol/acetone ([**1**] = 10^{-3} M) results in a noticeable red shift and broadening of the MLCT band; the absorption maximum shifts from 411 nm to 419 nm. Anhydrous ethanol and acetone (as received from the suppliers) contain approximately 0.5 % v/v or ~ 0.3 M water, so this treatment corresponds to an increase in the relative [H_2O]:[**1**] ratio from approximately 1000:1 to 10000:1. The observed shift in the absorption spectrum is consistent with the small equilibrium constant (K_{eff} = (6 ± 3) × 10^{-4}) determined from the NMR spectroscopic data (section 2.4.2.1). For a sample containing 10^{-3} M **1**, an increase from 0.3 M to 3 M water should result in a change in the **1•OH$_2$**:**1** ratio from ~ 1.0:1.9 to 2.5:1.0, which is a large enough change in speciation to produce noticeable spectral changes for two species with significantly different MLCT transition energies.

3.4.1.1 Concentration-dependent absorption and emission spectra

Absorption spectra of complex **1** in 2:1 ethanol/acetone solution were determined over a range of concentrations (10^{-3} to 10^{-5} M) after it was discovered that the complex showed different emission spectra depending on the concentration of **1**. Both the MLCT absorption

References begin on page 119.

band and the emission spectrum become red-shifted as the concentration of **1** is decreased, as shown in Figures 3.7 and 3.8. The onset of the spectral red shift occurs at the same concentration, approximately 10^{-4} M, for both absorption and emission, and the shift is complete by 10^{-5} M. At the high-concentration limit (10^{-3} M), complex **1** shows a maximum MLCT absorption at 414 nm and maximum emission at 588 nm, whereas at the low-concentration limit (10^{-5} M), maximum MLCT absorption occurs at 448 nm and maximum emission occurs at 629 nm. The two absorption bands are of similar intensity (ε_{414} = 6700 ± 100 $M^{-1}cm^{-1}$; ε_{448} = 8000 ± 600 $M^{-1}cm^{-1}$); however, the lower energy band is broadened slightly relative to the high-energy band. The dramatic 30 – 40 nm red shift of both the absorption and maxima of the emission spectra that occurs when the concentration of **1** is decreased from 10^{-3} M to 10^{-5} M is significant and considered unusual for two reasons. Firstly, Ru(II) bipyridyl complexes do not typically show concentration-dependent absorption or emission spectra. Secondly, no evidence for dimerization or other intermolecular interactions has yet been encountered in the studies of complex **1**.

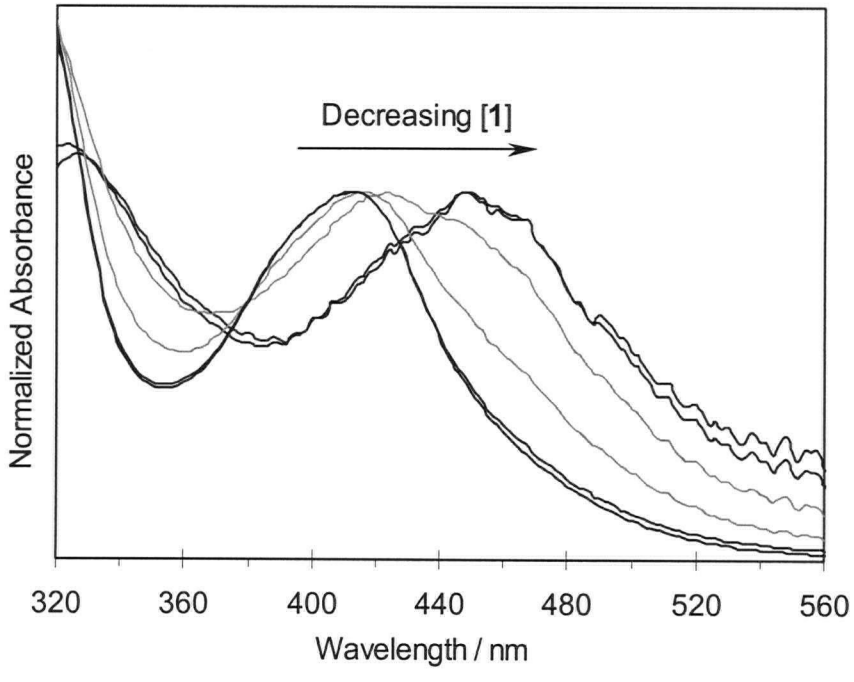

Figure 3.7. Absorption spectra (RT) for **1** at various concentrations in 2:1 ethanol/acetone solution containing residual water; [**1**] = 1 × 10^{-3}, 5 × 10^{-4}, 2 × 10^{-4}, 1 × 10^{-4}, 5 × 10^{-5}, and 3 × 10^{-5} M from left to right.

References begin on page 119.

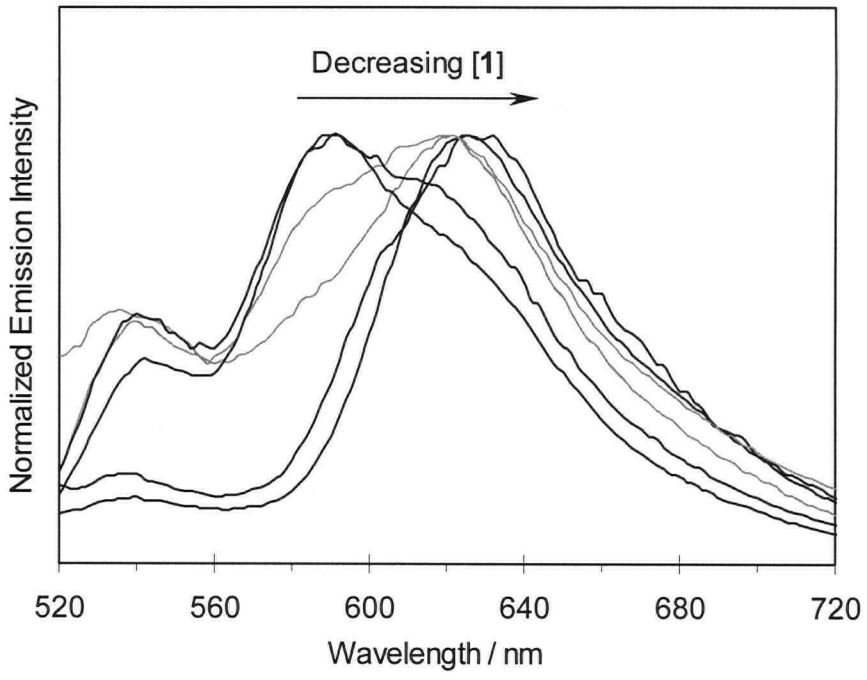

Figure 3.8. Emission spectra (77 K) for **1** at various concentrations in 2:1 ethanol/acetone solution containing residual water; [**1**] = 1×10^{-3}, 5×10^{-4}, 2×10^{-4}, 1×10^{-4}, 5×10^{-5}, and 3×10^{-5} M from left to right.

Given that NMR spectroscopic experiments have shown that complex **1** is in equilibrium with an aquo complex in 'wet' solvents, this concentration dependence can, in fact, be explained based on the presence of adventitious water in the solvent. Indeed, the magnitude of the absorption spectral red shift at low concentrations depends on how dry the solvents are. Low-concentration solutions in ethanol/acetone (10^{-5} M) show larger red shifts when prepared using anhydrous solvents as received from the suppliers (~ 0.3 M H_2O) than when prepared using solvents rigorously dried using accepted protocols; addition of 5 – 10 % water (v/v) to dry solutions restores the larger red shift. In Chapter Two (section 2.4.2.1), it was shown that addition of a large excess of water (~ 3 M) to solutions of **1** ([**1**] = 10^{-3} M) clearly leads to the formation of a new species, according to $^{31}P\{^1H\}$ NMR spectroscopy. However, efforts to confirm the presence of this species in dilute solution (4×10^{-4} M and 4×10^{-5} M in Ru) in the absence and presence of added water were unsuccessful due to the insufficient signal-to-noise ratios obtained even after overnight acquisitions of the $^{31}P\{^1H\}$ NMR spectra. When K_{eff} is

References begin on page 119.

considered, however, the low-concentration limit (3×10^{-5} M in Ru, ~ 0.3 M in H_2O) emission spectrum corresponds to a mixture of **1•OH$_2$** and **1** in a ratio of approximately 6.9:1.0. Thus, at low metal concentrations in the absence of added water, the predominant species is the aquo complex **1•OH$_2$**, while at high metal concentrations the observed spectra arise predominantly from **1**.

The altered coordination sphere accounts for the observed differences in photophysical properties of **1** and **1•OH$_2$**. The MLCT transition is lowered in energy by ~ 0.23 eV according to the absorption spectrum (34 nm red shift). The observed MLCT absorption energy for **1•OH$_2$** is in close agreement with that calculated (2.84 eV) from Equation 3.1 using the predicted value of $\Delta E_{(redox)calc}$. The overall emission from the MLCT state is also lowered in energy relative to **1**, but by a larger amount (0.32 eV) as determined from the 87 nm red shift of the maximum emission band. A small shoulder at high energy (536 nm, 2.31 eV) is likely the 0–0 emission band, which is in excellent agreement with the prediction from Equation 3.3 (2.35 eV). The lower MLCT energy of **1•OH$_2$** signifies either stabilization of the bpy π^* acceptor orbitals or destabilization of the filled metal dπ donor orbital. It is difficult to see how the energetics of the bpy π^* orbitals would be strongly affected by coordination sphere changes since the faces of the bpy rings are rather distant from the labile site. Removal of the *P,O*-chelate ring strain upon displacement of the ether, however, may play a role; the dπ orbital destabilization may arise from improved ligand-metal orbital overlaps and their effect on the electron density at the metal centre.

3.4.1.2 Effect of water coordination on emission lifetime

The lifetime for emission from **1** at the low-concentration limit (3×10^{-5} M) was determined at 77 K for a sample in 2:1 ethanol/acetone solution containing residual water (~ 0.3 M) by collaborators at SUNY Binghamton. At this concentration in this solvent, the dominant species present is the aquo complex **1•OH$_2$**, according to the UV/vis and emission spectra. The time-resolved emission data are well fit by a single exponential model as shown in Figure 3.9, with lifetime $\tau = 1.94 \pm 0.02$ μs. The emission lifetime of the aquo complex is comparable to that of **1** ($\tau = 2.04 \pm 0.07$ μs), determined in the same solvent mixture at 100× higher concentration (section 3.3.2). The fact that the emission lifetimes of these two species

References begin on page 119.

are essentially equivalent suggests that the geometric constraints imposed by the chelate ring do not dramatically affect the nonradiative deactivation pathways available to the excited state at low temperature. From this result, it appears that *O*-coordinated ligands might themselves be responsible for decreasing the MLCT excited-state lifetime relative to other Ru(II) bis(bipyridyl) complexes.

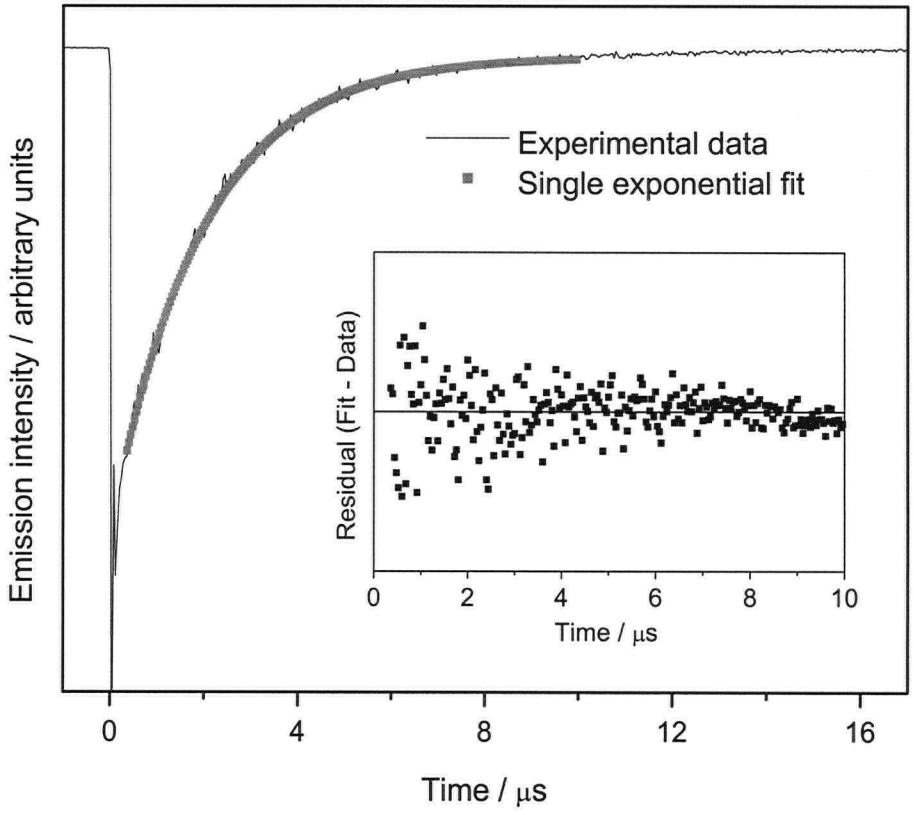

Figure 3.9. Emission (630 nm) decay trace for lifetime determination of **1•OH$_2$** at 77 K in solid 2:1 ethanol/acetone solution containing residual water (~ 0.3 M); [**1** + **1•OH$_2$**] = 3 × 10^{-5} M, τ = 1.94 ± 0.02 μs. Inset plot shows residuals (first order decay model - data).

References begin on page 119.

3.4.1.3 Effect of water coordination on the temperature dependence of the emission

Sufficient emission intensity is produced by **1•OH$_2$** over a range of temperatures that the temperature dependence of the emission lifetime for the aquo complex could be studied. Time-resolved emission data were obtained from 77 K, where the emission is strong enough to be observed by eye, to approximately 180 K, above which temperature no emission is detectable. The emission lifetimes show typical nonlinear temperature dependence that can be fitted to Equation 2.1, as shown in the plot of -ln(τ) *vs.* 1/T in Figure 3.10.

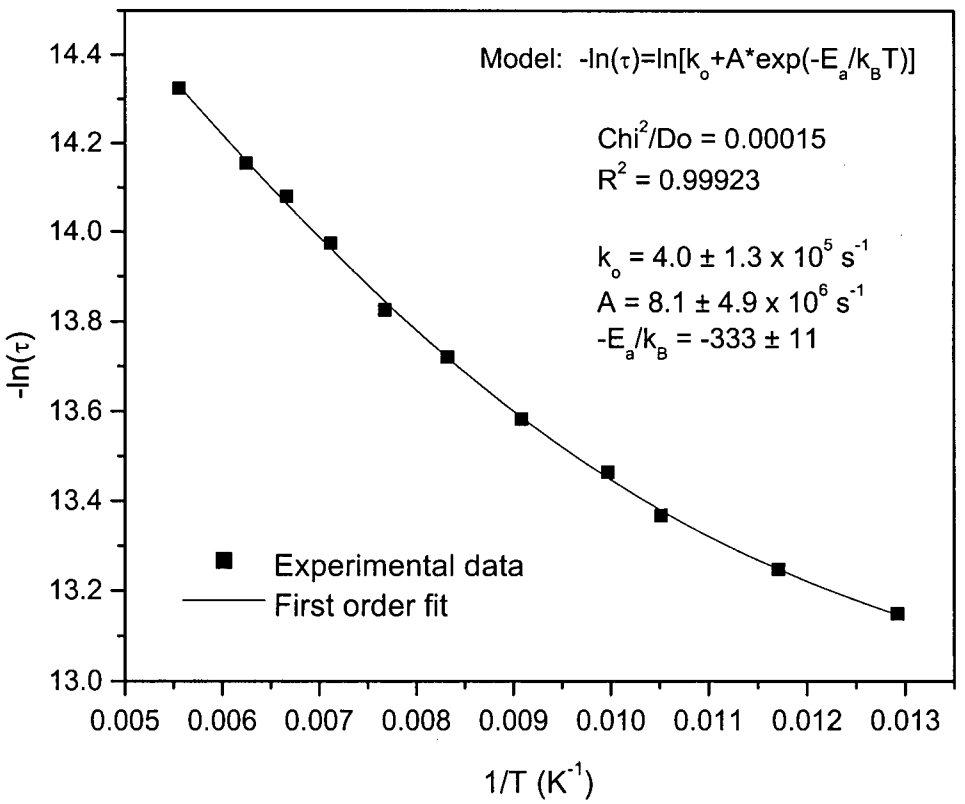

Figure 3.10. Plot of -ln(τ) *vs.* 1/T for emission from **1•OH$_2$** in 2:1 ethanol/acetone solution containing residual water (~ 0.3 M); [**1**] = 3 × 10^{-5} M. The best-fit model and parameters are shown in the inset.

References begin on page 119.

From this treatment, the MLCT-dd thermal activation barrier was calculated: E_a = 230 ± 10 cm^{-1} (2.7 ± 0.1 kJ/mol, 0.028 ± 0.001 eV). This is within the range estimated in the literature for [*cis*-Ru(bpy)$_2$L$_2$]$^{2+}$ phosphine and arsine complexes that are nonemissive at ambient temperatures, *i.e.*, $E_a \leq 850$ cm^{-1}. The rate constant for the observed decay of the MLCT excited state through the combination of both radiative and nonradiative processes, k_o = 4.0 (± 0.2) × 10^{-5} s^{-1}, is of the same magnitude as those determined for a variety of [*cis*-Ru(bpy)$_2$L$_2$]$^{2+}$ complexes.[9] However, the pre-exponential factor (A) is several orders of magnitude smaller than usually found; the photophysical implication of this is unknown.

3.4.2 Photophysical response of 1 to nitrogen donors

3.4.2.1 Colour and emission changes due to acetonitrile

Addition of MeCN to **1** induces a colour change from orange to yellow, over several orders of magnitude of concentration of **1**. Surprisingly, the absorption spectrum is nearly identical to that of **1**, shifted only 2 nm to higher energy across the whole spectrum, even with complete conversion of **1** to **1•MeCN** (CH_2Cl_2 solution, [**1**] = 2 × 10^{-4} M, [MeCN] = 0.2 M). The visible absorption energy (λ_{max} = 410 nm; E_{abs}(MLCT) = 3.03 eV) matches the MLCT energy gap determined from the observed solution redox couples ($\Delta E_{(redox)}$ = 2.83 eV; E_{abs}(MLCT) = 3.04 eV). This is in close agreement with the MLCT energy predicted from the redox gap estimated using Lever parameters ($\Delta E_{(redox)calc}$ = 2.85 eV; E_{abs}(MLCT) = 3.06 eV), and is nearly identical to the MLCT energy observed for the parent complex **1** (E_{abs}(MLCT)= 3.01 eV). These correlations imply that the photoexcited state is indeed derived from an MLCT transition.[9]

More dramatic than the colour change is the difference in photoluminescence observed for **1•MeCN**. Samples of **1•MeCN** frozen in liquid nitrogen and viewed under 366 nm UV light exhibit bright yellow emission that appears much more intense than the orange emission observed for **1**. Furthermore, the yellow emission from **1•MeCN** persists considerably longer after removal of the sample from the liquid nitrogen bath. Thus, the analyte-induced

References begin on page 119.

perturbation of the excited-state energetics produces a double effect: spectral shifting and an obvious change in the temperature dependence of the emission.

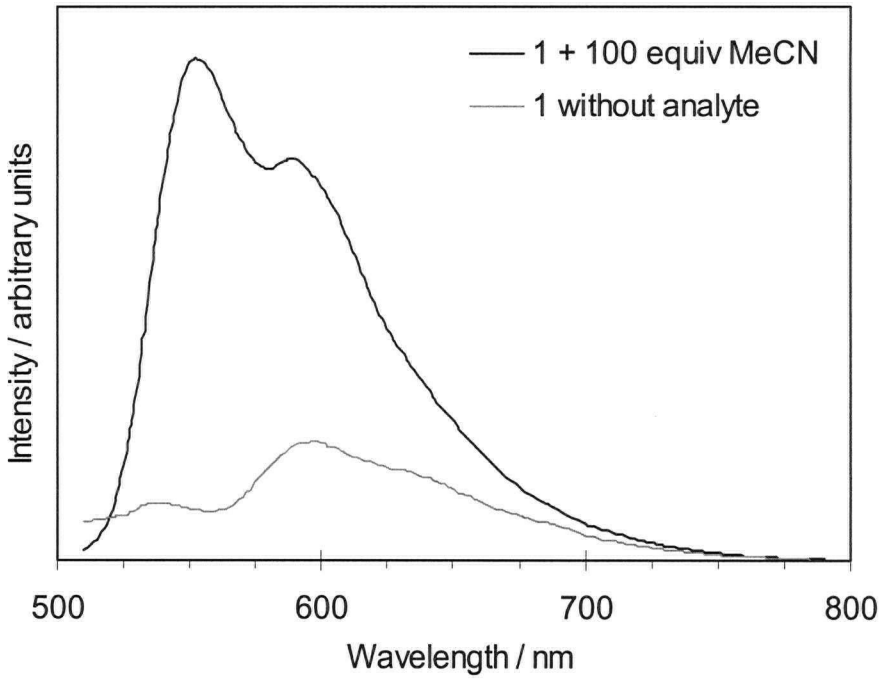

Figure 3.11. Photoluminescence spectra of **1** at 77 K in solid 2:1 ethanol/acetone solution, [**1**] ≈ 6×10^{-3} M. A: **1** in absence of analyte. B: **1** + 100 equiv MeCN ([MeCN] = 0.6 M). The spectra in this figure exaggerate the relative intensity of the emission from **1**; the emission from **1•MeCN** was so intense that less sensitive fluorometer settings were necessary, so a direct intensity comparison cannot be made.

The emission spectrum for **1•MeCN** measured at 77 K in 2:1 EtOH/acetone solution is shown in Figure 3.11. Under similar conditions ([**1**] = 6.8×10^{-3} M, [MeCN] = 0.68 M, in 2:1 EtOH/acetone-d_6), $^{31}P\{^1H\}$ NMR spectroscopy showed that there was full conversion to the acetonitrile complex, so this spectrum is due solely to emission from **1•MeCN**. The maximum emission occurs at 552 nm (2.25 eV), which accounts for the visibly blue-shifted emission of **1•MeCN** compared to **1**, for which the 0–0 is of higher energy but such weak intensity that the visible emission is dominated by the lower energy vibronic bands. The shape of the emission

References begin on page 119.

spectrum of **1•MeCN** is typical for Ru(II) polypyridyl complexes, and suggests that the band at 552 nm corresponds to the 0–0 transition; the magnitude of the vibrational spacing between the two dominant bands is also typical ($\nu_M \approx 1140$ cm^{-1}). However, the 0–0 energy predicted from the observed redox gap is 2.45 eV, similar to that predicted from the calculated redox gap using Equation 3.3 ($\Delta E_{(redox)calc} = 2.85$ V; $E_{em}(0\text{-}0)_{calc} = 2.50$ eV), so assignment of the 552 nm band to the 0–0 transition is tentative.

The retention of luminescence to higher temperatures shows that the energy barrier between the emissive MLCT and nonemissive dd excited states is larger when MeCN is coordinated to the Ru in place of the ether moiety, as has been noted to be the typical case for nitrogen-donor ancillary ligands. Photoluminescence is faintly visible from dilute solutions containing **1•MeCN** at temperatures as high as 210 K. Unfortunately, the validity of a preliminary temperature-dependence study performed recently is uncertain; the absorbance spectrum of the low concentration ([**1**] = [MeCN] = 3×10^{-5} M) sample studied did not match that observed for higher concentration ([**1**] = [MeCN] $\geq 10^{-4}$ M) samples in which the speciation had been conclusively identified by NMR spectroscopy. Further investigations into the temperature dependence of emission from **1•MeCN** will be undertaken by our collaborators at SUNY.

3.4.2.2 Luminescence response to triethylamine

The reaction of **1** with triethylamine, which was studied only superficially due to the instability of the product, is accompanied by an orange-to-reddish-brown colour change and substantially altered photoluminescence. Dim cherry red emission is observable by eye from samples in 2:1 EtOH/acetone solution ([**1**] = 6.8×10^{-3} M , [NEt_3] = 0.68 M) excited by UV light at 77 K, and the emission fades almost immediately upon removal from the liquid nitrogen bath. The temperature dependence of this luminescence was not examined in further detail. Under the conditions studied, the emission arises primarily from **1•NEt$_3$**; according to $^{31}P\{^1H\}$ NMR spectroscopy, only ~10 % unreacted **1** remained. The corresponding emission spectrum is broad and structureless, as shown in Figure 3.12, with maximum intensity at 675 nm. This ~ 90 nm red shift is the largest observed for all the analytes. A poorly resolved broad feature at ~ 532 nm (2.33 eV) may correspond to the 0-0 band, which is in agreement

References begin on page 119.

with that predicted from Equation 3.3 using the calculated redox gap ($\Delta E_{(redox)calc}$ = 2.67 V; $E_{em}(0\text{-}0)_{calc}$ = 2.37 eV). The dominance of the low-energy vibronic bands indicates that the geometries of the excited state and ground state of **1**•**NEt$_3$** are substantially different, and this difference is even more pronounced than for **1**.

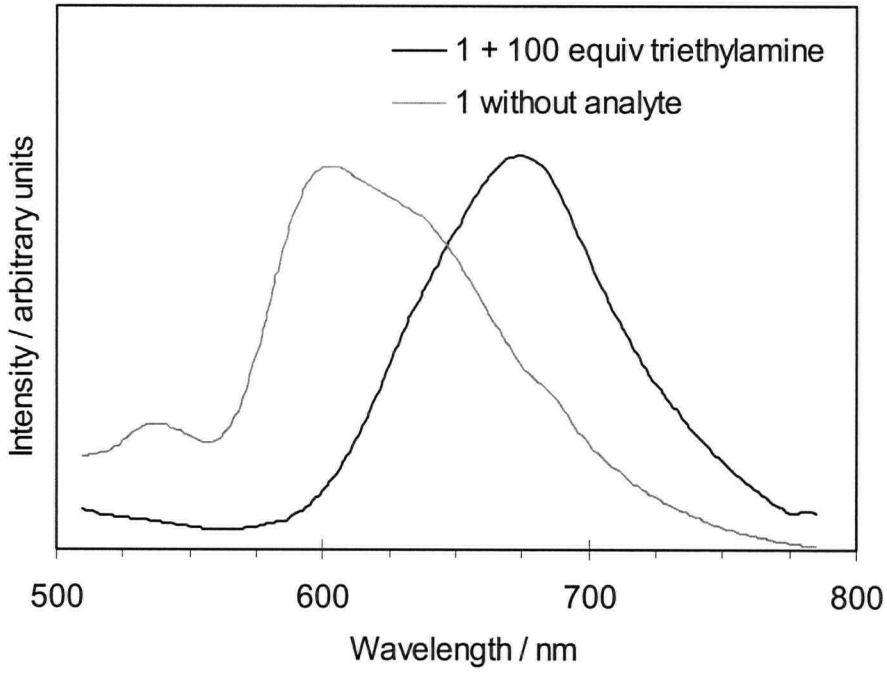

Figure 3.12. Photoluminescence spectra of **1** at 77 K in solid 2:1 ethanol/acetone solution, [**1**] ≈ 6 × 10^{-3} M. A: **1** in absence of analyte. B: **1** + 100 equiv NEt_3.

3.4.3 Photophysical response of 1 to sulfur donors

Although colour changes were observed for the reactions of **1** with all of the sulfur-containing small molecules studied by NMR spectroscopy, the luminescence response was studied in detail only for DMSO and dodecanethiol. The photophysical response to the more strongly odiferous analytes H_2S and SO_2, which also showed complicated chemistry, was not studied.

References begin on page 119.

3.4.3.1 Absorption and emission changes due to thiols

In concentrated solution (10^{-2} M), solutions of **1** gradually (< 1 h) change from orange to olive in colour when treated with ~ 10 equiv of ethanethiol or dodecanethiol. In more dilute solution, the colour change is less dramatic. In fact, the absorption spectrum of a solution of **1** (2.1×10^{-4} M) in acetone in the presence of ~ 1000 equiv of dodecanethiol shows decreased absorbance at 410 nm but only a slight broadening of the spectrum in the 450 – 550 nm range suggestive of a new absorption band. These concentration effects are consistent with the magnitude of the effective equilibrium constants for the formation of the **1**-thiol complexes (**1•EtSH**: $K_{eff} = 0.11 \pm 0.02$; **1•dodecaneSH**: $K_{eff} = 0.12 \pm 0.03$). The maximum absorption was observed at 410 nm (3.02 eV), as predicted from Equation 3.1 using the calculated redox gap ($\Delta E_{(redox)calc} = 2.82$ V; $E_{abs}(MLCT)_{calc} = 3.03$ eV).

When cooled to 77 K, samples of **1** in 2:1 ethanol/acetone solution with 100 equiv of dodecanethiol ([**1**] = 6×10^{-3} M; [thiol] = 0.6 M) irradiated with UV light emit intense olive-tinged yellow luminescence ('dirty yellow' in Table 3.5). The photoluminescence spectrum measured under the same conditions shows changes in band intensity compared to that of **1**, as shown in Figure 3.13. The vibrational structure is more pronounced, and two highest energy bands (545, 597 nm) are noticeably stronger in intensity than for **1**. There are no significant energetic shifts of the emission bands ($\nu_M \approx 1420$ cm^{-1}, same as for **1**), but the changes in intensity are significant enough to make the emission in the presence of dodecanethiol appear distinctly different by eye than the orange emission of **1**. The highest energy emission band (545 nm, 2.28 eV) is again lower in energy than predicted for the 0–0 band ($E_{em}(0–0)_{calc} = 2.44$ eV), which suggests that the true 0–0 band is not observed.

References begin on page 119.

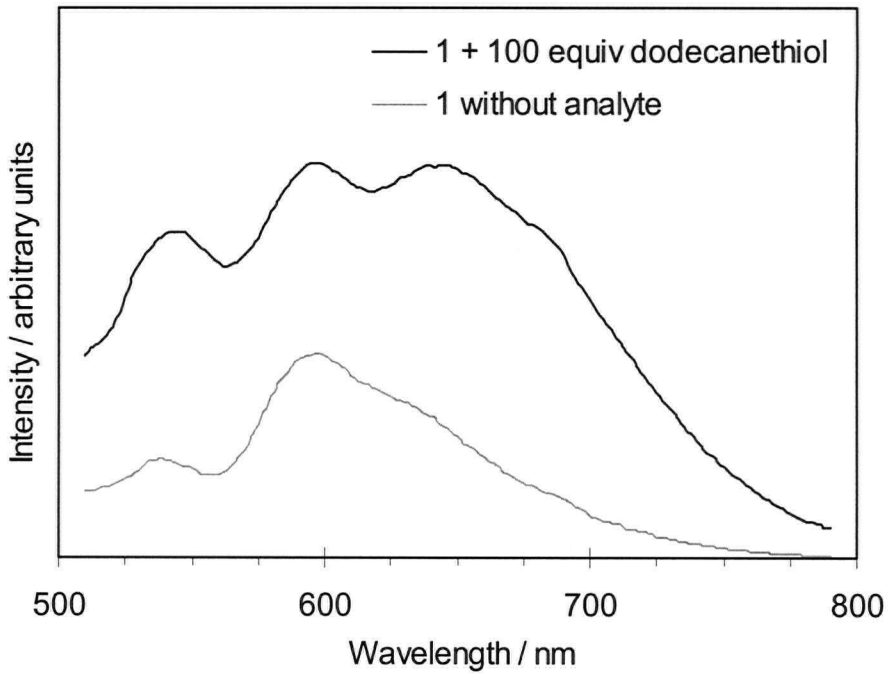

Figure 3.13. Photoluminescence spectra of **1** at 77 K in solid 2:1 ethanol/acetone solution, [**1**] ≈ 6 × 10^{-3} M. A: **1** in absence of analyte. B: **1** + 100 equiv dodecanethiol ([thiol] = 0.6 M).

It should be noted that at the concentration studied, the emission spectrum is composed of overlapping emission from the thiol complex and a small amount of **1**. The $^{31}P\{^1H\}$ NMR spectrum measured under the similar conditions ([**1**] = 6.8 × 10^{-3} M, [dodecanethiol] = 0.68 M), showed that the major species present was the thiol complex (roughly 15 % **1**, 85 % **1•dodecanethiol**); this likely represents the composition of the sample at 77 K as well because of the rapid freezing process. If it is assumed that the two complexes have similar emission efficiencies such that the emission spectrum is largely due to the thiol complex, then replacement of the ether moiety in **1** by dodecanethiol does little to perturb the MLCT state energetically. It is possible that any changes in the metal's electron density due to thiol coordination (indeterminable by CV because of oxidation of excess thiol) are balanced out by coincident changes in the bpy reduction potentials, so that over all there is no significant energetic impact on the MLCT transition or the emission from the MLCT excited state.

References begin on page 119.

Indeed, this matches the predictions made using Lever parameters and trends from the literature on Ru(II) diimine complexes. The observed photophysical response arises predominantly from geometric/conformational changes that influence which vibrational states of the ground state are involved in vertical transitions from the MLCT state.

3.4.3.2 Absorption change due to dimethylsulfide

The reaction with SMe_2 produces a visible colour change from orange to olive at concentrations of [**1**] $\approx 10^{-2}$ M in the presence of an excess of SMe_2. At lower concentrations, the colour change is less obvious due to limited formation of **1•SMe$_2$** ($K_{eff} = 1.7 \pm 0.3$), similar to the concentration effects observed for the reactions with thiols discussed above. At 10^{-4} M, the visible absorption spectrum changes only in the intensity of the main band, such that with 100 equiv of SMe_2 present, the absorptivity decreases by roughly 15 % ($\varepsilon_{410} = 6040$ M^{-1}cm^{-1} compared to 6900 M^{-1}cm^{-1} for **1**). Luminescence studies of **1•SMe$_2$** were not performed on account of the volatile analyte's stench, because the low-temperature emission studies at UBC were performed in nonsealable capillary cells. Thus, detailed information regarding the effect of SMe_2 coordination on the MLCT state's energetics is unavailable.

3.4.3.3 Colour and emission changes due to DMSO

Addition of DMSO to solutions of **1** (10^{-2} M) causes the initially orange solutions to immediately become deeper red in colour, with the extent of reddening dependent upon the relative concentration of **1**:DMSO. Solutions of **1** in neat DMSO appear blood red. This colour change corresponds to a shift of the visible absorption band to lower energy, as shown in Figure 3.14 for a solution of **1** in acetone ([**1**] = 1.5×10^{-4} M) treated with an incremental increase in DMSO concentration. At DMSO concentrations above ~ 1 M ([**1**] = 1.5×10^{-4} M), the spectrum remains essentially unchanged with maximum MLCT absorption at 442 nm (2.81 eV). Thus, the MLCT transition is roughly 0.20 eV lower in energy when DMSO is coordinated to the metal in place of the POMe ether, and the transition is of slightly lower probability ($\varepsilon = 6020$ M^{-1}cm^{-1} *vs.* $\varepsilon = 7020$ M^{-1}cm^{-1} for **1** in acetone solution). This MLCT energy is in good agreement with that predicted for the oxygen-bound DMSO complex ($\Delta E_{(redox)calc} = 2.58$ V; $E_{abs}(MLCT)_{calc} = 2.79$ eV) rather than the sulfur-bound complex ($\Delta E_{(redox)calc} = 2.94$ V; $E_{abs}(MLCT)_{calc} = 3.15$ eV). Thus, it would seem that the absorption

References begin on page 119.

spectrum is dominated by **1•DMSO-*O***; this implies that **1•DMSO-*O*** absorbs much more strongly than **1•DMSO-*S***, since even in neat DMSO solution there is more **1•DMSO-*S*** present than **1•DMSO-*O***.

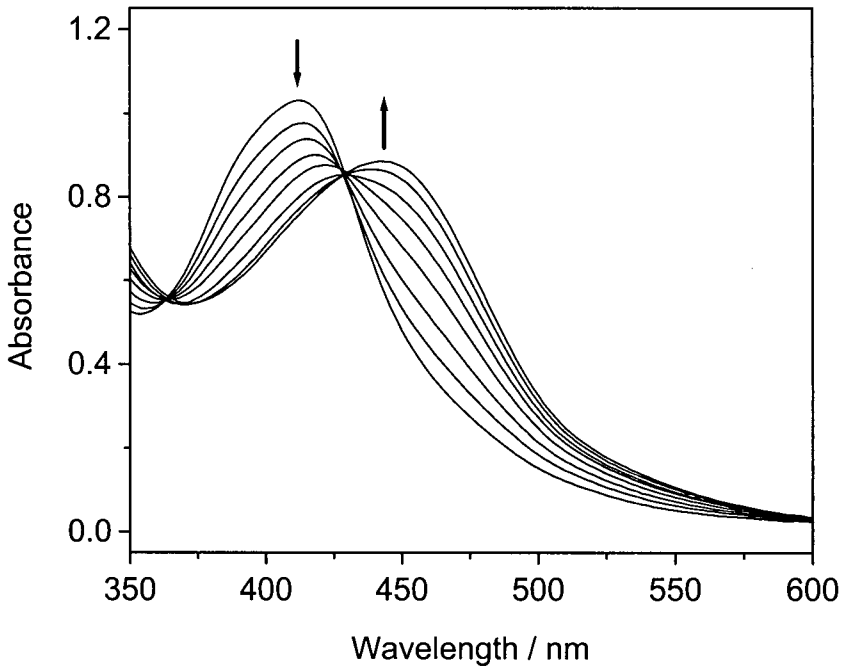

Figure 3.14. Change in the visible absorption spectrum of **1** upon addition of DMSO, in acetone solution: [**1**] = 1.5 × 10^{-4} M, [DMSO] = 0 – 1.9 M. The arrows indicate the direction of change as [DMSO] was increased. The spectral shift was complete at [DMSO] ≈ 1 M.

Two isosbestic points (364 and 430 nm) are observed in these visible spectra. Isosbestic points are wavelengths at which interconverting species have identical molar absorptivities, and their presence is generally correlated with conversion of one species into another single species. For the reaction of **1** with DMSO, however, two reaction products (*S*-bound and *O*-bound) are clearly formed according to the interpretation of the NMR spectra described previously in section 2.4.4.5. In this case, therefore, the presence of the isosbestic

References begin on page 119.

points suggests that the minor product **1•DMSO-*O*** and the major product **1•DMSO-*S*** are in equilibrium with one another, such that their ratios are fixed.[19-21]

When monitored at a wavelength corresponding to the maximum absorption of the new complex **1•DMSO-*S***, the absorbance increases with the concentration of DMSO as shown in Figure 3.15. The absorbance is relatively constant in the presence of greater than 4000 equiv of DMSO, which suggests that at these concentrations there is complete conversion of **1** to the DMSO complexes.

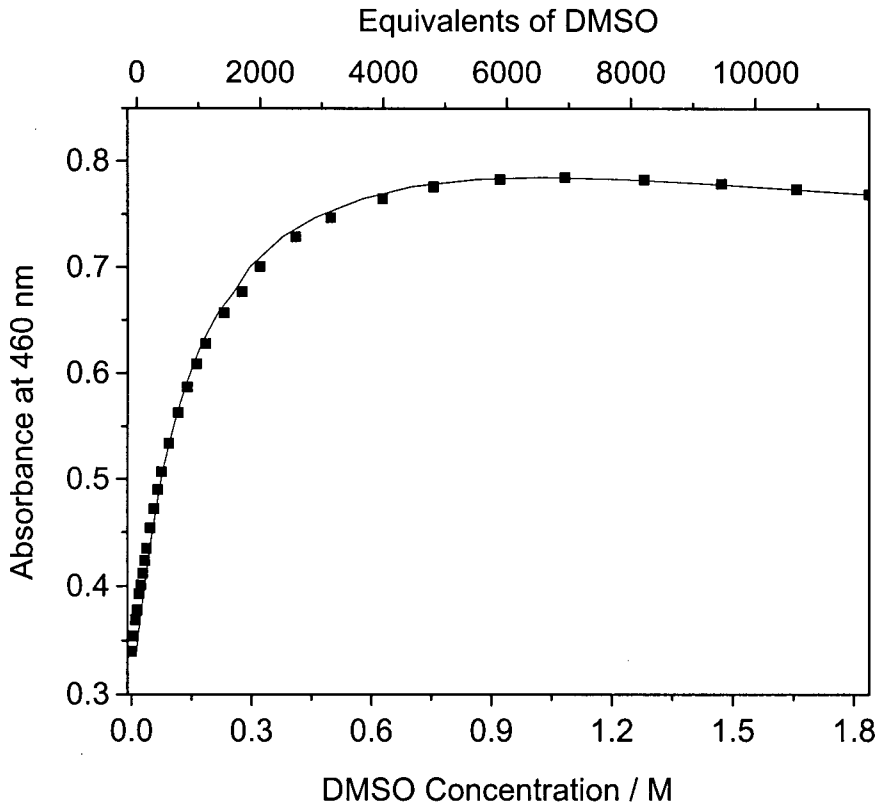

Figure 3.15. Absorbance of **1** at 460 nm as a function of added DMSO: [**1**] = 1.47 × 10^{-4} M, in acetone solution, [DMSO] = 0 – 1.84 M. The best-fit curve is meant to guide the eye only.

References begin on page 119.

The reaction of **1** with DMSO also leads to significantly altered photoluminescence. When samples of **1** containing an excess of DMSO are frozen in liquid nitrogen are illuminated with UV light, intense poppy red emission is observed by eye. The luminescence appears to have similar temperature dependence to the orange emission of **1**, as the emission fades very quickly once the sample is removed from the liquid nitrogen. However, a full study of the temperature dependence of the emission from **1•DMSO** has not been performed.

Figure 3.16 compares the low temperature emission spectra of **1** in the absence and presence of DMSO ([1] = 6×10^{-3} M, [DMSO] = $\approx$ 0.6 M), measured in frozen ethanol/acetone solution. In the presence of ~ 100 equiv DMSO, the emission maximum is red shifted by approximately 70 nm. The vibrational structure is not clearly resolved, but the spectrum appears at first to have a more typical shape for this family of complexes than that observed for **1** alone. However, a weak shoulder at ~ 551 nm (2.25 eV) may correspond to the 0–0 emission band, which agrees well with the 0–0 energy predicted for **1•DMSO-*O*** using Equation 3.3 ($E_{em}(0–0)_{calc}$ = 2.32 eV) rather than that for **1•DMSO-*S*** ($E_{em}(0–0)_{calc}$ = 2.50 eV). Again, this implies significant differences in structure for the excited state relative to the ground state, which must be more significant than for **1** since the spectrum in the presence of DMSO is dominated by even lower energy vibronic bands.

It should be noted that the emission spectrum shown in Figure 3.16 is a combination of the emission from **1** and the DMSO complexes. Under similar conditions to those in which the spectrum was measured ([**1**] = 6.8×10^{-3} M, [DMSO] = 0.68 M), $^{31}P\{^1H\}$ NMR spectroscopy showed the speciation to be 58 % **1**, 37 % **1•DMSO-*S*** and 5 % **1•DMSO-*O***. In the emission spectrum, however, there appears to be little contribution from **1**. This may imply that the emission of **1** is quenched by the other complexes, or simply that the DMSO complexes are considerably more emissive than **1**.

References begin on page 119.

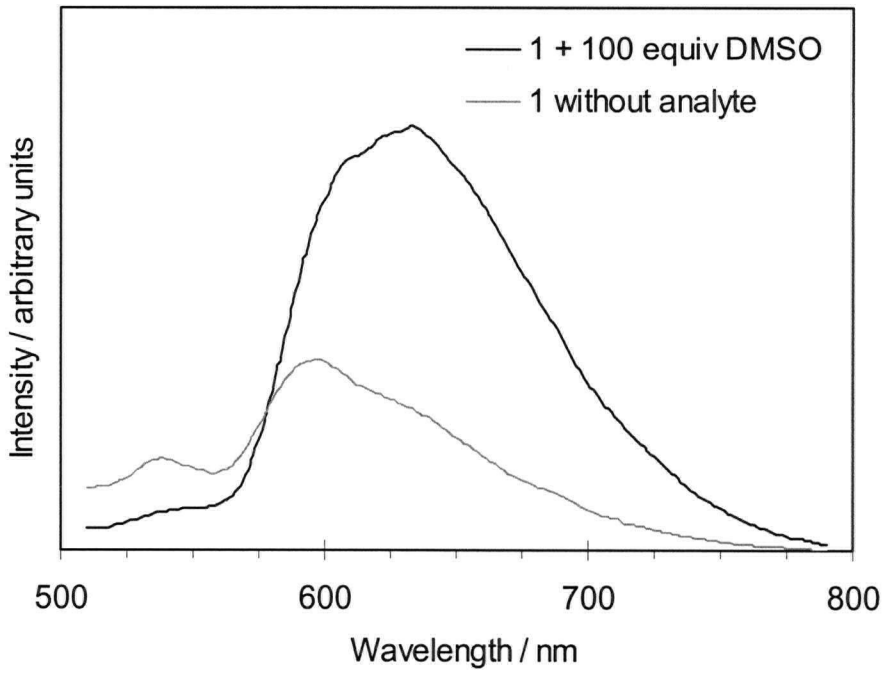

Figure 3.16. Photoluminescence spectra of **1** at 77 K in solid 2:1 ethanol/acetone solution, [**1**] ≈ 6×10^{-3} M. A: **1** in absence of analyte. B: **1** + 100 equiv DMSO ([DMSO] = 0.6 M).

3.4.4 Summary of photophysical response of 1 to small-molecule coordination

Coordination of small molecules to the metal centre in **1** causes changes in both the MLCT absorption and corresponding LMCT emission spectra. The effects of coordination sphere changes on the visible absorption and emission properties of **1** are summarized in Table 3.5, for samples of **1** in the presence of 100 or 1000 equiv of each analyte, as noted. Thus, for the case of DMSO in particular, the absorption maximum is shifted less relative to **1** than reported in Figure 3.14 and Table 3.5.

References begin on page 119.

Table 3.5. Summary of photophysical data for **1** in the absence and presence of small-molecule analytes

Analyte	Absorption[a] λ_{max} / nm (ε / $M^{-1}cm^{-1}$)	Solution Colour	Emission[b] λ_{max} / nm	Emission Colour
—	412 (6900)	orange	542, 588	orange
CH_3CN	410 (6900)[c]	yellow	552, 589	bright yellow
Et_3N	ND	red-brown	675	cherry red
CH_3CH_2SH	410 (6090)[c,d]	olive	ND	ND
$CH_3(CH_2)_{11}SH$	410 (6040)[c,d]	olive	545, 597, 645	dirty yellow
DMSO	418 (5900)[c,d]	red	663	poppy red
SMe_2	410 (6040)[c,d]	olive	ND	ND
H_2O[e]	448 (8000)	faintly reddish	629	red

ND = not determined. [a]In acetone solution at RT, [**1**] $\approx 2 \times 10^{-4}$ M. [b]In 2:1 ethanol/acetone solid solution, [**1**] $\approx 6 \times 10^{-3}$ M with 100 equivalents of analyte $\approx$ [L] = 6×10^{-1} M, measured at 77 K in 2 mm I.D. quartz capillary cell. [c]Upon addition of 100 equivalents of analyte $\approx$ [L] = 10^{-2} M, 5 minute equilibration time. [d]Pseudo-ε intended to show relative intensity of absorption band. [e][**1**] = 3×10^{-5} M in presence of ~ 0.3 M residual water.

Replacement of the hard ether moiety in **1** by softer donors such as N and S was initially expected to cause large changes in the electron density at the metal, based on improvements in orbital overlap between the soft Ru(II) and soft bases. However, from application of Lever's ligand electrochemical series, it is clear that these changes in ligands should, in fact, not cause very dramatic changes in the solution redox gap (see predicted redox gaps, $\Delta E_{(redox)calc}$, in Table 3.2). A small degree of MLCT stabilization (0.07 – 0.34 eV) was predicted to accompany analyte binding, by considering the general trend for Ru(II) diimine complexes, for which the MLCT absorption energy is approximately ~ 0.2 eV higher in energy than the redox gap (Equation 3.1). For this prediction, the calculated redox gaps ($\Delta E_{(redox)calc}$; Table 3.2) were used because experimental electrochemical data were available only for **1** and

References begin on page 119.

1•MeCN, and partially ($Ru^{III/II}$ couple only) for **1•DMSO**. The experimentally observed and predicted MLCT energies are presented in Table 3.6. In general, displacement of the labile ether moiety in **1** by Lewis basic small molecules was indeed observed to lead to red shifted absorption, which corresponds to energetic stabilization of the MLCT excited state relative to that of **1**. There is excellent agreement between the predicted and observed MLCT absorption energies over all. The observed stabilization of the excited states relative to **1** are small but may be related to increased conformational freedom in the analyte-bound complexes because of the absence of the *PO*-chelate ring.

Table 3.6. Observed *vs.* predicted MLCT absorption energy and highest energy emission (eV) for **1** and sensor-analyte complexes, **1•L**.

	E_{abs}(MLCT)		E_{em}(0–0)		
Complex	Observed	Predicted[a]	Observed[b]	Predicted[c]	Predicted[d]
1	3.01	2.98	2.29	3.48	2.42
1•MeCN	3.03	3.06	2.31	3.58	2.50
1•NEt$_3$	---	2.88	2.33	3.35	2.37
1•EtSH	3.02	3.03	2.28	3.54	2.44
1•DMSO-*S*	2.81[e,f]	3.15	2.25[e,g]	3.70	2.50
1•DMSO-*O*	2.81[e,f]	2.79	2.25[e,g]	3.23	2.32
1•Me$_2$S	---	3.03[h]	---	3.55[h]	2.44[h]
1•OH$_2$	2.77	2.84	2.31	3.29	2.35

[a]Calculated from $\Delta E_{(redox)calc}$ using Eq. 3.1. [b]Highest energy emission observed; may not be true 0–0 band. [c]Calculated from $\Delta E_{(redox)calc}$ using Eq. 3.2, trend for all Ru(II) bpy complexes. [d]Calculated from $\Delta E_{(redox)calc}$ using Eq. 3.3, trend for $[Ru(bpy)(biq)LL']^{2+}$ complexes. [e]Measured from samples containing both **1•DMSO-*S*** and **1•DMSO-*O***. [f]High [DMSO] spectrum from Figure 3.14. [g]100 equiv DMSO. [h]Approximated as Me_2S.

References begin on page 119.

Despite these small changes in MLCT energies, complex **1** undergoes dramatic changes in its photoluminescence when exposed to coordinating small molecules. To illustrate this response, a photograph of the emission from samples of **1** treated with various analytes is shown in Figure 3.17. Coordination of small molecules to **1** results in visible changes in the colour of light emitted from the lumophore, and different sensor-analyte complexes yield different coloured emission.

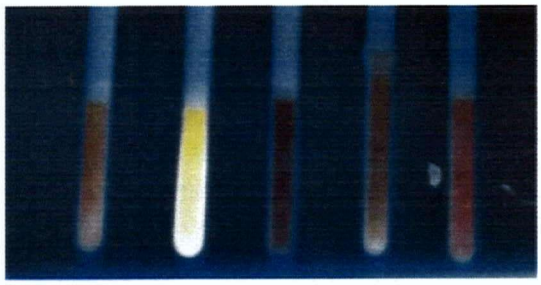

Figure 3.17. A photograph of the analyte-responsive emission from **1**. From left to right: **1** alone; **1** + 100 equiv MeCN; **1** + 100 equiv NEt_3; **1** + 100 equiv dodecanethiol; **1** + 100 equiv DMSO. [**1**] $\approx 10^{-2}$ M in 2:1 ethanol/acetone solution; λ_{ex} = 366 nm; T $\geq$ 77 K.

The emission spectra measured for all the analytes examined are presented together for comparison in Figure 3.18. In all cases, there are actually only small changes in the energies of the emission bands, but clearly the relative intensities of these bands is strongly dependent on the nature of the bound analyte. The energetic similarities are expected based on the predictions from the solution redox chemistry. The predicted 0–0 emission energies listed in Table 3.6 (note: those predicted using Equation 3.3 are considered to be applicable; Equation 3.2 appears to be erroneous) are consistently higher in energy than the highest energy emission observed from the complexes, even though the predicted MLCT absorption energies are quite accurate. Thus, it is very likely that the 0–0 emission bands are simply too low in intensity to be observed; the implications of this are discussed in the following paragraph.

References begin on page 119.

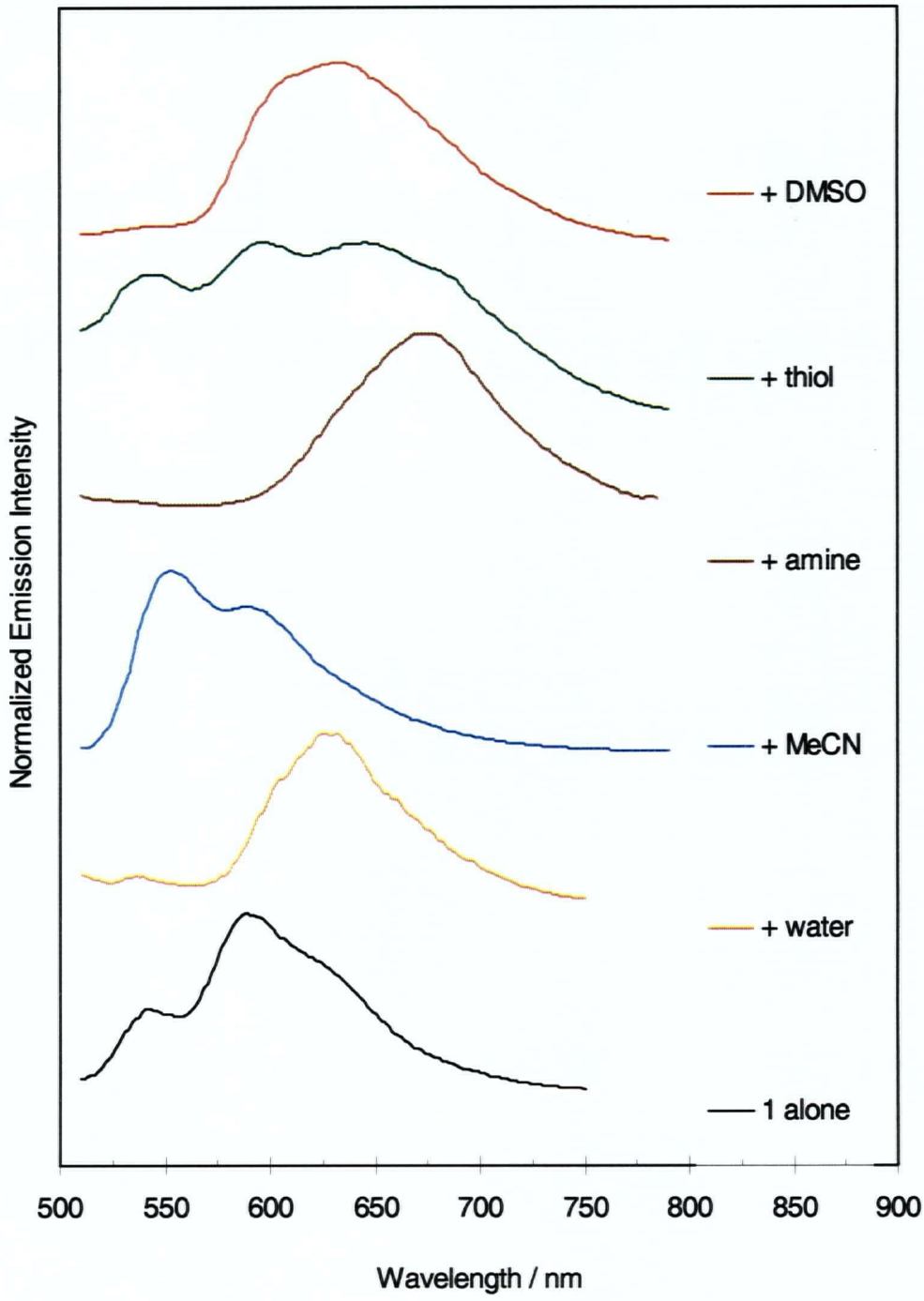

Figure 3.18. Comparison of the 77 K emission spectra from **1** ([[**1**] ≈ 6 × 10^{-3} M]) in the absence and presence of various analyte species (100 equiv); from bottom to top: **1**, **1** + OH_2, **1** + MeCN, **1** + NEt_3, **1** + dodecanethiol, **1** + DMSO; in 2:1 EtOH/acetone solid solution.

References begin on page 119.

In the case of **1**, the emission spectrum is dominated by a vibronic band at ~ 588 nm, which is lower in energy than the 0–0 band but difficult to identify because the 0–0 band itself (predicted to be at ~ 512 nm) does not appear in the spectrum. The emission spectra of **1•MeCN** and **1•EtSH** show more contribution from the higher energy bands below 600 nm, while the emission spectra of **1•OH$_2$**, **1•NEt$_3$** and **1•DMSO** are dominated by the lower energy bands above 600 nm. The observed differences in emission band intensities imply differences in the structures of the excited and ground states of the complexes. In other words, the bond lengths in the excited *vs.* ground states are different enough that the probability of the 0–0 transition is diminished compared to the probability of transitions from the lowest vibrational state of the emissive excited state to higher vibrational states of the ground state (*e.g.*, 0–1, 0–2, 0–3, *etc.*), as shown in Figure 3.19.

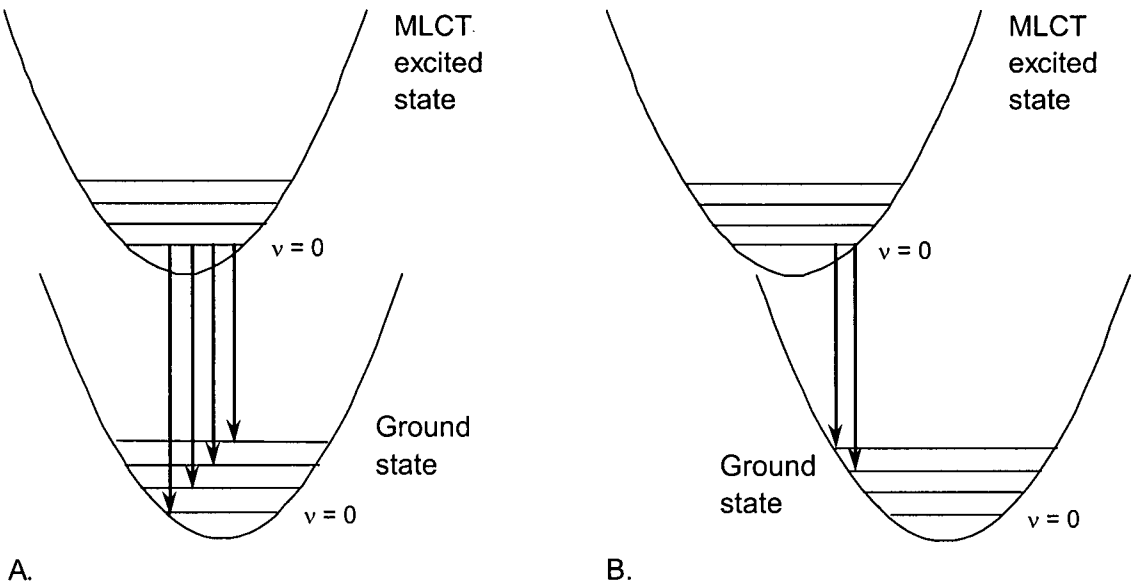

Figure 3.19. Schematic energy diagrams to illustrate how vertical transitions introduce vibrational structure into emission spectra. A. Nuclear positions in excited and ground states are similar; 0–0 emission band is observed. B. Nuclear positions in excited and ground states are quite different; 0–0 emission band is not observed.

References begin on page 119.

Based on the observed differences in the intensities of the vibronic bands, the different analytes distort the excited state relative to the ground state to different extents: the largest distortions are apparent for triethylamine, followed by water and DMSO, then the ether moiety in **1** and dodecanethiol. It is unclear whether or not the highest energy emission from **1•MeCN** corresponds to the 0–0 band; if not, acetonitrile should fall between DMSO and dodecanethiol in terms of the degree of structural disparity between the excited and ground states.

3.4.4.1 Redox properties of the excited state and the effect of analyte coordination

Photoexcited Ru(II) bipyridyl complexes act as both strong reducing agents and oxidizing agents because of the 'extra' electron on the bpy ligand and the 'hole' at the metal centre. For this reason, they have been extensively studied for their ability to promote photoinduced electron transfer processes, which are important for light harvesting and the development of solar cells. Because of the short lifetimes of excited states, however, the reduction potentials of excited molecules cannot be measured via standard voltammetric techniques. Nonetheless, the reduction potentials for the excited state can be estimated[9] from the ground-state reduction potentials and the energy of the 0–0 emission band using Equations 3.6 and 3.7.

$$E^{o\prime}(Ru(bpy)_2L_2^{3+/2+*}) \approx E^{o\prime}(Ru(bpy)_2L_2^{3+/2+}) - E_{em} \qquad [3.6]$$

$$E^{o\prime}(Ru(bpy)_2L_2^{2+*/+}) \approx E^{o\prime}(Ru(bpy)_2L_2^{2+/+}) + E_{em} \qquad [3.7]$$

The ground- and excited-state reduction potentials for **1**, **1•MeCN** and related bipyridyl complexes are presented in Table 3.7. Complex **1** has very similar excited-state redox properties to [*cis*-Ru(bpy)$_2$(PPh$_2$Me)$_2$]$^{2+}$, which is not surprising given their similar absorption and emission properties. When photoexcited, both of these complexes are stronger oxidizing agents but weaker reducing agents than [Ru(bpy)$_3$]$^{2+}$. When **1** is exposed to acetonitrile, however, the oxidizing power of the excited complex is diminished. Thus, complex **1** might be useful as a photosensitized electron acceptor whose ability to oxidize other species could be modulated by the presence or absence of acetonitrile. The same might be true for interaction of **1** with other small molecules, but prediction of this is limited due to the lack of ground-state redox data for other analyte complexes of **1**.

References begin on page 119.

Table 3.7. Emission energy (eV) and reduction potentials (V *vs.* SCE) for ground- and excited-state redox couples

Compound	$E_{1/2}$ (Ru^{III}/Ru^{II})	$E_{1/2}$ (bpy/bpy•$^-$)	E_{em}	$E_{1/2}$ (Ru^{III}/Ru^{II*})	$E_{1/2}$ (Ru^{II*}/Ru^{I})
$[Ru(bpy)_3]^{2+}$	1.23[a]	-1.35[a]	2.12	-0.89[e]	0.77[e]
$[Ru(bpy)_2(dppe)]^{2+}$	1.41[a]	-1.37[a]	2.24	-0.83[e]	0.85[e]
$[Ru(bpy)_2(PPh_2Me)_2]^{2+}$	1.56[a]	-1.27[a]	2.30	-0.74[e]	1.03[e]
1	1.56[b,d]	-1.27[b,d,g]	2.29	-0.73[f]	1.02[f]
1•MeCN	1.53[c]	-1.54[c]	2.25	-0.72[f]	0.71[f]

[a]In acetonitrile solution, 0.1 M $^nEt_4NClO_4$ electrolyte, 25 °C.[9] [b]In CH_2Cl_2 solution, 0.1 M $^nBu_4NPF_6$ electrolyte, 25 °C. [c]In CH_3CN solution, 0.1 M $^nBu_4NPF_6$ electrolyte, 25 °C. [d]Irreversible process. [e]From E_{em}(0–0) measured at 77 K in 4:1 EtOH/MeOH glass.[9] [f]From E_{em}(0–0) measured at 77 K in 2:1 EtOH/acetone glass, [1] ≈ 10^{-3} M. [g]The assignment of this wave is uncertain.

3.5 Discussion of the properties of 1 with respect to chemical sensing

All of the Lewis basic small molecules shown to react with **1** by NMR spectroscopy were also found to produce a detectable change in the photophysical properties of the complex. The photophysical changes are manifested as energetic shifts in both the absorption and emission spectra, as well as changes in the temperature dependence of the emission. It is not necessary that complex **1** be completely transformed into an analyte-bound complex for these photophysical effects to be clearly noticeable both visually and spectroscopically. With most of the analytes studied, complex **1** reaches an equilibrium that leaves a significant proportion of **1** unreacted (at concentrations 10^{-2} to 10^{-3} M); however, this does not detract from the ability of **1** to report the presence of these analytes through changes in its emission.

Different classes of small molecules lead to recognizably different emission spectra, even when the same donor atom is involved in coordination to the metal. The fact that an amine induces a change in the colour of the emitted light that is energetically opposite to that

References begin on page 119.

induced by another nitrogen-based analyte (*i.e.*, MeCN) reflects the different chemical natures of these small molecules. Furthermore, complex **1** responds to the binding of thiols and DMSO with easily distinguishable changes in the emission spectra. In the context of designing coordination-based multianalyte sensors, these results are encouraging because they show that differential sensor-analyte response is not limited to distinguishing analytes with different donor atoms.

Analyte-induced changes in emission spectra and intensities are particularly appealing for chemical sensing applications because of the sensitivity of the detection method. Given the different emission spectra observed for **1** when presented with various Lewis basic small molecules, one can envision sensor chips based on arrays of this type of sensory complex immobilized at various concentrations in a gel or other porous medium. Comparison of measured arrays of emission spectra to standard libraries of emission response for a variety of sensor and analyte concentrations might permit identification of the analytes present. Preliminary studies suggest that **1** can be immobilized in a cation-exchange polymer (Nafion®) and in a sol-gel matrix; studies to determine whether or not **1** retains its reactivity toward small molecules in such matrices have yet to be performed. However, given that the photoluminescence of **1** is limited to extremely low temperatures, the impregnation of solid matrices with this complex was not considered a very practical approach to chemical sensing. Thus, further efforts were instead focused on improving the room temperature luminescence output of the sensory complex (see Chapters Six and Seven).

References begin on page 119.

3.6 Summary and outlook

In this chapter, the redox and photophysical properties of the hemilabile phosphine-ether complex [*cis*-Ru(bpy)$_2$(POMe-*P,O*)]$^{2+}$, **1**, were described, as well as its response to small-molecule coordination. Like many other [*cis*-Ru(bpy)$_2$LL']$^{2+}$ complexes, **1** is luminescent at low temperatures, but not at room temperature because the MLCT excited state is efficiently deactivated via population of a thermally accessible nonemissive dd state. The photophysical properties of **1** are sensitive to the binding of Lewis basic small molecules to the metal centre. Small-molecule binding induces changes in absorption and emission spectra and intensities; the emission spectral changes in particular are different depending on the type of small molecule to which **1** is exposed. Analyte-specific changes in the emission spectrum of **1** make complexes of this type attractive for further study as coordination-based luminescent molecular sensors.

One of the shortcomings of complex **1** in terms of its utility as a molecular sensor is the fact that its luminescence is completely quenched at room temperature. Chapter Six deals with attempts to modify the hemilabile ligand in order to improve the room temperature luminescence output of the sensor complex while retaining the reactivity toward small molecules.

References begin on page 119.

3.7 Experimental section

3.7.1 Cyclic voltammetry

Electrochemical measurements were performed with a Pine Instruments AFCBP1 bipotentiostat using a 3-electrode cell (Pt disc working electrode, Pt wire coil counter electrode, Ag wire quasi-reference electrode) in CH_2Cl_2 solution that contained ~0.1 M *n*-Bu_4NPF_6 as supporting electrolyte. Either decamethylferrocene ($Me_{10}Fc$) or ferrocene (Fc) was added to samples as an internal standard in order to quote reduction potentials versus the saturated Calomel electrode, SCE ($Me_{10}Fc$ $E_{1/2}$ = -0.120 V *vs.* SCE; Fc $E_{1/2}$ = 0.454 V *vs.* SCE). Methylene chloride was distilled from calcium hydride immediately before use in electrochemical experiments. *n*-Bu_4NPF_6 was recrystallized three times from methanol, dried *in vacuo* at 110 °C for 3 days, and stored in a desiccator.

3.7.2 Photophysical experiments

UV/vis spectra were acquired with either a UNICAM Series II double beam spectrophotometer or a HP8453 single-beam diode array spectrophotometer. Photoluminescence measurements were performed using a PE LS5B luminescence spectrometer, either at RT with a standard 10 mm quartz solution cell or at 77 K using the manufacturer's low temperature accessory and a quartz capillary sample tube (3 mm O.D., 2 mm I.D.). Luminescence measurements were made using air-saturated solutions.

Photophysical experiments were also conducted in collaboration with Ph.D. student Yan Zhang and Prof. Wayne E. Jones, Jr. at the State University of New York (SUNY) in Binghamton, NY. At SUNY, absorbance spectra were measured using a Perkin-Elmer Lambda 2S spectrophotometer, and low temperature emission spectra were acquired with a SLM 48000S fluorometer equipped with a sample holder cooled to 77 K. Variable temperature emission lifetime measurements were carried out in a sealed suprasil quartz cell (10 mm × 10 mm) housed in an Oxford Instruments liquid-nitrogen cooled cryostat, using samples that were degassed via 4-5 freeze-pump-thaw cycles. A pulsed Laser Photonics

References begin on page 119.

nitrogen laser was used as the excitation source (337 nm). Time-resolved emission was collected through a one-stage monochromator at 90 degrees from the incident excitation beam and detected by a Hamamastsu R4220P photomultiplier tube interfaced with a Tektronix TDS544A transient digitizer. Emission lifetimes were determined by fitting the data to exponential decay using a nonlinear least-squares fitting routine available in Microcal Origin 6.0.

3.7.2.1 Emission lifetime determination of 1

This experiment was performed by Yan Zhang at SUNY Binghamton. The best-fit single exponential decay model for the time-resolved emission from **1** at 77 K ([**1**] = 1×10^{-3} M) shown in Figure 3.6 was described by the following parameters: $y = y_0 + A_1\exp[-(x-x_0)/\tau)]$, where $y_0 = -0.00133$; $x_0 = -0.44$; $A_1 = -0.0271 \pm 0.0002$; $\tau = 2.13 \pm 0.02$ μs; $\chi^2 = 6.89 \times 10^{-7}$; $R^2 = 0.986$.

3.7.2.2 Emission lifetime determination of 1•OH$_2$

This experiment was performed by Yan Zhang at SUNY Binghamton. The time-resolved emission from **1•OH$_2$** at 77 K ([**1**] = 3×10^{-5} M) (Figure 3.9) was fit to a single exponential decay model: $y = y_0 + A_1\exp[-(x-x_0)/\tau)]$, where $y_0 = -0.00049 \pm 0.00008$; $x_0 = -0.106$; $A_1 = -0.0548$; $\tau = 1.95 \pm 0.02$ μs; $\chi^2 = 4.15 \times 10^{-7}$; $R^2 = 0.996$.

3.7.2.3 Temperature dependence of emission lifetime of 1•OH$_2$

This experiment was performed by Yan Zhang at SUNY Binghamton. Emission lifetimes were determined at 10 degree intervals from 77 K until the emission was no longer detectable. Temperature (K), Lifetime (μs): 77.4, 1.946; 85.4, 1.764; 95.1, 1.564; 100.3, 1.420; 110.1, 1.262; 120.2, 1.099; 130.3, 0.989; 140.5, 0.853; 150.1, 0.767; 160.1, 0.712; 180, 0.601. The plot of $-\ln(\tau)$ *vs.* 1/T (Figure 3.10) for emission at 630 nm was fitted to the following single-exponential curve for determination of the MLCT-dd activation barrier (E_a): $y = \ln[P1+P2*\exp(x*P3)]$ where $P1 = k_o$; $P2 = A$; $P3 = -E_a/k_B$. Fitting parameters (for $\chi^2 = 0.00015$; $R^2 = 0.999$): $k_o = 404000 \pm 13000$ s^{-1}; $A = 8110000 \pm 490000$ s^{-1}; $-E_a/k_B = -333.7 \pm 10.8$. Thus, $E_a = 2.77 \pm 0.09$ kJ/mol $= 0.0287 \pm 0.0009$ eV $= 232 \pm 8$ cm^{-1}.

References begin on page 119.

3.8 References

(1) Kalyanasundaram, K. *Coord. Chem. Rev.* **1982**, *46*, 159.

(2) Kalyanasundaram, K. *Photochemistry of Polypyridine and Porphyrin Complexes*; Academic Press: London, 1992.

(3) Dodsworth, E. S.; Lever, A. B. P. *Chem. Phys. Lett.* **1986**, *124*, 152.

(4) Lever, A. B. P.; Dodsworth, E. S. *Electrochemistry, Charge Transfer Spectroscopy, and Electronic Structure* in *Inorganic Electronic Structure And Spectroscopy*; Solomon, E. I. and Lever, A. B. P., Ed.; John Wiley & Sons, Inc.: New York, 1999; Vol. II: Applications and Case Studies, pp. 227-289.

(5) Lever, A. B. P. *Can. J. Anal. Sci. Spec.* **1997**, *42*, 22.

(6) Vlcek, A. A.; Dodsworth, E. S.; Pietro, W. J.; Lever, A. B. P. *Inorg. Chem.* **1995**, *34*, 1906.

(7) Juris, A.; Campagna, S.; Balzani, V.; Gremaud, G.; von Zelewsky, A. *Inorg. Chem.* **1988**, *27*, 3652.

(8) Johnson, S. R.; Westmoreland, T. D.; Caspar, J. V.; Barqawi, K. R.; Meyer, T. J. *Inorg. Chem.* **1988**, *27*, 3195.

(9) Caspar, J. V.; Meyer, T. J. *Inorg. Chem.* **1983**, *22*, 2444.

(10) Lever, A. B. P. *Inorg. Chem.* **1990**, *29*, 1271.

(11) Dodsworth, E. S.; Vlcek, A. A.; Lever, A. B. P. *Inorg. Chem.* **1994**, *33*, 1045.

(12) Perrin, L.; Clot, E.; Eisenstein, O.; Loch, J.; Crabtree, R. H. *Inorg. Chem.* **2001**, *40*, 5806.

(13) Dovletoglou, A.; Adeyemi, S. A.; Meyer, T. J. *Inorg. Chem.* **1996**, *35*, 4120.

(14) Sullivan, B. P.; Salmon, D. J.; Meyer, T. J. *Inorg. Chem.* **1978**, *17*, 3334.

References begin on page 119.

(15) Brown, G. M.; Callahan, R. W.; Meyer, T. J. *Inorg. Chem.* **1975**, *14*, 1915.

(16) Durham, B.; Walsh, J. L.; Carter, C. L.; Meyer, T. J. *Inorg. Chem.* **1980**, *19*, 960.

(17) Crutchley, R. J.; Lever, A. B. P. *Inorg. Chem.* **1982**, *21*, 2276.

(18) Demas, J. N.; Crosby, G. A. *J. Am. Chem. Soc.* **1971**, *93*, 2841.

(19) Cohen, M. D.; Fischer, E. *J. Chem. Soc.* **1962**, 3044.

(20) Nowicka-Jankowska, T. *J. Inorg. Nucl. Chem.* **1971**, *33*, 2043.

(21) Stynes, D. V. *Inorg. Chem.* **1975**, *14*, 453.

References begin on page 119.

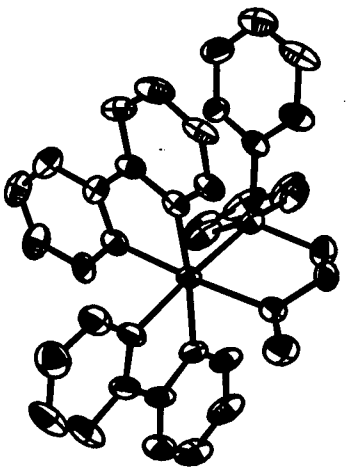

Chapter Four

Ligand-assisted *O*-dealkylation of Ru(II) bis(bipyridyl) phosphine-ether complexes

4.1 An introduction to the dealkylation of metal-bound ethers

As discussed in Chapters Two and Three, ruthenium bis(bipyridyl) complexes that contain hemilabile phosphine-ether ligands are of interest for the purpose of developing new types of molecule-based chemical sensors.[1] In the course of investigations into this class of complexes, it was observed that the ruthenium-bound ether in **1**, [*cis*-Ru(bpy)$_2$(POMe-*P,O*)]$^{2+}$ (POMe = 2-methoxyphenyldiphenylphosphine), is susceptible to *O*-demethylation in the presence of free POMe. In general, *O*-dealkylation of both free and metal-coordinated ethers can be accomplished by a variety of reagents, commonly through the action of alkali metals, organometallic reagents, and strong Lewis or Brönsted acids.[2] C-O bond activation by transition metal complexes has recently been reviewed;[3] a recent example from the literature describes metal-specific regioselectivity in aryl-alkyl ether cleavage.[4] Metal-mediated ether

References begin on page 151.

cleavage is an important class of reactions that is relevant to diverse fields of study, ranging from understanding metabolic processes in biological systems (*e.g.*, P450 enzymes),[5] to designing catalysts for the hydrocracking of coal and oil,[6] to interfering with the photoyellowing of paper.[7,8]

A considerable number of transition metal complexes have been reported using the family of triphenylphosphine derivatives with *ortho*-methoxy substituents.[9-12] Those containing multiple methoxy groups are highly basic and nucleophilic, with the basicity increasing with the degree of ether substitution: Ph_3P (pK_a = 2.73) < (2,6-dimethoxyphenyl)-diphenylphosphine, MDMPP (pK_a = 5.39) < bis(2,6-dimethoxyphenyl)phenylphosphine, BDMPP (pK_a = 7.28) < tris(2,4,6-trimethoxyphenyl)phosphine, TMPP (pK_a = 11.02).[13,14] These phosphine-ether ligands typically dealkylate when reacted with metal halides to form σ-bonded aryloxide complexes.[9,14-16] However, a variety of ether complexes has also been prepared with these ligands, and in some cases, ligand-assisted *O*-dealkylation has been observed.[11,17-21] Such *ligand-assisted* dealkylations proceed via nucleophilic attack by the free ligand's phosphorus to produce the stable alkylphosphonium salt, which drives the reaction. For example, (Cp*)Rh(Cl)(MDMPP),[16] Pt and Pd BDMPP methylallyl complexes,[17] and Pt and Pd TMPP complexes[11] are all known to demethylate in the presence of excess phosphine-ether; however, similar dealkylations on Ru(II) have not been reported prior to this study.

Although Pt and Pd halide complexes bearing phosphine-ether ligands such as POMe have been observed to dealkylate via loss of MeX, there are no other examples of ligand-assisted *O*-dealkylation of complexes containing phosphine-ether ligands with only one ether substituent.[22] This type of dealkylation reaction provides an alternate route to linked phosphine-aryloxide complexes from readily prepared phosphine-ether complexes, which may be convenient for syntheses where use of a phosphine-phenol or -phenolate directly is undesirable. In this context, studies were undertaken to investigate the occurrence of ligand-assisted dealkylation in a set of [*cis*-$Ru(bpy)_2$(POR-*P,O*)]$^{2+}$ complexes that contain phosphines with only one ether substituent. Much of the work reported in this chapter has been published.[23]

References begin on page 151.

4.2 Motivation of this study: dealkylation of 1 by free POMe

Phosphine-ether complex **1** is unstable in the presence of free phosphine-ether. It was observed that when an excess of the phosphine-ether ligand POMe is used in the synthesis of **1**, a new complex is formed that conspicuously lacks the MeO ^{1}H resonance in its ^{1}H NMR spectrum. This compound was determined to be the monocationic Ru(II) aryloxide complex **4**, which forms under these conditions through dealkylation of the metal-bound ether of **1**. A second phosphorus-containing product (^{31}P{^{1}H} NMR δ21.9) with a distinctive large doublet in the ^{1}H NMR spectrum (δ3.14, $^2J_{PH}$ = 14.4 Hz) can be observed by NMR spectroscopy to form concurrently with **4**. This product was identified as the *P*-methylated phosphine-ether, [Me(POMe)]$^+$, by comparison of its ^{1}H and ^{31}P{^{1}H} NMR spectra to those of an authentic sample of [Me(POMe)]I prepared by another route. The presence of the phosphonium salt suggests that the side reaction proceeds via nucleophilic attack of the free ligand's phosphorus on the carbon of the Ru-bound methoxy group.

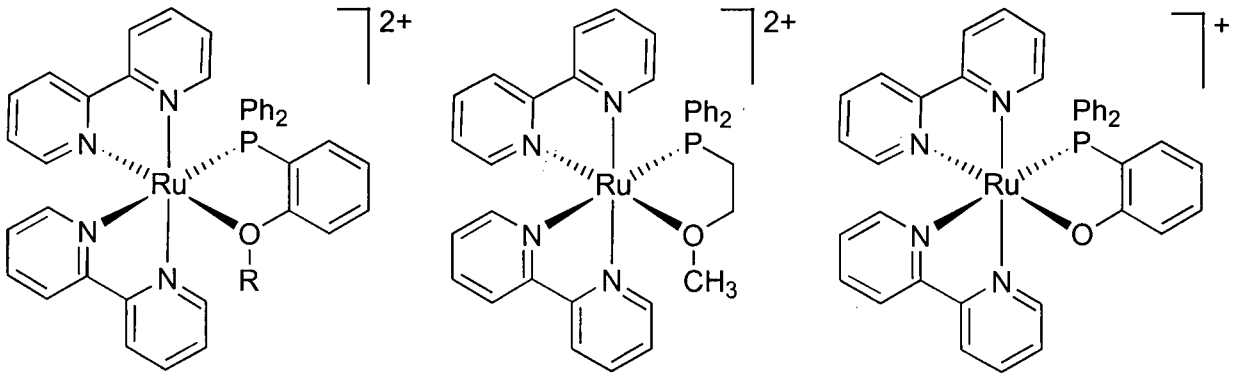

1 R = CH_3
2 R = CH_2CH_3

3

4

It became of interest to discover which factors are important in determining whether such a ligand-assisted dealkylation reaction occurs. To this end, complexes **2** and **3** shown above were prepared, which contain the modified phosphine-ether ligands POEt (2-ethoxyphenyldiphenylphosphine) and PC2OMe (2-methoxyethyldiphenylphosphine). The phenoxide complex **4** and bis(phosphine) complex **5**, which forms if complex **3** is prepared in

References begin on page 151.

the presence of excess PC2OMe, were also prepared. The preparation and characterization of complexes **2-5** and the *P*-alkylated phosphine-ether ligands (*i.e.*, R[POR]$^{+}$I^{-}; R = Me, Et) will be described in sections 4.3 and 4.4, respectively; discussion of the dealkylation of complexes **1-3** by free phosphine-ethers will be resumed in section 4.5.

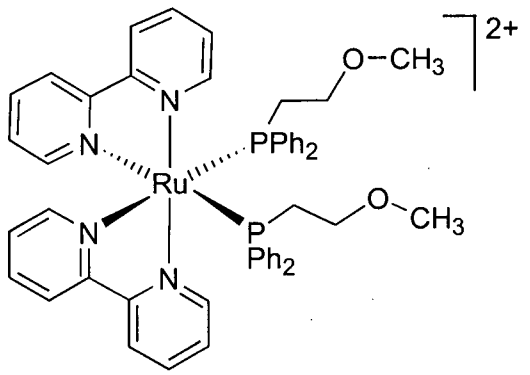

5

4.3 Preparation and characterization of complexes 2-5

4.3.1 Phosphine-ether complexes 2 and 3

Complexes **2** and **3** were prepared using the same synthetic route described for complex **1** in section 2.3.1, via the reaction of the Ru(II) bis(bipyridyl) bis(acetone) solvate complex with the appropriate phosphine-ether. The differences in the phosphine-ether ligands used in these reactions do not significantly affect the synthesis of the complexes. Complexes **2** and **3** are readily prepared in high yields and purified using the same methods used for **1**; both complexes are isolated as orange powders and can be crystallized by gradual cooling of hot solutions of methanol to yield pale orange needles and reddish-orange prisms respectively. The complexes are robust and can be stored for long periods under air as solids; air-saturated solutions in methanol are not noticeably changed after a period of months, although in acetone solution both complexes undergo slow oxidation by air to form greenish solutions.

According to $^{31}P\{^{1}H\}$ NMR spectroscopy, the phosphine-ether ligands in both **2** and **3** are *P,O*-coordinated in solution. The phosphine environments are similar to that in **1**, as shown

References begin on page 151.

by their comparable ^{31}P chemical shift values: δ 51.1 for **2** and 50.5 for **3**, *vs.* 50.9 for **1** in CD_2Cl_2 solution. No evidence was found for dissociation of the ether moieties in dichloromethane or acetone solution on the NMR timescale. However, the complexes do react with Lewis basic small molecules such as acetonitrile, as will be discussed in Chapter Five.

4.3.1.1 Crystallographic analysis of complexes 2 and 3

Crystals of both **2** and **3** suitable for X-ray crystallographic analysis were grown from methanol. The crystallographic data, collection and refinement details for the structural determinations of these crystals are presented in Appendix 4.1. The molecular structures of **2** and **3** are depicted in Figures 4.1 and 4.2 respectively.

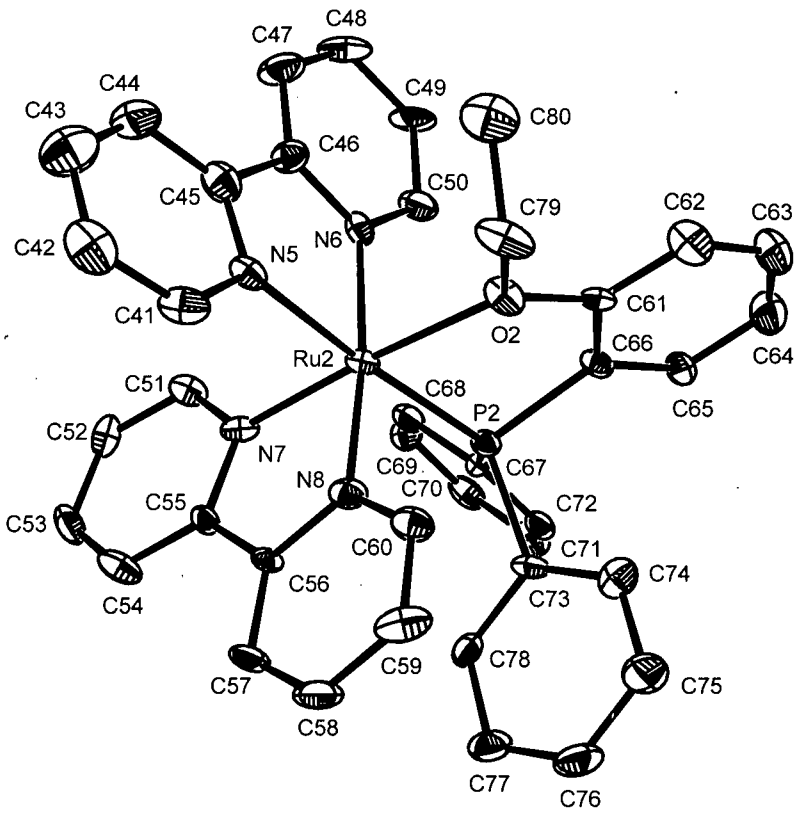

Figure 4.1. ORTEP representation of the solid state molecular structure of **2**, [*cis*-Ru(bpy)$_2$(POEt-*P,O*)](PF$_6$)$_2$. Note that there are two inequivalent salt moieties in the asymmetric unit, but only one cationic unit, containing Ru(2) as listed in Table 4.1, is depicted here. Hydrogen atoms and hexafluorophosphate ions are omitted for clarity.

References begin on page 151.

Table 4.1. Selected bond distances and angles for **2**

		Distances (Å)	
Ru(1)-O(1)	2.199(6)	Ru(1)-P(1)	2.289(2)
Ru(1)-N(1)	2.126(6)	Ru(1)-N(2)	2.082(7)
Ru(1)-N(3)	2.018(7)	Ru(1)-N(4)	2.064(7)
O(1)-C(21)	1.403(10)	O(1)-C(39)	1.482(11)
Ru(2)-O(2)	2.200(6)	Ru(2)-P(2)	2.277(2)
Ru(2)-N(5)	2.109(6)	Ru(2)-N(6)	2.092(7)
Ru(2)-N(7)	2.012(7)	Ru(2)-N(8)	2.064(7)
O(2)-C(61)	1.419(10)	O(2)-C(79)	1.460(11)
		Angles (°)	
P(1)-Ru(1)-O(1)	79.48(17)	P(1)-Ru(1)-N(2)	98.25(19)
P(1)-Ru(1)-N(3)	100.7(2)	P(1)-Ru(1)-N(4)	89.0(2)
O(1)-Ru(1)-N(1)	95.5(2)	O(1)-Ru(1)-N(2)	84.3(2)
O(1)-Ru(1)-N(4)	97.9(3)	N(1)-Ru(1)-N(2)	77.7(3)
N(1)-Ru(1)-N(3)	84.5(3)	N(1)-Ru(1)-N(4)	95.2(3)
N(2)-Ru(1)-N(3)	98.8(3)	N(3)-Ru(1)-N(4)	78.8(3)
P(2)-Ru(2)-O(2)	79.41(17)	P(2)-Ru(2)-N(6)	99.0(2)
P(2)-Ru(2)-N(7)	99.6(2)	P(2)-Ru(2)-N(8)	89.3(2)
O(2)-Ru(2)-N(5)	97.4(2)	O(2)-Ru(2)-N(6)	84.9(2)
O(2)-Ru(2)-N(8)	96.7(3)	N(5)-Ru(2)-N(6)	77.7(3)
N(5)-Ru(2)-N(7)	83.8(3)	N(5)-Ru(2)-N(8)	94.0(3)
N(6)-Ru(2)-N(7)	99.1(3)	N(7)-Ru(2)-N(8)	79.4(3)

References begin on page 151.

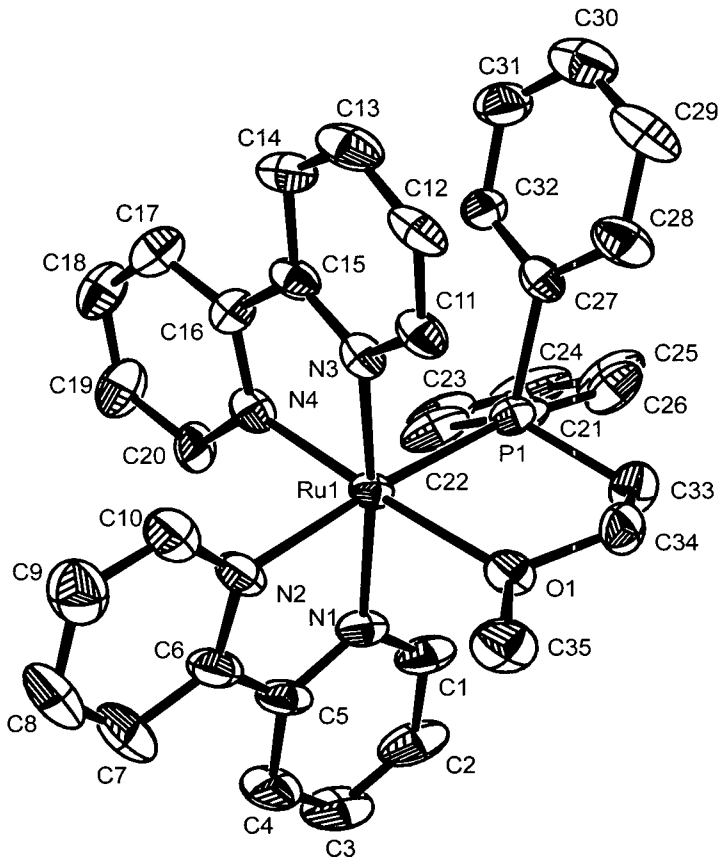

Figure 4.2. ORTEP representation of the solid state molecular structure of **3**, [*cis*-Ru(bpy)$_2$(PC2OMe-*P,O*)](PF$_6$)$_2$. Hydrogen atoms and hexafluorophosphate ions are omitted for clarity.

Both complexes contain chelating *P,O*-coordinated phosphine-ether ligands in the solid state, like complex **1**. The geometry at the metal in each of these complexes is distorted octahedral because of the three 5-membered chelate rings. Relevant bond lengths and angles in the complexes **2** and **3** are listed in Tables 4.1 and 4.2. The Ru-O bond lengths of 2.199(6) Å and 2.200(6) Å for **2** and 2.174(3) Å for **3** are similar to that in **1** (Ru-O = 2.172(2) Å), but shorter than the Ru-O bonds in the neutral $RuCl_2(POR)_2$ complexes with the same phosphine-ether ligands (2.299 Å and 2.257 Å in the POMe complex; 2.262 Å and 2.265 Å in the PC2OMe complex; the POEt complex was not structurally characterized).[9,24,25] These relatively short Ru-O distances are consistent with the observation that complexes **1-3** show

References begin on page 151.

diminished reactivity with respect to ether substitution by nucleophilic small molecules (*e.g.*, MeCN, DMSO, CO) compared to other Ru(II) phosphine-ether complexes.[9,10,26] The Ru-P bond lengths of 2.2908(6) Å in **1**, 2.289(2) Å and 2.277(2) Å in **2**, and 2.286(2) Å in **3** are somewhat longer than those in the corresponding $RuCl_2(POR)_2$ complexes (~ 2.218 Å).[24,25]

Table 4.2. Selected bond distances and angles for **3**

		Distances (Å)	
Ru(1)-O(1)	2.174(3)	Ru(1)-P(1)	2.286(2)
Ru(1)-N(1)	2.098(4)	Ru(1)-N(2)	2.118(4)
Ru(1)-N(3)	2.055(4)	Ru(1)-N(4)	2.029(5)
O(1)-C(34)	1.434(6)	O(1)-C(35)	1.405(7)
		Angles (°)	
P(1)-Ru(1)-O(1)	81.4(1)	P(1)-Ru(1)-N(1)	99.5(1)
P(1)-Ru(1)-N(3)	88.2(1)	P(1)-Ru(1)-N(4)	96.7(1)
O(1)-Ru(1)-N(1)	83.3(1)	O(1)-Ru(1)-N(2)	95.3(2)
O(1)-Ru(1)-N(3)	98.0(2)	N(1)-Ru(1)-N(2)	77.8(2)
N(1)-Ru(1)-N(4)	99.9(2)	N(2)-Ru(1)-N(3)	94.5(2)
N(2)-Ru(1)-N(4)	86.8(2)	N(3)-Ru(1)-N(4)	79.1(2)

4.3.1.2 Characterization of complexes 2 and 3 by cyclic voltammetry

(i) Complex 2

The CV of the phenyl-ethyl ether complex **2** is very similar to that of **1** (Figure 3.1). The waves are all irreversible ($E_{ox}(Ru^{III/II})$ = 1.59 V; E_{red} = -1.16 (sh), -1.22, -1.65 V), and occur at very similar potentials to those of **1** ($E_{ox}(Ru^{III/II})$= 1.56 V; E_{red} = -1.19 (sh), -1.27, -1.71 V). The two complexes are predicted using Lever parameters (see Chapter Three, section 3.2) to have essentially the same reduction potentials: $E_{1/2}(Ru^{III/II})_{calc}$ = 1.62 V; $E_{1/2}(bpy^{0/-})_{calc}$ = -1.30 V. Thus, the first bpy reduction is likely the one observed at E_{red} = -1.27 V, and the

References begin on page 151.

shoulder may be due to the presence of water in the solution. By comparing the observed reduction potentials, it can be concluded that there is a very small decrease in the electron density at the metal centre that arises from replacement of the methyl group by an ethyl group. As observed for **1**, a new small oxidation wave ($E_{1/2}$ = 0.93 V) due to decomposition products appears if the potential is scanned past the first reduction wave. This unidentified reduction product is different than that formed upon reduction of **1** ($E_{1/2}$ = 0.86 V); thus, the reductive decomposition does not appear to involve loss of the ether substituent, which would lead to the same product in both cases (complex **4**). All considered, the electrochemical processes in **2** are generally analogous to those in **1**. The observed redox gap suggests that the MLCT absorption for **2** should be observed at ~ 3.07 eV, comparable to the predicted value of 3.13 eV; the photophysical properties of **2** are discussed further in Chapter Five.

(ii) Complex 3

Unlike **1** and **2**, the CV of the ethyl-methyl ether complex **3** (Figure 4.3) reveals an unusually sharp quasireversible metal redox wave (anodic sweep $E_{ox}(Ru^{III/II})$ = 1.56 V; $E_{1/2}(Ru^{III/II})$ = 1.48 V). The reduction waves (E_{red} = -1.33, -1.75 V) are irreversible but more typical in appearance. Aside from the shape of the oxidation wave, the CV of **3** is similar to those of its congeners, as would be predicted given the similarities in the ligands. There is one metal-based oxidation and two ligand-based reductions, the more negative of which appears to correspond to coincident bpy reductions based on the approximate size of the wave. The metal is somewhat more electron-rich than in **1** or **2**, and the purported bpy reductions are also more facile in **3**. Similar to the other complexes, the one-electron reduction of **3** leads to a decomposition product that undergoes reversible oxidation ($E_{1/2}$ = 1.09 V); again, the reduction product has not been identified.

The shape of the $Ru^{III/II}$ redox wave of **3** is dependent upon both the sample concentration and the potential scan rate. It must be noted that the samples used routinely for electrochemical measurements of **3** were more concentrated than those of other complexes (~ 10 mg/mL = 1×10^{-2} M *cf.* ~ 2 mg/mL = 2×10^{-3} M for **1** and **2**), merely because the crystals of **3** used for these studies were relatively large. At such high concentrations, the oxidation

References begin on page 151.

wave appears sharp, as in Figure 4.3. At faster scan rates (1000 mV/s *cf.* typical 200 mV/s), the wave approaches the appearance of a typical quasireversible solution redox wave, with the splitting of the anodic and cathodic waves increasing as a function of the sweep rate. At very slow scan rates (10 mV/s), the wave is extremely sharp but lacks a matching sharp return wave.

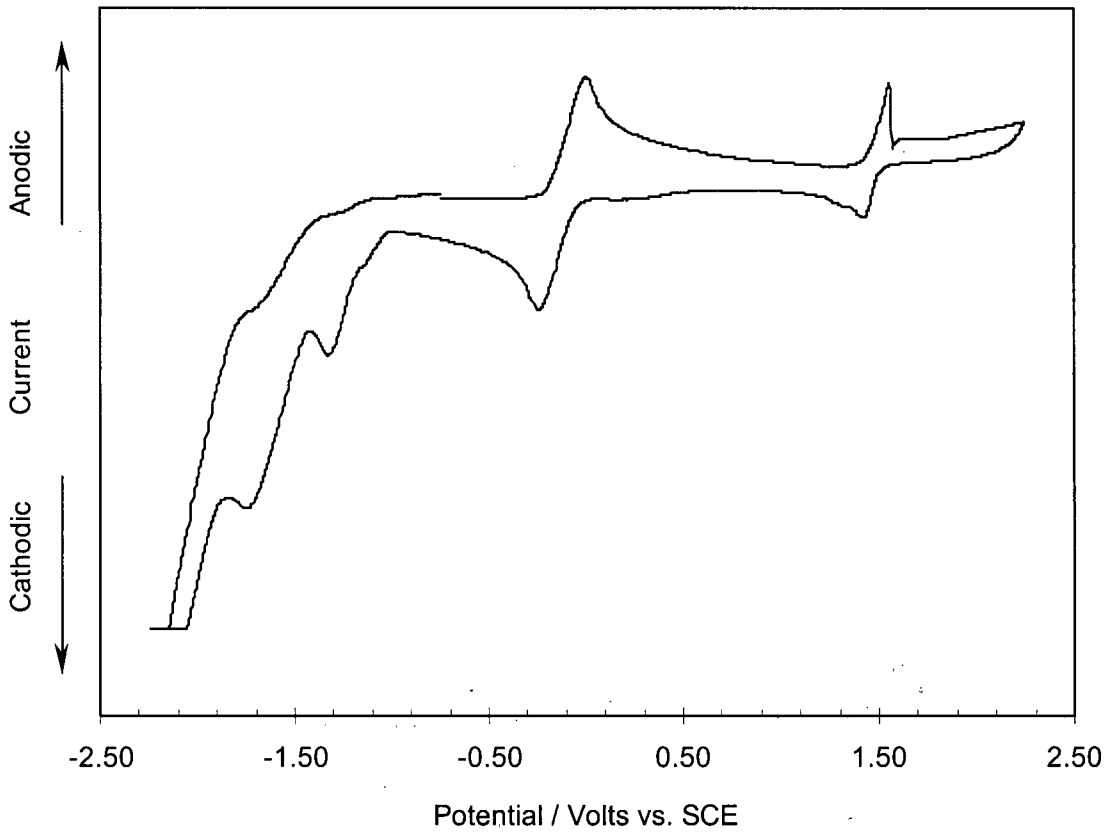

Figure 4.3. Cyclic voltammogram of **3** in CH_2Cl_2 solution containing 0.1 M $^nBu_4NPF_6$ as supporting electrolyte, [**3**] $\approx 1 \times 10^{-2}$ M, scan rate 200 mV/s. The potential sweep program was: -0.75 $\rightarrow$ + 2.25 $\rightarrow$ -2.25 $\rightarrow$ -0.75 V *vs.* SCE. The large reversible wave at -0.12 V is due to the reference standard, $Me_{10}Fc$.

Sharp redox waves are usually attributed to species confined to the electrode surface.[27] If a complex adsorbs to the electrode, it is slightly more stabilized with respect to oxidation or

References begin on page 151.

reduction than the species in bulk solution; this results in an extra redox wave from the surface-confined molecules, which occurs at slightly higher energy than the solution wave, and this 'post-wave' is somewhat narrower. For weak adsorption, the two waves overlap and the wave simply appears sharpened. In contrast, if it is the redox product that adsorbs to the electrode rather than the starting complex, the redox process is energetically more favourable than if the product remained in solution. Thus, there is a sharp 'pre-wave' in the CV; the sharpness arises from depletion of the surrounding solution. It should be noted that voltammograms that are complicated because of redox product adsorption are often simplified at lower concentration, where only the surface-confined waves are observed.

The effect of concentration on the shape of the $Ru^{III/II}$ redox wave is illustrated in Figure 4.4, for a slow scan rate (10 mV/s) at which the changes in peak shape are most dramatic. At high concentration (Panel A, [**3**] = 1.1×10^{-2} M), the wave is very sharp on the oxidative sweep but lacks a sharp return reductive wave, while at lower concentration (Panel C, [**3**] = 5.5×10^{-3} M), the couple appears as a more typical-looking reversible solution process at a microelectrode. This data is consistent with a situation in which the oxidized species in solution is in equilibrium with oxidized species adsorbed weakly to the electrode surface, as depicted below. It should be noted that complex **3** itself does not adsorb to the electrode to form an insulating layer, as evidenced by the fact that the redox wave from other species in the solution (*e.g.*, $Me_{10}Fc$) is readily observed in the presence of **3**.

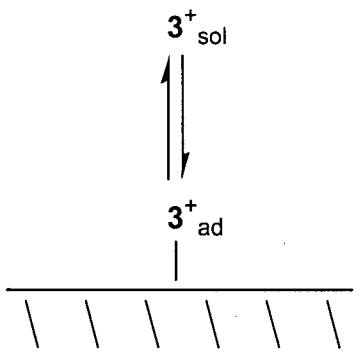

References begin on page 151.

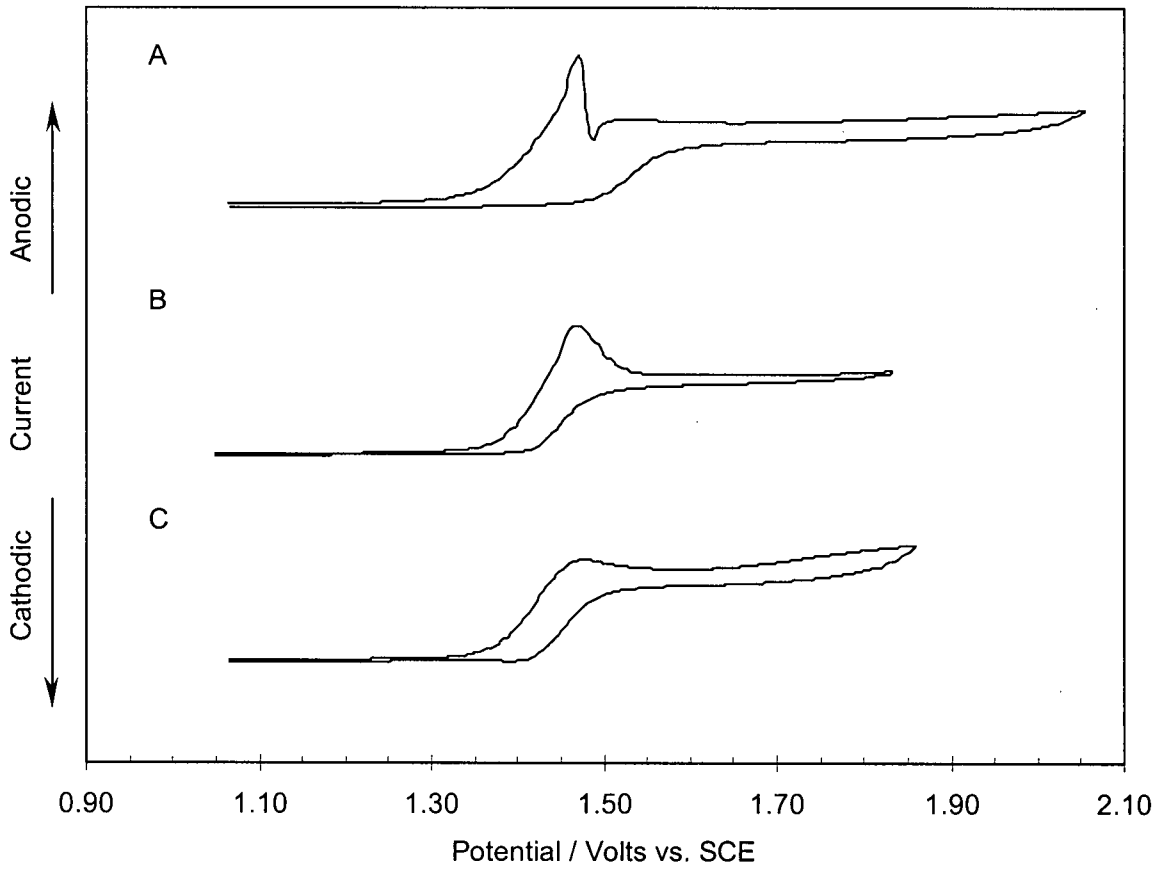

Figure 4.4. Effect of concentration on the shape of the $Ru^{III/II}$ redox wave of complex **3** at slow scan rate (10 mV/s). Panel A: [**3**] = 1.1×10^{-2} M; Panel B: [**3**] = 5.5×10^{-3} M; Panel C: [**3**] = 2.8×10^{-3} M. The potential sweep programs were: +1.05 → ~2.00 → +1.05 V *vs.* SCE. The current axis is not to scale.

It is not surprising that oxidized **3** should adsorb onto the electrode, since air-oxidized solutions of **3** in CH_2Cl_2 precipitate a green material that is soluble in methanol but poorly soluble in CH_2Cl_2. The high-concentration CV observations in Figure 4.4 suggest that as the oxidized species builds up in solution, it adsorbs to form a thin, nearly insulating layer on the electrode, which causes a sharp drop in the current since it blocks further oxidation of **3**. At lower concentrations, the effect is less pronounced since it takes longer for the concentration of

References begin on page 151.

oxidized species to build up such that the adsorbed layer forms. On the return scan, the absence of sharp features suggests that desorption occurs at a potential above that at which the surfaced-confined oxidized species is reduced back to **3**. Thus, the return wave appears broadened like a solution wave, but it is of low intensity since the slow sweep rate leaves sufficient time for the desorbed species to diffuse away from the vicinity of the electrode.

It was found that the CV of complex **1** obtained at high concentrations shows similar concentration dependence, although the changes in wave shape (data not shown) are not as dramatic as those observed for **3**. Thus, this adsorption process does not seem to be particular to complex **3** but may be general for the phosphine-ether complexes studied here. For the present studies, the values of the reduction potentials are of interest, but a detailed understanding of the solution electrochemistry of the complexes is not essential. Thus, investigation into this matter was not pursued further, but this unusual behaviour may be of interest for future studies.

4.3.2 Preparation of aryloxide complex 4

The aryloxide complex **4** was prepared by the nucleophilic attack of free phosphine-ether POMe on **1**, *i.e.*, via ligand-assisted dealkylation. The dealkylation can be achieved either by direct reaction of pure **1** with one equivalent of POMe, or by treatment of the solvate complex [*cis*-Ru(bpy)$_2$(acetone)$_2$](BF$_4$)$_2$ with two equivalents of the phosphine-ether. Both methods provide **4** in quantitative yield as a brown-black powder after metathesis to the hexafluorophosphate salt, which also removes the phosphonium salt coproduct. The aryloxide complex can be crystallized from hot methanol as brown-black needles but was not crystallographically analyzed.

Complex **4** is stable in air as a solid but slowly turns greenish in air-saturated solution due to oxidation. The phenoxide oxygen in **4** is bound strongly to the metal, unlike the phenyl ether oxygens in complexes **1** and **2**. The dealkylated complex does not undergo substitution reactions with coordinating solvents such as DMSO and acetonitrile, which rapidly react with the phosphine-ether complexes.

References begin on page 151.

4.3.2.1 Characterization of aryloxide complex 4 by CV

The CV of **4** is shown in Figure 4.5. The metal oxidation wave ($E_{1/2}(Ru^{III/II})$ = 0.63 V) occurs at significantly lower potential than in the phosphine-ether complexes due to increased electron donation from the anionic phenoxide ligand compared to the ether; this is consistent with the fact that anionic ligands generally have negative Lever parameters.[28] Using the observed reduction potential for **4**, the ligand electrochemical parameter for phenoxide is estimated to be E_L = -0.18 V (*i.e.*, E_L = -0.59 V for the bidentate ligand *o*-Ph_2PPhO^-), which is similar to those reported for oxalate (E_L = -0.17 V per oxygen) and thiophenolate (E_L = -0.13 V).[28] When the potential is scanned just past the first oxidation wave, the process is quasireversible (Figure 4.5, Panel B). The higher energy oxidation processes have not been assigned. The first reduction wave likely corresponds to the bpy reduction (E_{red} = -1.54 V), given the similarity to the value of -1.56 V predicted from the observed metal reduction potential (using Equation 3.2, Chapter Three). The observed redox gap ($\Delta E_{(redox)}$ = 2.17 V) should correspond to an MLCT absorption energy of ~ 2.38 eV (521 nm); although the photophysical properties of this complex were not studied, solutions of **4** are dark brown in colour, suggestive of a broad absorption band shifted to lower energy compared to the phosphine-ether complexes (~ 412 nm) that is consistent with the electrochemical data.

The CV of this complex was originally measured during investigation of the reductive decomposition of complexes **1** and **2**. As for the other *P,O*-complexes, the first reduction process of **4** ($E_{1/2}$ = -1.54 V) produces a small amount of a new complex that can be reversibly oxidized (reduction product: $E_{1/2}$ = 1.05 V). When the potential is scanned over a limited range (Panel B), the first oxidation and reduction waves are quasireversible, so the decomposition of both the oxidized and reduced species is relatively slow. Although the reduction products from these two complexes are oxidized at different potentials, the CV of **4** clearly establishes that the reductive decomposition of **1** and **2** is not a simple dealkylation. Given that complexes **1•MeCN**, **3** and **5** (*vide infra*) also undergo reductive decomposition, it is reasonable to conclude that these processes involve the ether moiety and are not dependent upon its coordination to the Ru centre.

References begin on page 151.

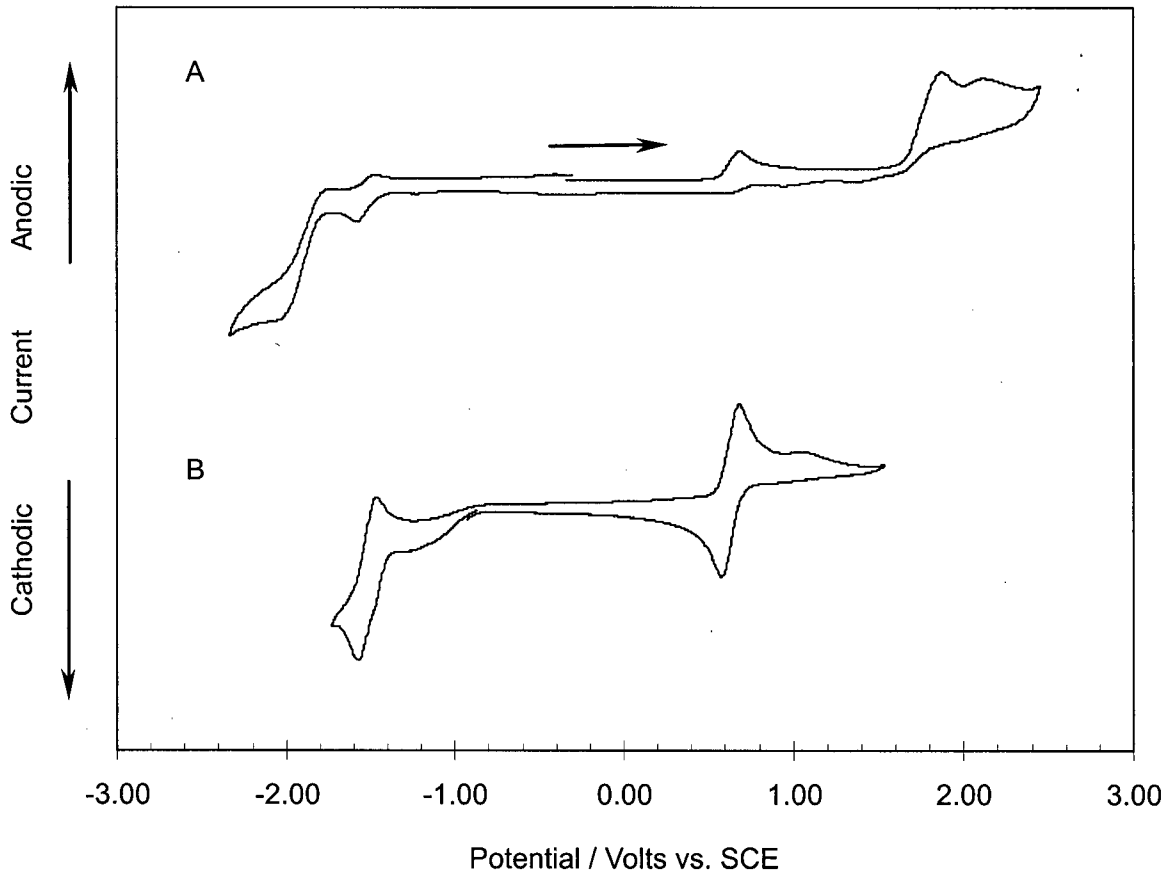

Figure 4.5. Cyclic voltammograms of **4** in CH_2Cl_2 solution containing 0.1 M $^nBu_4NPF_6$ as supporting electrolyte, [**4**] $\approx 2 \times 10^{-3}$ M. A: Full-range potential scan (-0.35 → +2.45 → -2.35 → -0.35 V) yields partially reversible waves; arrow denotes the direction of the potential sweep. B: Limited-range potential scan (-0.80 → -1.75 → +1.55→ -0.80 V) yields quasireversible waves. The current axis is not to scale.

4.3.3 Preparation of bis(phosphine) complex 5

Complex **5** was isolated in low yield from the reaction of the Ru(II) bis(bipyridyl) bis(acetone) solvate complex with 2 equiv of the ethyl-methyl ether PC2OMe, performed in an attempt to achieve the ligand-assisted dealkylation of complex **3**. Complex **5** was separated

References begin on page 151.

from the crude mixture of PF_6^- salts (mostly complex **3**) by crystallization from hot acetone and isolated as a bright orange powder. The complex was readily assigned as the bis(PC2OMe) complex by virtue of its relatively simple ^1H NMR spectrum, which arises from the high symmetry of the complex. Complex **5** displays considerably lower solubility than the phosphine-ether complexes; it is most soluble in acetonitrile, somewhat soluble in dichloromethane, and crystallizes well from acetone. The phosphines are strongly bound to the metal and, unsurprisingly, no evidence was found for reaction of this complex with acetonitrile.

4.3.3.1 Characterization of bis(PC2OMe) complex 5 by CV

Because of its limited solubility in dichloromethane, the voltammetry of complex **5** was carried out in acetonitrile solution. Similar to other $[cis\text{-}Ru(bpy)_2(PR_3)_2]^{2+}$ complexes,[29] this complex shows a quasireversible metal-based oxidation wave ($E_{1/2}(Ru^{III/II})$ = 1.60 V) in its CV, shown in Figure 4.6, and two irreversible bpy-based reductions (E_{red} = -1.45, -1.65 V). The reduction potentials predicted using the Lever parameters for the model complex $[cis\text{-}Ru(bpy)_2(PPh_3)_2]^{2+}$ are: $E_{1/2}(Ru^{III/II})_{calc}$ = 1.57 V and $E_{1/2}(bpy^{0/-})_{calc}$ = -1.32 V. In addition, there two irreversible ligand reduction waves (E_{red} = -1.13, -1.23 V) that give rise to reductive decomposition products as observed for the *P,O*-complexes. In this case, however, the reductive decomposition is more complicated; several new oxidation waves and a new reduction wave appear in the CV. The reductive decomposition was not studied in further detail.

References begin on page 151.

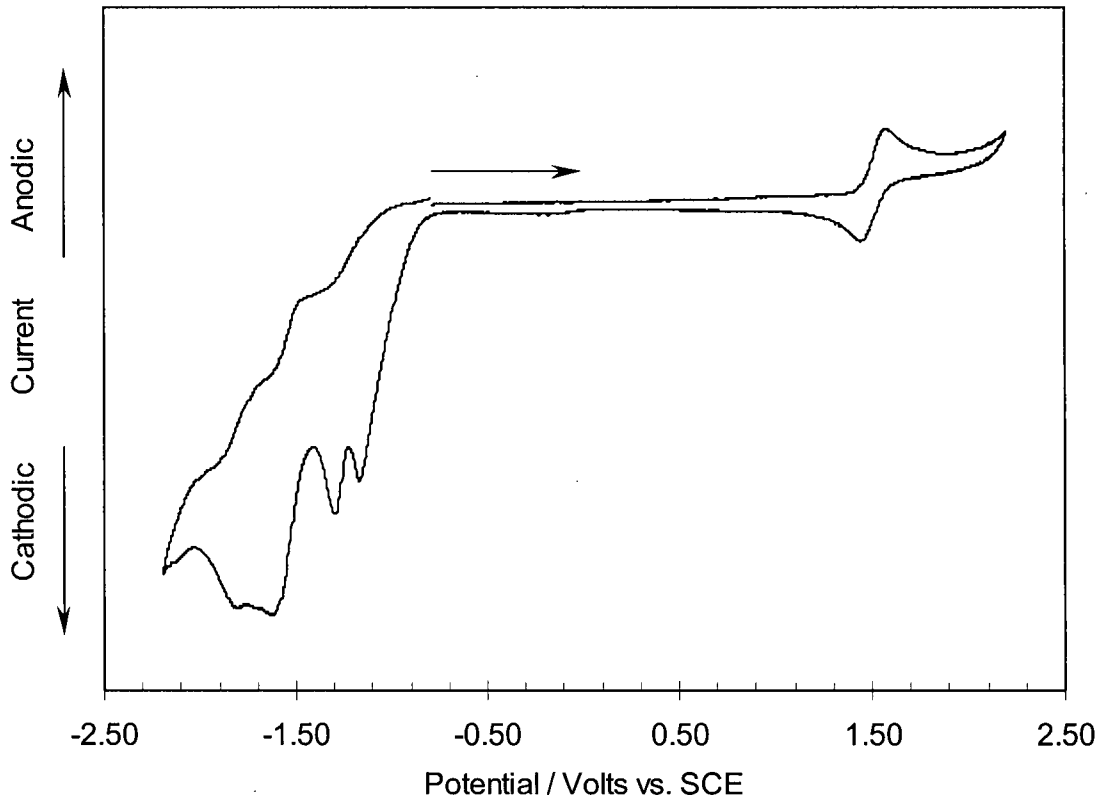

Figure 4.6. Cyclic voltammogram of **5** in CH_3CN solution containing 0.1 M $^nBu_4NPF_6$ as supporting electrolyte, [**5**] $\approx 2 \times 10^{-3}$ M. The potential sweep program was: -0.80 $\rightarrow$ +2.20 $\rightarrow$ -2.20 $\rightarrow$ -0.80 V *vs.* SCE.

4.4 Preparation of the phosphonium salts

The methyl and ethyl phosphonium iodide salts of the phosphine-ether ligands were prepared in order to compare them spectroscopically to products formed when complexes **1-3** were treated with phosphine-ethers. The salts were readily prepared by alkylation of the phosphine-ethers with methyl iodide or ethyl iodide in diethyl ether solution. The alkylations with MeI were carried out at room temperature, while those with EtI required heating to increase the rate of the reaction; in all cases, the phosphonium salts precipitated from the

References begin on page 151.

reaction mixture and were isolated as white powders. Satisfactory analyses (NMR, EA) were obtained for all of the salts after minimal purification efforts. The phosphonium iodide salts have characteristic single-resonance $^{31}P\{^{1}H\}$ NMR spectra (δ 21-31), and the ^{31}P chemical shifts do not shift significantly when the counterion is changed to PF_6^-. As well, the ^{1}H spectra contain distinctive ^{1}H-^{31}P coupling ($^{2}J_{PH}$ = 14 Hz; $^{3}J_{PH}$ = 20 Hz) in the resonances of the phosphorus-bound alkyl groups. Thus, the phosphonium salts were easy to identify by NMR spectroscopy even in mixtures with several components, such as the reaction mixtures after treatment of complexes **1-3** with free phosphine-ethers (see section 4.5).

4.5 Studies of the dealkylation of 1-3 by free phosphine-ethers

In theory, the reactivity of a metal-bound ether moiety should be tunable via appropriate selection of substituents on the oxygen. For example, increasing the electron-donating ability of the ether R group should lead to decreased electrophilicity of the carbon α to the Ru-bound oxygen, and therefore, decreased nucleophilic attack at this site by free ligand. Indeed, changing the ether R group to Et sufficiently alters the electronic environment of the α-carbon that performing the synthesis of the POEt complex, **2**, with 2 equiv of POEt does not result in dealkylation. Modification of the ligand framework to include an alkyl linker between the phosphorus and oxygen in place of the phenylene bridge also reduces the occurrence of ligand-assisted *O*-dealkylation. Specifically, reacting $[cis\text{-}Ru(bpy)_2(acetone)_2]^{2+}$ with two equiv of the less sterically demanding phosphine PC2OMe in acetone at 56 °C leads to formation of the bis(phosphine) complex, **5**, rather than the alkoxide complex that would arise from *O*-dealkylation of **3**.

In order to compare α-carbon electrophilicity in the complexes, **1-3** were each treated with free POMe in acetone at 56 °C for 18 h. For **1**, an orange-to-dark brown colour change occurred within 2 h, and the $^{31}P\{^{1}H\}$ NMR spectrum of the crude reaction mixture showed the presence of the aryloxide complex **4**, $[Me(POMe)]^+$, and small amounts of unreacted **1** and POMe. The reaction mixtures containing **2** and **3** changed colour more slowly, requiring several hours, and exhibited more complicated $^{31}P\{^{1}H\}$ NMR spectra. Analysis of the $^{31}P\{^{1}H\}$

References begin on page 151.

spectrum showed that free POEt, **1**, and $[Me(POMe)]^+$ were present in the **2**+POMe reaction mixture, along with aryloxide **4**, $[Et(POMe)]^+$, and a small amount of unreacted **2**. No unreacted POMe remained. From this it was concluded that **2** undergoes two reactions with POMe: primarily *O*-dealkylation by POMe, but also ligand exchange with POMe to form **1**, which then gets dealkylated by free POMe.

The $^{31}P\{^1H\}$ NMR spectrum of the **3**+POMe reaction mixture showed mainly unreacted **3**, as well as some bis(phosphine) complex **5** and small amounts of the products of dealkylation of **1** by POMe. Two other small peaks were likely due to the bis(phosphine) complex $[cis\text{-}Ru(bpy)_2(PC2OMe\text{-}P)(POMe\text{-}P)]^{2+}$, based on the similarity of the ^{31}P chemical shifts (δ24.4, 24.2) to that of bis(PC2OMe) complex **5** (δ22.3); however, this complex has not been isolated. In summary, the dominant reaction of **3** with POMe is ligand exchange to release free PC2OMe, which reacts by ether displacement with **3** to form the bis(phosphine) complex. Based on the increase in phosphine size involved (estimated using cone angles: θ = 171° for POMe, $\theta \approx$ 141° for PC2OMe by comparison to $^n BuPPh_2$),[13,30,31] it is not surprising that the PC2OMe-POMe ligand exchange would not proceed to completion. Any dealkylation that occurred in this case was of **1** formed by ligand exchange; complex **3** was not directly dealkylated.

To help clarify the importance of the incoming nucleophile, complexes **1-3** were also reacted with free POEt and PC2OMe. The NMR spectral data were interpreted as described above and the complete set of results is presented in Table 4.4; $^{31}P\{^1H\}$ NMR spectral data are listed in Table 4.3. To ease comparison of the ligands (POR) and complexes, the complexes have been labeled both numerically as in the text and as Ru(POR).

References begin on page 151.

Table 4.3. $^{31}P\{^{1}H\}$ NMR chemical shift data[a] (δ) and peak assignments for reactions[b] of *P,O*-complexes with free POR

	POMe		POEt		PC2OMe	
Ru(POMe)[c]	55.0	Ru(PO^-)	55.0	Ru(PO^-)	55.0	Ru(PO^-)
1	51.9	Ru(POMe)	52.6	Ru(POEt)	52.1	Ru(PC2OMe)
	21.7	$[Me(POMe)]^+$	51.9	Ru(POMe)	26.9	ligand-derived
	-15.0	POMe	21.7	$[Me(POMe)]^+$	25.1	$[Me(PC2OMe)]^+$
			21.3	$[Me(POEt)]^+$	24.4	mixed bisPR_3
			-13.9	POEt	24.2	mixed bisPR_3
			-15.0	POMe	22.3	$Ru(PC2OMe)_2$
					21.7	$[Me(POMe)]^+$
					-15.0	POMe
					-21.2	PC2OMe
Ru(POEt)	55.0	Ru(PO^-)	55.0	Ru(PO^-)	52.6	Ru(POEt)
2	52.6	Ru(POEt)	52.6	Ru(POEt)	52.1	Ru(PC2OMe)
	51.9	Ru(POMe)	25.7	$[Et(POEt)]^+$	23.9	unassigned
	21.7	$[Me(POMe)]^+$	24.2	unassigned	22.3	$Ru(PC2OMe)_2$
	21.3	$[Me(POEt)]^+$	-13.9	POEt	-13.9	POEt
	-13.9	POEt				
Ru(PC2OMe)	55.0	Ru(PO^-)	52.6	Ru(POEt)	52.1	Ru(PC2OMe)
3	52.1	Ru(PC2OMe)	52.1	Ru(PC2OMe)	26.9	ligand-derived
	24.4	mixed bisPR_3	23.9	unassigned	22.2	$Ru(PC2OMe)_2$
	24.2	mixed bisPR_3	22.3	$Ru(PC2OMe)_2$	-21.1	PC2OMe
	22.3	$Ru(PC2OMe)_2$	-13.9	POEt		
	21.7	$[Me(POMe)]^+$				
	-15.0	POMe				

[a] δ values ± 0.4 ppm as determined from variation between experiments. [b] Conditions: 1:1 stoichiometry, refluxing acetone solution, 18 h. NMR spectra obtained in acetone-d_6 after removal of acetone-h_6. [c] Reaction time = 48 h for Ru(POMe) + PC2OMe.

References begin on page 151.

Table 4.4. Summarized results of reactions[a] of Ru(POR) with free POR as determined from $^{31}P\{^{1}H\}$ NMR spectra[b]

	POMe	POEt	PC2OMe
Ru(POMe) **1**	Dealkylation of Ru(POMe) by POMe.	Dealkylation of Ru(POMe) by POMe and POEt. Ligand exchange to form Ru(POEt).	[c] Ligand exchange to form Ru(PC2OMe). $Ru(PC2OMe)_2$ formation. Dealkylation of Ru(POMe) by POMe and PC2OMe.
Ru(POEt) **2**	Ligand exchange to form Ru(POMe). Dealkylation of Ru(POMe) by POEt and POMe.	Mostly no reaction. Dealkylation of Ru(POEt) by POEt (trace).	Mostly no reaction. Ligand exchange to form Ru(PC2OMe). $Ru(PC2OMe)_2$ formation.
Ru(PC2OMe) **3**	Mostly no reaction. Ligand exchange to form Ru(POMe) (trace). Dealkylation of Ru(POMe) by POMe. $Ru(PC2OMe)_2$ formation.	Mostly no reaction. Ligand exchange to form Ru(POEt) (trace).	$Ru(PC2OMe)_2$ formation.

[a]Conditions: 1:1 stoichiometry, refluxing acetone solution, 18 h. [b]Spectra obtained in acetone-d_6 after removal of acetone-h_6. [c]48 h reaction.

References begin on page 151.

4.6 Summary of dealkylation results

Not surprisingly, in all the cases where a smaller phosphine is reacted with a complex containing a larger phosphine, ligand displacement dominates (*e.g.*, **1** + PC2OMe, **2** + POMe or PC2OMe). This pathway occurs to a lesser extent when a larger phosphine reacts with a complex containing a smaller one (*e.g.*, **1** + POEt, **3** + POMe or POEt). Additionally, **3** reacts with the relatively small PC2OMe to form the bis(phosphine) complex **5**. In general, dealkylation is the preferred reaction of **1**, and is effected by free POMe, POEt and PC2OMe, as determined by the observation of the corresponding methylphosphonium salts' resonances in the $^{31}P\{^{1}H\}$ NMR spectra. Complex **2** is dealkylated to a small extent by POEt, but there is no evidence for dealkylation of **3** by any of the free phosphine-ethers studied. In summary, the aryl ether complexes **1-2** are more prone to dealkylation than the alkyl ether complex **3**. There appears to be little dependence on the nature of the incoming phosphine-ether nucleophile.

4.7 Explanation of the propensities of 1-3 toward dealkylation

4.7.1 Consideration of the redox properties of 1-3

It was hypothesized that dealkylation of the metal-bound ethers might be related to the electron density at the metal, since electron withdrawal by the metal would likely increase the electrophilicity of the carbon α to the coordinated oxygen. Therefore, complexes **2** and **3** were examined by cyclic voltammetry to obtain a measure of the electron density at the metal centre to compare to that of **1**. In all three complexes the metal centre is notably electron-deficient, but the reduction potential of the metal varies insignificantly from **1-3** (for **1**, $E_{ox}(Ru^{III/II}) = 1.56$ V; for **2**, $E_{ox}(Ru^{III/II}) = 1.59$ V; for **3**, $E_{ox}(Ru^{III/II}) = 1.56$ V *vs.* SCE). Clearly, the differences in the reactivity of **1-3** cannot be explained in this manner. The fact that complexes **1** and **2** are susceptible to dealkylation at all may be attributed to the inductive effects of the electron-deficient metal, but the observed differences in the dealkylation propensities of **1-3** must be due to other factors.

References begin on page 151.

4.7.2 Consideration of the molecular structures of 1-3 and 4

A structural study was undertaken to assist in the understanding of these reactivity trends. Surprisingly, the differences in the phosphine-ether ligands do not cause significant differences in the Ru-P or Ru-O bond lengths in **1-3**. The O-C_α bond that connects the ether's alkyl moiety to the complex is, however, sensitive to the changes in ligand structure. The O-C_α bond length varies as follows: 1.441(3) Å in **1**; 1.482(11) Å and 1.460(11) Å in **2**; and 1.405(7) Å in **3**. The O-C_α bond lengths in the aryl ether complexes **1** and **2** are significantly longer than in the alkyl ether complex **3**, which may correlate with a difference in C_α electrophilicity that would be consistent with the observed dealkylation reactivities. This difference in electrophilicity would arise from a balance of inductive effects, in which the electron withdrawal by the metal is countered by electron donation from the alkyl group(s) to varying degrees in **1-3**, most for **3** because of its two electron-rich alkyl substituents and least for **1**. More importantly, however, the aryl ethers are thermodynamically predisposed to dealkylation because the reaction yields a resonance-stabilized phenoxide (**4**). The difference between the two aryl ether complexes' reactivity can be justified simply: complex **2** undergoes less dealkylation than **1** because of the lower electrophilicity of the ethyl group's C_α compared to the methyl group's carbon.

The resistance to dealkylation seen for **3** results from a combination of factors whose relative importance was not clarified by the structural study. The two O-C_α bond lengths are significantly different (O-C(35) = 1.405(7) Å *vs.* O-C(34) = 1.434(6) Å), but neither C_α is susceptible to nucleophilic attack by free phosphines. Based on bond lengths, one might expect the longer O-C(34) bond to be cleavable. However, attack at this carbon would require a sterically disfavoured approach from inside the chelate ring; moreover, such a reaction is also entropically unfavourable because the resulting phosphonium salt would be tethered to the metal complex. Although attack at the methoxy carbon C(35) is both sterically and entropically favoured, this carbon may simply have insufficient electrophilicity to compete with attack of free phosphine directly at the uncrowded and electron-deficient Ru centre in **3**.

References begin on page 151.

4.8 Summary

In this chapter, an investigation into the dealkylation of Ru(II) bis(bipyridyl) phosphine-ether complexes by free phosphine-ethers was presented. Complexes **1** and **2** contain triphenylphosphine derivatives with an ether substituent on one of the phenyl rings. These complexes undergo ligand-assisted *O*-dealkylation by the same weakly basic phosphines, a reaction that has typically been observed for complexes containing highly basic phosphines with multiple ether substituents, such as TMPP. The high electron-deficiency of the Ru(II) centre in these complexes is likely responsible for the ease with which these complexes are dealkylated to yield the aryloxide complexes. When the phenylene bridge between the phosphorus and oxygen moieties is replaced by an ethylene bridge as in **3**, the complex is not susceptible to ligand-assisted dealkylation. This difference in reactivity can be justified primarily by steric arguments, but the lack of resonance stabilization of the hypothetical alkoxide product may also play a role. Dealkylation of ether complexes may provide a synthetic route to aryloxide complexes that contain groups incompatible with phenols and/or phenoxides, such as metal alkyls that are susceptible to protonolysis or ancillary ligands with deprotonatable (*e.g.*, carboxylic acid) or protonatable (*e.g.*, amine) functionalities.

References begin on page 151.

4.9 Experimental section

4.9.1 General procedures

General experimental procedures and instrumental details are described in Chapter Two (section 2.6.1); cyclic voltammetric details are given in Chapter Three (section 3.7.1).

4.9.2 Materials

2-Ethoxyphenyldiphenylphosphine (POEt),[32] and 2-methoxyethyldiphenylphosphine (PC2OMe)[33] were prepared according to published procedures. For synthetic details regarding the preparation of complex **1**, see section 2.6.3.1.

4.9.3 Preparation of complexes

4.9.3.1 Synthesis of [cis-Ru(bpy)$_2$(POEt-P,O)](PF$_6$)$_2$, 2

This complex was prepared as described for **1** in section 2.6.3.1, using 2-ethoxyphenyldiphenylphosphine[32] in place of POMe and obtained pure after metathesis to PF_6^- salt (yield 85 %). ^{1}H NMR (200 MHz, 25°C, CD_2Cl_2): δ8.61 – 8.54 (m, 2H), 8.31 (d, $^3J_{HH}$ = 5.6 Hz, 1H), 8.22 – 8.08 (m, 3H), 7.96 – 7.35 (m, 18H), 7.26 – 7.12 (m, 2H), 6.97 – 6.88 (m, 2H), 6.42 – 6.33 (m, 2H), 4.64 – 4.47 (m, 1H), 4.14 – 3.97 (m, 1H), 0.72 (t, J = 7.0 Hz, 3H). ^{31}P{^{1}H} NMR (81 MHz, 25°C, CD_2Cl_2): δ51.1 (s, PO), -144 (sept, $^1J_{PF}$ = 711 Hz, PF_6). Elemental analysis calcd. for $C_{40}H_{35}F_{12}N_4OP_3Ru$ (%): C, 47.58; H, 3.49; N, 5.55; found: C, 47.32; H, 3.58; N, 5.49. CV (200 mV/s, 25 °C, CH_2Cl_2/^{n}Bu$_4$NPF$_6$, V *vs.* SCE): similar appearance to CV of **1**; $E_{ox}(Ru^{III/II})$ = 1.59 V; E_{red} = -1.16 (sh), -1.22, -1.65 V; reductive decomposition product $E_{1/2}$ = 0.93 V. Crystals suitable for X-ray crystallographic analysis were obtained by slow crystallization from methanol.

References begin on page 151.

4.9.3.2 Synthesis of [cis-Ru(bpy)$_2$(PC2OMe-P,O)](PF$_6$)$_2$, 3

This complex was prepared as described for **1** in section 2.6.3.1, using 2-methoxyethyldiphenylphosphine[33] in place of POMe. Crude yield: 85 %. Impurities (~ 10 % by $^{31}P\{^1H\}$ NMR) were removed by repeated recrystallization from hot methanol. ^1H NMR (200 MHz, 25°C, CD_2Cl_2): δ8.80 (d, J = 5.69 Hz, 1H), 8.59 – 8.50 (m, 3H), 8.23 – 7.77 (m, 7H), 7.75 – 7.32 (m, 10H), 7.19 – 7.12 (m, 1H), 6.99 – 6.91 (m, 2H), 6.53 – 6.45 (m, 2H), 4.46 – 4.26 (m, 1H), 3.91 – 3.72 (m, 1H), 3.25 – 2.85 (m, 2H), 2.97 (s, 3H, OCH_3). $^{31}P\{^1H\}$ NMR (81 MHz, 25°C, CD_2Cl_2): δ50.5 (s, PO), -144 (sept, $^1J_{PF}$ = 711 Hz, PF_6). Elemental analysis calcd. for $C_{35}H_{32}F_{12}N_4OP_3Ru$ (%): C, 44.36; H, 3.51; N, 5.91; found: C, 44.00; H, 3.63; N, 5.86. CV (200 mV/s, 25 °C, CH_2Cl_2/^{n}Bu$_4$NPF$_6$, V *vs.* SCE): $E_{1/2}(Ru^{III/II})$ = 1.48 V, unusually sharp wave; E_{red} = -1.33 (irrev), -1.55 V (rev); reductive decomposition product $E_{1/2}$ = 1.09 V. Crystals suitable for X-ray crystallographic analysis were obtained by crystallization from hot methanol.

4.9.3.3 Synthesis of [cis-Ru(bpy)$_2$(2-(diphenylphosphino)phenoxide-P,O)](PF$_6$), 4

This complex can be prepared by reacting [*cis*-Ru(bpy)$_2$(acetone)$_2$](BF$_4$)$_2$ with 2 equiv POMe in refluxing acetone, or by reacting [*cis*-Ru(bpy)$_2$(POMe-*P,O*)](PF$_6$)$_2$ with 1 equiv of POMe in refluxing acetone. Metathesis to the PF_6^- salt by precipitation of an acetone solution of the BF_4^- salt with aqueous NH_4PF_6 provides the aryloxide complex as a black powder in quantitative yield. Recrystallization from acetone/ether or hot methanol yields brown-black needles. ^1H NMR (400 MHz, 25°C, CD_2Cl_2): δ8.66 (d, J = 8.20 Hz, H), 8.62 (d, J = 7.97 Hz, 1H), 8.51 (d, J = 5.12 Hz, 1H), 8.38 – 8.34 (m, 2H), 8.27 (d, J = 5.52 Hz, 1H), 8.11 – 8.05 (m, 2H), 8.00 – 7.96 (m, 2H), 7.84 – 7.76 (m, 3H), 7.59 – 7.40 (m, 8H), 7.16 – 7.03 (m, 3H), 6.92 – 6.88 (m, 2H), 6.73 (dd, J_1 = 5.49, J_2 = 5.60 Hz, 1H), 6.65 – 6.56 (m, 3H). $^{31}P\{^1H\}$ NMR (81 MHz, 25°C, CD_2Cl_2): δ54.0 (s, PO), -144 (sept, $^1J_{PF}$ = 711 Hz, PF_6). Elemental analysis calcd. for $C_{38}H_{30}F_6N_4OP_2Ru$ (%): C, 54.62; H, 3.62; N, 6.70; found: C, 54.37; H, 3.73; N, 6.72. CV (200 mV/s, 25 °C, CH_2Cl_2/^{n}Bu$_4$NPF$_6$, V *vs.* SCE): $E_{1/2}(Ru^{III/II})$ = 0.63 V; E_{red} = -1.54, -2.38 V; reductive decomposition product $E_{1/2}$ = 1.05 V.

References begin on page 151.

4.9.3.4 Synthesis of [cis-Ru(bpy)$_2$(PC2OMe-P)$_2$](PF$_6$)$_2$, 5

To a solution of [*cis*-Ru(bpy)$_2$(acetone)$_2$](BF$_4$)$_2$ (0.496 mmol) in N_2-sparged acetone (65 mL) was added 2 equiv of 2-methoxyethyldiphenylphosphine (0.249 g, 1.02 mmol) as a solution in N_2-sparged acetone (35 mL). The mixture was heated to reflux for 3 days, then the clear red solution was filtered through Celite and evaporated to dryness. The residue was converted to the PF_6 salt and the bis(phosphine) complex was isolated by recrystallization from acetone to yield a bright orange powder. Purified by crystallization from methanol-acetone. Yield: ~ 35 % by $^{31}P\{^1H\}$ NMR of crude product mixture, remainder bidentate *P,O*-complex and other unidentified products. ^1H NMR (200 MHz, 25°C, CD_3CN): δ8.84 (d, J = 5.46 Hz, 4H), 7.99 (t, J = 7.73 Hz, 4H), 7.87 (d, J = 7.90 Hz, 4H), 7.56 (dd, J_1 = 5.96, J_2 = 7.38 Hz, 4H), 7.26 (dd, J_1 = 7.34, J_2 = 7.89 Hz, 4H), 6.98 (dd, J_1 = 7.82, J_2 = 7.38 Hz, 8H), 6.41 (m, 8H), 2.75 (s, 6H, MeO), 2.69 (m, 4H), 1.71 (dd, J_1 = 7.27, J_2 = 6.82 Hz, 4H). $^{31}P\{^1H\}$ NMR (81 MHz, 25°C, CD_3CN): δ22.0 (s, PO), -144 (sept, $^1J_{PF}$ = 711 Hz, PF_6). Elemental analysis calcd. for $C_{50}H_{50}F_{12}N_4O_2P_4Ru$ (%): C, 50.39; H, 4.23; N, 4.70; found: C, 50.58; H, 4.33; N, 4.75. CV (200 mV/s, 25 °C, CH_3CN/^{n}Bu$_4$NPF$_6$, V *vs.* SCE): $E_{1/2}(Ru^{III/II})$ = 1.60 V; E_{red} = -1.13 (irrev), -1.23 (irrev), 1.47, 1.72 V; after reductive scanning, E_{ox} = -0.48, -0.17, 0.23 V; E_{red} = -0.99 (irrev), -1.24 (irrev), -1.45, -1.69 V.

4.9.4 Preparation of phosphonium salts

4.9.4.1 Synthesis of [Me(POMe)]I

An excess of MeI (0.10 mL, 1.61 mmol) was added to a solution of 2-methoxyphenyldiphenylphosphine (0.197 g, 0.673 mmol) in dry diethyl ether (30 mL) under nitrogen. The mixture immediately became cloudy upon formation of the insoluble phosphonium salt. The mixture was stirred overnight then evaporated to dryness to remove excess MeI. The residue was suspended in ether and the white powder collected by filtration, washed with ether and hexanes, and dried by suction. Yield: 100 %. ^1H NMR (200 MHz, 25°C, acetone-d_6): δ7.97 – 7.72 (m, 11H), 7.50 – 7.43 (m, 1H), 7.30 – 7.23 (m, 2H), 3.86 (s,

References begin on page 151.

3H, MeO), 3.14 (d, $^2J_{PH}$ = 14.4 Hz, 3H). $^{31}P\{^1H\}$ NMR (81.0 MHz, 25°C, acetone-d_6): δ21.9 (s). Elemental analysis calcd. for $C_{20}H_{20}IOP$ (%): C, 55.32; H, 4.64; found: C, 55.32; H, 4.69.

4.9.4.2 Synthesis of [Me(POEt)]I

Prepared as for [Me(POMe)]I using POEt. Yield: 58 %. ^1H NMR (200 MHz, 25°C, acetone-d_6): δ7.96 – 7.33 (m, 11H), 7.45 – 7.17 (m, 3H), 4.16 (q, J = 7.0 Hz, 2H), 3.13 (d, $^2J_{PH}$ = 14.1 Hz, 3H), 0.99 (t, J = 7.0 Hz, 3H). $^{31}P\{^1H\}$ NMR (81.0 MHz, 25°C, acetone-d_6): δ21.5 (s). Elemental analysis calcd. for $C_{21}H_{22}IOP$ (%): C, 56.27; H, 4.95; found: C, 56.27; H, 4.90.

4.9.4.3 Synthesis of [Me(PC2OMe)]I

Prepared as for [Me(POMe)]I using PC2OMe. Yield: 40 %. Recrystallized from acetone-ether. ^1H NMR (200 MHz, 25°C, acetone-d_6): δ8.16 – 7.94 (m, 4H), 7.90 – 7.62 (m, 6H), 3.85 – 3.62 (m, 4H), 3.19 (s, 3H, MeO), 2.87 (d, $^2J_{PH}$ = 14.4 Hz, 3H). $^{31}P\{^1H\}$ NMR (81.0 MHz, 25°C, acetone-d_6): δ25.4 (s). Elemental analysis calcd. for $C_{16}H_{20}IOP$ (%): C, 49.76; H, 5.22; found: C, 49.54; H, 5.35.

4.9.4.4 Synthesis of [Et(POMe)]I

EtI (6.88 mmol) was added to a solution of 2-methoxyphenyldiphenylphosphine (0.197 g, 0.673 mmol) in dry diethyl ether (30 mL) under nitrogen. The mixture was heated to reflux and monitored by TLC (silica/ether). After 2 d, the mixture was evaporated to dryness to remove solvent and unreacted EtI. The residue was suspended in ether and the white powder collected by filtration, washed with ether and hexanes, and dried by suction. Yield: 0.27 g (87 %). ^1H NMR (200 MHz, 25°C, acetone-d_6): δ7.97 – 7.27 (m, 14H), 3.84 (s, 3H, MeO), 3.97 – 7.27 (m, 2H), 1.34 (dt, J = 7.50, $^3J_{PH}$ = 20.4 Hz, 3H). $^{31}P\{^1H\}$ NMR (81.0 MHz, 25°C, acetone-d_6): δ26.5 (s). Elemental analysis calcd. for $C_{21}H_{22}IOP$ (%): C, 56.26; H, 4.95; found: C, 55.98; H, 4.96.

References begin on page 151.

4.9.4.5 Synthesis of [Et(POEt)]I

Prepared as for [Et(POMe)]I using POEt. Yield: 82 %. ^{1}H NMR (200 MHz, 25°C, acetone-d_6): δ7.98 – 7.26 (m, 14H), 4.16 (q, J = 6.99 Hz, 2H), 3.73 – 3.55 (m, 2H), 1.34 (dt, J = 7.53, $^{3}J_{PH}$ = 20.2 Hz, 3H), 0.98 (t, J = 6.99 Hz, 3H). ^{31}P{^{1}H} NMR (81.0 MHz, 25°C, acetone-d_6): δ26.0 (s). Elemental analysis calcd. for $C_{22}H_{24}IOP$ (%): C, 57.16; H, 5.23; found: C, 57.08; H, 5.14.

4.9.4.6 Synthesis of [Et(PC2OMe)]I

Prepared as for [Et(POMe)]I using PC2OMe. Yield: 87 %. Recrystallized from acetone-ether. ^{1}H NMR (200 MHz, 25°C, acetone-d_6): δ8.08 – 7.71 (m, 10H), 3.76 – 3.52 (m, 4H), 3.37 – 3.19 (m, 2H), 3.17 (s, 3H, MeO), 1.24 (dt, J = 7.51 Hz, $^{3}J_{PH}$ = 20.0 Hz, 3H). ^{31}P{^{1}H} NMR (81.0 MHz, 25°C, acetone-d_6): δ31.0 (s). Elemental analysis calcd. for $C_{17}H_{22}IOP$ (%): C, 51.02; H, 5.54; found: C, 50.96; H, 5.53.

4.9.5 X-ray crystallographic structural determinations (Dr. B. O. Patrick)

Suitable crystals of **2** and **3** grown from methanol were selected and mounted on thin glass fibres. The crystallographic data and refinement details are summarized in Table A.4.1 (Appendix 4.1). Data were collected at 173 (± 1) K on a Rigaku/ADSC CCD area detector in two sets of scans (ϕ = 0.0 to 190.0°, χ = -90.0°; and ω = -19.0 to 23.0°, χ = -90.0°) using 0.50° oscillations with 77.0 and 12.0 second exposures for **2** and **3** respectively. Data were collected and processed using the d*TREK program (Molecular Structure Corporation). The structure of **2** was solved using heavy-atom Patterson methods[34] while that of **3** was solved using direct methods;[35] both were expanded using Fourier techniques.[36] The nonhydrogen atoms were refined anisotropically. Hydrogen atoms were included but not refined. All calculations were performed using the teXsan crystallographic software package (Molecular Structure Corporation). ORTEP representations of the solid-state molecular structures of **2** and **3** were prepared using Ortep-3 for Windows.[37]

References begin on page 151.

Complex **2** crystallizes in the orthorhombic space group $Pna2_1$ with two salt moieties, related by a pseudo-inversion centre, in the asymmetric unit. This pseudo-inversion centre is located at 0.8756 0.0228 0.8735, or roughly x = 7/8, y = 0. The existence of pseudo-centres in non-centrosymmetric structures has been studied in detail by Marsh *et al.*[38] and usually results in large correlations between refined parameters of each crystallographically independent moiety. In order to obtain reasonable anisotropic displacement parameters, refinements were carried out using restraints that called for equivalent anisotropic displacement parameters for pairs of atoms related by the pseudo-inversion centre.

Complex **3** crystallizes in the non-centrosymmetric orthorhombic space group $P2_12_12_1$. A parallel refinement was carried out on both enantiomers. The enantiomer reported herein was assigned on the basis of the better final residual values.

References begin on page 151.

4.10 References

(1) Rogers, C. W.; Wolf, M. O. *Chem. Commun.* **1999**, 2297.

(2) Maercker, A. *Angew. Chem., Int. Ed. Engl.* **1987**, *26*, 972.

(3) Lin, Y.-S.; Yamamoto, A. *Activation of C-O Bonds: Stoichiometric and Catalytic Reactions* in *Activation of Unreactive Bonds and Organic Synthesis*; Murai, S., Ed.; Springer-Verlag: Berlin, 1999; Vol. 3, p. 161.

(4) Van der Boom, M. E.; Liou, S.-Y.; Ben-David, Y.; Shimon, L. J. W.; Milstein, D. *J. Am. Chem. Soc.* **1998**, *120*, 6531.

(5) Montanari, F.; Casella, L. *Metalloporphyrins Catalyzed Oxidations*; Kluwer Academic: Dordrecht, 1994.

(6) Matsuhashi, H.; Nakamura, H.; Arata, K.; Yoshida, R.; Maekawa, Y. *Fuel* **1997**, *76*, 913.

(7) Weinstock, I. A.; Atalla, R. H.; Reiner, R. S.; Houtman, C. J.; Hill, C. L. *Holzforschung* **1998**, *52*, 304.

(8) Weinstock, I. A.; Hammel, K. E.; Moen, M. A.; Landucci, L. L.; Ralph, S.; Sullivan, C. E.; Reiner, R. S. *Holzforschung* **1998**, *52*, 311.

(9) Bader, A.; Lindner, E. *Coord. Chem. Rev.* **1991**, *108*, 27.

(10) Slone, C. S.; Weinberger, D. A.; Mirkin, C. A. *Prog. Inorg. Chem.* **1999**, *48*, 233.

(11) Sun, J.-S.; Uzelmeier, C. E.; Ward, D. L.; Dunbar, K. R. *Polyhedron* **1998**, *17*, 2049.

(12) Dunbar, K. R.; Sun, J.-S.; Haefner, S. C.; Matonic, J. H. *Organometallics* **1994**, 2713.

(13) Rahman, M. M.; Liu, H. Y.; Prock, A.; Giering, W. P. *Organometallics* **1987**, *6*, 650.

(14) Yamamoto, Y.; Sato, R.; Matsuo, F.; Sudoh, C.; Igoshi, T. *Inorg. Chem.* **1996**, *35*, 2329.

References begin on page 151.

(15) Yamamoto, Y.; Sato, R.; Ohshima, M.; Matsuo, F.; Sudoh, C. *J. Organomet. Chem.* **1995**, *489*, C68.

(16) Han, X.-H.; Yamamoto, Y. *J. Organomet. Chem.* **1998**, *561*, 157.

(17) Kurosawa, H.; Tsuboi, A.; Kawasaki, Y.; Wada, M. *Bull. Chem. Soc. Jpn.* **1987**, *60*, 3563.

(18) Chen, S. J.; Dunbar, K. R. *Inorg. Chem.* **1991**, *30*, 2018.

(19) Haefner, S. C.; Dunbar, K. R.; Bender, C. *J. Am. Chem. Soc.* **1991**, *113*, 9540.

(20) Dunbar, K. R.; Matonic, J. H.; Saharan, V. P. *Inorg. Chem.* **1994**, *33*, 25.

(21) Dunbar, K. R. *Inorg. Chim. Acta* **1995**, *240*, 527.

(22) Jones, C. E.; Shaw, B. L.; Turtle, B. L. *J. Chem. Soc., Dalton Trans.* **1974**, 992.

(23) Rogers, C. W.; Patrick, B. O.; Rettig, S. J.; Wolf, M. O. *J. Chem. Soc., Dalton Trans.* **2001**, 1278.

(24) Jeffrey, J. C.; Rauchfuss, T. B. *Inorg. Chem.* **1979**, *18*, 2658.

(25) Lindner, E.; Scheytt, C.; Wegner, P. *Chem. Ber.* **1987**, *120*, 1621.

(26) Lindner, E.; Pautz, S.; Haustein, M. *Coord. Chem. Rev.* **1996**, *155*, 145.

(27) Bard, A. J.; Faulkner, L. R. *Electrochemical Methods: Fundamentals and Applications*; Wiley: New York, 1980.

(28) Lever, A. B. P. *Inorg. Chem.* **1990**, *29*, 1271.

(29) Sullivan, B. P.; Salmon, D. J.; Meyer, T. J. *Inorg. Chem.* **1978**, *17*, 3334.

(30) Tolman, C. A. *Chem. Rev.* **1977**, *77*, 313.

(31) Golovin, M. N.; Rahman, M. M.; Belmonte, J. E.; Giering, W. P. *Organometallics* **1985**, *4*, 1981.

References begin on page 151.

(32) Horner, L.; Simons, G. *Phosph. Sulf.* **1983**, *14*, 189.

(33) Lindner, E.; Meyer, S.; Wegner, P.; Karle, B.; Sickinger, A.; Steger, B. *J. Organomet. Chem.* **1987**, *335*, 59.

(34) Beurskens, P. T.; Admiraal, G.; Beurskens, G.; Bosman, W. P.; Garcia-Granda, S.; Gould, R. O.; Smits, J. M. M.; Smykalla, C. "The DIRDIF program system, Technical Report of the Crystallography Laboratory," University of Nijmegen, 1992.

(35) Altomare, A.; Burla, M. C.; Cammalli, G.; Cascarano, M.; Giacovazzo, C.; Guagliardi, A.; Moliterni, A. G. G.; Polidori, G.; Spagna, A. *J. Appl. Cryst.* **1999**, *32*, 115.

(36) Beurskens, P. T.; Admiraal, G.; Beurskens, G.; Bosman, W. P.; deGelder, R.; Israel, R.; Smits, J. M. M. "The DIRDIF-94 program system, Technical Report of the Crystallography Laboratory," University of Nijmegen, 1994.

(37) Farrugia, L. J. *J. Appl. Cryst.* **1997**, *30*, 565.

(38) Marsh, R. E.; Schomaker, V.; Herbstein, F. H. *Acta Cryst.* **1998**, *B54*, 921.

References begin on page 151.

Appendix 4.1 Crystallographic details

The crystallographic data for complexes **2** and **3** have been deposited into the CCDC archives (reference numbers: 153810 and 153811). The data can be accessed in CIF and other electronic formats on the world wide web through the Royal Society of Chemistry website (supplement to ref 23): http://www.rsc.org/suppdata/dt/b0/b0089311.

Table A.4.1. Crystallographic data, collection and refinement details for **2** and **3**

	2	**3**
Formula	$C_{40}H_{35}F_{12}N_4OP_3Ru$	$C_{35}H_{33}F_{12}N_4OP_3Ru$
M	1009.71	947.64
μ / cm^{-1}	5.77	6.41
T / K	173 ± 1	173 ± 1
Colour, habit	orange, needle	red, prism
Crystal system	orthorhombic	orthorhombic
Space group	$Pna2_1$ (No. 33)	$P2_12_12_1$ (No. 19)
a / Å	29.844(1)	13.2591(4)
b / Å	10.7577(6)	14.2123(5)
c / Å	26.255(1)	19.930(1)
β / deg	90	90
V / $Å^3$	8429(1)	3755.7(2)
ρ / $g{\cdot}cm^{-3}$	1.591	1.676
Z	8	4
Refl. collected/unique/R_{int}	35277/12548/ 0.115	32001/8135/0.059
R_1	0.055[b]	0.048[a]
wR_2[c]	0.118	0.119
GOF	0.92	1.34

[a] $I > 3\sigma(I)$. [b] $I > 2\sigma(I)$. [c] all data. $R_1 = \Sigma \big| |F_o| - |F_c| \big| / \Sigma |F_o|$ (observed data). $wR_2 = (\Sigma(F_o^2 - F_c^2)^2 / \Sigma w(F_o^2)^2)^{½}$ (all data).

References begin on page 151.

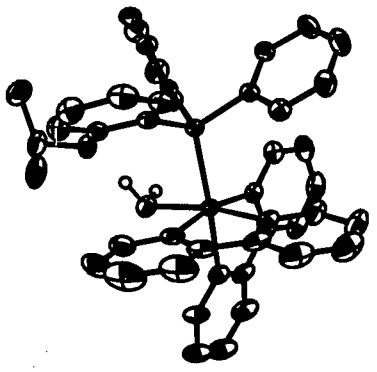

Chapter Five

Enhanced lability of phosphine-ether ligands in Ru(II) bis(bipyridyl) complexes

5.1 The potential for tunable small-molecule sensors

In the context of small-molecule chemosensing, the possibility of tuning both the sensitivity of the sensory material and its specificity for different analytes has distinct appeal. With sensors based on metal complexes with hemilabile phosphine-ether ligands, it is immediately evident that the ability of the labile ether moiety to coordinate to the metal may be influenced by the substituents on the oxygen atom. Substituents with high steric demand may encourage dissociation of the labile donor, particularly in the presence of small Lewis basic molecules with little steric encumbrance. This would lead to large binding constants. Since more of the sensory complex would be analyte-bound at lower analyte concentrations, this translates into higher sensitivity toward coordinating analytes.

References begin on page 178.

Indeed, variations in the ether moiety in complexes of the type $RuCl_2(POR)_2$ clearly lead to differences in the reactivity of the complexes.[1] Lindner and co-workers have studied a series of POR ligands with both acyclic alkyl ethers and cyclic ethers of varying ring size.[2,3] The reactivity of these complexes correlates with the nucleophilicity of the ether oxygen atom and is influenced by both sterics (ring size) and electronics (the number of oxygen atoms in the ring). Complexes containing strongly nucleophilic ethers (*i.e.*, POR ligands with small cyclic ether moieties, *e.g.*, (oxetane-2-ylmethyl)diphenylphosphine) are less reactive toward nucleophilic small molecules than complexes with less nucleophilic large-ring ethers (*e.g.*, POR = (1,3-dioxoctane-2-ylmethyl)diphenylphosphine). Thus, modification of the ether substituent in POR ligands has well-established precedent as a means of tuning the reactivity of Ru(II) *P,O*-complexes.

Furthermore, changes in the electronic demand of the ether substituents may be expected to influence the reactivity of the complex in a similar manner. Electron withdrawal or electron donation by substituents would influence the electron density available for donation from the ether oxygen to the metal. Moreover, even upon displacement of the ether from the metal centre, its substituents may inductively affect the electron density at the metal centre. In addition, it should be noted that in the $[cis\text{-}Ru(bpy)_2(POR)]^{2+}$ system under study in this work variations could also be made to the chromophoric ligands. Introduction of substituents onto the bpy rings is known to mildly influence the reduction potential of the metal.[4] Thus, electronic factors may influence which types of small molecules are coordinated by the metal. For example, a dramatic increase in the electron-richness of the metal may invite coordination of π-acidic molecules, whereas only strong σ-donors may coordinate if the metal's electron density is extremely low. Although past work in the Wolf laboratory has involved the incorporation of substituents into the chromophoric ligands,[5] this thesis deals only with modification of the hemilabile ligands.

5.1.1 $[cis\text{-}Ru(bpy)_2(POR)]^{2+}$ complexes with modified POR ligands

With the goal of tuning the sensitivity and selectivity of $[cis\text{-}Ru(bpy)_2(POR)]^{2+}$ sensor complexes in mind, a set of phosphine-ethers closely related to the POMe ligand in **1** were

References begin on page 178.

chosen for study. The ligands studied in this chapter are depicted below and differ from POMe only in the substituent on the ether moiety: POEt, introduced in Chapter Four; 2-(2-propoxy)phenyldiphenylphosphine (abbreviated here as PO^{i}Pr); and 2-trifluoromethoxy-phenyldiphenylphosphine (denoted $POCF_3$). On steric grounds, replacement of the methyl group in POMe by an ethyl group would be expected to lead to a small increase in ether lability, whereas introduction of the bulky isopropyl group would induce more dramatic increases in ether displacement by small molecules. Similarly, the strongly electron-withdrawing CF_3 group was predicted to significantly weaken the Ru-O coordination.

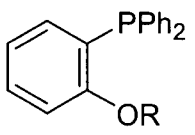

POMe: R = CH_3
POEt: R = CH_2CH_3
PO^{i}Pr: R = $CH(CH_3)_2$
$POCF_3$: R = CF_3

In this chapter, [*cis*-Ru(bpy)$_2$(POR)]$^{2+}$ complexes containing the above P,O-ligands are described, in terms of their preparation, reactivity and photophysical properties. The predicted trends in the enhancement of the lability of the metal-bound ether moieties were indeed observed. The chapter concludes with a discussion of the set of phosphine-ether complexes and a comparison of their reactivities to the parent POMe complex **1**.

5.2 Complexes of the ethyl ether ligand, POEt

The synthesis and characterization of [*cis*-Ru(bpy)$_2$(POEt)](PF$_6$)$_2$, complex **2**, are described in Chapter Four. Even though the structural differences between the POMe complex **1** and POEt complex **2** are small, the two complexes show distinctly different susceptibility to dealkylation by phosphine nucleophiles, as discussed in Chapter Four. This difference in reactivity is not limited to **2** being less prone to dealkylation, however. In the following sections, the ability of **2** to coordinate small molecules that are known to react with **1** is described. In addition, the photophysical response of **2** to these small molecules is presented and compared to complex **1**.

References begin on page 178.

5.2.1 Reactivity of 2 toward small molecules

Just as described for **1** in Chapter Two (section 2.6.4), reactivity trials were performed on NMR-scale samples of **2**, and the formation of new analyte-bound species was monitored by $^{31}P\{^{1}H\}$ and ^{1}H NMR spectroscopy. In general, complex **2** exhibits the same patterns of reactivity toward small molecules as complex **1**. The differences between **1** and **2** are manifested as differences in the magnitudes of the effective equilibrium constants (K_{eff}) for the reactions with these small molecules. Because the behaviour of **2** is so similar to that of **1**, detailed descriptions of the reactions are not presented here; brief descriptions are included in the experimental section. The characteristic NMR spectroscopic data and the corresponding values of K_{eff} are summarized in Table 5.1.

Table 5.1. Summary of NMR spectroscopic data for **2** and analyte-bound **2**, and comparison to **1**

Analyte	^{1}H NMR, OCH_2CH_3 δ(ppm)[a]	$^{31}P\{^{1}H\}$ NMR, δ(ppm)[a]	K_{eff}[a,b] for **2**	K_{eff}[a,b] for **1**
—	0.70	51.2	—	—
MeCN	0.43	38.7	> 360[c]	> 360[c]
Et_3N	obscured	40.1	< 0.005	5 ± 1
Me_2S	0.60	31.4	15 ± 3	1.7 ± 0.3
EtSH	0.52	36.6	0.9 ± 0.2	0.11 ± 0.02
DMSO	0.32[d]	39.7[d]	0.09 ± 0.01[d]	0.016 ± 0.002[d]
	0.54[e]	28.2[e]	0.0042 ± 0.0007[e]	0.0006 ± 0.0001[e]

[a]10^{-2} M in CD_2Cl_2 solution. [b]> 3 hour equilibration time. [c]No unreacted **1** remained. [d]Major product. [e]Minor product. [d,e]Pseudo-equilibrium constants calculated as if the two products formed independently of each other.

References begin on page 178.

Complex **2** tends to show higher affinity for sulfur-donor analytes than complex **1**. There is an ~ 8-fold difference in the magnitude of K_{eff} for the reactions of **1** and **2** with EtSH and Me_2S. This may be reconciled by consideration of the steric demand of the analyte species in comparison to the space available in the vicinity of the metal centre. There is more congestion near the metal in the ethyl ether complex **2** than in **1**, so the higher steric demand of the ethyl-substituted thiol relative to the methyl-substituted compounds Me_2S and DMSO results in complex **2** discriminating between these analytes. As well, compared to **1**, the ethyl ether complex **2** shows a considerably lower affinity for NEt_3, which further supports this steric argument. These observed sensitivities to sterics are, however, consistent with both mechanisms proposed in Chapter Two for the reaction of these phosphine-ether complexes with coordinating small molecules. The increased size of the ether's alkyl chain in **2** restricts the ability of larger analyte species to approach the metal centre and therefore leads to lower affinity for these analytes. Although it is conceivable that the slight decrease in electron density at the metal centre ($E_{ox}(Ru^{III/II})$ = 1.59 V for **2**; 1.56 V for **1**) in **2** relative to **1** is responsible for the enhanced affinity of **2** for the smaller electron-rich sulfur donors, this difference is so small that it is unlikely to be the dominant factor. Steric effects are probably the most influential in determining the relative magnitude of K_{eff} when the methyl and ethyl ether complexes **1** and **2** are compared. The observed differences in analyte affinity suggest that sensor complexes can be designed to react specifically with certain analytes and may be used to distinguish analytes with closely related structures.

As expected, the modification of the ether substituent in the P,O-ligand served only to alter the reactivity of the complex; the change had no significant effect on the photophysical properties of the lumophore. As for complex **1**, changes in both the complex's colour and its low-temperature photoluminescence properties are observed when **2** reacts with coordinating small molecules. Both in the absence and presence of analytes, the absorption and emission spectra are qualitatively similar to those of complex **1**. For this reason, the spectra are not shown here, nor are the MLCT absorption and 0–0 emission energies predicted from the redox gap since they are the same as for **1** (presented in Table 3.6). The relevant spectral data are summarized in Table 5.2.

References begin on page 178.

Table 5.2. Summary of photophysical data for **2** in the absence and presence of small-molecule analytes

Analyte	Absorption[a] λ_{max} / nm (ε / $M^{-1}cm^{-1}$)	Solution colour	Emission[d] λ_{max} / nm	Emission colour
____	412 (7000)	orange	598	orange
CH_3CN	410 (7060)[b]	yellow	545, 581	bright yellow
Et_3N	416 (6000)[b,c]	red-brown	608 sh, 643	red
Me_2S	410 (6200)[b,c]	olive	ND	ND
EtSH	408 (6200)[b,c]	olive	ND	ND
$C_{12}H_{25}SH$	410 (6300)[b,c]	olive	544, 596, 632 sh	dirty yellow
DMSO	434 (5800)[b,c]	red-orange	645	poppy red

ND = not determined. [a]In acetone solution at RT, [**2**] ≈ 2×10^{-4} M. [b]Upon addition of 100 equivalents of analyte ≈ [L] = 2×10^{-2} M, 5 minute equilibration time. [c]Pseudo-ε (more than one complex present) intended to show relative intensity of absorption band. [d]In 2:1 ethanol/acetone solid solution, [**2**] ≈ 6×10^{-3} M, with 100 equivalents of analyte ≈ [L] = 6×10^{-1} M, measured at 77 K in 2 mm I.D. quartz capillary cell, λ_{ex} = 455 nm.

5.3 Complexes of the isopropyl ether ligand, PO^{i}Pr

5.3.1 Preparation and reactivity of PO^{i}Pr complexes

Typically, bidentate *P,O*-bound phosphine-ether complexes (*e.g.*, **1-3**) are easily prepared in pure form via the reaction of the phosphine-ether with the solvate complex [*cis*-$Ru(bpy)_2(acetone)_2](BF_4)_2$ followed by metathesis to the hexafluorophosphate salt.[6,7] Using the analogous isopropyl-substituted phosphine-ether (PO^{i}Pr), however, this synthetic procedure gave a mixture comprised of three major products, as determined by $^{31}P\{^1H\}$ NMR spectroscopy. In CD_2Cl_2 solution, the $^{31}P\{^1H\}$ NMR spectrum of the material as it was isolated from a typical reaction mixture contained singlets at δ 50.7, 40.9 and 36.9 in a ~ 7:5:1 ratio. The spectrum also contained a septet at δ -144 due to the PF_6^- counterions and a small

References begin on page 178.

singlet at δ 29.9 due to an unidentified impurity. The singlet at δ 50.7 was assigned as the chelate complex [*cis*-Ru(bpy)$_2$(PO^{i}Pr-*P,O*)](PF$_6$)$_2$ (**6**) based on comparison to the chemical shift of **1** (δ 50.9). The other two major components were assigned by addition of water and acetone to the NMR samples, which resulted in changes in the spectra. Addition of water caused an increase in the peak at δ 40.9, which suggests that this resonance is due to the complex [*cis*-Ru(bpy)$_2$(PO^{i}Pr-*P*)(OH$_2$)](PF$_6$)$_2$ (**6•OH$_2$**) in which water is coordinated to the metal. Addition of acetone resulted in an increase in the resonance at δ 36.9, which was then assigned as the acetone complex [*cis*-Ru(bpy)$_2$(PO^{i}Pr-*P*)(O=C(CH$_3$)$_2$)](PF$_6$)$_2$ (**6•O=C(CH$_3$)$_2$**). Both of these experiments also led to a decrease in the intensity of the resonance at δ 50.7.

Consistent with these spiking experiments, the ^{31}P{^{1}H} NMR spectrum of the mixture of isopropyl ether complexes was found to be highly solvent dependent. At 10^{-2} M in CD_2Cl_2, resonances corresponding to the *P,O*-complex **6**, aquo complex **6•OH$_2$** and acetone complex **6•O=C(CH$_3$)$_2$** were all present, as described above. In acetone-d_6 solution, the resonance due to **6** was greatly diminished because of formation of **6•O=C(CD$_3$)$_2$**. Under the conditions used in this work for low-temperature photophysical studies of the [*cis*-Ru(bpy)$_2$(POR)](PF$_6$)$_2$ complexes (*i.e.*, 10^{-3} M in 2:1 ethanol/acetone-d_6 solution), the *P,O*-complex **6** was absent. In this solvent, the resonances due to the aquo complex **6•OH$_2$** (δ 39.2) and acetone complex **6•O=C(CD$_3$)$_2$** (δ 38.0) were present, as was an additional resonance (δ 37.5) that was likely due to an ethanol complex. Upon addition of 5 % (v/v) H_2O, the resonance at δ 37.5 disappeared, and the intensity of the resonance due to the aquo complex **6•OH$_2$** increased relative to that of **6•O=C(CD$_3$)$_2$**.

From these results, it is clear that the isopropyl ether complex is considerably more reactive toward oxygen-containing small molecules than the other phosphine-ether complexes studied so far in this work. As expected, the mixture of complexes also reacted with MeCN to yield a single complex, which based on its ^{31}P{^{1}H} NMR spectrum (δ 40.1, s, in CD_3CN) appears to be analogous to **1•MeCN** (δ 41.1, s, in CD_3CN). Furthermore, preliminary experiments showed that the mixture is also reactive toward SO_2, CO and DMSO, but the reactions led to multiple products. However, detailed investigations into the reactivity of the

References begin on page 178.

isopropyl derivative were not conducted because of the fact that the pure *P,O*-complex **6** was not available.

Attempts were made to remove water and acetone from the mixture in order to obtain pure *P,O*-complex **6**. Heating the solid *in vacuo* over P_2O_5 at 60 °C for 3 weeks resulted in only a slight improvement in the relative amount of **6** present. Heating the solid to higher temperatures to drive off water and acetone resulted in gradual decomposition. Crystallization and chromatographic techniques also did not effect bulk separation of the three complexes. Modified synthetic routes using anhydrous $Ru(bpy)_2Cl_2$ as a starting material and employing rigorously dried solvents (acetone, THF) were also unsuccessful. Attempts to use $Ru(bpy)_2(OTf)_2$ as a starting material led to very sluggish reactions and did not give the desired products. Finally, attempts were made to access **6** via removal of metal-bound analytes from purified **6•L** complexes, but for example, even after drying **6•MeCN** in vacuo at 80 °C overnight, there was no evidence for generation of the bidentate *P,O*-complex. Over all, bulk preparation of pure *P,O*-complex **6** was not achieved.

5.3.2 Structural characterization of 6•OH_2

Crystallization of the complex mixture via slow evaporation of a solution in CH_2Cl_2/hexanes, although not useful for the bulk separation of the complexes, did yield some high quality crystals. A single crystal picked from the crystallized mixture was structurally characterized by X-ray crystallographic analysis and determined to be the aquo complex **6•OH_2**. The crystallographic data are summarized in Appendix 5.1 (Tables A.5.1 and A.5.3), and selected interatomic distances and bond angles are listed in Table 5.3. An ORTEP representation of the solid-state molecular structure of **6•OH_2** is depicted in Figure 5.1.

References begin on page 178.

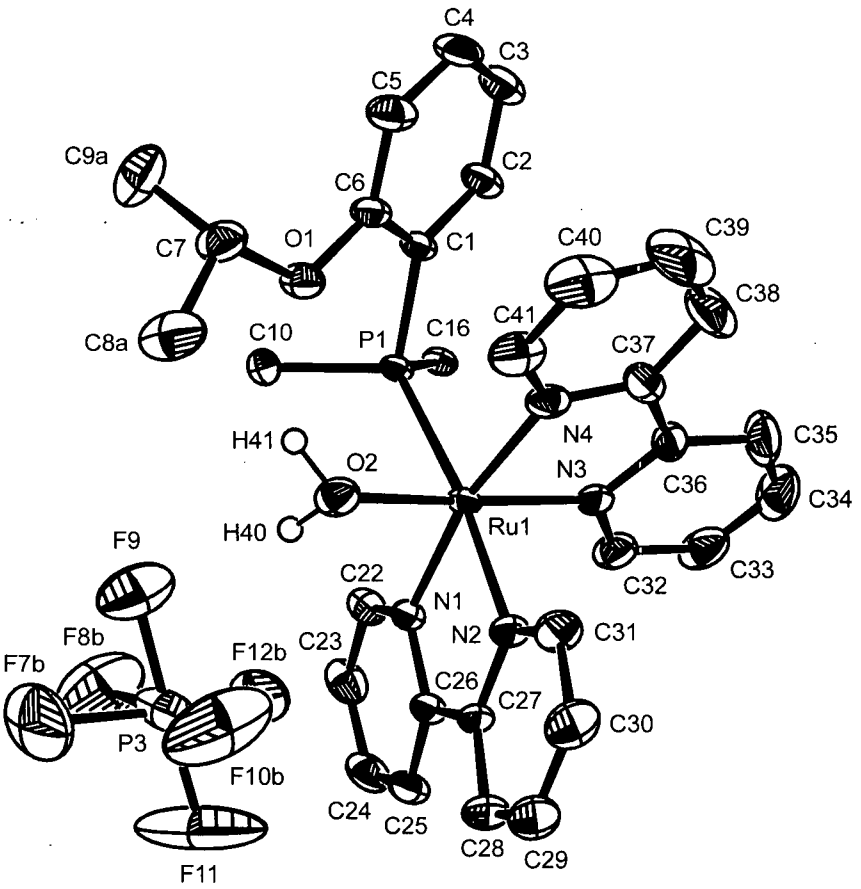

Figure 5.1. ORTEP representation of the solid-state molecular structure of **6•OH$_2$**. Hydrogen atoms, the ring carbons of two of the phenyl rings (C11 – C15; C17 – C21), one of the PF_6^- counterions and the cocrystallized solvent molecule are omitted for clarity. H(40) and H(41) were located but not refined.

The geometry about the Ru(II) centre in **6•OH$_2$** is distorted octahedral with one of the coordination sites occupied by a water molecule. The coordinated water molecule is engaged in intramolecular hydrogen bonding, with interactions both between H(41) and the isopropyl ether oxygen atom, and between H(40) and the fluorines of one of the disordered hexafluorophosphate anions. The Ru-O distance (2.138(2) Å) is similar to that found in other Ru(II) aquo complexes (Ru-O = 2.122(16) Å in $[Ru(OH_2)_6]^{2+}$;[8] Ru-O = 2.15 Å in [*cis*-$RuH(OH_2)(CO)_2(PPh_3)_2]^+$[9]). The Ru-N bond lengths are typical of those observed in related

References begin on page 178.

dicationic Ru(II) bipyridyl phosphine-ether complexes **1-3**.[7] The Ru-P distance (2.3401(8) Å) is significantly longer than in these related phosphine-ether complexes (Ru-P = 2.2908(6) Å in **1**), but is similar to that observed in an analogous [*cis*-Ru(bpy)$_2$(POR-*P*)L]$^{2+}$ complex (R = CF_3, L = CH_3CN; Ru-P = 2.3561(8) Å) discussed later in this chapter.

Table 5.3. Selected interatomic distances and bond angles for **6•OH$_2$**

		Distances (Å)	
Ru(1)-O(2)	2.138(2)	Ru(1)-P(1)	2.3401(8)
Ru(1)-N(1)	2.096(3)	Ru(1)-N(2)	2.115(3)
Ru(1)-N(3)	2.032(3)	Ru(1)-N(4)	2.060(3)
F(8a)[a]-H(40)	2.12(6)	F(12b)[a]-H(40)	2.24(6)
O(1)-H(41)	2.07(5)		
		Angles (°)	
P(1)-Ru(1)-O(2)	90.06(7)	P(1)-Ru(1)-N(1)	99.10(8)
P(1)-Ru(1)-N(3)	95.40(8)	P(1)-Ru(1)-N(4)	90.67(8)
O(2)-Ru(1)-N(1)	95.3(1)	O(2)-Ru(1)-N(2)	83.7(1)
O(2)-Ru(1)-N(4)	91.0(1)	N(1)-Ru(1)-N(2)	78.0(1)
N(1)-Ru(1)-N(3)	93.2(1)	N(2)-Ru(1)-N(3)	91.3(1)

[a]F(8a) and F(12b) are part of a disordered PF_6 group.

5.3.3 Visible absorption studies of the PO^{i}Pr complexes

Because the complexes were not available in pure form, their photophysical properties were not studied in detail. However, the mixture of isopropyl derivatives (**6**, **6•OH$_2$**, **6•O=C(CH$_3$)$_2$**) as prepared shows visible absorption behaviour similar to **1** (see Chapter Three). In CH_2Cl_2 solution, spectra measured at high and low concentrations are essentially superimposable (λ_{max} = 419 – 420 nm). In dry 2:1 ethanol/acetone solution, low-concentration samples (10^{-5} M, λ_{max} = 454 nm) show red-shifted spectra relative to high-concentration

References begin on page 178.

samples (10^{-3} M, λ_{max} = 434 nm). At the high-concentration limit, the absorption band is at lower energy than for complex **1** because even in anhydrous solvents, **2** contains *P,O*-complex **6**, aquo complex **6•OH$_2$**, acetone complex **6•O=C(CH$_3$)$_2$** and ethanol complex **6•EtOH**. The addition of 5 % (v/v) water to these solutions has a negligible effect on the spectra, likely due to the complex equilibria involving acetone, ethanol and water in competition for reaction with the *P,O*-coordinated complex. In combination with the crystallographic characterization of the aquo complex **6•OH$_2$**, the similarities between the solvent-dependent absorption properties of **6** and those of **1** were helpful in establishing the fact that **1** reacts with water (see Chapter Two, section 2.4.2.1 and Chapter Three, section 3.4.1).

5.4 Complexes of the trifluoromethyl ether ligand, POCF$_3$

5.4.1 The trifluoromethyl ether ligand, POCF$_3$

This compound was synthesized from commercially available starting materials via the simple route shown in Scheme 5.1. The phosphine-ether was isolated in analytically pure form as a faintly yellow-tinged viscous oil in ~ 60 % yield after purification via column chromatography followed by distillation. The oil slowly solidified under a stream of nitrogen gas to yield a waxy white solid (m.p. 29 – 31 °C). This phosphine is more susceptible to oxidation by air than the other phosphine-ethers used in this work. The material must be stored under nitrogen, but any phosphine oxide that does form can be removed easily by column chromatography on silica gel (POCF$_3$ elutes with ether; oxide stays on the support and can be eluted with MeOH). The oxide has also been prepared and characterized, and the details are included in the experimental section for comparison.

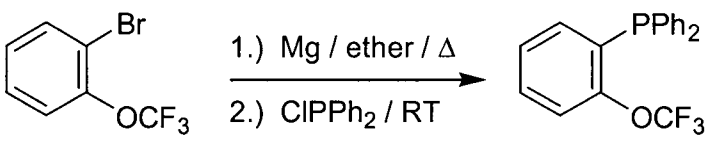

Scheme 5.1.

References begin on page 178.

Curiously, $POCF_3$ is highly luminescent as isolated from the synthetic route described above. The material luminesces strongly both in neat form (solid and oil) and in solution; in fact, blue emission is still noticeable by eye in concentrations as low as ~ 10^{-5} M in a number of different solvents. Thus, it is convenient to monitor the chromatographic purification of this compound by illuminating the column and TLC plates with a hand-held UV lamp (466 nm), as the band containing $POCF_3$ exhibits intense blue luminescence. This luminescence is intriguing because the emission that is spectroscopically observed from triphenylphosphine derivatives when excited by UV light is typically so weak that it is not readily apparent by eye.[10,11] At the present time, however, it has not been definitively established that the luminescence from $POCF_3$ arises from the phosphine itself rather than from a trace amount of an intensely luminescent impurity that has so far eluded detection. Further investigations into the photophysical properties of $POCF_3$ are currently underway in the Wolf laboratory. The absorption and emission spectra available from preliminary studies have therefore not been included here.

Interestingly, $POCF_3$ also exhibits another striking spectroscopic trait. NMR spectra reveal that the phosphorus and fluorine nuclei are scalar coupled to one another even though they are separated by five bonds. The P-F coupling constant is large enough that the $^{31}P\{^1H\}$ resonance appears as a well-resolved quartet ($^5J_{PF}$ = 7.8 Hz), and the $^{19}F\{^1H\}$ resonance appears as a doublet. Long-range scalar coupling between ^{31}P and ^{19}F nuclei is often observed over extended π-systems or between nuclei that are close in space.[12] This coupling constant is of the same order of magnitude as that observed for 4-fluorophenylphosphine ($^5J_{PF}$ = 3.1 Hz).[13]

5.4.2 Reaction of $POCF_3$ with [*cis*-$Ru(bpy)_2(acetone)_2]^{2+}$

As for the isopropyl ether ligand, the trifluoromethyl-substituted ether ligand did not lead exclusively to the desired *P,O*-chelate complex when reacted with [*cis*-$Ru(bpy)_2(acetone)_2](BF_4)_2$. A brownish-yellow powder was obtained that was determined to be a mixture when analyzed by NMR spectroscopy (CD_2Cl_2: $^{31}P\{^1H\}$ δ41.4 major component, 40.5, 39.9; $^{19}F\{^1H\}\delta$20.0 major component, 19.0, 18.4). None of the $^{31}P\{^1H\}$ resonances is

References begin on page 178.

comparable to the singlet at $\delta \sim 51$ typically observed for [*cis*-Ru(bpy)$_2$(POR-*P,O*)]$^{2+}$ complexes. This suggests that the *P,O*-chelate complex (**7**) is not formed at all with $POCF_3$, although it is possible that the electronically demanding CF_3 group simply causes the ligand-based ^{31}P resonance for **7** to shift considerably. Furthermore, unlike for the PO^{i}Pr case, spiking experiments did not permit unambiguous assignment of these resonances as those arising from the bidentate, aquo or acetone complexes. In addition, treatment of this mixture with acetonitrile did not lead to quantitative conversion to the MeCN complex; two species in an estimated ratio of ~ 2:1 were evident upon examination of the NMR spectra (CD_3CN: $^{31}P\{^1H\}$ δ42.4 major, 40.7 minor; $^{19}F\{^1H\}\delta$20.4 major, 20.2 minor). Thus, the $POCF_3$ ligand does not lead to complexes that exhibit behaviour directly analogous to the other phosphine-ether complexes studied in this thesis. Nonetheless, it was concluded from these results that the introduction of the strongly electron-withdrawing CF_3 substituent into the ether moiety leads to enhanced lability of the ether, as expected. Considering that the goal of this work was to compare the *P,O*-chelate complexes, $POCF_3$ was not investigated further as a hemilabile ligand.

5.4.3 Structural characterization of 7•MeCN-d_3

Although two species were present in samples of the crude mixture of $POCF_3$-derived complexes dissolved in acetonitrile, slow evaporation of an acetonitrile-d_3 solution produced crystals suitable for crystallographic analysis. A suitable single crystal was structurally characterized by X-ray crystallography and determined to be the acetonitrile complex, [*cis*-Ru(bpy)$_2$(POCF$_3$-*P*)(CD$_3$CN)](PF$_6$)$_2$, **7•MeCN-d_3**. The crystallographic data are summarized in Appendix 5.1 (Tables A.5.2 and A.5.4), and selected interatomic distances and bond angles are listed in Table 5.4. An ORTEP representation of the solid-state molecular structure is depicted in Figure 5.2.

This molecular structure determination provided confirmation of the $POCF_3$ ligand's connectivity, which had been in question because of its unusual spectroscopic properties. However, the complex clearly contains a triphenylphosphine derivative with an *ortho*-positioned trifluoromethoxy substituent, as expected. In the solid-state molecular structure of

References begin on page 178.

7•MeCN-d_3, the $POCF_3$ ligand is bound to the Ru centre via the phosphorus atom, and the ether moiety is aimed well away from the metal. The geometry of the complex is distorted octahedral, with one coordination site occupied by a molecule of CD_3CN. The metal-nitrogen and metal-phosphorus distances are similar to those determined for the isopropyl derivative's aquo complex. The complex crystallized in an irregular habit with one molecule of uncoordinated acetonitrile-d_3 in the asymmetric unit. In summary, there are no unusual features in the molecule's structure. The complex was not characterized further.

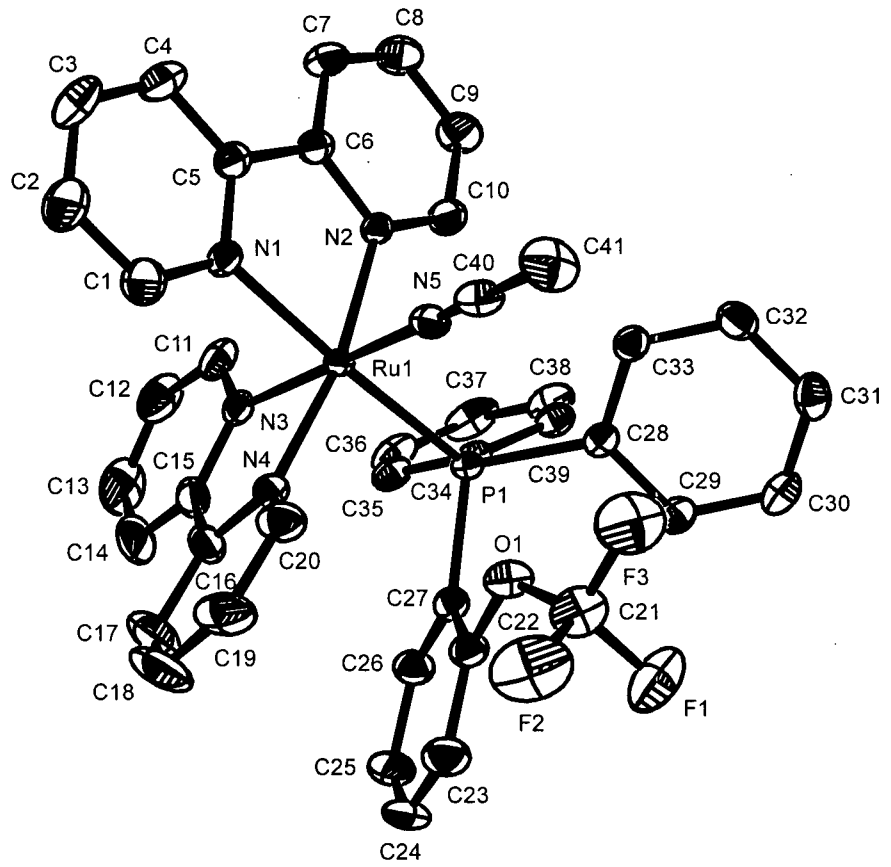

Figure 5.2. ORTEP representation of the solid-state molecular structure of **7•MeCN-d_3**. Hydrogen atoms, hexafluorophosphate counterions and the cocrystallized solvent molecule are omitted for clarity.

References begin on page 178.

Table 5.4. Selected interatomic distances and bond angles for **7**•**MeCN-d_3**

		Distances (Å)	
Ru(1)-N(1)	2.099(3)	Ru(1)-N(2)	2.095(2)
Ru(1)-N(3)	2.063(3)	Ru(1)-N(4)	2.064(3)
Ru(1)-N(5)	2.034(3)	Ru(1)-P(1)	2.3561(8)
		Angles (°)	
P(1)-Ru(1)-N(2)	98.10(7)	P(1)-Ru(1)-N(3)	91.95(8)
P(1)-Ru(1)-N(4)	91.00(8)	P(1)-Ru(1)-N(5)	92.82(8)
N(1)-Ru(1)-N(2)	78.2(1)	N(1)-Ru(1)-N(3)	88.5(1)
N(1)-Ru(1)-N(4)	92.7(1)	N(1)-Ru(1)-N(5)	87.2(1)
N(2)-Ru(1)-N(3)	94.9(1)	N(2)-Ru(1)-N(5)	91.3(1)
N(3)-Ru(1)-N(4)	79.0(1)	N(4)-Ru(1)-N(5)	93.9(1)

5.5 Summary and outlook

The motivation behind the work presented in this chapter was an interest in being able to tune the reactivity of molecule-based chemosensors. Ru(II) bis(bipyridyl) lumophores with hemilabile phosphine-ether ligands are clearly able to coordinate nucleophilic small-molecule analytes, and it was hoped that modification of the substituents on the labile ether moiety might result in complexes with different selectivities and specificities. The methyl and ethyl ether complexes **1** and **2** show very similar abilities to coordinate small molecules, with preference for sulfur-based donors and acetonitrile. The small alkyl substituents on the ether oxygen in these complexes allow the ether group to compete well with ligating small molecules for the coordination site on the metal, which results in rather small binding constants (estimated by K_{eff}). These complexes show extremely low affinities for oxygen donors in general, although **1** was shown in Chapter Two to undergo reaction with water ($K_{eff} = (6 \pm 3) \times 10^{-4}$).

When the steric or electronic demand of the ether substituent is dramatically increased, as in the isopropyl and trifluoromethyl derivatives respectively, the lability of the ether moiety in the corresponding $[cis\text{-Ru(bpy)}_2\text{(POR)}]^{2+}$ complexes is greatly enhanced. In fact, the

References begin on page 178.

labilizing influence of the ^{i}Pr and CF_3 substituents is so marked that isolation of the PO^{i}Pr and $POCF_3$ *P,O*-chelate complexes in pure form has so far not been achieved. These complexes are so much more susceptible to ether displacement than **1** and **2** that the oxygen-containing solvents involved in their synthesis effectively out-compete the ether for the labile coordination site. Furthermore, efforts to purify the bidentate complexes have been unsuccessful.

Although this increased reactivity has limited the present studies of these phosphine-ether complexes to a qualitative glimpse, it is still compatible with the goal of obtaining tunable small-molecule sensors. Chemosensory devices are often based on arrays of sensory materials that each has a slightly different level of response to a given analyte. In such a context, it may not be necessary that each chemosensor complex be fully understood at a molecular level, as long as the array can provide a combined response that acts as a 'signature' for a particular analyte species. Thus, complexes such as **6** and **7** may in fact have some promise for application in molecule-based sensor devices, in conjunction with other more well-defined phosphine-ether complexes such as **1-3**, since they would contribute to the ability of the sensor to detect oxygen-containing analytes such as water. Further studies of the ^{i}Pr complex are being undertaken in the Wolf laboratory because the complex shows potential for use in humidity sensors.

At this point, it is important to note that the phosphine-ether complexes presented thus far in this thesis are rather limited in their practical applicability by factors other than their reactivity. Specifically, all of the complexes discussed thus far only exhibit their photoluminescence response to small-molecule analytes at extremely low temperatures. For this reason, new approaches were sought in an effort to enhance the luminescence properties of the $[cis\text{-}Ru(bpy)_2(L\text{-}L')]^{2+}$ lumophore such that this response would occur at ambient temperature. The final two chapters of this thesis report on approaches to this challenge. In Chapter Six, the phosphine moiety is replaced by a pyridine unit in an attempt to prepare small-molecule responsive $[cis\text{-}Ru(bpy)_2(L\text{-}L')]^{2+}$ lumophores that are emissive at room temperature. In Chapter Seven, a different approach is described that combines hemilabile ligands with a lumophore known to emit at room temperature; ultimately, it was this approach that was successful in achieving the goal of room-temperature luminescent hemilabile ligand-based chemosensors.

References begin on page 178.

5.6 Experimental section

5.6.1 Materials and methods

General experimental procedures and instrumental details are described in Section 2.6.1. $Ru(bpy)_2Cl_2 \cdot 2H_2O$[14] and 2-(2-propoxy)bromobenzene[15] were prepared by literature procedures. 2-Trifluoromethoxybromobenzene was purchased from Alfa Aesar; chlorodiphenylphosphine was purchased from Strem.

5.6.2 Reactions of 2 with small molecules

The reactivity of **2** was investigated using the procedures described in Chapter Two (section 2.6.4). The NMR spectroscopic response of **2** to the addition of small molecules was similar to that of **1**. There was no evidence to suggest that the complexes **2•L** were significantly different from **1•L**. Only the MeCN complex was fully characterized in solution; none of the complexes **2•L** was isolated. Brief descriptions of the reactions investigated are included here. Values of K_{eff}, where determined, are listed in Table 5.1 (p. 157).

5.6.2.1 Reaction of 2 with CO

No immediate visible changes were apparent after solutions of **2** (both in acetone-d_6 and in CD_2Cl_2) were sparged with $CO_{(g)}$. No reaction was evident by NMR spectroscopy after 1 h reaction time. A trace of a new species was evident after 2 days at RT under 1 atm CO in acetone-d_6 solution: $^{31}P\{^1H\}\delta 37.5$; ν_{CO} = 2005 cm^{-1}. The IR spectrum was unaffected by sparging the solution with nitrogen gas. This slow reaction was not pursued further.

5.6.2.2 Reaction of 2 with nitrogen donors

(i) Reaction with MeCN

As for **1•MeCN**, this yellow-orange complex was prepared simply upon treatment of **2** in solution with MeCN. **2•MeCN** was not isolated but was characterized by solution methods. ^1H NMR (400 MHz, 25 °C, CD_3CN): δ 9.01 (d, $^3J_{HH}$ = 5.6 Hz, 1H), 8.71 (d, $^3J_{HH}$ = 5.4 Hz,

References begin on page 178.

1H), 8.52 (d, $^3J_{HH}$ = 8.0 Hz, 1H), 8.45 (d, $^3J_{HH}$ = 8.1 Hz, 1H), 8.22–8.14 (overlapping m, 3H), 8.05 (d, $^3J_{HH}$ = 7.9 Hz, $^4J_{HH}$ = 1.5 Hz, 1H), 7.97 (d, $^3J_{HH}$ = 7.9 Hz, $^4J_{HH}$ = 1.4 Hz, 1H), 7.82 (d, $^3J_{HH}$ = 7.9 Hz, $^4J_{HH}$ = 1.4 Hz, 1H), 7.49–7.19 (m, 17H), 6.99 (m, 1H), 6.90 (m, 1H), 6.66 (dd, J_1 = 4.0 Hz, J_2 = 7.9 Hz, 1H, PhOR H *ortho* to O), 3.48 (m, 2H inequiv, OCH_2CH_3), 0.37 (t, $^3J_{HH}$ = 7.0 Hz, 3H, OCH_2CH_3). Selected ^{1}H resonances (200 MHz, 25 °C, CD_2Cl_2, **2** + 1 equiv MeCN): δ 3.50 (m, 2H, OCH_2CH_3), 2.33 (s, 3H, Ru-NCCH_3), 0.43 (t, OCH_2CH_3). $^{31}P\{^1H\}$ NMR (81.0 MHz, CD_2Cl_2, **2** + 1 equiv MeCN): δ 38.7 (s, PO), -144.1 (sept, $^1J_{PF}$ = 711 Hz, PF_6). Vis (CH_2Cl_2, λ_{max}, ε): 410 nm, 7060 $M^{-1}cm^{-1}$. CV (200 mV/s, 25 °C, $CH_3CN/^nBu_4NPF_6$, V *vs.* SCE): $E_{1/2}(Ru^{III/II})$ = 1.52 V; E_{red} = -1.21 (irrev), -1.32 (irrev), -1.53, -1.83 V; reductive decomposition product $E_{1/2}$ = 0.42 V (appearance of CV similar to that of **1•MeCN**).

^{1}H NMR NOE difference spectrum (400 MHz, 25 °C, CD_3CN): Irradiation of the methylene protons' resonance at δ 3.48 enhanced the methyl triplet at δ 0.37 and one aromatic resonance at δ 6.66 (dd, PhOR H *ortho* to O).

(ii) Reaction with NEt_3

Treatment of **2** with NEt_3 in CD_2Cl_2 led to a colour change from orange to deep red-brown. In the presence of 5 equiv NEt_3, only a small amount of new product was evident, even after > 8 h reaction time: $^{31}P\{^1H\}$ NMR δ 40.1; ^{1}H resonances more difficult to resolve: POEt CH_2 peaks at δ 3.40, 3.25 (overlapping). The longitudinal relaxation times (T_1) of the phosphorus nuclei were found (experiment performed by Ms. Liane Darge) to be quite different (T_1 = 2.42 ± 0.03 s for **2**, 1.9 ± 0.1 s for **2•NEt$_3$**). Thus, the error in K_{eff} determined via $^{31}P\{^1H\}$ NMR spectroscopy is large, and only an upper limit is presented in Table 5.1.

5.6.2.3 Reaction of 2 with sulfur donors

(i) Reaction with H_2S

As for **1**, the reaction of **2** with H_2S yielded small amounts of several products and was not pursued further.

References begin on page 178.

(ii) Reaction with SO_2

Slow reaction between **2** and SO_2 was evident; product resonances grew into the NMR spectra, from a trace at 2 h to ~ 50 % conversion to products after 1 d: $^{31}P\{^1H\}$ δ37.1, s; -13.9 t, J = 960 Hz; -18.8 broad t, J = 968 Hz. After 1 d in the presence of SO_2, the solution was poppy red rather than orange. A preparative attempt (SO_2 treatment in CH_2Cl_2 at reflux for 5h yielded red solution) was unsuccessful because attempts to isolate the new complex failed due to conversion back to orange **2** when the SO_2 atmosphere was removed. The reaction was not pursued further because of the evidence for reaction between SO_2 and the PF_6^- counterions (as for **1**).

(iii) Reaction with dodecanethiol

After addition of 1 equiv dodecanethiol, the solution changed colour slightly from orange to more reddish. NMR spectroscopy revealed approximately 25 % conversion to a new product: ^1H NMR OC*H*$_2$ δ3.72 m, 3.45 m (C*H*$_3$ resonance overlapped with thiol alkyl signals in the very congested alkyl region; the resonance from the thiol H was not located). The limited resolution in the spectra forbade determination of K_{eff} for this reaction.

(iv) Reaction with ethanethiol

The reaction of **2** with EtSH was slower than with other analytes and required a few hours to reach equilibrium. For a sample with 2 equiv of EtSH, ([**2**] = 5×10^{-2} M in CD_2Cl_2), a very slight reddening of the solution was observed compared to **2**, and the NMR spectra showed clear evidence of reaction: $^{31}P\{^1H\}$ δ36.6; ^1H OC*H*$_2$CH$_3$ δ3.75 m, 3.46 m; SCH$_2$C*H*$_3$ 1.12 triplet-like dd, OCH$_2$C*H*$_3$ 0.52 triplet-like dd; SC*H*$_2$CH$_3$ buried under water and free thiol peaks according to the ^1H COSY spectrum (δ1.22 – 1.72), as for **1•EtSH**. A broad resonance at δ3.23 (1 H) is assigned to the SH in **2•EtSH**, although as for **1•EtSH**, the COSY spectrum did not resolve any coupling between this resonance and the methylene resonances. Addition of a drop of D_2O to the sample resulted in the disappearance of the free EtSH's SH resonance; this simplified the alkyl region and revealed the presence of the SC*H*$_2$CH$_3$ multiplet resonances. Furthermore, the broad resonance at δ3.23 shifted downfield to δ4.77, which

References begin on page 178.

supports assignment of this resonance as due to an acidic metal-bound SH proton, as discussed in section 2.4.4.3 for **1•EtSH**.

(v) Reaction with Me_2S

In the presence of 2 equiv of Me_2S ([**2**] = 5×10^{-2} M in CD_2Cl_2), there was > 90 % conversion to **2•DMS**: $^{31}P\{^1H\}$ δ 31.4; ^1H OCH_2CH_3 δ 3.23 overlapped m, less inequivalent than in **2•EtSH**, where the 2 H's resonances were separated by 0.3 ppm; $S(CH_3)_2$ 1.05 s; OCH_2CH_3 0.52 t.

(vi) Reaction with DMSO

In the presence of ~ 7 equiv of DMSO ([**2**] = 5×10^{-2} M in CD_2Cl_2), small amounts of two new products **2•DMSO-*S*** and **2•DMSO-*O*** were evident by NMR spectroscopy. Major product **2•DMSO-*S***: $^{31}P\{^1H\}$ δ 39.6 s; ^1H OCH_2CH_3 δ 0.32 t. Minor product **2•DMSO-*O***: $^{31}P\{^1H\}$ δ 28.1 s; ^1H OCH_2CH_3 δ 0.54 t. As for **1**, the reaction of **2** with DMSO was accompanied by a reddening of the solution colour.

5.6.3 Preparation of the PO^iPr and $POCF_3$ ligands

5.6.3.1 Preparation of 2-(2-propoxy)phenyldiphenylphosphine, PO^iPr

This compound was prepared by a modification of the literature method[16] with 2-(2-propoxy)bromobenzene used as the starting material rather than (2-propoxy)benzene. A solution of 2-(2-propoxy)bromobenzene[15] (7.7 mL, 48 mmol) in freshly distilled diethyl ether (30 mL) was cooled to -78 °C in a dry ice/acetone bath, then treated with 1.5 equiv of *n*BuLi (47 mL, 75 mmol, 1.6 M in hexanes) added dropwise via addition funnel. The mixture was warmed to RT and stirred for an additional 1.5 h. To the cloudy reaction mixture was added 1 equiv of chlorodiphenylphosphine (8.9 mL, 48 mmol) as a solution in dry ether (50 mL), which immediately produced a cream-coloured precipitate. Once the reaction was complete, the mixture was treated with saturated $NH_4Cl_{(aq)}$. The organic layer was collected and the aqueous fraction extracted with ether (3 × 50 mL). The combined organic fractions were dried with

References begin on page 178.

anhydrous Na_2SO_4 and evaporated to dryness to yield a golden oil, which was purified by column chromatography (silica gel; 2:1 hexanes/chloroform; R_f = 0.43). The desired phosphine was isolated in similar yield (70 %) to that previously reported (61 %).

5.6.3.2 Preparation of 2-trifluoromethoxyphenyldiphenylphosphine, $POCF_3$

A suspension of Mg powder (0.354 g, 14.6 mmol) in freshly distilled diethyl ether (15 mL) was treated with a few crystals of iodine and the resulting colour allowed to fade. To this mixture was dropwise added a solution of 2-trifluoromethoxybromobenzene (3.19 g, 13.2 mmol) in ether (7 mL) over 1 h, and the mixture was heated to reflux for 2 h (note that the Grignard reagent is not stable over extended reflux times, *e.g.*, overnight). The cooled mixture was cannula-filtered into a new vessel. To the deep brown Grignard solution was dropwise added a solution of chlorodiphenylphosphine (2.7 mL, 15.0 mmol) in ether (8 mL). The mixture was stirred at room temperature for 2 h, then treated with saturated $NH_4Cl_{(aq)}$ (25 mL). Water was added to dissolve precipitated salts before the mixture was extracted with ether (3 × 50 mL). The combined ether extracts were dried with anhydrous Na_2SO_4 and evaporated to dryness to yield an orange oil. The crude oil was purified by column chromatography (silica gel; ether; R_f = 0.89) followed by short-path distillation (b.p. 128 °C/0.2 mm Hg). Purified yield: 60 %, faintly yellow-tinged oil (strong blue fluorescence). Solidified en masse under a stream of nitrogen to yield a white waxy solid, m.p. 29 – 31 °C. ^{1}H NMR (300.1 MHz, 25 °C, acetone-d_6): δ7.52 (m, 1H), 7.43 – 7.36 (m, 7H), 7.33 – 7.26 (m, 5H), 6.89 (ddd, 1H, $^3J_{PH}$ = 3.6 Hz, $^3J_{HH}$ = 7.6 Hz, $^4J_{HH}$ = 1.6 Hz). ^{19}F NMR (282.4 MHz, 25 °C, toluene-d_8): δ-56.8 (dd, $^5J_{FP}$ = 7.8 Hz, $^5J_{FH}$ = 1.8 Hz). ^{31}P{^{1}H} NMR (121.5 MHz, 25 °C, toluene-d_8): δ-15.2 (quartet, $^5J_{PF}$ = 7.8 Hz). Elemental analysis calcd. for $C_{19}H_{14}F_3OP$ (%): C, 65.90; H, 4.07; found: C, 65.86; H, 4.15.

5.6.3.3 Preparation of 2-trifluoromethoxyphenyldiphenylphosphine oxide, O=$POCF_3$

$POCF_3$ (0.106 g, 0.305 mmol) was dissolved in acetone (5 mL) and treated with an excess of 30 % H_2O_2 (1 mL). The mixture was stirred at room temperature overnight, then the solvent was removed using a rotary evaporator. Methanol was added to assist in the removal of the water and excess peroxide as the azeotropes; the crude product was dried *in vacuo* overnight. The oily product was dissolved in ether, extracted with dilute $NaOH_{(aq)}$ to remove

References begin on page 178.

formic acid (formed by oxidation of methanol by excess H_2O_2) and the organic extracts were dried over anhydrous Na_2SO_4. Removal of the solvent *in vacuo* yielded a waxy white solid (0.085 g, 80 %) that when recrystallized from hot cyclohexane yielded white needles, m.p. 113 – 113.5 °C. ^{1}H NMR (300.1 MHz, 25 °C, acetone-d_6): δ7.79 – 7.68 (m, 6H), 7.65 – 7.41 (m, 8H). ^{19}F NMR (282.4 MHz, 25 °C, acetone-d_6): δ-57.2 (d, $^5J_{FH}$ = 1.7 Hz). ^{31}P{^{1}H} NMR (121.5 MHz, 25 °C, acetone-d_6): δ23.3 s. Elemental analysis calcd. for $C_{19}H_{14}F_3O_2P$ (%): C, 62.99; H, 3.89; found: C, 63.21; H, 3.94.

5.6.4 Preparation and characterization of the Ru complexes

The preparation and characterization of complex **1** is described in Chapter Two (section 2.6.3.1). Complex **2** is described in Chapter Four (section 4.9.3.1).

5.6.4.1 Reaction of PO^{i}Pr with [cis-Ru(bpy)$_2$(acetone)$_2$]$^{2+}$

A suspension of $Ru(bpy)_2Cl_2 \cdot 2H_2O$ (0.670 g, 1.29 mmol) in nitrogen-sparged acetone 50 mL) was treated with $AgBF_4$ (0.506 g, 2.60 mmol) in acetone (20 mL). The mixture was thoroughly sparged with $N_{2(g)}$, stirred at RT overnight to ensure complete precipitation of AgCl, then filtered through Celite to yield a deep wine-red solution of the solvate complex. To this solution was added 1 equiv of 2-(2-propoxy)phenyl-diphenylphosphine (0.414 g, 1.29 mmol) as a solution in nitrogen-sparged acetone (5 mL), and the mixture was heated to reflux under $N_{2(g)}$ for 2 d to yield a reddish orange solution. The cooled reaction mixture was filtered, evaporated to dryness and the residue dissolved in a small volume of acetone and precipitated with aqueous NH_4PF_6. The flocculent orange solid was collected, washed with water, dried by suction and stored in a desiccator. Yield: 1.17 g. The isolated material was identified as a mixture of three complexes as determined by ^{31}P{^{1}H} NMR spectroscopy (identification established by spiking samples with water and acetone): [*cis*-Ru(bpy)$_2$(PO^{i}Pr-*P,O*)](PF$_6$)$_2$ **6**, [*cis*-Ru(bpy)$_2$(PO^{i}Pr-*P*)(OH$_2$)](PF$_6$)$_2$ **6•OH$_2$**, [*cis*-Ru(bpy)$_2$(PO^{i}Pr-*P*)(O=C(CH$_3$)$_2$)](PF$_6$)$_2$, **6•O=C(CH$_3$)$_2$**. ^{31}P{^{1}H} NMR (81 MHz, 25 °C, CD_2Cl_2, ~10^{-2} M): δ50.7 (s, **6**), 40.9 (s, **6•OH$_2$**), 36.9 (s, **6•O=C(CH$_3$)$_2$**), 29.9 (s, trace unidentified impurity), -144 (septet, $^1J_{PF}$ = 711 Hz, PF_6). The complexes could not be separated in bulk nor prepared independently of each

References begin on page 178.

other. A single crystal suitable for X-ray crystallographic analysis picked from material crystallized by slow evaporation of a solution in CH_2Cl_2/hexanes was determined to be the aquo complex **6•OH$_2$**.

5.6.4.2 X-ray crystallographic structural determination of [cis-Ru(bpy)$_2$(PO^{i}Pr-P)(OH$_2$)](PF$_6$)$_2$, 6•OH$_2$ (Dr. B. O. Patrick)

A single crystal of **6•OH$_2$** grown from CH_2Cl_2/hexanes was mounted on a thin glass fibre. Measurements were made at 173 (± 1) K on a Rigaku/ADSC CCD area detector using graphite monochromated Mo-Kα radiation. Data were collected in two sets of scans (ϕ = 0.0 to 190.0°, χ = -90.0°; and ω = -19.0 to 23.0°, χ = -90.0°) using 0.50° oscillations with 12.0 second exposures. Data were collected and processed using the d*TREK program (Molecular Structure Corporation); the structure was solved using direct methods[17] and expanded using Fourier techniques.[18] The nonhydrogen atoms were refined anisotropically. One disordered molecule of CH_2Cl_2 was found to crystallize in the asymmetric unit. One PF_6^- anion displayed considerable thermal motion, which was modeled successfully as two separate fragments, with relative populations of 0.65 and 0.35 respectively. In addition, the isopropyl group [C(8)-C(7)-C(9)] was also found to be disordered and was modeled as two separate fragments, with relative populations of 0.57 and 0.43 respectively. Hydrogen atoms were included but not refined. All calculations were performed using the teXsan crystallographic software package (Molecular Structure Corporation). Crystallographic data for **6•OH$_2$** are summarized in Tables A.5.1 and A.5.3, and selected interatomic distances and angles are listed in Table 5.3. The ORTEP representation of the solid-state molecular structure of **6•OH$_2$** depicted in Figure 5.1 was prepared using ORTEP-3 for Windows.[19]

5.6.4.3 Reaction of POCF$_3$ with [cis-Ru(bpy)$_2$(acetone)$_2$]$^{2+}$

Under similar conditions as the reaction of [*cis*-Ru(bpy)$_2$(acetone)$_2$]$^{2+}$ with PO^{i}Pr, the reaction with $POCF_3$ also led to a brownish-yellow powder that was found to be a mixture of multiple components according to NMR spectroscopy (CD_2Cl_2: $^{31}P\{^1H\}$ δ 41.4 major component, 40.5, 39.9; $^{19}F\{^1H\}$ δ 20.0 major component, 19.0, 18.4). Efforts to conclusively identify the species responsible for these resonances failed.

References begin on page 178.

5.6.4.4 X-ray crystallographic structural determination of [cis-Ru(bpy)$_2$(POCF$_3$-P)(CD$_3$CN)](PF$_6$)$_2$, 7•MeCN-d_3 (Dr. B. O. Patrick)

A red irregular crystal of **7•MeCN-d_3** grown from acetonitrile-d_3 solution was mounted on a glass fibre. Measurements were made at 173 (± 1) K on a Rigaku/ADSC CCD area detector using graphite monochromated Mo-Kα radiation. Data were collected in two sets of scans (ϕ = 0.0 to 190.0°, χ = -90.0°; and ω = -19.0 to 23.0°, χ = -90.0°) using 0.50° oscillations with 50.0 second exposures. Data were collected and processed using the d*TREK program (Molecular Structure Corporation); the structure was solved using direct methods[17] and expanded using Fourier techniques.[18] The nonhydrogen atoms were refined anisotropically. Hydrogen atoms were included but not refined. All calculations were performed using the teXsan crystallographic software package (Molecular Structure Corporation). The material crystallized with one molecule of acetonitrile-d_3 in the asymmetric unit. The deuterium atoms were refined as hydrogens; however, the final formula weight and density were adjusted to reflect the presence of deuterium. Crystallographic data for **7•MeCN-d_3** are summarized in Tables A.5.2 and A.5.4, and selected interatomic distances and angles are listed in Table 5.4. The ORTEP representation of the solid-state molecular structure of **7•MeCN-d_3** depicted in Figure 5.2 was prepared using ORTEP-3 for Windows.[19]

References begin on page 178.

5.7 References

(1) Lindner, E.; Pautz, S.; Haustein, M. *Coord. Chem. Rev.* **1996**, *155*, 145.

(2) Lindner, E.; Mockel, A.; A., M. H.; Kuhbauch, H.; Fawzi, R.; Steimann, M. *Inorg. Chem.* **1993**, *32*, 1266.

(3) Lindner, E.; Geprags, M.; Gierling, K.; Fawzi, R.; Steimann, M. *Inorg. Chem.* **1995**, *34*, 6106.

(4) Balzani, V.; Bolletta, F.; Gandolfi, M. T.; Maestri, M. *Top. Curr. Chem.* **1978**, *75*, 1.

(5) Wolf, M. O.; Saran, N. S., unpublished results.

(6) Rogers, C. W.; Wolf, M. O. *Chem. Commun.* **1999**, 2297.

(7) Rogers, C. W.; Patrick, B. O.; Rettig, S. J.; Wolf, M. O. *J. Chem. Soc., Dalton Trans.* **2001**, 1278.

(8) Bernhard, P.; Burgi, H.-B.; Hauser, J.; Lehmann, H.; Ludi, A. *Inorg. Chem.* **1982**, *21*, 3936.

(9) Boniface, S. M.; Clark, G. R.; Collins, T. J.; Roper, W. R. *J. Organomet. Chem.* **1981**, *206*, 109.

(10) Changenet, P.; Plaza, P.; Martin, M. M.; Meyer, Y. H.; Rettig, W. *Chem. Phys.* **1997**, *221*, 311.

(11) Rozanel'skaya, N. A.; Bokanov, A. I.; Uzhinov, B. M.; Stepanov, B. I. *J. Gen. Chem. USSR* **1975**, *45*, 263.

(12) Ebsworth, E. A. V.; Rankin, D. W. H.; Cradock, S. *Structural Methods in Inorganic Chemistry*; 2nd ed.; CRC Press: Boca Raton, FL, 1991.

(13) Gorenstein, D. G. *Phosphorus-31 NMR: Principles and Applications*; Academic Press, Inc.: Toronto, 1984.

References begin on page 178.

(14) Lay, P. A.; Sargeson, A. M.; Taube, H. *Inorg. Synth.* **1986**, *24*, 292.

(15) Aroyan, A. A. *Izv. Akad. Nauk. Arm. SSR., Khim. Nauki* **1964**, *17*, 532.

(16) Horner, L.; Simons, G. *Phosph. Sulf.* **1983**, *14*, 189.

(17) Altomare, A.; Burla, M. C.; Cammalli, G.; Cascarano, M.; Giacovazzo, C.; Guagliardi, A.; Moliterni, A. G. G.; Polidori, G.; Spagna, A. *J. Appl. Cryst.* **1999**, *32*, 115.

(18) Beurskens, P. T.; Admiraal, G.; Beurskens, G.; Bosman, W. P.; deGelder, R.; Israel, R.; Smits, J. M. M. "The DIRDIF-94 program system, Technical Report of the Crystallography Laboratory," University of Nijmegen, 1994.

(19) Farrugia, L. J. *J. Appl. Cryst.* **1997**, *30*, 565.

References begin on page 178.

Appendix 5.1 Crystallographic details

The crystallographic data for **6•OH$_2$** have not been deposited into the CCDC. Atomic coordinates are provided in Table A.5.3.

Table A.5.1. Crystallographic data, collection and refinement details for **6•OH$_2$**

	6•OH$_2$•CH$_2$Cl$_2$
Formula	$C_{42}H_{41}Cl_2F_{12}N_4O_2P_3Ru$
M	1126.69
μ / cm^{-1}	6.59
T / K	173(1)
Colour, habit	red, block
Crystal system	triclinic
Space group	$P\bar{1}$ (No. 2)
a / Å	12.5278(8)
b / Å	13.554(2)
c / Å	14.1049(8)
α / deg	77.313(3)
β / deg	76.841(2)
γ / deg	89.064(4)
V / Å^3	2273.8(3)
ρ_{calc} / g·cm^{-3}	1.646
Z	2
Refl. collected / unique / R_{int}	19508/8682/0.050
R_1[a]	0.043
wR_2[b]	0.117
GOF	1.45

[a]$R_1 = \Sigma \big| |F_o| - |F_c| \big| / \Sigma |F_o|$ (observed data), $I > 3\sigma(I)$. [b]$wR_2 = (\Sigma(F_o^2 - F_c^2)^2 / \Sigma w(F_o^2)^2)^{½}$ (all data), $I > 0.00\sigma(I)$.

References begin on page 178.

The crystallographic data for **7•MeCN-d_3** have been neither published nor submitted to the CCDC. Atomic coordinates are provided in Table A.5.4.

Table A.5.2. Crystallographic data, collection and refinement details for **7•MeCN-d_3**

	7•MeCN-d_3•CD_3CN
Formula	$C_{43}H_{30}D_6F_{15}N_6OP_3Ru$
M	1137.76
μ / cm^{-1}	5.52
T / K	173(1)
Colour, habit	red, irregular
Crystal system	monoclinic
Space group	$P2_1/c$ (No. 14)
a / Å	16.5744(6)
b / Å	12.9015(4)
c / Å	21.9220(8)
α / deg	90
β / deg	102.751(3)
γ / deg	90
V / $Å^3$	4572.1(3)
ρ_{calc} / $g{\cdot}cm^{-3}$	1.65
Z	4
Refl. collected / unique / R_{int}	35317/10306/0.070
R_1[a]	0.039
wR_2[b]	0.102
GOF	1.01

[a]$R_1 = \Sigma \big| |F_o| - |F_c| \big| / \Sigma |F_o|$ (observed data), $I > 3\sigma(I)$. [b]$wR_2 = (\Sigma(F_o^2 - F_c^2)^2 / \Sigma w(F_o^2)^2)^{½}$ (all data), $I > 0.00\sigma(I)$.

References begin on page 178.

Table A.5.3. Atomic coordinates, B_{iso}/B_{eq} and occupancy (occ) for **6•OH$_2$**

Atom	x	y	z	B_{eq}[a]	occ
Ru(1)	0.76707(2)	0.24761(2)	0.26817(2)	1.458(6)	
Cl(1)	0.7373(1)	-0.0582(1)	1.1416(1)	5.86(4)	
Cl(2A)	0.6790(1)	-0.1380(1)	0.9875(1)	3.49(3)	0.710
Cl(2B)	0.5565(4)	-0.0894(4)	1.0662(4)	5.0(1)	0.290
P(1)	0.66930(6)	0.35458(6)	0.36394(6)	1.39(2)	
P(2)	0.75338(9)	0.18572(8)	0.80358(9)	3.06(2)	
P(3)	1.19934(9)	0.2815(1)	0.2378(1)	4.17(3)	
F(1)	0.6878(3)	0.2015(3)	0.7183(3)	6.46(9)	
F(2)	0.6417(3)	0.1755(3)	0.8840(3)	8.4(1)	
F(3)	0.7572(3)	0.3037(2)	0.7941(3)	6.8(1)	
F(4)	0.8651(2)	0.1936(2)	0.7220(3)	6.14(8)	
F(5)	0.7506(2)	0.0670(2)	0.8103(2)	4.31(6)	
F(6)	0.8201(4)	0.1684(3)	0.8877(3)	8.0(1)	
F(7A)	1.1381(5)	0.2833(5)	0.1432(5)	6.2(2)	0.650
F(8A)	1.0799(6)	0.2441(6)	0.3086(6)	6.0(2)	0.650
F(9)	1.1586(3)	0.3921(2)	0.2297(3)	5.95(8)	
F(10A)	1.3089(4)	0.3145(5)	0.1535(6)	6.7(2)	0.650
F(11)	1.2333(3)	0.1692(3)	0.2507(4)	11.2(1)	
F(12A)	1.2532(7)	0.2760(6)	0.3215(6)	8.6(2)	0.650
O(1)	0.8070(2)	0.5311(2)	0.2338(2)	2.23(5)	
O(2)	0.9112(2)	0.3423(2)	0.2372(2)	2.51(5)	
N(1)	0.8111(2)	0.1396(2)	0.3826(2)	1.82(6)	
N(2)	0.8729(2)	0.1565(2)	0.1869(2)	2.03(6)	
N(3)	0.6336(2)	0.1640(2)	0.2689(2)	2.06(6)	
N(4)	0.7223(2)	03291(2)	0.1426(2)	2.21(6)	
C(1)	0.6215(2)	0.4693(3)	0.2918(2)	1.68(6)	
C(2)	0.5108(3)	0.4834(3)	0.2925(3)	2.20(7)	
C(3)	0.4755(3)	0.5688(3)	0.2359(3)	2.85(9)	

References begin on page 178.

Atom	x	y	z	B_{eq} [a]	occ
C(4)	0.5519(3)	0.6416(3)	0.1751(3)	2.95(9)	
C(5)	0.6620(3)	0.6307(3)	0.1731(3)	2.73(8)	
C(6)	0.6972(3)	0.5456(3)	0.2320(3)	1.88(7)	
C(7)	0.8851(3)	0.6179(3)	0.1997(3)	2.97(9)	
C(8A)	1.0011(6)	0.5787(6)	0.1839(8)	4.6(2)	0.570
C(9A)	0.8677(7)	0.6903(6)	0.2682(7)	4.3(2)	0.570
C(10)	0.7423(2)	0.4078(3)	0.4414(2)	1.66(6)	
C(11)	0.7009(3)	0.4918(3)	0.4785(3)	2.18(7)	
C(12)	0.7533(3)	0.5309(3)	0.5399(3)	2.56(8)	
C(13)	0.8453(3)	0.4860(3)	0.5664(3)	3.07(9)	
C(14)	0.8867(3)	0.4035(3)	0.5301(3)	2.98(9)	
C(15)	0.8365(3)	0.3656(3)	0.4664(3)	2.17(7)	
C(16)	0.5449(2)	0.2959(2)	0.4553(2)	1.63(6)	
C(17)	0.5332(3)	0.2864(3)	0.5575(3)	2.08(7)	
C(18)	0.4417(3)	0.2362(3)	0.6249(3)	2.83(8)	
C(19)	0.3599(3)	0.1961(3)	0.5905(3)	3.20(9)	
C(20)	0.3703(3)	0.2056(3)	0.4899(3)	2.70(8)	
C(21)	0.4619(3)	0.2545(3)	0.4212(3)	2.13(7)	
C(22)	0.7721(3)	0.1274(3)	0.4824(3)	2.33(7)	
C(23)	0.7955(3)	0.0460(3)	0.5516(3)	2.95(9)	
C(24)	0.8610(3)	-0.0286(3)	0.5184(3)	3.16(9)	
C(25)	0.9022(3)	-0.0177(3)	0.4179(3)	2.85(9)	
C(26)	0.8784(3)	0.0664(3)	0.3507(3)	2.13(7)	
C(27)	0.9197(3)	0.0825(3)	0.2425(3)	2.23(8)	
C(28)	1.0039(3)	0.0280(3)	0.1981(4)	3.3(1)	
C(29)	1.0389(3)	0.0494(4)	0.0958(4)	3.8(1)	
C(30)	0.9896(3)	0.1240(4)	0.0391(3)	3.6(1)	
C(31)	0.9055(3)	0.1759(3)	0.0875(3)	2.73(8)	
C(32)	0.5938(3)	0.0780(3)	0.3337(3)	2.89(9)	
C(33)	0.5040(3)	0.0229(3)	0.3265(4)	3.9(1)	

References begin on page 178.

Atom	x	y	z	B_{eq} [a]	occ
C(34)	0.4552(3)	0.0583(4)	0.2476(5)	4.6(1)	
C(35)	0.4947(3)	0.1462(4)	0.1810(4)	4.0(1)	
C(36)	0.5840(3)	0.1989(3)	0.1918(3)	2.58(8)	
C(37)	0.6311(3)	0.2929(3)	0.1236(3)	2.53(8)	
C(38)	0.5886(4)	0.3445(5)	0.0439(4)	4.3(1)	
C(39)	0.6408(5)	0.4296(5)	-0.0173(4)	5.5(2)	
C(40)	0.7380(5)	0.4631(4)	-0.0020(3)	4.5(1)	
C(41)	0.7760(4)	0.4114(3)	0.0786(3)	3.26(9)	
C(42A)	0.6403(7)	-0.0524(9)	1.0637(6)	3.8(2)	0.710
F(7B)	1.3074(8)	0.3421(9)	0.250(1)	7.8(3)	0.350
F(8B)	1.161(1)	0.2822(8)	0.3654(9)	7.8(3)	0.350
C(8B)	0.9534(9)	0.5951(9)	0.2778(9)	4.1(3)	0.430
C(9B)	0.9391(9)	0.6236(9)	0.1004(8)	4.6(3)	0.430
F(10B)	1.229(2)	0.285(1)	0.1405(8)	9.8(5)	0.350
F(12B)	1.0902(9)	0.225(1)	0.266(1)	6.3(4)	0.350
C(42B)	0.690(2)	-0.036(2)	1.041(2)	8.0(7)	0.290
H(1)	0.4561	0.4305	0.3344	2.8483	
H(2)	0.3968	0.5787	0.2384	3.4774	
H(3)	0.5274	0.7019	0.1339	3.6808	
H(4)	0.7161	0.6839	0.1303	3.3131	
H(5)	0.8466	0.6815	0.2047	3.5960	
H(6A)	1.0135	0.5369	0.2475	6.0562	0.570
H(6B)	0.9063	0.5888	0.3458	5.2166	0.430
H(7A)	1.0139	0.5368	0.1340	6.0562	0.570
H(7B)	0.9890	0.5287	0.2762	5.2166	0.430
H(8A)	1.0568	0.6352	0.1613	6.0562	0.570
H(8B)	1.0107	0.6469	0.2666	5.2166	0.430
H(9A)	0.9216	0.7479	0.2408	5.8871	0.570
H(9B)	0.9822	0.5576	0.0973	5.5544	0.430
H(10A)	0.7932	0.7185	0.2716	5.8871	0.570

References begin on page 178.

Atom	x	y	z	B_{eq} [a]	occ
H(10B)	0.8903	0.6272	0.0572	5.5544	0.430
H(11A)	0.8743	0.6567	0.3340	5.8871	0.570
H(11B)	0.9958	0.6782	0.0758	5.5544	0.430
H(12)	0.6338	0.5230	0.4620	2.6070	
H(13)	0.7249	0.5908	0.5647	3.1354	
H(14)	0.8821	0.5124	0.6108	3.8300	
H(15)	0.9524	0.3712	0.5478	3.7111	
H(16)	0.8681	0.3076	0.4394	2.6969	
H(17)	0.5907	0.3158	0.5820	2.4578	
H(18)	0.4339	0.2296	0.6979	3.3221	
H(19)	0.2950	0.1603	0.6387	3.7812	
H(20)	0.3117	0.1776	0.4663	3.1188	
H(21)	0.4685	0.2608	0.3492	2.7582	
H(22)	0.7242	0.1797	0.5070	2.9012	
H(23)	0.7655	0.0390	0.6241	3.4014	
H(24)	0.8791	-0.0874	0.5662	4.0745	
H(25)	0.9488	-0.0698	0.3925	3.6427	
H(26)	1.0389	-0.0253	0.2400	4.4596	
H(27)	1.0978	0.0092	0.0640	5.0107	
H(28)	1.0143	0.1418	-0.0350	4.6102	
H(29)	0.8668	0.2277	0.0478	3.5093	
H(30)	0.6283	0.0528	0.3909	4.1276	
H(31)	0.4751	-0.0392	0.3762	5.3603	
H(32)	0.3910	0.0210	0.2411	6.3299	
H(33)	0.4596	0.1714	0.1247	5.8616	
H(34)	0.5210	0.3185	0.0318	5.8568	
H(35)	0.6085	0.4662	-0.0723	7.2569	
H(36)	0.7783	0.5241	-0.0476	5.9312	
H(37)	0.8463	0.4353	0.0892	4.3676	
H(38A)	0.5663	-0.0692	1.1056	5.3374	0.710

References begin on page 178.

Atom	x	y	z	B_{eq} [a]	occ
H(38B)	0.7447	-0.0634	0.9852	12.2426	0.290
H(39A)	0.6418	0.0172	1.0229	5.3374	0.710
H(39B)	0.6955	0.0403	1.0096	12.2426	0.290
H(40A)	0.9357	0.3227	0.2917	3.1600	
H(40B)	0.9040	0.4040	0.2530	3.1600	

[a] $B_{eq} = (8/3)\pi^2(U_{11}(aa^*)^2 + U_{22}(bb^*)^2 + U_{33}(cc^*)^2 + 2U_{12}aa^*bb^*\cos\gamma + 2U_{13}aa^*cc^*\cos\beta + 2U_{23}bb^*cc^*\cos\alpha)$

References begin on page 178.

Table A.5.4. Atomic coordinates and B_{iso}/B_{eq} for **7•MeCN-*d*$_3$**

Atom	x	y	z	B_{eq} [a]
Ru(1)	0.21589(2)	0.22402(2)	0.01698(1)	1.206(5)
P(1)	0.34151(5)	0.14444(6)	0.01009(4)	1.23(2)
P(2)	0.26124(7)	0.6280(1)	0.16614(5)	3.06(2)
P(3)	-0.14606(7)	0.47068(9)	0.17558(5)	2.93(2)
F(1)	0.5706(2)	0.3290(2)	0.1127(1)	4.31(7)
F(2)	0.4990(2)	0.4118(2)	0.1164(1)	4.94(7)
F(3)	0.4789(2)	0.4379(2)	0.0675(1)	4.46(7)
F(4)	0.2531(3)	0.5532(3)	0.2217(1)	7.7(1)
F(5)	0.2685(3)	0.7001(3)	0.1103(2)	7.6(1)
F(6)	0.3373(2)	0.5596(2)	0.1544(1)	4.47(7)
F(7)	0.2012(2)	0.5533(3)	0.1200(2)	5.73(8)
F(8)	0.3204(2)	0.6974(3)	0.2137(2)	9.6(1)
F(9)	0.1845(2)	0.6949(2)	0.1766(1)	4.77(7)
F(10)	-0.1527(3)	0.4114(4)	0.2359(2)	10.4(2)
F(11)	-0.1370(2)	0.5263(3)	0.1136(1)	6.54(9)
F(12)	-0.1600(2)	0.3679(2)	0.1361(2)	6.6(1)
F(13)	-0.0496(2)	0.4527(4)	0.1901(1)	7.6(1)
F(14)	-0.2407(2)	0.4903(4)	0.1613(2)	10.7(1)
F(15)	-0.1298(2)	0.5720(3)	0.2158(2)	8.5(1)
O(1)	0.4368(2)	0.2943(2)	0.0983(1)	2.14(5)
N(1)	0.1014(2)	0.2937(2)	0.0168(1)	1.69(6)
N(2)	0.1560(2)	0.2135(2)	-0.0775(1)	1.39(5)
N(3)	0.1689(2)	0.0865(2)	0.0423(1)	1.86(6)
N(4)	0.2529(2)	0.2313(2)	0.1132(1)	1.83(6)
N(5)	0.2586(2)	0.3683(2)	0.0039(1)	1.71(6)
N(6)	0.0033(4)	0.6153(5)	0.3764(3)	8.2(2)
C(1)	0.0783(3)	0.3325(3)	0.0670(2)	2.92(9)
C(2)	0.0018(3)	0.3780(4)	0.0632(2)	3.6(1)

References begin on page 178.

Atom	x	y	z	B_{eq} [a]
C(3)	-0.0511(3)	0.3872(4)	0.0060(2)	3.3(1)
C(4)	-0.0276(2)	0.3489(3)	-0.0463(2)	2.60(8)
C(5)	0.0487(2)	0.3011(3)	-0.0396(2)	1.76(7)
C(6)	0.0776(2)	0.2530(3)	-0.0920(2)	1.73(7)
C(7)	0.0276(2)	0.2437(3)	-0.1514(2)	2.65(8)
C(8)	0.0576(3)	0.1955(4)	-0.1976(2)	3.08(9)
C(9)	0.1365(2)	0.1574(3)	-0.1843(2)	2.64(8)
C(10)	0.1831(2)	0.1679(3)	-0.1242(2)	2.07(7)
C(11)	0.1183(2)	0.0216(3)	0.0040(2)	2.39(8)
C(12)	0.0951(3)	-0.0734(3)	0.0246(2)	3.5(1)
C(13)	0.1252(3)	-0.1021(4)	0.0847(3)	4.2(1)
C(14)	0.1744(3)	-0.0349(4)	0.1254(2)	3.6(1)
C(15)	0.1938(2)	0.0614(3)	0.1035(2)	2.34(8)
C(16)	0.2386(2)	0.1439(3)	0.1434(2)	2.52(8)
C(17)	0.2589(3)	0.1391(4)	0.2082(2)	3.8(1)
C(18)	0.2911(3)	0.2245(5)	0.2415(2)	4.6(1)
C(19)	0.3040(3)	0.3137(4)	0.2114(2)	3.7(1)
C(20)	0.2846(2)	0.3146(3)	0.1467(2)	2.50(8)
C(21)	0.4945(3)	0.3655(3)	0.1109(2)	2.90(9)
C(22)	0.4486(2)	0.1949(3)	0.1253(2)	1.78(7)
C(23)	0.4922(2)	0.1780(3)	0.1860(2)	2.57(8)
C(24)	0.4984(3)	0.0785(4)	0.2095(2)	2.92(9)
C(25)	0.4619(3)	-0.0032(3)	0.1726(2)	2.80(9)
C(26)	0.4183(2)	0.0151(3)	0.1120(2)	2.13(7)
C(27)	0.4091(2)	0.1150(3)	0.0867(1)	1.60(7)
C(28)	0.4089(2)	0.2151(3)	-0.0316(1)	1.43(6)
C(29)	0.4933(2)	0.1926(3)	-0.0211(2)	1.83(7)
C(30)	0.5423(2)	0.2433(3)	-0.0556(2)	2.12(7)
C(31)	0.5085(2)	0.3152(3)	-0.1005(2)	2.31(8)
C(32)	0.4247(2)	0.3387(3)	-0.1111(2)	2.16(8)

References begin on page 178.

Atom	x	y	z	B_{eq} [a]
C(33)	0.3750(2)	0.2878(3)	-0.0771(1)	1.67(7)
C(34)	0.3302(2)	0.0191(3)	-0.0316(1)	1.55(6)
C(35)	0.2849(2)	-0.0620(3)	-0.0122(2)	1.96(7)
C(36)	0.2664(2)	-0.1509(3)	-0.0483(2)	2.77(9)
C(37)	0.2914(3)	-0.1615(3)	-0.1038(2)	3.14(9)
C(38)	0.3368(2)	-0.0826(3)	-0.1231(2)	2.70(8)
C(39)	0.3567(2)	0.0063(3)	-0.0876(2)	1.94(7)
C(40)	0.2806(2)	0.4503(3)	-0.0011(2)	2.00(7)
C(41)	0.3097(3)	0.5544(3)	-0.0093(2)	3.2(1)
C(42)	0.0412(4)	0.6177(4)	0.3390(3)	4.8(1)
C(43)	0.0891(3)	0.6217(4)	0.2920(2)	4.6(1)
H(1)	0.1174	0.3290	0.1084	3.5396
H(2)	-0.0139	0.4038	0.1014	4.1843
H(3)	-0.1058	0.4213	0.0024	3.9947
H(4)	-0.0648	0.3550	-0.0888	3.2604
H(5)	-0.0296	0.2718	-0.1602	3.0614
H(6)	0.0227	0.1901	-0.2405	3.6010
H(7)	0.1593	0.1231	-0.2172	3.1882
H(8)	0.2407	0.1401	-0.1148	2.5314
H(9)	0.0962	0.0423	-0.0401	2.9065
H(10)	0.0563	-0.1188	-0.0047	4.4302
H(11)	0.1113	-0.1717	0.0991	4.8641
H(12)	0.1973	-0.0547	0.1700	4.4189
H(13)	0.2493	0.0729	0.2298	4.5134
H(14)	0.3064	0.2219	0.2876	5.7296
H(15)	0.3263	0.3765	0.2361	4.4680
H(16)	0.2954	0.3795	0.1246	3.0482
H(17)	0.5192	0.2376	0.2118	3.1430
H(18)	0.5294	0.0653	0.2531	3.5380
H(19)	0.4672	-0.0750	0.1897	3.4216

References begin on page 178.

Atom	x	y	z	B_{eq} [a]
H(20)	0.3928	-0.0438	0.0858	2.6208
H(21)	0.5178	0.1403	0.0106	2.2201
H(22)	0.6025	0.2284	-0.0475	2.5708
H(23)	0.5436	0.3498	-0.1254	2.7102
H(24)	0.4006	0.3914	-0.1425	2.6753
H(25)	0.3152	0.3031	-0.0854	1.9800
H(26)	0.2663	-0.0555	0.0275	2.4913
H(27)	0.2340	-0.2072	-0.0334	3.2675
H(28)	0.2778	-0.2251	-0.1294	3.7916
H(29)	0.3549	-0.0898	-0.1632	3.1687
H(30)	0.3899	0.0619	-0.1015	2.4169
H(31)	0.3700	0.5537	-0.0079	3.8610
H(32)	0.2815	0.5825	-0.0506	3.8610
H(33)	0.2995	0.6010	0.0233	3.8610
H(34)	0.0874	0.5536	0.2705	5.4743
H(35)	0.0677	0.6746	0.2604	5.4743
H(36)	0.1475	0.6375	0.3110	5.4743

[a] $B_{eq} = (8/3)\pi^2(U_{11}(aa^*)^2 + U_{22}(bb^*)^2 + U_{33}(cc^*)^2 + 2U_{12}aa^*bb^*\cos\gamma + 2U_{13}aa^*cc^*\cos\beta + 2U_{23}bb^*cc^*\cos\alpha)$

References begin on page 178.

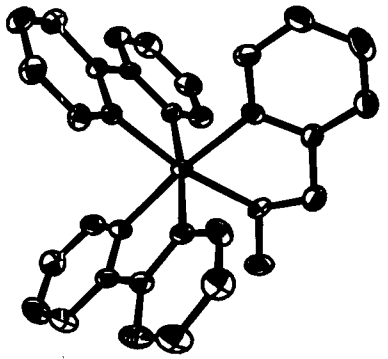

Chapter Six

Ru(II) bis(bipyridyl) complexes containing pyridine-ether ligands: an attempt to achieve room-temperature luminescence

6.1 A possible route to improved room-temperature luminescence

So far in this thesis, hemilabile ligand complexes based on the $[cis\text{-Ru(bpy)}_2\text{(L-L')}]^{2+}$ framework have been shown to exhibit reactivity toward small molecules that can be tuned through judicious selection of substituents. In these complexes, the metal serves a dual role as both small-molecule receptor and lumophore; complex **1**, $[cis\text{-Ru(bpy)}_2\text{(POMe-}P,O\text{)}]^{2+}$, in particular displays dramatically analyte-dependent photoluminescence properties, which makes this complex attractive for further study as a multianalyte sensor. Thus, this work provides proof-of-concept that hemilabile ligands can be used in conjunction with metal-based lumophores to yield relatively simple coordination-based small-molecule sensors with analyte-responsive luminescence properties. However, practical application of this class of complexes as luminescent chemosensors is intrinsically limited because emission from these complexes is only observable at extremely low temperatures.

References begin on page 208.

To this point, the reactivity of the metal-based lumophore toward small molecules has been achieved through the use of hemilabile ligands based on linked phosphorus-oxygen donors. As described in Chapter Two (section 2.1), it has been established in the literature[1] that the presence of phosphine ligands in $[cis\text{-}Ru(bpy)_2(L\text{-}L')]^{2+}$ complexes is correlated with strongly temperature-dependent luminescence properties. At low temperatures, strong emission from an MLCT excited state is observed from phosphine complexes, but as the temperature increases, a nonemissive metal-based dd excited state depopulates the emissive state, and the luminescence is efficiently quenched. On the other hand, $[cis\text{-}Ru(bpy)_2(L\text{-}L')]^{2+}$ complexes in which the nonchromophoric ligands contain nitrogen donors rather than phosphorus donors yield strong luminescence at room temperature because the thermal barrier between the MLCT and dd states is considerably larger.[1]

With this in mind, it was postulated that replacement of the phosphine moiety in the hemilabile ligand with a nitrogen-based donor would lead to complexes with improved luminescence properties. It was anticipated that the affinity of Ru(II) for nitrogen-based donors would be sufficiently high that these new ligands would also be hemilabile. The nitrogen donor group selected for this purpose was pyridine, based on the fact that the complex $[cis\text{-}Ru(bpy)_2(py)_2]^{2+}$ is luminescent at room temperature[1] as well as stable with respect to thermal displacement of the pyridine ligands under mild conditions.[2] In addition, the asymmetric bidentate pyridine-amine ligand AEP (AEP = 3-(2-aminoethyl)pyridine) also yields a Ru(II) bis(bipyridyl) complex that luminesces strongly at room temperature.[1] The precedented lability of ethers in Ru(II) bis(bipyridyl) phosphine-ether complexes suggested that pyridine-ether ligands might afford new lumophoric complexes that can coordinate small molecules at a hemilabile site.

The ability of pyridine-ethers to behave as hemilabile ligands on Ru(II) has not been reported, although hemilabile pyridine-based heterochelates are known.[3] A pyridine-ketone ligand has been shown to undergo fluxional processes involving dissociation of the oxygen from a Re(I) carbonyl complex.[4] Other ligands with substitutionally inert pyridine moieties[3] that have been reported to be hemilabile on Ru(II), in particular, contain labile amine or thiophene groups. It should also be noted that a number of phosphine-pyridine ligands are known in which the pyridine moiety is substitutionally labile on Ru(II).[3,5-7] To investigate the

References begin on page 208.

potential of pyridine-ethers to act as hemilabile ligands on Ru(II), a comparison was undertaken of the reactivity and properties of [*cis*-Ru(bpy)$_2$(PyCnOMe)]$^{2+}$ complexes that differ only in the size of the pyridine-ether chelate ring. Thus, three pyridine-ethers with different distances between the nitrogen and oxygen atoms, namely 2-methoxypyridine, 2-(methoxymethyl)pyridine[8] (denoted PyC1OMe) and 2-(2-methoxyethyl)pyridine (denoted PyC2OMe), were initially selected for study. Bidentate *N,O*-coordination of these ligands would lead to complexes with 4-, 5- and 6-membered chelate rings respectively, and it was expected that the 4- and 6-membered chelates would be more reactive toward ether displacement than the 5-membered chelate complex because of enhanced ring strain. No predictions were made regarding the possible effects that the metallocycle size might have on the photophysical properties of the complexes.

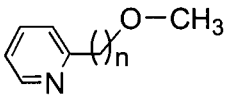

PyC1OMe: n = 1
PyC2OMe: n = 2

In this chapter, [*cis*-Ru(bpy)$_2$(PyCnOMe-*N,O*)]$^{2+}$ complexes **8** and **9** are reported, which contain the pyridine-ether ligands (PyC1OMe in **8**; PyC2OMe in **9**) depicted above. The preparation and reactivity of these complexes are presented, along with a limited study of their photophysical properties. Neither the goal of pyridine-ether hemilability nor that of improved luminescence was achieved using these ligands, and possible reasons for these observations are discussed.

6.2 Synthesis and characterization of pyridine-ether complexes

6.2.1 Preparation of [*cis*-Ru(bpy)$_2$(PyCnOMe)]$^{2+}$ complexes

Complexes **8** and **9**, shown in Scheme 6.1, were easily prepared via treatment of the solvate complex [*cis*-Ru(bpy)$_2$(acetone)$_2$]$^{2+}$ with the appropriate pyridine-ether, by way of the same procedures used to prepare the phosphine-ether complexes **1-3** presented earlier in this

References begin on page 208.

thesis. Similar attempts to prepare the 4-membered chelate complex with 2-methoxypyridine, however, led to mixtures of unidentified products, and this complex was not pursued further.

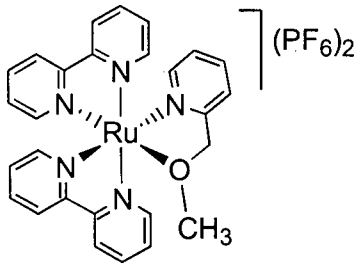

8

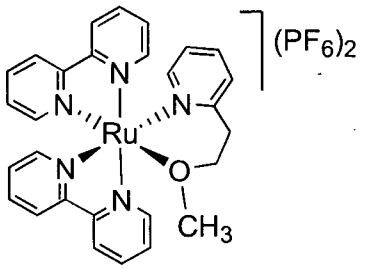

9

Scheme 6.1.

Complexes **8** and **9** were obtained in high yield (85 – 95 %) as orange-red and brick-red powders respectively, in high purity directly after metathesis to the PF_6^- salts. Both complexes are soluble in polar organic solvents such as acetone, but, unlike the related phosphine-ether complexes, they are only sparingly soluble in CH_2Cl_2. The complexes can be crystallized by slow evaporation of solutions in acetone.

Both complexes slowly oxidize over the course of several days in air-saturated acetone solution to yield soluble green material. The metal centres in **8** and **9** are more easily oxidized than those in the related phosphine-ether complexes, as judged by the $Ru^{III/II}$ reduction potentials determined by cyclic voltammetry (for **8**: $E_{ox}(Ru^{III/II}) = 1.31$ V; for **9**: $E_{ox}(Ru^{III/II}) = 1.36$ V *vs.* SCE; compared to ~ 1.5 V for the *P,O*-complexes), although these reduction potentials are close to that of $[cis\text{-}Ru(bpy)_2(py)_2]^{2+}$ ($E_{1/2}(Ru^{III/II}) = 1.28$ V *vs.* SCE).[2] These observed reduction potentials agree well with that predicted using Lever parameters (see Chapter Three, section 3.2; used $E_L = 0.24$ for ether moiety): $E_{1/2}(Ru^{III/II})_{calc} = 1.28$ V *vs.* SCE. Nonetheless, the pyridine-ether complexes can be stored as solids for years in air without noticeable oxidation. It should be noted, however, that slight fogging of the glass vials in which these PF_6^- salts are stored does occur after prolonged storage (> 2 years); this observation is suggestive of a slow degradation process that involves evolution of $HF_{(g)}$,

References begin on page 208.

although this has not been investigated. In the CV, the waves corresponding to the reduction of the bipyridyl rings were not well resolved. The Lever parameter predicted reduction potential for this type of complex is $E_{1/2}(bpy^{0/-})_{calc}$ = -1.39 V *vs.* SCE; thus, the predicted redox gap for pyridine-ether complexes is $\Delta E_{1/2(redox)calc}$ ~ 2.67 eV.

6.2.2 Structural determination of 8

Red prismatic crystals of the PyC1OMe complex **8** suitable for X-ray crystallographic analysis were grown from acetone solution; the complex crystallized with one solvent molecule in the asymmetric unit. An ORTEP representation of the solid-state molecular structure of **8** is shown in Figure 6.1. The crystallographic data, collection and refinement details are presented in Table A.6.1. Relevant bond lengths and angles are presented in Table 6.1.

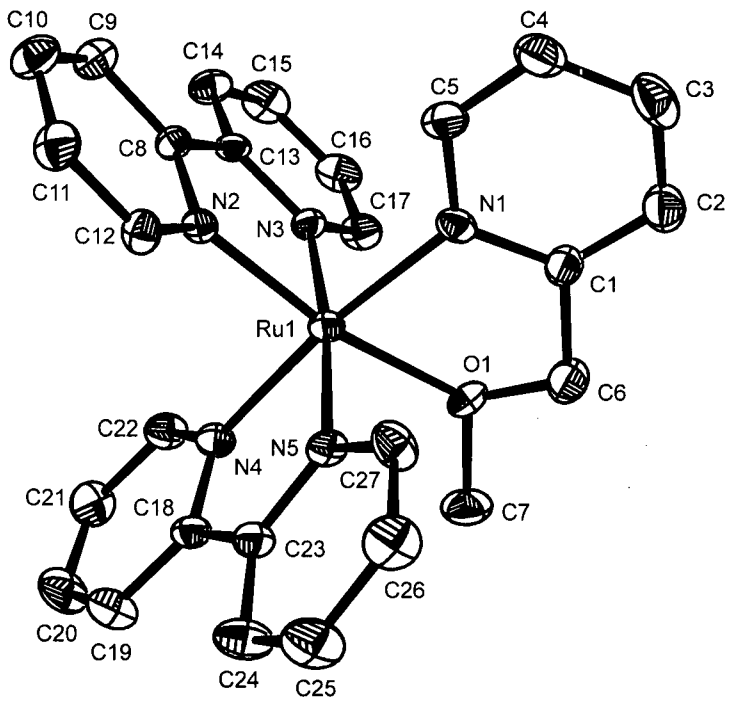

Figure 6.1. ORTEP representation of the solid-state molecular structure of **8**. Hydrogen atoms, hexafluorophosphate counterions and the cocrystallized acetone molecule are omitted for clarity.

References begin on page 208.

Table 6.1. Selected interatomic distances and bond angles for **8**

		Distances (Å)	
Ru(1)-O(1)	2.119(2)	Ru(1)-N(1)	2.076(3)
Ru(1)-N(2)	2.017(2)	Ru(1)-N(3)	2.046(3)
Ru(1)-N(4)	2.061(3)	Ru(1)-N(5)	2.071(3)
		Angles (°)	
O(1)-Ru(1)-N(1)	77.79(9)	O(1)-Ru(1)-N(3)	93.00(10)
O(1)-Ru(1)-N(4)	97.48(9)	O(1)-Ru(1)-N(5)	90.77(9)
N(1)-Ru(1)-N(2)	94.70(10)	N(1)-Ru(1)-N(3)	90.83(10)
N(1)-Ru(1)-N(5)	95.18(10)	N(2)-Ru(1)-N(3)	79.39(10)
N(2)-Ru(1)-N(4)	90.76(10)	N(2)-Ru(1)-N(5)	97.53(10)
N(3)-Ru(1)-N(4)	95.45(11)	N(4)-Ru(1)-N(5)	78.76(11)

The pyridine-ether ligand in **8** is bound in a bidentate fashion via the nitrogen and oxygen atoms; the geometry at the metal centre is distorted octahedral. The 5-membered pyridine-ether chelate ring (N1-Ru-O1 = 77.79(9)°) does not appear to be significantly more strained than the bpy-based chelate rings (N2-Ru-N3 = 79.39(10)°; N4-Ru-N5 = 78.76(11)°). The pyridyl and bipyridyl-based Ru-N distances are essentially equivalent. The Ru-N bond lengths are similar to those measured in the solid-state structures of **1-3**, although in the phosphine-ether complexes the Ru-N bond *trans* to P was lengthened relative to those *trans* to nitrogen and oxygen. The slightly shorter Ru(1)-N(2) bond *trans* to oxygen reflects the π-donation from the oxygen, as was also observed in the structures of **1-3**. However, the Ru-O distance of 2.119(2) Å is significantly shorter than the Ru-O bonds in the phosphine-ether complexes **1-3** (2.172 – 2.200 Å). This short bond combined with the lack of obvious strain in the pyridine-ether chelate ring suggest that the complex may be less predisposed to ether dissociation than the phosphine-ether complexes.

References begin on page 208.

6.2.3 Solution structures of 8 and 9

Unlike the phosphine-ether complexes discussed in the preceding chapters, these complexes lack the convenient ^{31}P NMR spectroscopic tag provided by the phosphine moiety. However, both pyridine-ether complexes **8** and **9** yield solution ^{1}H NMR spectra in which the methoxy and methylene ^{1}H resonances are well resolved from the aromatic resonances. For both complexes, the CH_2 protons are inequivalent. Because the [*cis*-Ru(bpy)$_2$] centre is chiral, however, these protons are diastereotopic; therefore, their magnetic inequivalence does not indicate that the pyridine-ether ligands are bound to the metal in a bidentate fashion. Somewhat surprisingly, the difference in chemical shift ($\Delta\delta$) between the resonances of these diastereotopic protons is larger when the ligand is *N*-bound rather than *N,O*-bound; after reaction of **9** with MeCN, $\Delta\delta$ increases to 1.03 from 0.31.

COSY and NOE ^{1}H NMR spectroscopies were used to probe the solution structure of **8**. Unlike for the *P,O*-complexes, the ^{1}H spectrum of **8** is sufficiently well resolved that the full spectrum could be assigned based on the COSY and NOE spectra. The ^{1}H NOE difference spectrum obtained for **8** upon selective irradiation of the methoxy ^{1}H resonance (δ 3.32) contained enhanced signals from the methylene protons (δ 5.55, d, 1H; 5.24, d, 1H) and from two bipyridine protons (δ 9.24, d, 1H; 8.00, d, 1H). These enhanced bpy resonances correspond to protons in the 6-positions on different bpy rings. If the ether is not coordinated to the metal, it should be free to rotate, and NOEs should therefore also be observed between the methoxy protons and pyridyl protons; however, this was not observed. Thus, the ^{1}H NMR studies of **8** suggest bidentate coordination of the PyC1OMe ligand in solution, just as is observed in the solid-state structure.

The ^{1}H NMR spectrum of the PyC2OMe complex **9** is very similar to that of **8**. The methoxy protons give rise to a singlet resonance at δ 3.06, and the methylene protons yield complex multiplets that span a chemical shift range of ~ 1 ppm (δ 4.23 – 3.98, m, 2H; 3.69, m, 1H; 3.36, m, 1H). Furthermore, the chemical shifts of the methylene and methoxy proton resonances change upon small-molecule coordination in a manner similar to **8**. Given these similarities, it is reasonable to conclude that the pyridine-ether ligand in this complex is also *N,O*-coordinated.

References begin on page 208.

6.3 Reactivity of pyridine-ether complexes toward small molecules

The reactions of complexes **8** and **9** with nucleophilic small molecules were studied via ^{1}H NMR spectroscopy, as described in Chapter Two for the phosphine-ether complex **1**. The opening of the *N,O*-chelate rings in **8** and **9** upon ether displacement was readily monitored by following the changes in chemical shifts of the resonances of the methoxy groups and the alkyl bridges between the ether and pyridine. The PyC2OMe complex **9** is more reactive toward ether displacement than the C1 congener **8**, as expected based on the assumption that its 6-membered chelate ring is slightly more strained than the 5-membered metallocycle in **8**. Both pyridine-ether complexes show considerably diminished reactivity toward small molecules compared to the phosphine-ether complexes described earlier in this thesis.

6.3.1 Reactions of 8 with small molecules

Complex **8** was treated with a variety of nucleophilic small molecules to investigate the potential hemilability of the pyridine-ether ligand. The reactions were carried out on NMR-scale samples ([**8**] ~ 5×10^{-3} M, in acetone-d_6 solution) at room temperature with 1 equiv of the analyte in question. Under these conditions, no reaction was detected between **8** and 1,4-dioxane, DMSO and MeCN; samples were analyzed again after a 16 h reaction time, with no noticeable changes observed. Similarly, no reaction was detected between **8** and CO (1 atm) and SO_2 (sample sparged with $SO_{2(g)}$).

6.3.1.1 Reaction with 3-methylpyridine

Treatment of **8** (~ 5×10^{-3} M) at room temperature with 1 equiv of 3-methylpyridine (δ 2.30 (s, CH_3Py)) slowly led to the formation of new products. After 3 d at temperature, approximately ~ 50 % of the complex had been consumed, to liberate free PyC1OMe ligand (δ 4.49 (s, CH_3O), 3.40 (s, CH_2)) and a complex whose ^{1}H NMR spectrum was tentatively assigned as [*cis*-Ru(bpy)$_2$(3-MePy)$_2$]$^{2+}$ (δ 2.19 (s, CH_3Py)). To confirm this assignment, the bis(3-MePy) complex was synthesized on a preparative scale, starting from **8**. Reaction of **8** with 1 equiv of 3-methylpyridine overnight in boiling acetone (56 °C) permitted isolation of

References begin on page 208.

this complex in ~ 25 % yield. Characterization of this complex by ^{1}H NMR confirmed that it indeed was the product formed via reaction between **8** and 3-MePy at room temperature. The analogous pyridine complex, [*cis*-Ru(bpy)$_2$(py)$_2$]$^{2+}$, is well known[2,9] and the 3-MePy complex was not characterized further.

6.3.1.2 Reaction with acetonitrile

Although no reaction was observed between **8** and acetonitrile when the complex was treated with 1 equiv of MeCN in acetone solution at room temperature, evidence of reaction was observed for a sample of **8** dissolved in neat MeCN. The ^{1}H NMR spectrum of **8** obtained in CD_3CN solution after a 2 h reaction time showed new methylene-derived resonances (δ 3.22, d; 4.25, d) consistent with partial conversion to a species with diastereotopic methylene protons that could be the product of ether displacement, **8•MeCN**. The system did not reach an equilibrium state after short reaction times because another reaction pathway was available to the complex. After 5 d, the major components in the mixture were unreacted **8** (~ 71 %) and **8•MeCN** (~ 16 %), according to integration of the methylene resonances; in addition, a significant amount (~ 13 %) of free PyC1OMe was also evident in the sample. Thus, both the ether and pyridine moieties were slowly displaced by MeCN. As for the reaction with 3-MePy, heating of the orange-red PyC1OMe complex **8** overnight in MeCN solution (81.5 °C) resulted in clean conversion to the orange bis(MeCN) complex (δ 2.46, s, CH_3). The identity of this product was confirmed by comparison of the ^{1}H NMR spectrum of this reaction mixture to that of an authentic sample of [*cis*-Ru(bpy)$_2$(MeCN)](PF$_6$)$_2$ prepared via the literature route.[10]

6.3.2 Reactions of 9 with small molecules

Similar experiments were performed with the PyC2OMe complex **9**. No reaction was observed for **9** when treated with CO (1 atm), H_2S or SO_2 (after sparging solution with the gases) at room temperature in acetone solution.

References begin on page 208.

6.3.2.1 Reaction of 9 with DMSO

Unlike complex **8**, **9** does react with DMSO. After overnight equilibration with 10 equiv of DMSO, a sample of **9** in acetone-d_6 solution ([**9**] $\approx 5 \times 10^{-3}$ M) gave rise to a ^{1}H NMR spectrum with a new resonance (δ3.25, s, CH_3O) consistent with formation of a DMSO-bound complex **9•DMSO**. However, the effective equilibrium constant for this reaction is estimated to be very small ($K_{eff} \approx 1 \times 10^{-4}$) based on integration of the methoxy resonances. Other resonances for the new complex could not be conclusively identified, and the reaction was not studied further.

6.3.2.2 Reaction of 9 with acetonitrile

Treatment of **9** with ~ 1 equiv of MeCN in acetone solution led to the formation of both **9•MeCN** (δ 2.92, s, CH_3O) and [*cis*-Ru(bpy)$_2$(MeCN)$_2$](PF$_6$)$_2$ after short reaction times at room temperature. Further, after 5 d at room temperature, a sample of **9** in neat CD_3CN contained ~ 38 % unreacted **9**, ~ 18 % **9•MeCN** and ~ 44 % free ligand according to integration of the methoxy resonances. Thus, the PyC2OMe complex **9** is somewhat more reactive toward MeCN than the PyC1OMe complex **8**. As for **8**, after overnight heating of **9** in neat MeCN, the complex was converted quantitatively into [*cis*-Ru(bpy)$_2$(MeCN)$_2$](PF$_6$)$_2$ due to displacement of both the pyridine and ether moieties from the metal.

6.3.3 Summary of reactivity of pyridine-ether complexes 8 and 9

The pyridine moieties in the pyridine-ether complexes **8** and **9** are not bound sufficiently strongly to the metal to anchor the ligand to the metal, and the desired hemilabile reactivity has not been observed. The preferred reaction of **8** with the nitrogen-based nucleophilic small molecules 3-methylpyridine and acetonitrile involved displacement of both the pyridine and ether moieties from the metal. Acetonitrile did displace the ether preferentially, but with time the pyridine moiety was also displaced by MeCN. The PyC2OMe complex **9** shows slightly enhanced reactivity toward small molecules than the PyC1OMe complex **8**, and the ether does appear to be somewhat more prone to displacement from the

References begin on page 208.

metal in **9** than it is in **8**. However, in neither complex does the pyridine-ether truly act as a hemilabile ligand. Thus, these complexes are not appropriate for use in small-molecule sensing because they do not undergo reversible interactions with small molecules.

6.4 Absorption and luminescence properties of 8 and 9

Although the pyridine-ether complexes **8** and **9** were found to not be suitable for development into small-molecule chemosensors, the question still remained as to whether replacement of the phosphine moiety by pyridine would lead to an improvement in the photoluminescence properties of the complexes. As is typical of $[cis\text{-}Ru(bpy)_2(L\text{-}L')]^{2+}$ complexes, complexes **8** and **9** are orange-red and brick-red in colour respectively. Their absorption spectra at room temperature contain broad, nearly structureless MLCT bands in the visible region (λ_{max}, ε: 459 nm, 10000 $M^{-1}cm^{-1}$ for **8**; 462 nm, 8700 $M^{-1}cm^{-1}$ for **9**). The energies of these MLCT bands are similar to those observed for other complexes with nitrogen-based nonchromophoric ligands, such as $[Ru(bpy)_3]^{2+}$ (λ_{max} = 452 nm, ε = 14450 $M^{-1}cm^{-1}$)[11] and $[cis\text{-}Ru(bpy)_2(py)_2]^{2+}$ (λ_{max} = 460 nm, ε = 9200 $M^{-1}cm^{-1}$).[2] The MLCT absorption energy predicted from the reduction potentials is ~ 2.88 eV (~ 431 nm), which is significantly higher in energy than that observed from **8** and **9**.

The photoluminescence of complexes **8** and **9** in solution was studied both at low temperature and at room temperature. At low temperature, both complexes are highly luminescent, as is usually observed for Ru(II) bis(bipyridyl) complexes. Figure 6.2 shows the luminescence spectra of complexes **8** and **9** obtained for samples in frozen acetone solution at 77 K. Maximum emission occurs at 625 nm and 637 nm for **8** and **9** respectively. As well, a weak shoulder near 530 nm (~ 2.34 eV) is observed in both emission spectra; these weak high-energy bands are in good agreement with the 0–0 energy predicted from the calculated redox gap ($E_{em}(0\text{–}0)_{calc}$ ~ 2.37 eV, or 523 nm). The broad, slightly structured emission bands resemble those observed for the phosphine-ether complexes discussed previously in this thesis (see Chapter Three for discussion, section 3.4.4) and are typical of $[cis\text{-}Ru(bpy)_2L_2]^{2+}$ complexes in general. However, the orange-red emission observed from these pyridine-ether

References begin on page 208.

complexes at low temperature is shifted slightly to lower energies than observed for most other $[cis\text{-}Ru(bpy)_2L_2]^{2+}$ complexes with nitrogen-based nonchromophoric ligands. In comparison, the emission maxima for $[cis\text{-}Ru(bpy)_2(py)_2]^{2+}$ (589 nm; 2.11 eV) and $[Ru(bpy)_3]^{2+}$ (584 nm; 2.12 eV) are higher in energy, although the pyridine-amine complex $[cis\text{-}Ru(bpy)_2(AEP)]^{2+}$ emits at similar energy (637 nm; 1.95 eV) to the pyridine-ether complexes.[1] It should be noted, however, that the observed emission maximum depends on which transitions are preferred (Chapter Three, section 3.4.4). The MLCT gap and predicted 0–0 energies for these complexes ($E_{em}(0\text{–}0)_{calc} \sim 2.37$ eV for **8** and **9**) are identical those predicted for the symmetric complexes $[cis\text{-}Ru(bpy)_2(py)_2]^{2+}$ and $[Ru(bpy)_3]^{2+}$. Thus, the emission from the asymmetric pyridine-ether and pyridine-amine complexes is simply dominated by lower energy vibronic bands.

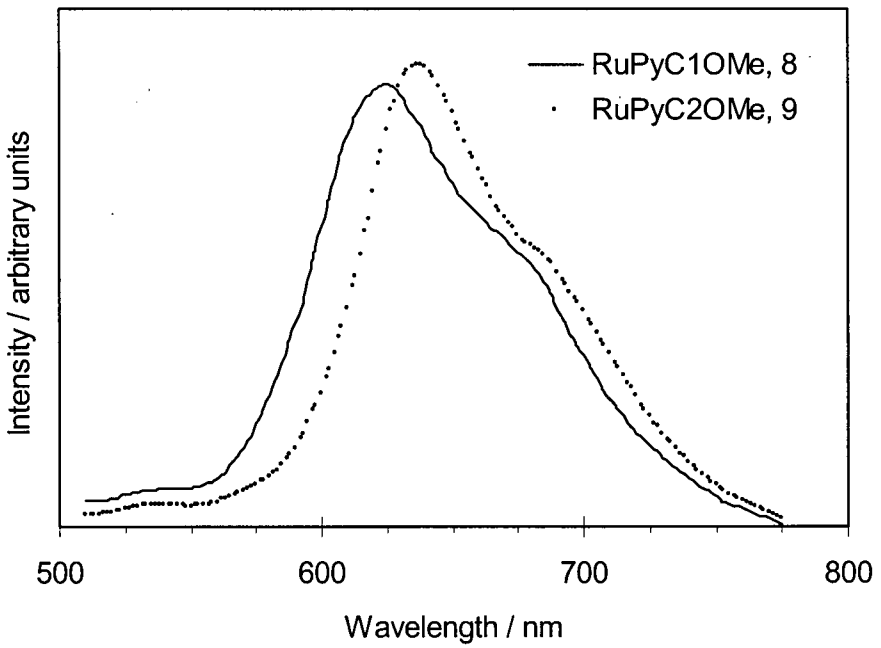

Figure 6.2. Photoluminescence spectra of **8** and **9** measured at 77 K in solid acetone solution, [**8**, **9**] = 7×10^{-3} M, λ_{ex} = 455 nm.

References begin on page 208.

At room temperature in deaerated CH_2Cl_2 solution, there is essentially no emission observable from either complex **8** or **9**. As noted in section 6.1, the pyridine-amine [*cis*-$Ru(bpy)_2(AEP)]^{2+}$ retains its emissive properties at room temperature (λ_{em} = 645 nm; E_{em}(0-0) = 1.92 eV), with a radiative efficiency ($\Phi = 6.6 \times 10^{-3}$) higher than that of [*cis*-$Ru(bpy)_2(py)_2]^{2+}$ ($\Phi = 4.2 \times 10^{-3}$).[1] This suggests that symmetry considerations are not responsible for the diminished luminescence yields from the pyridine-ether complexes. The ether moiety itself must, therefore, play a key role in decreasing the thermal energy barrier between the emissive MLCT excited state and nonemissive metal-based dd excited state. Detailed studies of the temperature dependence of the luminescence of **8** and **9** are underway in the laboratory of Prof. W. E. Jones, Jr., at SUNY Binghamton. Preliminary results from this collaboration suggest that these complexes may have a more complicated excited-state manifold than most [*cis*-$Ru(bpy)_2L_2]^{2+}$ complexes, with a second luminescent excited state that contributes to the emission observed from **8** and **9** at low temperatures. At this time, however, the simple conclusion can be made that replacement of the phosphine moiety in the hemilabile *P,O*-ligands with pyridine does not lead to an enhancement of the room temperature photoluminescence of [*cis*-$Ru(bpy)_2(L\text{-}L')]^{2+}$ complexes.

6.5 Summary

In this chapter, an attempt to rationally design small-molecule responsive [*cis*-$Ru(bpy)_2(L\text{-}L')]^{2+}$ complexes with improved room temperature photoluminescence was described. Based on the fact that complexes with nitrogen-based nonchromophoric ligands L-L' tend be luminescent at ambient temperatures, pyridine-ether ligands were investigated. Although the pyridine-ether complexes **8** and **9** do show sluggish reactivity toward certain small molecules, the reactions predominantly involve displacement of both the ether and the pyridine moieties. Thus, the PyCnOMe ligands studied here do not function as hemilabile ligands, which renders their [*cis*-$Ru(bpy)_2(L\text{-}L')]^{2+}$ complexes unsuitable as small-molecule chemosensors. Furthermore, complexes **8** and **9** do not luminesce in solution at room temperature, although they do show typical [*cis*-$Ru(bpy)_2(L\text{-}L')]^{2+}$ emission at 77 K.

References begin on page 208.

6.6 Experimental section

6.6.1 Materials and methods

2-Methoxypyridine (PyOMe) was purchased from Aldrich, and 2-(methoxymethyl)pyridine (PyC1OMe) was prepared via a literature route.[8] 2-(2-Hydroxyethyl)pyridine was available commercially (Aldrich).

6.6.2 Preparation and characterization of pyridine-ether ligands

6.6.2.1 Preparation of 2-(2-methoxyethyl)pyridine, PyC2OMe

Although this compound has been known for decades, a satisfactory synthetic procedure was not found in the literature. For this reason, the details regarding the preparation of this compound are reported here.

A suspension of NaH (3.14 g, 131 mmol) in freshly distilled diethyl ether (60 mL) was stirred and treated dropwise with ~1 equiv 2-(2-hydroxyethyl)pyridine (Aldrich, 14.9 mL, 132 mmol). Additional ether (total volume 150 mL) was added to maintain stirring as the mixture thickened to a brown-yellow slurry. The mixture was stirred overnight under nitrogen, then 1 equiv methyl iodide (8.1 mL, 130 mmol) as a solution in ether (20 mL) was added dropwise. An orange-brown, gummy solid precipitated. The mixture was stirred at RT for 2 h, heated to reflux for 2 h, then THF (30 mL) was added to improve solubility, and the mixture was stirred overnight. The reaction mixture was treated with water, then the dark brown aqueous fraction was extracted with ether (4 × 200 mL). The combined organic extracts were dried over anhydrous $MgSO_4$ and evaporated to dryness to yield a brown oil. Yield: ~ 25 mL. Purified by distillation (106 – 108 °C, 10 mm Hg). The colourless liquid slowly turned pale brown even when stored under N_2 at 5 °C in the dark. ^{1}H NMR (200 MHz, 25 °C, CD_3CN): δ8.46 (d, J = 3.43 Hz, 1H), 7.63 (m, 1H), 7.22 (d, J = 7.81 Hz, 1H), 7.14 (m, 1H), 3.70 (t, J = 6.59 Hz, 2H), 3.25 (s, 3H, OCH_3), 2.96 (t, J = 6.59 Hz, 2H).

References begin on page 208.

6.6.3 Preparation and characterization of complexes

6.6.3.1 Preparation of [cis-Ru(bpy)$_2$(PyC1OMe-N,O)](PF$_6$)$_2$, 8

This complex was prepared via the same route described for the phosphine-ether complexes **1-3**. Freshly distilled 2-methoxymethylpyridine (0.605 g, 4.91 mmol) was reacted with [*cis*-Ru(bpy)$_2$(acetone)$_2$](BF$_4$)$_2$ (4.83 mmol) in refluxing deaerated acetone solution (175 mL) overnight, under nitrogen atmosphere. The crude BF_4 salt was metathesized to the PF_6 salt, which was collected on a frit, washed with water and diethyl ether, and dried by suction. The orange-red PF_6 salt was obtained analytically pure after drying *in vacuo* at RT overnight. Yield: 3.8 g (95 %). Crystallization from acetone solution yielded red prismatic crystals of [*cis*-Ru(bpy)$_2$(PyC1OMe-*N,O*)](PF$_6$)$_2$•(acetone) of suitable quality for X-ray crystallographic analysis. ^{1}H NMR (400 MHz, 25 °C, acetone-d_6): δ9.24 (d, J_{HH} = 5.5 Hz, 1H), 8.92 (d, J_{HH} = 8.1 Hz, 1H), 8.81 (d, J = 8.2 Hz, 2H), 8.71 (d, J = 8.2 Hz, 1H), 8.66 (d, J = 5.7 Hz, 1H), 8.39 (ddd, J_1 = 7.76 Hz, J_2 = 8.09 Hz, J_3 = 1.45 Hz, 1H), 8.3 (ddd, J_1 = 7.81 Hz, J_2 = 8.03 Hz, J_3 = 1.48 Hz, 1H), 8.15 (ddd, J_1 = 7.81 Hz, J_2 = 8.15 Hz, J_3 = 1.47 Hz, 1H), 8.07 – 7.99 (m, 3H), 7.86 – 7.77 (m, 4H), 7.60 (d, J = 5.33 Hz, 1H), 7.51 (ddd, J_1 = 5.85 Hz, J_2 = 5.72 Hz, J_3 = 1.28 Hz, 1H), 7.38 (ddd, J_1 = 5.91 Hz, J_2 = 5.90 Hz, J_3 = 1.35 Hz, 1H), 7.34 (t, J = 6.6 Hz, 1H), 5.55 (d, J = 14.4 Hz, 1H), 5.24 (d, J = 14.4 Hz, 1H), 3.32 (s, 3H, OCH_3). Elemental analysis calcd. for $C_{27}H_{25}F_{12}N_5OP_2Ru$ (%): C, 39.24; H, 3.05; N, 8.47; found: C, 38.91; H, 2.96; N, 8.27. Vis (acetone, λ_{max}, ε): 459 nm, 10000 $M^{-1}cm^{-1}$; sh 414 nm, 6000 $M^{-1}cm^{-1}$; 350 nm, 10000 $M^{-1}cm^{-1}$. CV (200 mV/s, 25 °C, CH_2Cl_2/^{n}Bu$_4$NPF$_6$, V *vs.* SCE): $E_{ox}(Ru^{III/II})$ = 1.31 V, oxidized species adsorbs to Pt; ligand reduction waves not resolved.

^{1}H NMR NOE difference spectrum (400 MHz, 25 °C, acetone-d_6). Peaks enhanced from through-space effects independent of scalar coupling to the irradiated resonance are noted in bold. Irradiation of methoxy proton resonance at δ 3.32 enhanced two aromatic resonances and the methylene resonances: δ **9.24** (d), **8.00** (d), **5.55** (d), **5.24** (d). Selected aromatic resonances: irradiated δ9.24 (d), enhanced **8.00** (d, weak), 7.84 (m), **3.32** (s); irradiated 8.92 (d), enhanced **8.81** (d), 8.39 (m); irradiated 8.81 (d), enhanced **8.92** (d), 8.71 (d), **8.32** (d), **8.15** (d).

References begin on page 208.

^{1}H COSY spectrum (400 MHz, 25 °C, acetone-d_6). Ether-substituted pyridine: δ 7.60 (d, 3-position, NOE to CH_2) – 7.34 (m) – 8.01 (m) – 7.78 (d, 6-position). Bpy_A: δ 9.24 (d, 6-position, NOE to CH_3) – 7.81 (m) – 8.30 (m) – 8.83 (3-position) – NOE to 8.71 (d, 3'-position) – 8.05 (m) – 7.38 (m) – 7.84 (d, 6'-position). Bpy_B: δ 8.66 (d, 3"-position, weak NOE to CH_2) – 7.81 (m), 8.39 (m) – 8.92 (d, 6"-position) – NOE to 8.79 (m, 3'"-position) – 8.15 (m) – 7.51 (m) – 8.00 (d, 6'"-position).

X-ray crystallographic structural determination of 8 (Dr. S. J. Rettig)

A red prismatic crystal of **8** grown from acetone solution was selected and mounted on a thin glass fibre. Data were collected at 180 (± 1) K on a Rigaku/ADSC CCD area detector in two sets of scans (ϕ = 0.0 to 190.0°, χ = -90.0°; and ω = -23.0 to 18.0°, χ = -90.0°) using 0.50° oscillations with 8.0 second exposures. Data were collected and processed using the d*TREK program (Molecular Structure Corporation); the structure was solved using heavy-atom Patterson methods[12] and expanded using Fourier techniques.[13] The nonhydrogen atoms were refined anisotropically. All calculations were performed using the teXsan crystallographic software package (Molecular Structure Corporation). The complex crystallizes in the space group $P2_1/n$ (No. 14) with one molecule of acetone in the asymmetric unit. The crystallographic and refinement details are summarized in Table A.6.1. The ORTEP representation of the solid-state molecular structure of **8** was prepared using ORTEP-32 for Windows.[14]

6.6.3.2 Preparation of [cis-Ru(bpy)$_2$(3-MePy)$_2$](PF$_6$)$_2$

Complex **8** (0.257 g, 0.312 mmol) was dissolved in acetone (15 mL) and the solution was deaerated via sparging with nitrogen. To this solution was added 1 equiv of 3-methylpyridine (32 μL, 0.33 mmol) and the mixture was heated to reflux overnight, with no visible changes apparent. The solvent was evaporated, the residue was washed with hexanes and the solid was metathesized to the PF_6^- salt, collected on a frit, washed with ether and dried by suction. Yield: 73 mg (~ 25 %). ^{1}H NMR (200 MHz, 25 °C, acetone-d_6): δ9.33 (d, J_{HH} = 5.6 Hz, 2H), 8.64 (d, J_{HH} = 7.9Hz, 2H), 8.56 (d, J_{HH} = 8.0 Hz, 2H), 8.48 – 8.43 (m, 4H), 8.30 –

References begin on page 208.

8.21 (m, 4H), 8.09 – 8.00 (m, 2H), 7.95 – 7.88 (m, 2H), 7.76 (d, J_{HH} = 7.8 Hz, 2H), 7.54 – 7.47 (m, 2H), 7.32 (d, J_{HH} = 5.8 Hz, 1H), 7.28 (d, J_{HH} = 5.7 Hz, 1H), 2.19 (s, 3H).

6.6.3.3 Preparation of [cis-Ru(bpy)$_2$(PyC2OMe-N,O)](PF$_6$)$_2$, 9

Prepared as described for complex **8** but required a much longer reaction time. One equiv of 2-(2-methoxyethyl)pyridine (0.612 g, 4.46 mmol) as a solution in acetone (90 mL) was added to a deaerated solution of [*cis*-Ru(bpy)$_2$(acetone)$_2$](BF$_4$)$_2$ (4.47 mmol) in acetone (70 mL) and heated to reflux for one week under nitrogen (monitored by TLC on silica gel, 30:10:5 acetone/H_2O/sat. $KNO_{3(aq)}$). After precipitation of the complex with $NH_4PF_{6(aq)}$ and suction-drying on a frit, the PF_6 salt was obtained as an analytically pure brick-red powder. Yield: 3.3 g (85 %). ^{1}H NMR (200 MHz, 25 °C, acetone-d_6): δ9.62 (d, J = 5.65 Hz, 1H), 8.92 (d, J = 8.03 Hz, 1H), 8.82 – 8.71 (m, 3H), 8.62 (d, J = 7.59 Hz, 1H), 8.43 – 8.27 (m, 2H), 8.14 (m, 1H), 8.07 – 7.82 (m, 6H), 7.65 – 7.35 (m, 4H), 7.21 (m, 1H), 4.23 – 3.98 (m, 2H), 3.69 (m, 1H), 3.36 (m, 1H), 3.06 (s, 3H, OCH_3). Elemental analysis calcd. for $C_{28}H_{27}F_{12}N_5OP_2Ru$ (%): C, 40.01; H, 3.23; N, 8.33; found: C, 40.28; H, 3.17; N, 8.24. Vis (acetone, λ_{max}, ε): 462 nm, 8700 $M^{-1}cm^{-1}$; sh 430 nm, 6500 $M^{-1}cm^{-1}$. CV (200 mV/s, 25 °C, CH_2Cl_2/^{n}Bu$_4$NPF$_6$, V *vs.* SCE): $E_{ox}(Ru^{III/II})$ = 1.36 V, oxidized species adsorbs to Pt; ligand reduction waves not resolved.

References begin on page 208.

6.7 References

(1) Caspar, J. V.; Meyer, T. J. *Inorg. Chem.* **1983**, *22*, 2444.

(2) Durham, B.; Walsh, J. L.; Carter, C. L.; Meyer, T. J. *Inorg. Chem.* **1980**, *19*, 860.

(3) Slone, C. S.; Weinberger, D. A.; Mirkin, C. A. *Prog. Inorg. Chem.* **1999**, *48*, 233.

(4) Orrell, K. G.; Osborne, A. G.; Sik, V.; Da Silva, M. W. *Polyhedron* **1995**, *14*, 2797.

(5) Schutte, R. P.; Rettig, S. J.; Joshi, A. M.; James, B. R. *Inorg. Chem.* **1997**, *36*, 5809.

(6) Yang, H.; Alvarez-Gressier, M.; Lugan, N.; Mathieu, R. *Organometallics* **1997**, *16*, 1401.

(7) Jones, N. D.; MacFarlane, K. S.; Smith, M. B.; Schutte, R. P.; Rettig, S. J.; James, B. R. *Inorg. Chem.* **1999**, *38*, 3956.

(8) Naito, T.; Ueno, K. *Yakugaku Zasshi* **1959**, *79*, 1277; used translated procedure found in *Chem. Abstr.* **1960**, *51*, 4566h.

(9) Dwyer, F. P.; Goodwin, H. A.; Gyarfas, E. C. *Aust. J. Chem.* **1963**, *16*, 544.

(10) Brown, G. M.; Callahan, R. W.; Meyer, T. J. *Inorg. Chem.* **1975**, *14*, 1915.

(11) Crutchley, R. J.; Lever, A. B. P. *Inorg. Chem.* **1982**, *21*, 2276.

(12) Beurskens, P. T.; Admiraal, G.; Beurskens, G.; Bosman, W. P.; Garcia-Granda, S.; Gould, R. O.; Smits, J. M. M.; Smykalla, C. "The DIRDIF program system, Technical Report of the Crystallography Laboratory," University of Nijmegen, 1992.

(13) Beurskens, P. T.; Admiraal, G.; Beurskens, G.; Bosman, W. P.; deGelder, R.; Israel, R.; Smits, J. M. M. "The DIRDIF-94 program system, Technical Report of the Crystallography Laboratory," University of Nijmegen, 1994.

(14) Farrugia, L. J. *J. Appl. Cryst.* **1997**, *30*, 565.

References begin on page 208.

Appendix 6.1 Crystallographic details

The crystallographic data for **8** have been neither published nor submitted to the CCDC. Atomic coordinates are provided in Table A.6.2.

Table A.6.1. Crystallographic data, collection and refinement details for **8**

	8•acetone
Formula	$C_{30}H_{31}F_{12}N_5O_2P_2Ru$
M	884.61
μ / cm^{-1}	6.41
T / K	180(1)
Colour, habit	red, prism
Crystal system	monoclinic
Space group	$P2_1/n$ (No. 14)
a / Å	12.1374(14)
b / Å	12.1118(14)
c / Å	23.8647(4)
α / deg	90
β / deg	93.8140(5)
γ / deg	90
V / $Å^3$	3500.5(4)
ρ_{calc} / $g{\cdot}cm^{-3}$	1.68
Z	4
Refl. collected/unique/R_{int}	30649/9229/0.040
R_1[a]	0.043
wR_2[b]	0.080
GOF	1.51

[a]$R_1 = \Sigma \big| |F_o| - |F_c| \big| / \Sigma |F_o|$ (observed data), $I>3\sigma(I)$. [b]$wR_2 = (\Sigma(F_o^2 - F_c^2)^2 / \Sigma w(F_o^2)^2)^{½}$ (all data), $I>0.00\sigma(I)$.

References begin on page 208.

Table A.6.2. Atomic coordinates and B_{iso}/B_{eq} for **8**

Atom	x	y	z	B_{eq} [a]
Ru(1)	0.4567(2)	0.73005(2)	0.119994(10)	1.319(5)
P(1)	0.42040(9)	0.26070(9)	0.23410(4)	2.41(2)
P(2)	0.90538(8)	0.21679(9)	0.10035(4)	2.29(2)
F(1)	0.4255(2)	0.3198(2)	0.17547(8)	3.71(6)
F(2)	0.3006(2)	0.3090(3)	0.23872(9)	5.60(8)
F(3)	0.4698(2)	0.3682(2)	0.26514(9)	4.25(7)
F(4)	0.4151(3)	0.2023(2)	0.29244(9)	8.16(11)
F(5)	0.5416(2)	0.2150(2)	0.22879(12)	6.55(8)
F(6)	0.3726(3)	0.1535(2)	0.20302(10)	5.40(8)
F(7)	0.8418(2)	0.3131(2)	0.06791(9)	5.15(7)
F(8)	0.8360(3)	0.1286(2)	0.06562(13)	7.37(9)
F(9)	0.8188(2)	0.2183(2)	0.14708(10)	5.42(7)
F(10)	0.9703(2)	0.1196(2)	0.13283(9)	3.79(6)
F(11)	0.9754(2)	0.3066(2)	0.13580(10)	5.24(8)
F(12)	0.9941(3)	0.2155(3)	0.05478(10)	6.61(9)
O(1)	0.3841(2)	0.6891(2)	0.19668(8)	1.92(5)
O(2)	-0.1847(3)	0.7368(3)	0.04505(12)	5.07(9)
N(1)	0.3349(2)	0.6128(2)	0.09472(10)	1.53(6)
N(2)	0.4884(2)	0.7705(2)	0.04123(9)	1.33(5)
N(3)	0.3415(2)	0.8546(2)	0.10299(10)	1.41(6)
N(4)	0.5773(2)	0.8312(2)	0.15292(10)	1.47(6)
N(5)	0.5791(2)	0.6173(2)	0.13614(10)	1.45(6)
C(1)	0.2895(3)	0.5557(3)	0.13642(13)	1.81(8)
C(2)	0.2133(3)	0.4731(3)	0.12554(15)	2.37(9)
C(3)	0.1816(3)	0.4470(3)	0.0704(2)	2.89(10)
C(4)	0.2263(3)	0.5065(3)	0.02735(14)	2.44(9)
C(5)	0.3000(3)	0.5890(3)	0.04102(13)	2.04(8)
C(6)	0.3368(3)	0.5814(3)	0.19513(13)	2.26(9)

References begin on page 208.

Atom	x	y	z	B_{eq} [a]
C(7)	0.4400(3)	0.7103(3)	0.25060(13)	2.80(9)
C(8)	0.4235(3)	0.8496(3)	0.01573(12)	1.42(7)
C(9)	0.4307(3)	0.8761(3)	-0.04071(13)	2.07(8)
C(10)	0.5078(3)	0.8228(3)	-0.07096(13)	2.29(9)
C(11)	0.5760(3)	0.7448(3)	-0.04446(12)	2.16(8)
C(12)	0.5654(3)	0.7217(3)	0.01162(12)	1.70(7)
C(13)	0.3435(3)	0.9008(3)	0.05110(12)	1.39(7)
C(14)	0.2786(3)	0.9925(3)	0.03635(13)	2.01(8)
C(15)	0.2808(3)	1.0350(3)	0.07428(15)	2.46(9)
C(16)	0.2049(3)	0.9860(3)	0.12614(14)	2.24(9)
C(17)	0.2706(3)	0.8961(3)	0.13908(13)	1.96(8)
C(18)	0.6757(3)	0.7802(3)	0.16647(12)	1.54(7)
C(19)	0.7686(3)	0.8404(3)	0.18553(14)	2.37(9)
C(20)	0.7614(3)	0.9533(3)	0.19118(15)	2.79(10)
C(21)	0.6613(3)	1.0045(3)	0.17932(14)	2.40(9)
C(22)	0.5709(3)	0.9413(3)	0.16011(13)	1.90(8)
C(23)	0.6751(3)	0.6613(3)	0.15795(12)	1.63(8)
C(24)	0.7675(3)	0.5936(3)	0.17138(14)	2.40(9)
C(25)	0.7597(3)	0.4819(3)	0.1613(2)	2.77(10)
C(26)	0.6619(3)	0.4383(3)	0.13823(15)	2.47(9)
C(27)	0.5737(3)	0.5078(3)	0.12613(14)	2.08(8)
C(28)	-0.0494(4)	0.8706(4)	0.0701(2)	4.35(13)
C(29)	-0.0893(3)	0.7557(4)	0.06039(14)	2.89(10)
C(30)	-0.0084(4)	0.6663(4)	0.0689(2)	4.44(13)
H(1)	0.1819	0.4332	0.1565	2.8
H(2)	0.1285	0.3875	0.0618	3.5
H(3)	0.2053	0.4893	-0.0120	2.9
H(4)	0.3288	0.6328	0.0107	2.4
H(5)	0.3939	0.5270	0.2063	2.7
H(6)	0.2778	0.5781	0.2212	2.7

References begin on page 208.

Atom	x	y	z	B_{eq} [a]
H(7)	0.4983	0.6553	0.2581	3.4
H(8)	0.4726	0.7843	0.2507	3.4
H(9)	0.3870	0.7058	0.2798	3.4
H(10)	0.3816	0.9319	-0.0587	2.5
H(11)	0.5140	0.8400	-0.1107	2.7
H(12)	0.6314	0.7061	-0.0652	2.6
H(13)	0.6156	0.6680	0.0305	2.0
H(14)	0.2829	1.0268	-0.0006	2.4
H(15)	0.1610	1.0988	0.0643	2.9
H(16)	0.1561	1.0152	0.1537	2.7
H(17)	0.2661	0.8607	0.1758	2.4
H(18)	0.8388	0.8025	0.1949	2.8
H(19)	0.8268	0.9967	0.2035	3.3
H(20)	0.6538	1.0844	0.1844	2.9
H(21)	0.5000	0.9782	0.1515	2.3
H(22)	0.8365	0.6257	0.1877	2.9
H(23)	0.8232	0.4337	0.1704	3.3
H(24)	0.6552	0.3590	0.1306	3.0
H(25)	0.5045	0.4766	0.1096	2.5
H(26)	0.0073	0.8876	0.0441	5.2
H(27)	-0.0180	0.8778	0.1089	5.2
H(28)	-0.1113	0.9220	0.0639	5.2
H(29)	-0.0442	0.5954	0.0597	5.3
H(30)	0.0206	0.6656	0.1082	5.3
H(31)	0.0524	0.6781	0.0445	5.3

[a] $B_{eq} = (8/3)\pi^2(U_{11}(aa^*)^2 + U_{22}(bb^*)^2 + U_{33}(cc^*)^2 + 2U_{12}aa^*bb^*\cos\gamma + 2U_{13}aa^*cc^*\cos\beta + 2U_{23}bb^*cc^*\cos\alpha)$

References begin on page 208.

Chapter Seven

A luminescent Ru(II) complex containing a hemilabile phosphine pyrenyl-ether with reactivity toward carbon monoxide

7.1 Molecular sensors based on a metal-tethered lumophore

While the combination receptor-reporter design of the $[cis\text{-}Ru(bpy)_2(POR)]^{2+}$ lumophores discussed in Part 1 of this thesis (Chapters Two to Six) permits analytes to directly influence the photophysical properties of the lumophore, the lack of room temperature luminescence from these complexes provided the impetus to investigate another molecular sensor design. Instead of using a metal-based lumophore that performs both receptor and reporter functions, in this design an organic emitter is tethered to a metal-based receptor module. This modular assemblage was designed to exploit the distance dependence of energy- and electron-transfer processes introduced in Chapter One (section 1.2). With an organic emitter attached to the labile end of a hemilabile ligand, coordination of an analyte (A) to the metal changes the distance between the lumophore and the metal centre, as depicted in Scheme 7.1. If the metal is able to quench the luminescence of the organic emitter, then modulation of

References begin on page 256.

the distance between the two moieties may lead to analyte-induced OFF-ON switching of the luminescence.

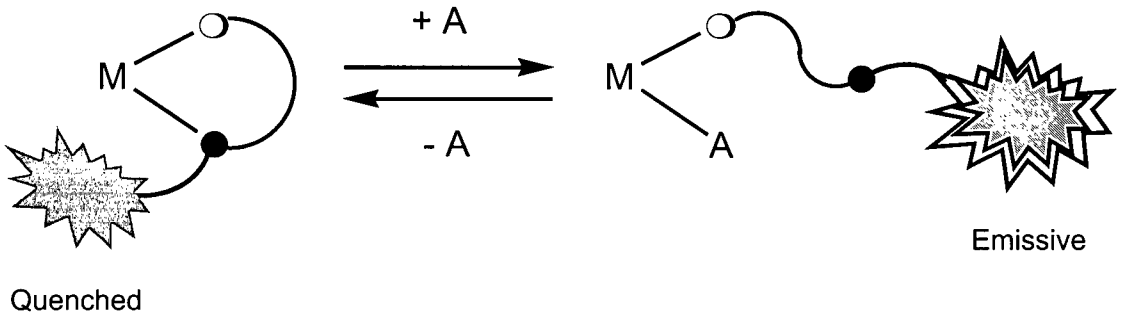

Scheme 7.1.

7.1.1 Hemilabile ligands with pendant pyrene lumophores

In light of the success thus far with Ru(II) phosphine-ether complexes as small-molecule receptors, phosphine-ether ligands with pendant organic lumophores were targeted for use in this modular molecular sensor design. The ether functionality provides sufficient synthetic versatility that a number of different organic lumophores may be incorporated into phosphine-ether ligands. Furthermore, the nature of the bridge between the phosphine and ether can be changed, as can the length of the tether between the ether oxygen and the organic lumophore. According to Scheme 7.1, the coordination of analyte to the metal centre should induce an increase in luminescence because the lumophore moves farther away from the open-shell metal. The magnitude of this response should, therefore, be dependent upon the difference between the lumophore-to-metal distance in the analyte-free and analyte-bound forms of the sensor complex. For this reason, it was of interest to compare the performance of complexes that contain hemilabile ligands with short *vs.* long tethers connecting the labile ether moiety and the pendant lumophore.

The modular-design molecular sensor presented in this chapter employs pyrene as the lumophore. Pyrene was selected based on both its well-understood room-temperature

References begin on page 256.

luminescence properties (see section 7.1.2) and the lack of functional groups within the lumophore. The simple unfunctionalized aromatic nature of pyrene is appealing for two reasons:

(a) there are no sensitive functional groups to protect during the preparation of the phosphine-ether, which makes the pyrene moiety quite versatile synthetically; and,

(b) the potential sites by which a pyrene-substituted phosphine-ether ligand might coordinate to a metal centre are limited to the phosphorus and oxygen atoms.

7.1.2 A brief introduction to pyrene as a lumophore

Pyrene is a well-studied polycyclic aromatic compound that absorbs in the UV region of the spectrum and emits intense indigo-blue fluorescence in dilute solution.[1] The emissive excited state arises from a π–π^* transition; it is singlet in character, relatively long-lived (τ = 450 ns) and leads to efficient fluorescence (Φ = 0.60) in solution at room temperature.[2] Even at room temperature, the emission spectra of pyrene-containing compounds show clearly resolved vibrational components, with several sharp bands in the range of 370 – 410 nm, plus broadened bands to lower energy. The relative intensities of the vibronic bands are markedly solvent dependent, with the highest energy (0–0) band strongly enhanced in polar solvents.[2] Furthermore, the long-lived excited state of pyrene is susceptible to quenching both via energy transfer to oxygen and many other molecules and via electron transfer to a variety of electron acceptors, including open-shell metal ions. Thus, pyrene emission can reveal information about the environment in which the lumophore sits, and pyrene is often used as a luminescent probe in studies of proteins, nucleic acids,[3] micellar systems[4] and synthetic polymers,[4,5] as well as in molecule-based sensors.[6-15]

The large planar structure of pyrene results in a strong propensity toward self-aggregation. The result of these hydrophobic interactions is that pyrene shows strongly concentration-dependent photoluminescence properties. In concentrated solution, π-stacked dimers can form between ground-state and excited-state pyrene molecules. These excited-state

References begin on page 256.

dimers, known as *excimers*, are stabilized relative to the pyrene monomer and therefore emit lower energy photons, such that pyrene excimer emission is blue-green rather than indigo-blue. Excimer emission is also observed from molecules that contain pyrene units held in close proximity to each other by short linkers,[16] even in dilute solution. Excellent discussions of pyrene excimers are available in a review by Winnik,[4] as well as in the book by Birks.[1] Pyrene excimer emission is characterized by its broad, structureless spectrum centred at ~ 480 nm and is less sensitive to quenching than monomer emission. Excimer emission from linked pyrenes, in particular, shows strong solvent dependence; the emission can often be switched from predominantly monomer to excimer simply by changing solvents.[3]

7.1.2.1 Pyrene as the response module in molecule-based sensors

Pyrene is a popular lumophore for molecule-based sensor applications, particularly those based on photoinduced electron-transfer (PET) processes.[17] For example, pyrenes have been attached to hydroxamate-based ligands and used to signal the presence of open-shell metals such as Fe^{3+},[7] Cu^{2+} and Ni^{2+},[8] which quench the luminescence. The binding of filled-shell metal ions, such as Zn^{2+}, can also lead to quenching if it induces conformational changes that alter the distance between the pyrene unit and an electron acceptor within the same molecule, or if the metal-receptor complex itself can act as an acceptor.[15] Similarly, pyrene moieties attached to crown ethers can respond to the presence of alkali metals,[18,19] and the distance between the pyrene unit and the quencher has indeed been shown to be critical for PET-based quenching to occur;[19] tethers of four-carbon alkyl chains are sufficiently long to dramatically reduce the efficiency of the PET process.

Switching between pyrene monomer and excimer emission is also a common approach to sensor response, whereby the ability of pyrene moieties to interact with one another is influenced by the binding of analyte to the receptor.[17] For example, pyrene units substituted with hydrogen bond donors specific for pyrophosphate switch from monomer to excimer emission when treated with pyrophosphate, because one pyrophosphate binds to, and brings together, two of the pyrene units.[14] In the same way, the hydroxamate system mentioned above[7] responds to the presence of Ga^{3+} by switching from monomer to excimer emission, since the metal ion coordinates three of the hydroxamate-functionalized pyrenes.

References begin on page 256.

7.1.3 The scope of this chapter

In this chapter, phosphine-ethers that contain a pyrene moiety as part of the ether substituent, but are otherwise similar to the POMe and PC2OMe ligands used earlier in this work, are discussed. Attempts to prepare phosphine-ethers with both short- and long-tether lengths between the oxygen and the pyrene unit are described. A long-tether version, 4-(2-(diphenylphosphino)phenoxy)butylpyrene (POC4Pyr), was successfully prepared, and its synthesis and characterization as a lumophore are presented. The bulk of the chapter is focused on the results of studies of POC4Pyr as a ligand on Ru(II) and the reactivity of the complex $RuCl_2$(POC4Pyr-*P,O*)$_2$, **10**, toward carbon monoxide. Displacement of the pyrenyl-ether from the metal centre upon CO coordination leads to changes in luminescence properties. These changes are different from the response expected from consideration of Scheme 7.1, with pyrene monomer-to-excimer emission switching observed rather than OFF-ON switching due to quenching; this is likely related to the length of the ether-pyrene tether.

7.2 Phosphine-ether ligands with a pendant pyrene

7.2.1 Attempts to synthesize short-tethered pyrenyl ethers

The pyrene-substituted phosphine-ethers directly analogous to the POMe and PC2OMe ligands in complexes **1** and **3** depicted below were the original ligands of interest for the investigations into the modular receptor-lumophore system shown in Scheme 7.1. These phosphine-ethers have short (one carbon) tethers between the ether oxygen and the pyrene, and the pyrene luminescence was anticipated to be quenched when bound to Ru(II).

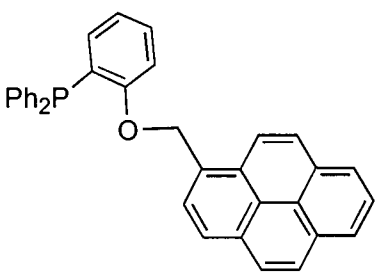

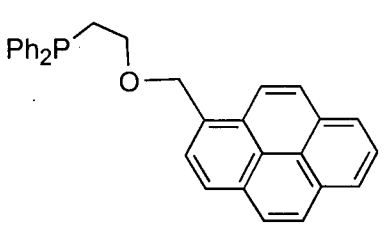

References begin on page 256.

However, methylpyrenyl ethers proved to be challenging synthetic targets, although a variety of routes was attempted. Each route was prone to an undesired reaction that dominated the chemistry, and ultimately the desired phosphine-ether was not successfully prepared in isolable quantities. These routes and their outcomes are summarized in the following schemes, with the hope that these results will provide insight for those who pursue these ligands in the future.

The route analogous to that used in the preparation of the phenyl-isopropyl-ether PO^{i}Pr is shown in Scheme 7.2. Reaction of the bromophenoxymethylpyrene intermediate with either Mg or butyllithium led to deeply coloured solutions that did not yield the desired products when treated with $ClPPh_2$. The pyrene moiety is believed to be incompatible with formation of Grignard and organolithium reagents due to reduction of the ring system by the metals.

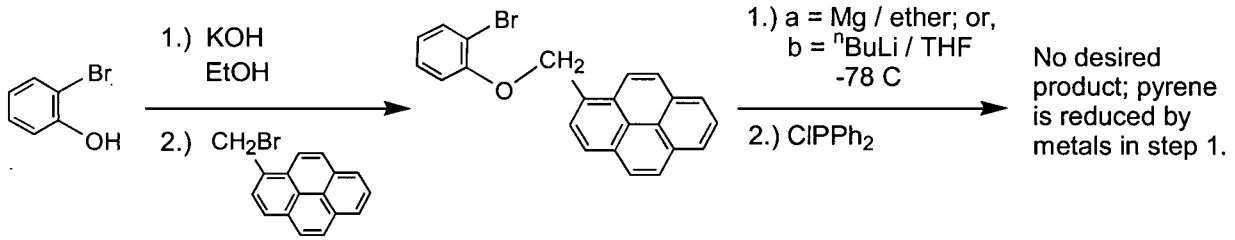

Scheme 7.2.

The reactions shown in Scheme 7.3 were hoped to yield the phenyl-bridged phosphine-ether via a crown-ether mediated Williamson ether synthesis route. Unfortunately, triaryl-substituted phosphines can be alkylated by benzyl halides;[20] thus, bromomethylpyrene very efficiently alkylated the phosphine and no desired product was formed. This route may prove to be viable if the starting phosphinophenol compound is first protected and is suggested for pursuit by future workers in the continuation of this project. Borane adducts,[21] however, have been shown to undergo alkylation[22] and are therefore likely unsuitable given the strong alkylating power of bromomethylpyrene.

References begin on page 256.

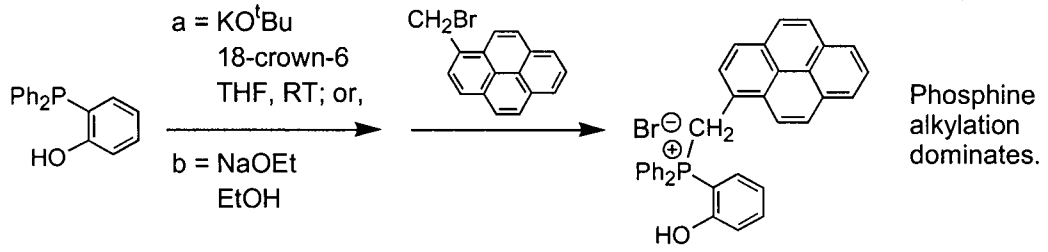

Scheme 7.3.

At this stage, ethyl-bridged phosphine-ethers were pursued, starting from hydroxymethylpyrene. Schemes 7.4 and 7.5 show attempts at Williamson ether synthesis routes involving the pyrenylmethoxide and a bromoethyl-substituted starting material. The reaction depicted in Scheme 7.4 led predominantly to vinyldiphenylphosphine, the product of base-mediated HCl elimination from $ClEtPPh_2$. It is likely that a similar process dominated under the conditions shown in Scheme 7.4, which was an attempt to prepare the bromoethoxymethylpyrene intermediate; however, elimination of ethylene was not confirmed.

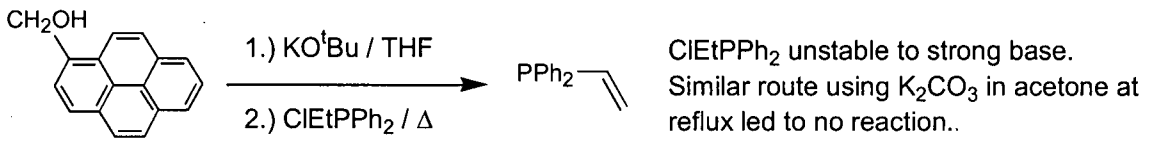

Scheme 7.4.

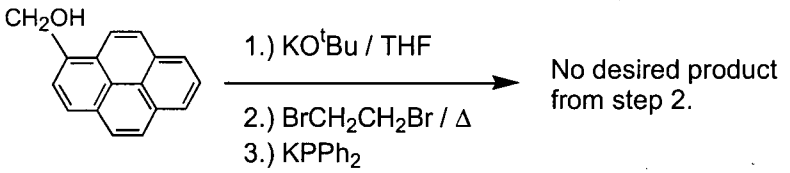

Scheme 7.5.

References begin on page 256.

The methylene-tethered pyrenyl-ether compounds were thus pursued but not achieved. It is suggested that future work on this project include further efforts to synthesize these short-tether *P,O*-pyrene ligands so that comparisons can be made between the photophysical properties of complexes containing these ligands to those complexes described later in this chapter.

7.2.2 Synthesis and characterization of POC4Pyr

The synthesis of the longer tether (four-carbon chain) pyrene-substituted phosphine-ether proved to be more facile. Many of the above routes were attempted, and the most successful, a Williamson ether synthesis route to the phenyl-bridged phosphine-ether, is depicted in Scheme 7.6. Bromobutylpyrene is a considerably less powerful alkylating agent than bromomethylpyrene; however, in order for the desired etherification reaction to dominate over phosphine alkylation, it was necessary to both activate the phenoxide anion through coordination of the K^+ counterion with 18-crown-6 and add the phenoxide to the bromobutylpyrene such that the alkylating agent was never in excess. When the reaction was performed in one pot using K_2CO_3 as base (in boiling acetone, or in boiling THF with 18-crown-6), phosphine alkylation dominated because only small amounts of the phenoxide were present at any given time.

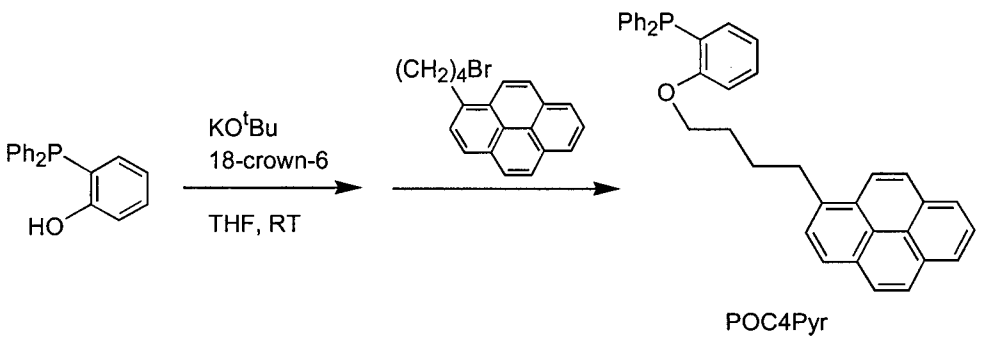

Scheme 7.6.

References begin on page 256.

Via the route shown in Scheme 7.6, phosphine-ether POC4Pyr was isolated in approximately 80 % yield, after purification by column chromatography (silica gel, CH_2Cl_2, R_f = 0.9, band strongly fluorescent under 366 nm light) to remove the crown ether. POC4Pyr is soluble in aromatic solvents, dichloromethane and chloroform but only sparingly soluble in other polar organic solvents, and even extremely dilute solutions of the compound are strongly fluorescent under UV light. The compound recrystallizes well from hot cyclohexane (86 % recovery after collection of three crops of crystals) to yield white plates, which melt sharply (156 – 157 °C) with no evidence of decomposition. Because the phosphine slowly oxidizes in air, POC4Pyr is best stored as a solid under an atmosphere of nitrogen. If oxidation is unavoidable, the oxide can be readily separated from the phosphine by column chromatography (silica gel, CH_2Cl_2) because the oxide adsorbs quite strongly to silica gel. The compound was fully characterized in solution by NMR spectroscopy (^1H, $^{31}P\{^1H\}$, $^{13}C\{^1H\}$, APT); the $^{31}P\{^1H\}$ spectrum of POC4Pyr (CD_2Cl_2: δ -14.2, s) is similar to those of the related phosphine-ethers, such as POMe (acetone-d_6: δ -15.0, s). A satisfactory elemental analysis was obtained for the compound after drying the solid *in vacuo* for 2 days at room temperature.

According to cyclic voltammetry, the pyrene moiety in POC4Pyr undergoes irreversible reduction at a potential slightly below -2 V ($CH_3CN/^nBu_4NPF_6$: E_{red} = -2.18 V *vs.* SCE). As an aside, the reduction potential for the Mg^{2+}/Mg couple is < -2.3 V (-2.36 V in acidic solution, -2.69 V in basic solution),[23] so in retrospect the difficulties with the synthetic route to pyrenyl ethers via the Grignard reagent are reasonable. The redox behaviour observed for POC4Pyr is comparable to that observed for both 1-ethylpyrene (E_{red} = -2.14 V) and an amide-substituted pyrene (E_{red} = -2.12 V)[7] under similar conditions. Thus, the phosphine in POC4Pyr does not appear to significantly influence the electronic nature of the pyrene unit, which suggests that the phosphine should not interfere with the photophysical processes localized on the pyrene moiety.

7.2.3 Absorption and photoluminescence properties of POC4Pyr

The absorption spectrum of POC4Pyr is shown in Figure 7.1. The highly structured spectrum with its well-resolved vibrational progression is typical of pyrene-containing

References begin on page 256.

compounds and arises because of the rigid fused-ring aromatic framework of the pyrene moiety. The spectrum is dominated by intense π-π* absorptions due to transitions within the fused aromatic rings. Of weaker intensity are the absorptions due to transitions within the triphenylphosphine portion of the molecule, which are buried beneath the strong pyrenyl π-π* absorptions. The absorption spectrum of an analogous phosphine-ether compound that lacks the pyrene moiety, POMe, is shown in Figure 7.1 for comparison.

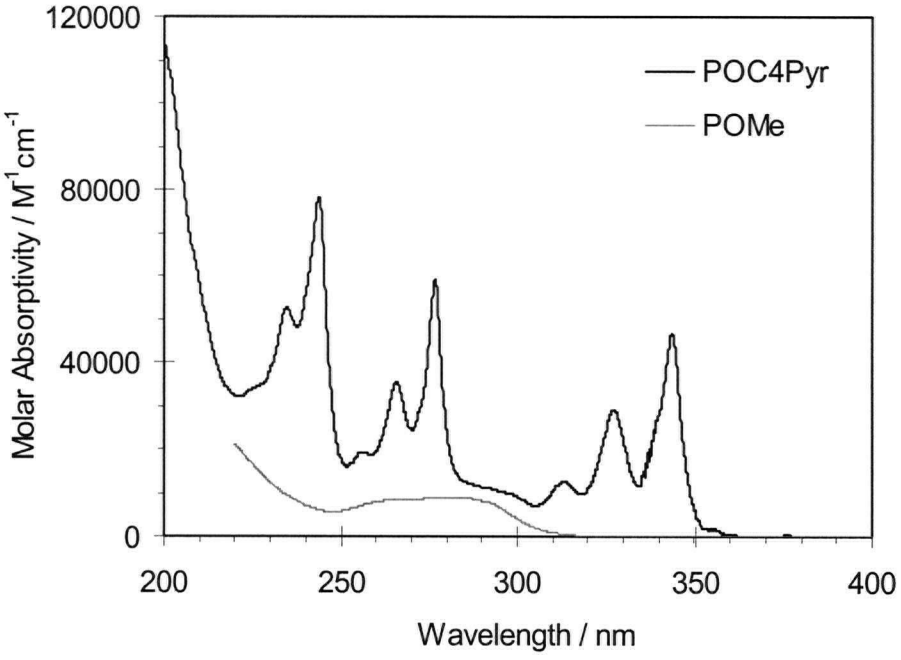

Figure 7.1. UV absorption spectrum of POC4Pyr in cyclohexane solution in comparison to that of POMe.

Excitation of POC4Pyr with UV light leads to strong indigo-blue emission, even in air-saturated chlorinated solvents. The excitation and emission spectra for POC4Pyr in dilute CH_2Cl_2 solution, shown in Figure 7.2, reveal the near mirror-image shapes and small Stokes shift typically observed for fluorescent aromatic compounds such as pyrene.[1] The excitation spectrum has the same general features as the absorption spectrum. The spectra obtained from solutions in cyclohexane, which is a more common solvent for luminescence studies because it has a large window of transparency in the UV (to 210 nm) and lacks heavy atoms, show slight

References begin on page 256.

variations in band intensities compared to spectra acquired from CH_2Cl_2 solution. In the less polar solvent, the lower energy vibronic bands (398 nm, 387 nm) are slightly increased in intensity at the expense of the 0–0 emission band (376 nm); in addition, the very weak vibronic bands between the strong bands at 376 nm and 398 nm are also more pronounced in cyclohexane.

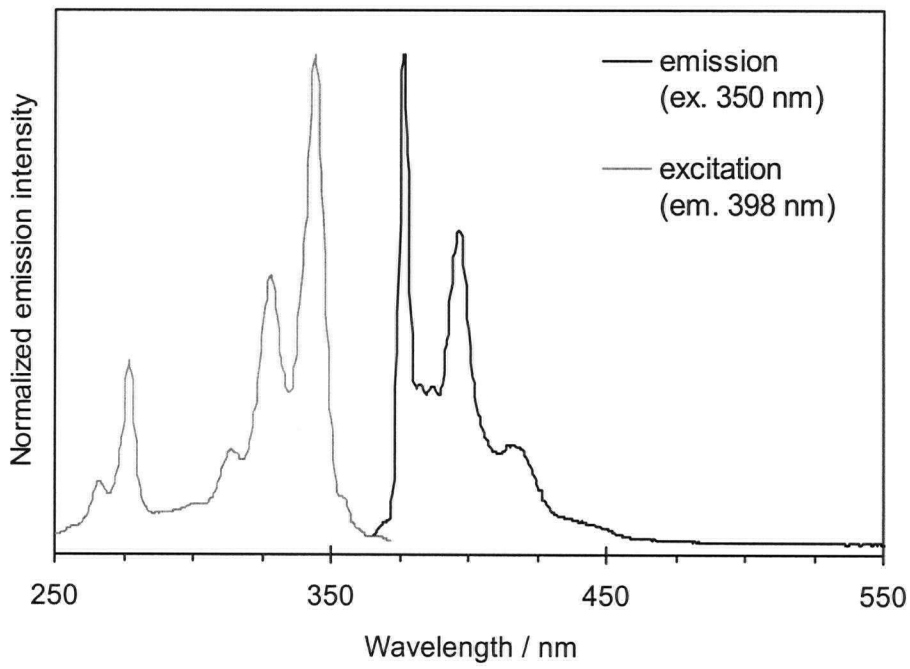

Figure 7.2. Excitation and photoluminescence spectra of POC4Pyr at RT in air-saturated CH_2Cl_2 solution; [POC4Pyr] = 4.1×10^{-6} M.

The solubility of POC4Pyr in dichloromethane is sufficiently high that emission spectra could be measured over several orders of magnitude of concentration. At low concentrations, blue pyrene monomer emission is observed, while at high concentrations ($\geq 1.0 \times 10^{-3}$ M), blue-green pyrene excimer emission is observed. The excimer's broad structureless emission band centred at ~ 480 nm grows in as the POC4Pyr concentration is increased, as shown in Figure 7.3. This behaviour is typical of pyrene-containing compounds, as described in section 7.1.2, and is consistent with formation of transient π-stacked dimers between ground-state and excited-state molecules such as that depicted in Scheme 7.7.

References begin on page 256.

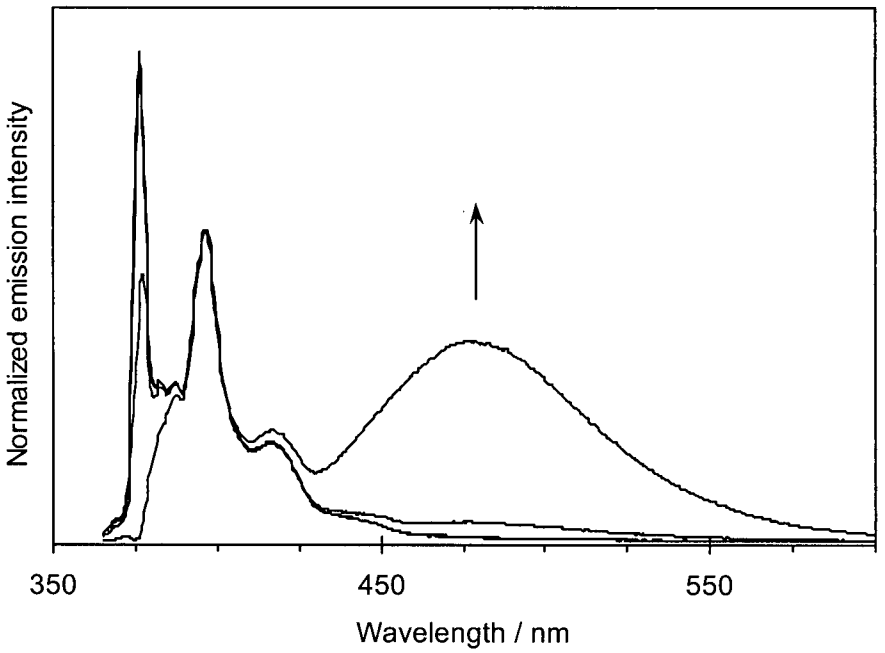

Figure 7.3. Effect of concentration on the emission from POC4Pyr. Broad excimer emission (~ 480 nm) grows in at high concentrations ($\geq 1.0 \times 10^{-3}$ M). [POC4Pyr] = 4.2×10^{-6}, 1.0×10^{-4}, 1.0×10^{-3}, 1.0×10^{-2} M, in air-saturated CH_2Cl_2 solution; $\lambda_{ex} = 350$ nm.

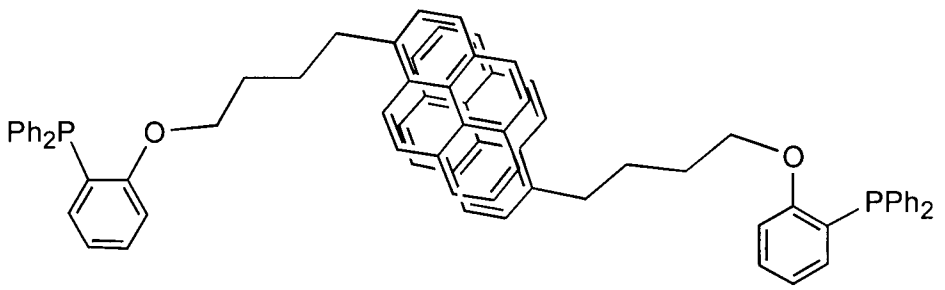

Scheme 7.7.

References begin on page 256.

7.3 POC4Pyr as a ligand on Ru(II)

The phosphine-ether POC4Pyr behaves very similarly to the POMe ligand that was the focus of Chapters Two and Three. The pendant pyrene moiety is tethered to the ether oxygen by a sufficiently long alkyl chain that there appears to be insignificant extra steric demand associated with its presence from the perspective of the ether's ability to coordinate to a metal centre. In the following sections, a preliminary investigation of this ligand's [*cis*-$Ru(bpy)_2(POR)]^{2+}$ complex and more detailed discussions of the $RuCl_2(POR)_2$ complex are presented.

7.3.1 A dual lumophore complex, [*cis*-$Ru(bpy)_2(POC4Pyr)]^{2+}$

The first use of the POC4Pyr ligand in this work was in the preparation of a [*cis*-$Ru(bpy)_2(POR)]^{2+}$ complex analogous to **1**. This complex, [*cis*-$Ru(bpy)_2(POC4Pyr)]^{2+}$, was not characterized in detail, but it is readily accessible via the same synthetic route used for **1**. NMR spectroscopy suggests that the complex parallels **1** in terms of the coordination environment of the metal ($^{31}P\{^1H\}$ CD_2Cl_2: δ 51.3 (s)), as well as its reactivity toward small molecules, such as water, acetonitrile and DMSO.

The reason this dual lumophore complex has not been studied in detail thus far is related to the fact that it contains two lumophores. Previous studies[24] of [*cis*-$Ru(bpy)_2(bpy')]^{2+}$ complexes with a pendant anthracene unit (bpy' = 4-[(9-anthrylmethoxy)methyl]-4'-methyl-2,2'-bipyridine) have shown that efficient intramolecular energy transfer occurs between the metal and anthracene moieties. The anthracene moiety cannot be exclusively excited because both the anthryl and MLCT excitations occur with UV light, but only extremely weak anthracene-based emission can be observed. MLCT excitation leads to rapid intramolecular energy transfer to anthracene, which quenches the bulk of the luminescence ($\Phi < 2$ % of that of $[Ru(dmb)_3)]^{2+}$; dmb = 4,4'-dimethyl-2,2'-bipyridine), since anthracene emission does not arise from this energy transfer process. Given that the tether between the metal complex and the organic lumophore in this system is of similar length to that in [*cis*-$Ru(bpy)_2(POC4Pyr)]^{2+}$, it was believed that similarly complicated photophysical properties would be observed for the

References begin on page 256.

POC4Pyr complex. Although this would be an interesting system to study as a chromophore-quencher complex, in the present context of small-molecule sensing, the added complication is unattractive. Thus, a simpler class of complex with only one type of lumophore was sought.

7.3.2 A simpler molecular design: *trans,cis,cis*-$RuCl_2(POR)_2$

A simpler type of Ru(II) complex was selected from the literature that has been well-studied with respect to its ability to reversibly coordinate small molecules through displacement of hemilabile phosphine-ether ligands: $RuCl_2(POR)_2$. As has been mentioned at various points in this thesis, the complex *trans,cis,cis*-$RuCl_2$(POMe-*P,O*)$_2$ exhibits reversible reactivity toward CO and numerous other Lewis basic small molecules.[25] The coordination of small molecules, particularly CO, leads to changes in the colour of the complex, but this type of complex is not luminescent. Thus, incorporation of a luminescent group into the hemilabile ligand in this type of complex should lead to a complex that has both the desired reactivity toward small molecules and relatively simple photophysical properties.

Use of a $RuCl_2(POR)_2$ complex as the basis for a molecular sensor is especially attractive because these complexes generally react rapidly and reversibly with CO,[26-28] which is a small-molecule analyte for which effective new sensory materials are in demand. The chemistry involved in the reaction of $RuCl_2$(POMe-*P,O*)$_2$ with CO is shown in Scheme 7.8. Upon treatment with CO, a colour change from red to yellow occurs coincident with formation of a dicarbonyl species. If CO is removed from the reaction mixture, one CO dissociates and a stable monocarbonyl species can be isolated. Reversion to the bis(*P,O*-coordinated) species can be achieved via photolysis. Thus, this type of phosphine-ether complex shows promise as the basis for a reversible sensor for CO.

References begin on page 256.

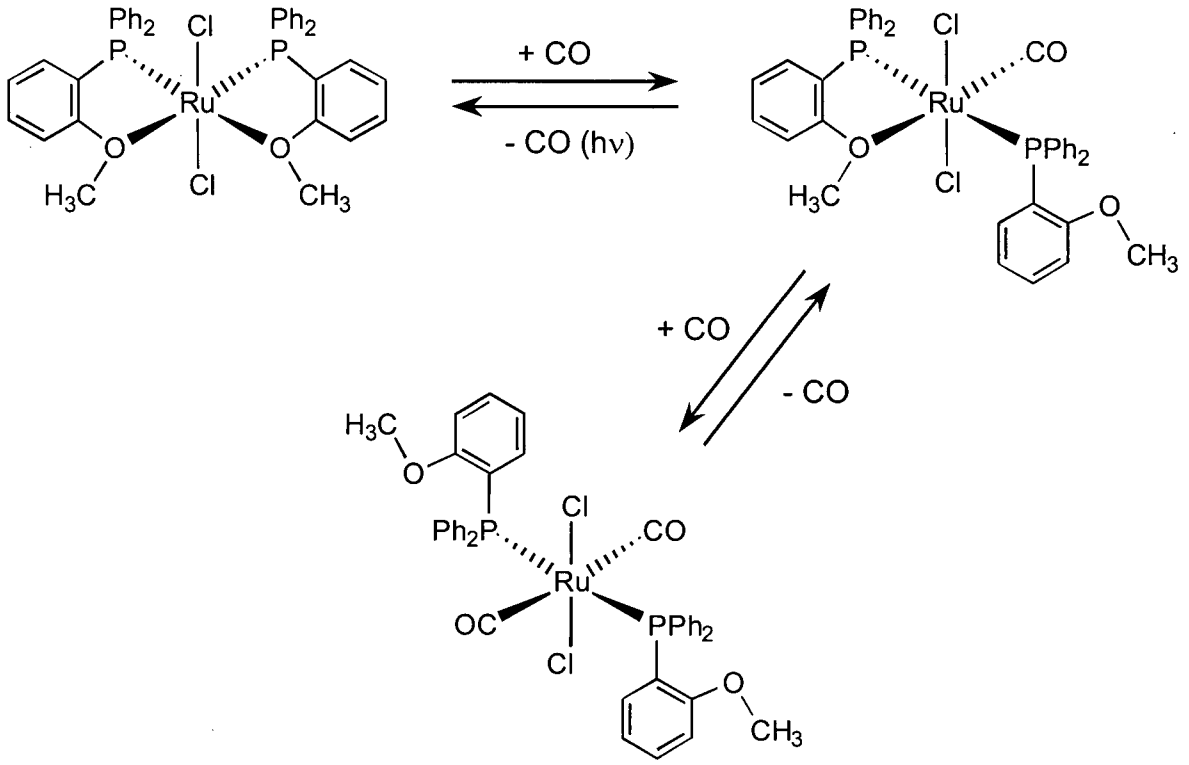

Scheme 7.8.

7.3.2.1 Synthesis and characterization of tcc-$RuCl_2$(POC4Pyr-P,O)$_2$, 10

The synthetic route to $RuCl_2$(POC4Pyr-*P,O*)$_2$, complex **10**, is shown in Scheme 7.9. The complex was readily prepared by reaction of 2 equiv of the phosphine-ether ligand with the commercially available metal starting material $RuCl_3 \cdot xH_2O$ in boiling deaerated ethanol/toluene solution. These conditions are similar to the published route to $RuCl_2$(POMe-*P,O*)$_2$,[29] although toluene was necessary to solubilize the pyrene-substituted phosphine-ether. The red complex was isolated from the cooled reaction mixture and precipitated as a burgundy-pink flocculent solid from dichloromethane/hexanes. Unreacted POC4Pyr was removed by repeatedly washing the solid with hot hexanes; the pure complex was obtained in an overall 38 % yield and a satisfactory elemental analysis was obtained after drying the solid *in vacuo* for 3 days at RT. The complex is soluble in aromatic solvents, dichloromethane and chloroform, and solutions of **10** undergo slow oxidation by air to form an unidentified greenish material.

References begin on page 256.

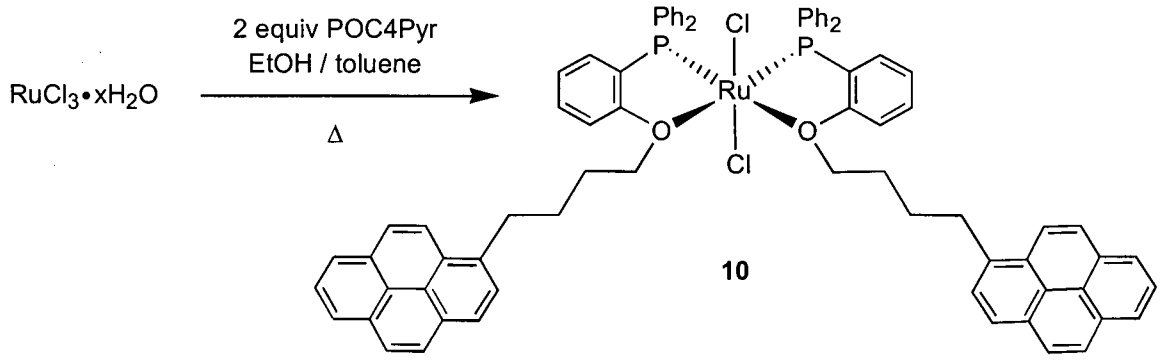

Scheme 7.9.

Complex **10** was characterized by solution methods; no solvent mixtures were found that yielded high quality crystals of **10** suitable for X-ray crystallographic analysis. According to cyclic voltammetric measurements, the metal centre in **10** (see Appendix 7.2 for CV) is slightly more electron-rich than in the POMe complex, $RuCl_2$(POMe-*P,O*)$_2$. For both complexes, the Ru(II) to Ru(III) oxidation is quite facile: the first oxidation process in **10** occurs at $E_{1/2}$ = 0.52 V *vs.* SCE, compared to 0.56 V for $RuCl_2$(POMe-*P,O*)$_2$. These observed reduction potentials do not match those predicted using Lever parameters if the ether is treated as equivalent to a dialkyl ether ($E_{1/2}(Ru^{III/II})_{calc}$ = 0.96 V *vs.* SCE for the model complex, $RuCl_2(PPh_3)_2(Me_2O)_2$).[30] However, using the Lever parameter calculated for POMe in Chapter Three (E_L = 0.63 for POMe; E_L = 0.24 for *o*-PhOMe), the predicted reduction potential matches that observed for **10**. It should be noted that the Lever parameter for the ether components of these POR ligands (E_L = 0.24) are considerably smaller than the value estimated for the ether components of POMe and POEt from the reduction potentials of **1** and **2** (E_L ~ 0.40); however, the electrochemical processes in **1** and **2** are not reversible and are therefore not ideal for use in this type of calculation.

By NMR spectroscopy, **10** is very similar to $RuCl_2$(POMe-*P,O*)$_2$, which has been crystallographically characterized[25] and found to contain two *P,O*-coordinated phosphine-ether ligands, with the phosphines *cis*-disposed to one another. The $^{31}P\{^1H\}$ NMR spectrum of **10** in CD_2Cl_2 solution contains one singlet resonance at δ63.7, as well as a small pair of doublets

References begin on page 256.

at δ 67.9 and δ 56.1 ($^2J_{PP}$ = 40 Hz) that is always present regardless of the extent of efforts to purify the complex; both spectral features are similar to those observed for samples prepared from pure, crystalline $RuCl_2$(POMe-*P,O*)$_2$. The small pair of doublets suggests that in solution at room temperature there exists a trace of a five-coordinate species that arises from dissociation of one of the ether moieties, even in relatively noncoordinating solvents such as chloroform.

The relative stereochemistry of the phosphines in **10** was determined via consideration of the complex's $^{13}C\{^1H\}$ NMR spectrum. It is well established[31-34] that virtual coupling between ^{13}C and ^{31}P nuclei is helpful in the assignment of the relative stereochemistry of bis(PR_3) complexes. For complexes with *trans*-disposed phosphines, the carbons in the positions *ipso*, *ortho* and *meta* to the phosphorus atom tend to appear as triplet-like multiplets in the $^{13}C\{^1H\}$ NMR spectrum; with *cis* phosphines, these resonances appear as doublets.[31] For complex **10**, the multiplicities of these resonances do not permit unambiguous assignment of the stereochemistry, since both doublet and triplet resonances are observed for the ^{31}P-coupled ^{13}C nuclei. Comparison of the $^{13}C\{^1H\}$ NMR spectrum of **10** to that of the known complex[29] *trans,cis,cis*-$RuCl_2$(POMe-*P,O*)$_2$, is more instructive. Selected ^{13}C resonances for the two complexes are presented in Table 7.1, and a portion of the aromatic region of their $^{13}C\{^1H\}$ NMR spectra is shown in Appendix 7.1. The chelating *P,O*-ligands clearly perturb the magnitude of the virtual ^{31}P-^{13}C coupling such that the typical "triplet-*trans*, doublet-*cis*" trend is not observed. The similarity of the spectra of these two complexes supports assignment of the phosphines as *cis*-disposed in complex **10**.

References begin on page 256.

Table 7.1. Selected $^{13}C\{^1H\}$ resonances for **10** and *trans,cis,cis*-$RuCl_2$(POMe-*P,O*)$_2$

Complex	δ [$^{13}C\{^1H\}$][a]	Type of carbon (from APT)	Line shape	J_{CP} / Hz
10	161.7	4°	t	5.2
	134.5	CH	t	4.9
	134.1	4°	d	25.3
	122.4	CH	br m	
	116.6	CH	br m	
$RuCl_2$(POMe-*P,O*)$_2$	164.0	4°	t	5.2
	134.4	CH	t	5.2
	134.4	4°	d	25.3
	122.5	CH	br m	
	114.6	CH	t	3.5

[a] $^{13}C\{^1H\}$ and APT NMR spectra measured in CD_2Cl_2 solution.

7.3.2.2 Absorption and photoluminescence of tcc-$RuCl_2$(POC4Pyr-P,O)$_2$, 10

The absorption spectrum of complex **10**, shown in Figure 7.4, is essentially a combination of those observed for $RuCl_2$(POMe-*P,O*)$_2$ and the pyrenyl ligand POC4Pyr. The complex is red in colour due to a weak metal-based visible absorption band (ε_{519} = 490 $M^{-1}cm^{-1}$ in cyclohexane solution) similar to that of $RuCl_2$(POMe-*P,O*)$_2$ (ε_{517} = 550 $M^{-1}cm^{-1}$ in $CHCl_3$ solution).[29] The highly structured absorptions in the UV region arise predominantly from pyrene-based π-π* transitions and are very similar to those observed in the spectrum of the free POC4Pyr ligand.

References begin on page 256.

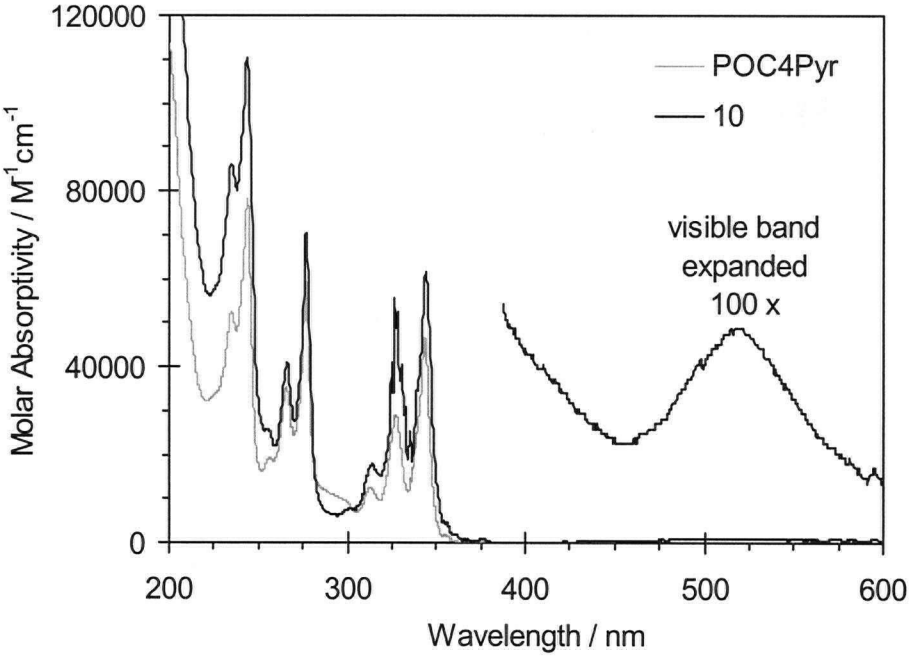

Figure 7.4. UV/Vis absorption spectrum of **10** in cyclohexane solution compared to that of the free ligand POC4Pyr.

The emission from the bis(POC4Pyr) complex **10** is also similar to that of free POC4Pyr. From the spectral overlay shown in Figure 7.5, subtle differences are observed in the intensities of some of the vibronic bands, consistent with very small changes in the environment experienced by the metal-tethered pyrene moiety relative to free POC4Pyr. Thus, as expected, the four-carbon linker between the coordinated ether and pyrene is long enough that the pyrene units are freely solvated and are not affected significantly by the metal centre. As judged by eye, the emission from **10** is weak compared to that of the free ligand. It is not possible to conclusively comment on the cause of this diminished emission intensity (*i.e.*, PET quenching *vs.* self-absorption) since quantum yield measurements and low temperature emission studies have not yet been performed. However, the complex does absorb slightly throughout the 370 – 600 nm region, which suggests a significant contribution from self-absorption of the emitted light.

References begin on page 256.

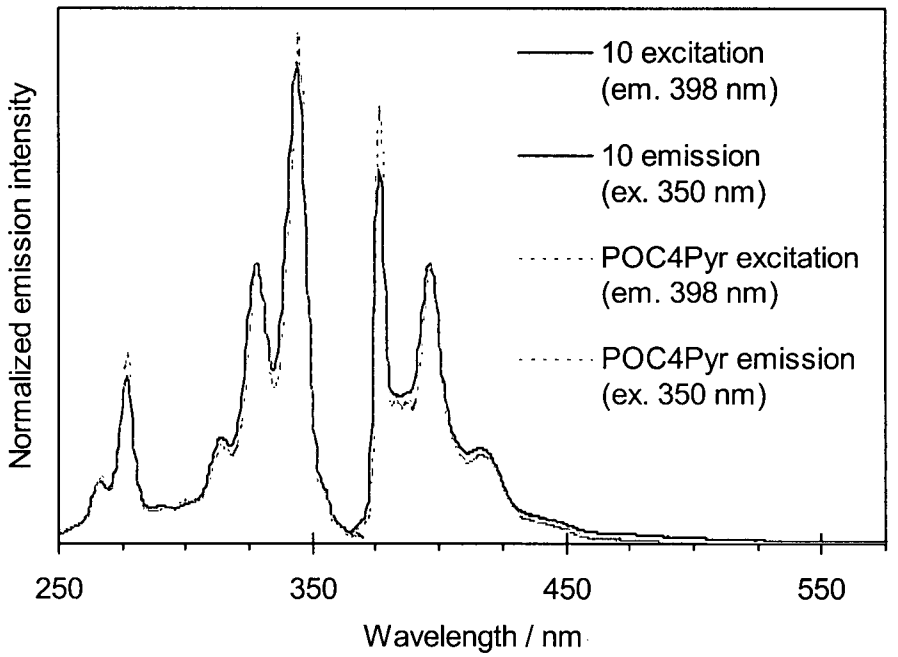

Figure 7.5. Comparison of excitation and emission spectra of **10** at RT in air-saturated CH_2Cl_2 solution to those of free POC4Pyr; [**10**] = 1.4×10^{-6} M, [POC4Pyr] = 4.1×10^{-6} M; excitation path 10 mm, emission path 2 mm.

The emission spectra obtained from concentrated solutions (10^{-2} M) of **10** are highly distorted due to absorption effects but do not contain a significant contribution from excimer emission. The high-energy region of the spectrum is diminished due to overlap with the tail end of the ligand-based absorption bands. Similarly, the absence of excimer emission (~ 430 – 550 nm) may result from efficient absorption of the emitted light by the complex because of its visible absorption band (~ 450 – 600 nm). However, the lack of excimer emission may imply that the pyrene moieties in **10** do not undergo intermolecular π-stacking in concentrated solution in the same manner as those in free POC4Pyr.

References begin on page 256.

7.4 $RuCl_2$(POC4Pyr-*P,O*)$_2$, 10, as a luminescent molecular sensor

7.4.1 Reactivity toward carbon monoxide

For this work, the interest in $RuCl_2$(POR-*P,O*)$_2$ complexes stemmed from their established reactivity toward CO, as introduced in section 7.3.2. As expected, the bis(POC4Pyr) complex **10** reacts rapidly with CO; of particular importance to this work is the fact that this reaction is indeed accompanied by a significant change in the photophysical properties of the complex. When a solution of **10** is treated with CO, the raspberry-red colour changes to greenish yellow, as is typical of $RuCl_2$(POR-*P,O*)$_2$ complexes. Interestingly, excitation with UV light reveals that the weak blue pyrene luminescence observed from **10** switches to strong blue-green excimer emission upon reaction with CO. A discussion of the chemistry involved in this reaction with CO will be presented in the subsequent sections, followed by insight into the absorption and fluorescence properties of the carbonyl complexes.

7.4.1.1 Reaction of 10 with CO to form kinetic product, dicarbonyl complex 11

When solutions of **10** ([**10**] ≈ 0.02 M) in aromatic or chlorinated solvents are treated with CO, the colour of the solution changes within seconds from deep raspberry red to pale greenish yellow. Analysis of the samples by $^{31}P\{^1H\}$ NMR spectroscopy immediately after the reaction reveals quantitative formation of a new complex, **11** (CD_2Cl_2: δ27.1, s). If prepared in aromatic solvents, this complex precipitates as a pale greenish-yellow powder over the course of several hours, although high quality crystals of this complex have so far not been obtained. The complex remains dissolved if prepared in dichloromethane or chloroform solution and is readily characterized *in situ* via solution methods. Solutions of **11** left exposed to air for long periods do not show signs of metal oxidation, although as will be elaborated in the following section, removal of the CO atmosphere from **11** encourages geometric isomerization.

Preparation of this complex with ^{13}C-labeled carbon monoxide permitted identification of **11** as a dicarbonyl complex based on the triplet multiplicity of the $^{31}P\{^1H\}$ resonance (CD_2Cl_2: δ27.1, t, $^2J_{PC}$ = 13.4 Hz). Similarly, the triplet multiplicity of the carbonyl resonance (CD_2Cl_2: δ197.6, t, $^2J_{CP}$ = 13.5 Hz) in the $^{13}C\{^1H\}$ NMR spectrum obtained for the same

References begin on page 256.

isotopically labeled sample revealed that the two equivalent CO moieties in **11** are coupled to two equivalent ^{31}P nuclei. The magnitude of the ^{13}C-^{31}P coupling constant is typical of $RuCl_2(CO)_2(PR_3)_2$ complexes with phosphines *cis* to the carbonyls ($^2J_{PC} < 20$ Hz).[33,35]

The relative stereochemistry of **11** was assigned by a combination of NMR and IR spectroscopic data obtained without isolation of the complex. The $^{13}C\{^1H\}$ resonances for the phenyl carbons directly bonded to ^{31}P (*ipso* Cs: δ 132.8, t, J_{CP} = 23.9 Hz; 118.8, t, J_{CP} = 24.4 Hz) and 2-bonds from phosphorus (C bound to O, *ortho* to P: δ 160.5, t, J_{CP} = 2.3 Hz) appear as well-resolved triplets. This pattern is consistent with a large virtual 3-bond ^{13}C-^{31}P coupling, which results when phosphines are *trans* to one another. The observed ^{13}C-^{31}P coupling constants ($J_{CP} = {}^1J_{CP} + {}^3J_{CP}$) are somewhat smaller than those observed for $RuCl_2(CO)_2(PPh_3)_2$ (48.0 Hz for *ipso* C; 10.3 Hz for *ortho* C),[33] but still permit clear resolution of the multiplets. By IR spectroscopy, a single absorption is observed in the C-O stretching region (ν_{CO} = 2005 cm^{-1} in $CHCl_3$ solution, for the natural abundance CO complex), consistent with a *trans* disposition of the two CO moieties in the complex. Thus, from the complete spectral data, complex **11** is identified as *trans,trans,trans*-$RuCl_2(CO)_2$(POC4Pyr-*P*)$_2$.

The coordination of CO to the metal is expected to result in a dramatic decrease in electron density at the metal centre because of CO's strong π-acidity, which should be manifested as an increase in the reduction potential of the $Ru^{III/II}$ couple. Indeed, the first oxidation of **11** occurs at $E_{1/2}$ = 1.18 V *vs.* SCE, more than 600 mV higher than the first oxidation process for **10** (see Appendix 7.2 for the CVs of **10** and **11**; for **11**: $E_{1/2}$ = 1.18, 1.39 V, and E_{ox} = 1.71 V *vs.* SCE). For comparison, the lowest energy oxidation of the related complex *ttt*-$RuCl_2(CO)_2$(POMe-*P*)$_2$ occurs at 1.31 V *vs.* SCE under similar conditions. These reduction potentials are considerably lower than that predicted for the $Ru^{III/II}$ couple by consideration of Lever electrochemical ligand parameters ($E_{1/2}(Ru^{III/II})_{calc}$ = 2.04 V *vs.* SCE for model complex $RuCl_2(CO)_2(PPh_3)_2$), which suggests that this process may be ligand-based rather than metal-based. The quasireversibility of the first two oxidation waves observed for **11** is inconsistent with either of these processes being related to chloride oxidation, so these processes are likely localized on the phosphine-ether ligand.

References begin on page 256.

7.4.1.2 Isomerization of 11 to dicarbonyl complex 12

Samples of **11** in CD_2Cl_2 that are sparged with N_2 or degassed via repeated freeze-pump-thaw cycles to remove free CO slowly undergo further conversion to form an isomeric complex, **12**. Samples maintained under CO atmosphere are almost entirely inert to this isomerization. Like **11**, complex **12** contains two equivalent phosphines according to the singlet resonance in its $^{31}P\{^1H\}$ NMR spectrum (CD_2Cl_2: δ13.9), and the ^{13}CO-labeled complex produces a triplet ^{31}P resonance ($^2J_{PC}$ = 11.2 Hz) consistent with the presence of two equivalent carbonyl moieties. The carbons *ipso* and *ortho* to phosphorus appear as triplets in the $^{13}C\{^1H\}$ NMR spectrum (*ipso* Cs: δ131.8, t, J_{CP} = 24 Hz; 119.3, t, J_{CP} = 23.5 Hz; and C bound to O, *ortho* to P: δ159.0, t, J_{CP} = 2.6 Hz). By IR spectroscopy, there are two carbonyl stretching bands (ν_{CO} = 2005, 2058 cm^{-1} in $CHCl_3$ solution). Thus, the spectroscopic data are consistent with assignment of the thermodynamically favoured dicarbonyl complex **12** as *cis,cis,trans*-$RuCl_2(CO)_2$(POC4Pyr-*P*)$_2$. Numerous attempts have been made to crystallize this complex, but thus far crystals suitable for X-ray crystallographic analysis have not been obtained.

It has been well established in the literature[32,33,36] that complexes of the type $RuCl_2(CO)_2(PR_3)_2$ undergo isomerization. The typical synthetic conditions under which these dicarbonyl complexes are prepared lead to formation of the all-*trans* isomer (herein denoted as *ttt*). This kinetic *ttt*-product thermally isomerizes in solution via a 5-coordinate intermediate, which is formed through CO dissociation; recoordination of the CO forms either the all-*cis* (*ccc*) isomer or the thermodynamically preferred *cis,cis,trans*-$RuCl_2(CO)_2(PR_3)_2$ (*cct*) isomer.[33] In the present case, the isomerization of **11** to **12** is essentially blocked if samples are maintained under CO atmosphere, but proceeds to completion in a matter of a few days if samples are degassed and left standing at room temperature; these observations are consistent with a mechanism that involves CO dissociation. At this point, however, the mechanism of this isomerization has not been definitively established, and future studies into the reactions of this complex should include a detailed study of this process.

References begin on page 256.

7.4.1.3 Summary and comparison to the POMe complexes

Scheme 7.10 shows the proposed chemistry involved in the reaction of **10** with CO and the further isomerization of the kinetic product, **11**, into the thermodynamically favoured isomer, **12**. The $^{13}C\{^{1}H\}$ NMR spectroscopic data used in the assignment of the geometry of the phosphines in complexes **11** and **12** are summarized in Table 7.2, with the corresponding data for complex **10** included for comparison. Table 7.3 summarizes the spectroscopic data (colour, IR, $^{31}P\{^{1}H\}$ NMR) obtained for complexes **10-12** in comparison to a set of related POMe complexes of known geometry from the literature.[25] The combinations of spectroscopic properties for each of the complexes (colour, NMR chemical shifts, IR bands) are similar to those observed for the analogous POMe complexes.

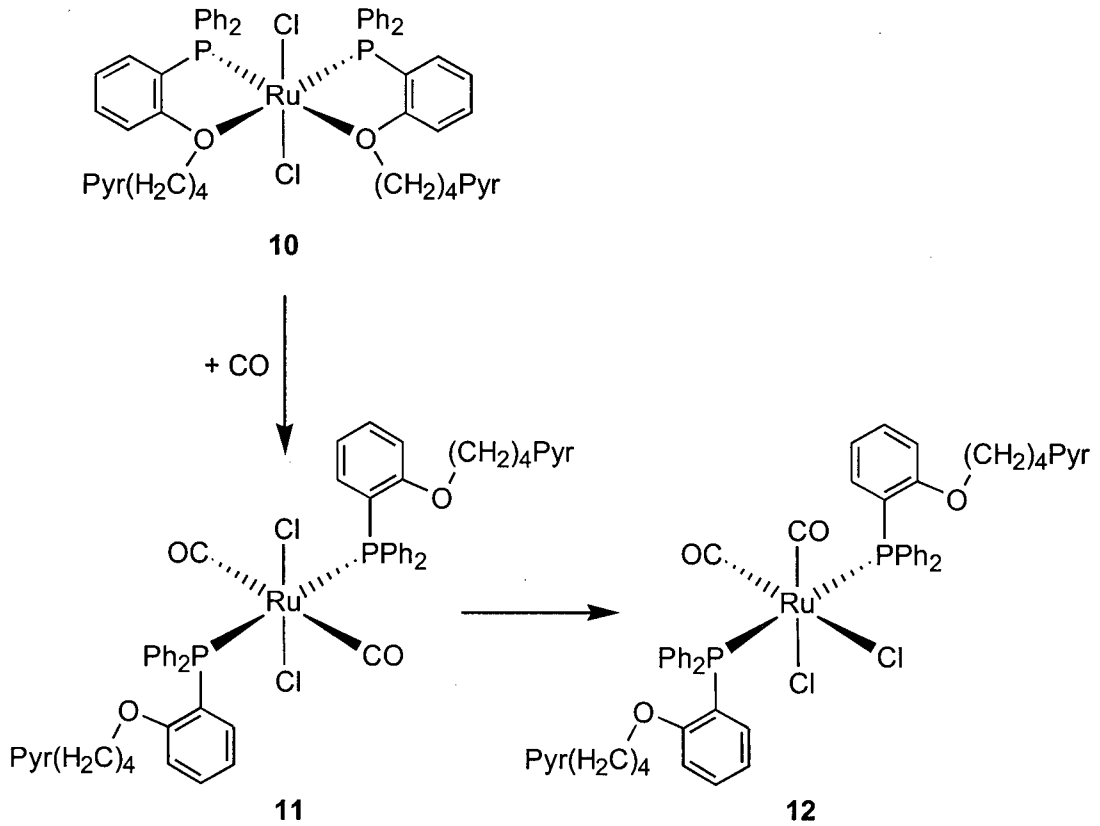

Scheme 7.10.

References begin on page 256.

Table 7.2. Summary of $^{13}C\{^1H\}$ NMR spectroscopic data[a] for **10**, **11** and **12**

Complex	$^{13}C\{^1H\}$ / δ(mult) [J / Hz]			
	CO	*ortho*[b]	*ipso*	*ipso*
10	—	161.7 (t)	134.1 (d)	ND
		[5.2]	[25.3]	
11	197.6 (t)	160.5 (t)	132.8 (t)	118.8 (t)
	[13.5]	[2.3]	[24.4]	[23.9]
12	193.7 (t)	159.0 (t)	131.8 (t)	119.3 (t)
	[10.9]	[2.3]	[24]	[23.5]

[a]NMR spectra measured in CD_2Cl_2 solution. [b]Phenyl carbon bound to oxygen.

Table 7.3. Comparison of **10**, **11** and **12** to analogous POMe complexes[a]

Complex	Colour	$^{31}P\{^1H\}$ / δ	ν_{CO} / cm^{-1}
tcc-**10**	red	63.7[b]	—
ttt-**11**	greenish-yellow	27.1[b]	2005[c]
cct-**12**	greenish-yellow	13.9[b]	2005, 2058[c]
tcc-$RuCl_2$(POMe-*P,O*)$_2$	red	62.7[d]	—
tt-$RuCl_2(CO)$(POMe-*P,O*)(POMe-*P*)	yellow	37.0	2000
ttt-$RuCl_2(CO)_2$(POMe-*P*)$_2$	yellow	26.7	1962
cct-$RuCl_2(CO)_2$(POMe-*P*)$_2$	white	10.6	2000, 2060

[a]From ref [25]; $^{31}P\{^1H\}$ NMR spectra measured in $CDCl_3$ solution; IR spectra measured in mineral oil mulls. [b] $^{31}P\{^1H\}$ NMR spectra measured in CD_2Cl_2 solution. [c]IR spectra measured in $CHCl_3$ solution. [d] $^{31}P\{^1H\}$ NMR spectrum measured in $CDCl_3$ solution.

References begin on page 256.

Despite many similarities, the reaction of the POC4Pyr complex **10** with CO is not directly analogous to the reaction of the POMe complex $RuCl_2$(POMe-*P,O*)$_2$, which was depicted in Scheme 7.8. $RuCl_2$(POMe-*P,O*)$_2$ reacts with CO to form the all-*trans* dicarbonyl complex *ttt*-$RuCl_2(CO)_2$(POMe-*P*)$_2$, but upon removal of the CO atmosphere, one CO dissociates to result in formation of a monocarbonyl complex with one coordinated ether moiety.[29] Thus, one equivalent of CO is reversibly coordinated by the POMe complex, and it was hoped that a similar reversible binding process would be observed for the POC4Pyr complex. So far, however, no evidence has been observed for formation of such a monocarbonyl complex in the presence of the POC4Pyr ligand. Furthermore, the all-*trans* complex *ttt*-$RuCl_2(CO)_2$(POMe-*P*)$_2$ does not spontaneously isomerize in solution at room temperature, although the thermodynamically favoured complex *cct*-$RuCl_2(CO)_2$(POMe-*P*)$_2$ is formed if $RuCl_2$(POMe-*P,O*)$_2$ is treated with CO at elevated temperature. Thus, it can be concluded that the alkylpyrene moiety in POC4Pyr slightly diminishes the ability of the ether to coordinate to the metal centre such that formation of a monocarbonyl complex is disfavoured. As well, the presence of the alkylpyrene may be related to an increase in the lability of metal-bound carbonyls such that isomerization via a 5-coordinate intermediate is enhanced relative to the analogous POMe complexes.

7.4.2 Photophysical response to carbon monoxide

The reaction of **10** with CO is accompanied by a dramatic colour change from raspberry red to pale greenish yellow. This colour change results from the displacement of the weak-field ether ligands with strong-field CO ligands and is the typical response of this family of $RuCl_2$(POR-*P,O*)$_2$ complexes to CO coordination.[29] Coordination of one CO is sufficient to shift the energy of the metal-based dd transitions such that the monocarbonyl complex $RuCl_2(CO)$(POMe-*P,O*)(POMe-*P*) is essentially the same colour as the all-*trans* dicarbonyl complex, but again, for the POC4Pyr complex a monocarbonyl species has not been observed. In the context of chemical sensing, it is the change in the luminescence properties of the complex upon reaction of **10** with CO that is of greater interest because of the low detection

References begin on page 256.

limits achievable for measurements based on luminescence compared to absorption. It is these changes that will be emphasized in the present discussion.

When concentrated solutions of **10** (~ 10^{-2} M) are treated with CO under UV irradiation, the dim blue pyrene emission from **10** switches to strong blue-green excimer emission as the reaction proceeds. This result was somewhat unexpected, since it was predicted that the effect of ether displacement would be an increase in pyrene monomer emission because it would remove the lumophore from the proximity of the open-shell metal centre. The length of the tether between the ether and the pyrene is large enough in the POC4Pyr ligand, however, to prevent distance-dependent electron-transfer quenching from playing a major role in the luminescence response to small-molecule coordination. Thus, displacement of the ether from the metal simply increases the conformational freedom of the alkylpyrene moiety by further lengthening the tether between the pyrene and the metal. This increased conformational freedom influences the ability of the pyrene moieties to interact with one another, and these interactions are manifested as excimer emission.

7.4.2.1 Emission from kinetic dicarbonyl product 11

In concentrated solution ([**11**] = 8.5 × 10^{-2} M), the emission from the kinetic dicarbonyl product **11** includes a significant contribution from excimer emission, as shown in Figure 7.6. This concentration dependence is similar to that observed for the free POC4Pyr ligand and is consistent with the formation of excimers between different molecules of **11**, in a manner similar to that depicted in Scheme 7.11. This contrasts with the behaviour shown by **10**, although for **11** there are no complications due to overlap between the absorption and emission spectra of the complex. Improved interaction between pyrene moieties on adjacent molecules in concentrated solution is expected based on sterics, considering the increased distance between the pyrene moieties and the metal centre in **11** compared to **10**. In dilute solution ([**11**] = 1.8 × 10^{-6} M), a trace of excimer emission persists. The fact that excimer emission remains at low concentration implies that excimers can also form intramolecularly, since intermolecular excimer emission from pyrene is typically insignificant for concentrations below ~ 10^{-3} M.[1]

References begin on page 256.

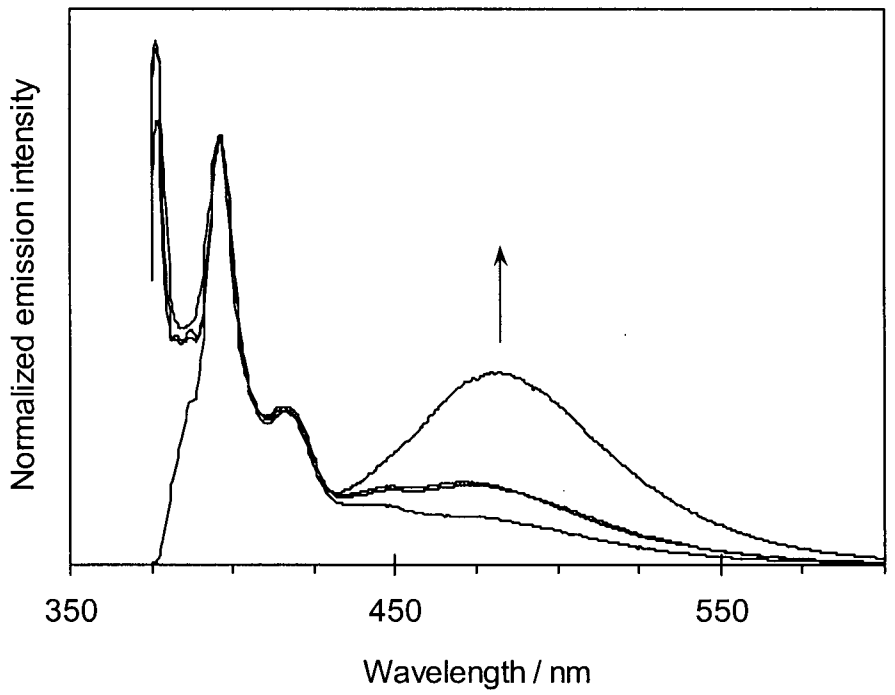

Figure 7.6. Intermolecular excimer emission grows in with increasing concentration of the kinetic dicarbonyl complex **11**. Emission measured at RT in air-saturated CH_2Cl_2 solution; [**11**] = 1.8×10^{-6}, 5.3×10^{-5}, 1.6×10^{-4}, 8.5×10^{-2} M; λ_{ex} = 350 nm.

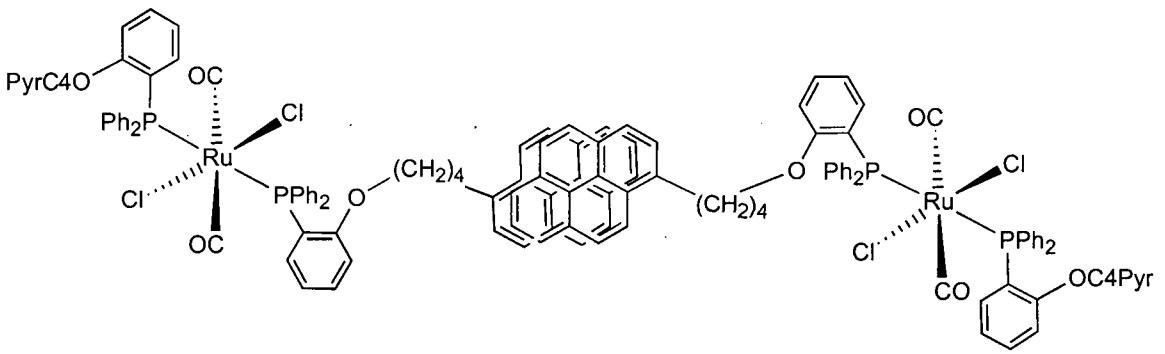

Scheme 7.11.

References begin on page 256.

7.4.2.2 Emission from dicarbonyl complex 12

After **11** isomerizes to form the *cct*-complex **12**, strong excimer emission is observed even in dilute solution, as shown in Figure 7.7. From this observation, it is concluded that the pyrene moieties in the thermodynamically preferred complex are readily able to interact with one another to form intramolecular excimers, such as that depicted in Scheme 7.12. Although both complexes **11** and **12** have *trans* phosphines, the complex with *cis* carbonyls and *cis* chlorides evidently provides a steric environment that favours π-stacking between the pyrenes. Indeed, it is possible that interactions between the pyrenes may be involved in the isomerization process and could conceivably stabilize a geometry in the purported 5-coordinate intermediate that favours formation of the *cct*-isomer **12**.

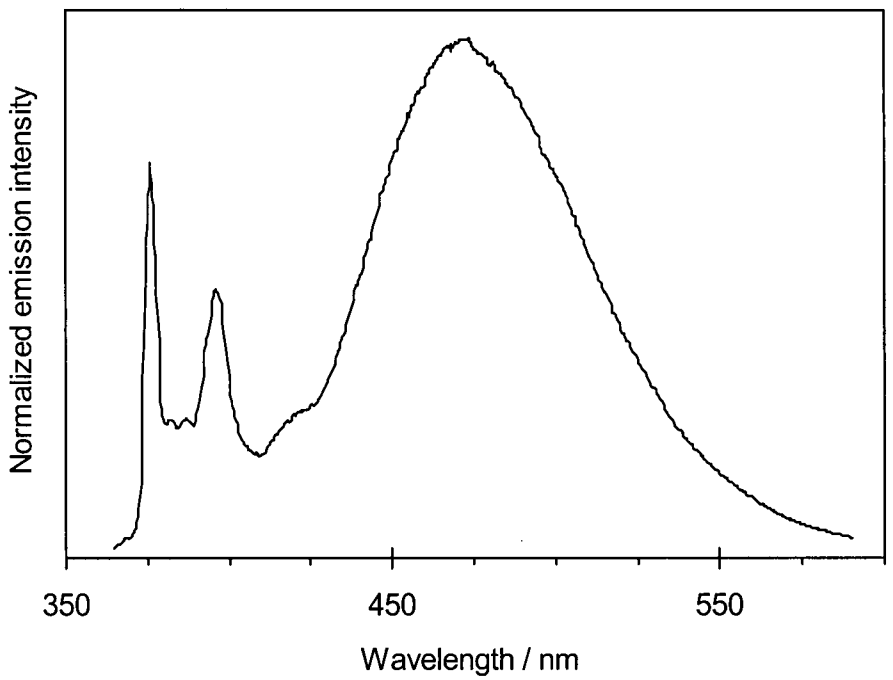

Figure 7.7. Excimer emission dominates even in dilute solutions of the thermodynamically preferred dicarbonyl complex **12**. Emission measured at RT in air-saturated CH_2Cl_2 solution; [**12**] = 3.4×10^{-6} M; λ_{ex} = 350 nm.

References begin on page 256.

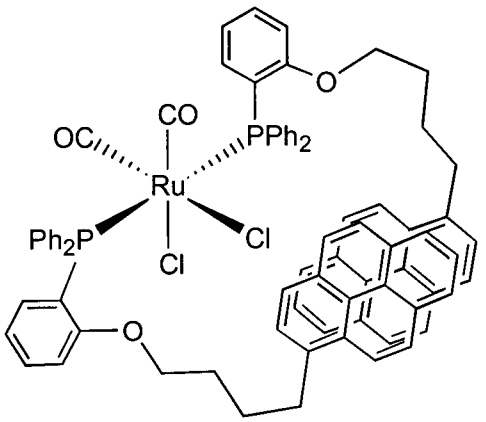

Scheme 7.12.

Future studies should be aimed toward determining whether the excimer emission from **12** arises from transient dimers between ground- and excited-state pyrenes (known as *dynamic excimers*) or from excitation of pyrenes that already exist as π-stacked dimers in the ground state (known as *static excimers*). Evidence for ground-state interactions between pyrenes can be obtained from UV absorption spectra and ^{1}H NMR spectra.[4,7] Also of interest is the packing of the pyrene moieties in the solid state, which provides another reason for continued attempts to obtain crystals of **12**, besides confirmation of the geometry assignment.

7.4.2.3 Summary of emission response to CO

For concentrated solutions, the rapid luminescence response of the phosphine-ether complex **10** to CO is observable by eye. Under UV illumination, the extremely weak blue pyrene emission from **10** is rapidly replaced by strong blue-green excimer emission upon exposure of the solution to CO. This effect, as well as the colour change observed under ambient lighting, is shown in Figure 7.8. In dilute solution, this effect is not readily observable by eye. Nevertheless, the immediate response of dilute solutions of **10** to CO is detected spectroscopically as a small increase in excimer emission, as shown in Figure 7.9. After the sample is allowed to age in the absence of CO, the excimer emission increases dramatically because of the isomerization of the all-*trans* dicarbonyl **11** to the more stable *cis,cis,trans*-dicarbonyl **12**.

References begin on page 256.

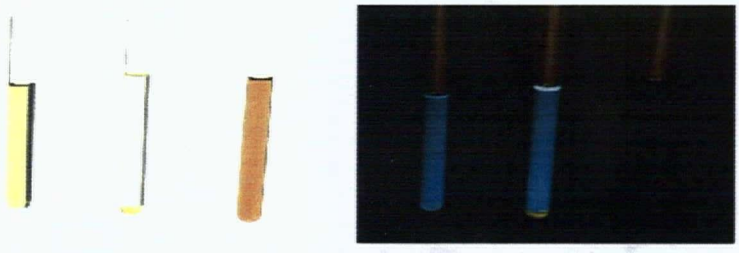

Figure 7.8. Visible response of **10** to CO in concentrated solution (~ 10^{-2} M). Panel A: appearance under ambient lighting. Panel B: appearance under UV light (366 nm). Sample identification: **10** (right); **11** (middle); **12** (left).

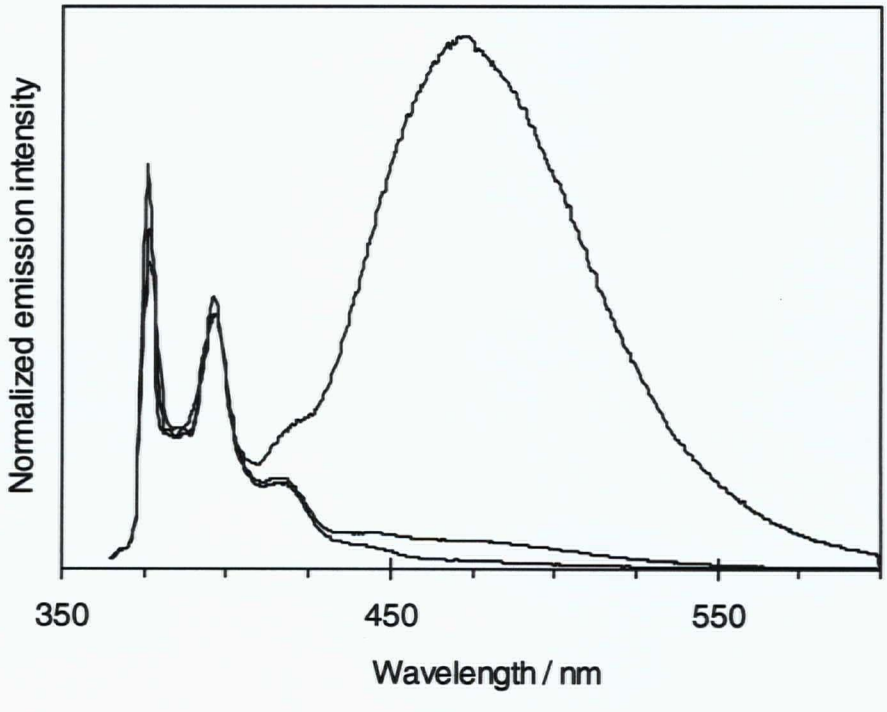

Figure 7.9. Comparison of the emission from dilute solutions of **10**, **11** and **12**. Emission measured at RT in air-saturated CH_2Cl_2 solution; λ_{ex} = 350 nm. Top trace (according to excimer band intensity): [**12**] = 3.4×10^{-6} M; middle: [**11**] = 1.8×10^{-6} M; bottom: [**10**] = 1.4×10^{-6} M.

References begin on page 256.

7.4.3 Complex 10 as a luminescent sensor

The dramatic, rapid CO-induced switching from weak pyrene monomer fluorescence to strong excimer emission makes **10** an attractive candidate for further study as a molecule-based sensor. This luminescence response to CO occurs within seconds at room temperature and is easily observable by eye, and the reaction with CO is also evidenced by a colour change that is readily observed under ambient lighting. The rapid response of **10** to CO is not necessarily limited to high concentrations of **10** even though the intermolecular excimer emission from the kinetic dicarbonyl complex **11** is relatively weak for dilute samples. Even at 10^{-6} M, excimer emission from **11** is spectroscopically measurable.

At present, the more exaggerated excimer emission from the thermodynamically preferred dicarbonyl **12** is not extremely applicable to sensing of the lethal gas CO. The thermodynamic dicarbonyl is limited in this respect by the fact that the isomerization from **11** to **12** occurs over the course of a few days and requires the removal of CO from the system. Further studies may reveal that **12** is formed directly when the reaction of **10** with CO is carried out at elevated temperature. If this is indeed found, the promise of complex **10** as a luminescent sensor would be substantial because of the large difference in emission intensity from the sensory material before and after CO exposure.

7.4.4 Suggestions for future study of 10

The reactivity of the phosphine-ether complex **10** with CO has been studied here in sufficient detail to realize that the system unquestionably deserves further study. At this stage, the dicarbonyl complexes have been characterized by solution methods; they should in future be isolated. Crystallographic determinations of **10-12** would not only confirm the geometric assignments made based on the solution studies, but also may provide insight into the observed differences in the photophysical properties of the three complexes. Detailed studies into the isomerization of **11** to **12** must be performed. The possibility of direct formation of the thermodynamically preferred isomer through the reaction of **10** with CO at elevated temperature, as occurs for $RuCl_2(POMe\text{-}P,O)_2$, should also investigated.

References begin on page 256.

More specifically related to the pursuit of **10** as a CO-sensing material, future work should include treatment of **10** with known quantities of CO in order to determine whether quantitative conversion to the dicarbonyl species is necessary to obtain a detectable luminescence response. Such studies may also permit determination of a detection limit for the sensing of CO by **10**, which would assist in the evaluation of the potential of this type of material for sensing applications. Efforts to immobilize **10** in solid or gel-based matrices should also be undertaken, although the large degree of structural reorganization that accompanies the conversion of **10** into the dicarbonyl complexes may limit the response of the complex to CO to fluid matrices. Preliminary investigations have shown that the reaction with CO does occur in solid **10**, although a film of sol-gel glass impregnated with **10** did not visibly change after several days under CO atmosphere. Furthermore, at this preliminary stage in the investigations of the reactivity of **10**, it appears that the reaction with CO is irreversible. Further study is required to determine if the dicarbonyl complexes can be converted back into **10**, possibly via photolysis.

In addition to its promising reactivity toward CO, preliminary studies have shown that complex **10** also reacts with other small molecules. When solutions of **10** are treated with SO_2, an immediate colour change from raspberry red to brownish orange occurs. This colour change largely reverses upon removal of the solvent and dissolution in $CDCl_3$ for spectroscopic analysis but is restored after a short sparge of the solution with SO_2. A new product consistent with a complex containing one metal-bound SO_2 and *cis* phosphines is evident in the $^{31}P\{^1H\}$ NMR spectrum ($CDCl_3$: δ42.8 d, 25.0 d, $^2J_{PP}$ = 26.7 Hz). Moreover, **10** reacts with acetonitrile, which leads to a red-to-yellow colour change, and it is probable that other classes of small molecules can also displace the ether moieties in **10** to produce changes in the photophysical properties of the complex, both in terms of colour changes and luminescence response.

In summary, the pyrene-substituted phosphine-ether complex **10** shows tremendous potential as a sensory material, and the investigations into the function of this complex as a small-molecule sensor are certainly just beginning. The reactivity of **10** toward a variety of small molecules requires investigation in order to determine which types of analytes lead to a luminescence response. Moreover, it is important to establish whether or not other gases or

References begin on page 256.

vapours will induce luminescence changes in the same way that CO does, so that potential interferences with the function of **10** and its congeners as CO sensory materials can be identified and understood.

7.5 Summary and outlook

In this chapter, an alternative approach to the design of luminescent coordination-based sensors was described that separates the small-molecule receptor function from the luminescence response module. The phosphine-ether POC4Pyr, which contains a luminescent pyrenyl substituent, was synthesized, and this hemilabile ligand was incorporated into a Ru(II) complex to provide the desired small-molecule coordination site. This complex, $RuCl_2$(POC4Pyr-*P,O*)$_2$, **10**, is sufficiently electron-rich that it reacts rapidly with the strong π-acceptor CO. The displacement of the pyrene-substituted ether moiety from the metal centre results in a dramatic change in photoluminescence, from weak indigo-blue pyrene monomer-based emission to strong blue-green pyrene excimer-based emission; this response occurs because the less restrained pyrene units are able to interact with one another. In terms of potential application to chemical sensing, the luminescence response of complex **10** to CO is extremely attractive because it is fast, dramatic, and occurs at room temperature. A more detailed understanding of the chemistry involved in the reaction of **10** with CO and the ensuing isomerization of the dicarbonyl complexes is required in order to further pursue this and related complexes as molecule-based gas sensors. It is hoped that the research presented in this chapter will provide the foundation for the development of a family of luminescent hemilabile-ligand complexes and stimulate further investigation into their application as molecule-based gas sensors.

7.5.1 Suggestions for future work

As introduced at the outset of this chapter, the original intent of the work on pyrenyl-substituted phosphine-ethers was to compare the luminescence properties of complexes in

References begin on page 256.

which the pyrene units are connected to the ether oxygen via short *vs.* long tethers. Thus, it is suggested that efforts toward the preparation of phosphine-ethers with short-length tethers be renewed, as discussed in section 7.2.1. Numerous suggestions have already been presented for further investigation into the reactivity and response of the POC4Pyr complex **10**. It is believed that this family of complexes shows strong potential as chemosensory materials, and particular emphasis should be placed on evaluating the performance of simple sensory devices based on these complexes.

Many other organic-based lumophores aside from pyrene are attractive for use as the luminescence response element of coordination-based molecular sensors. For example, coumarin-based lumophores, like pyrenes, are highly emissive in the blue region of the spectrum at room temperature, they show substituent-dependent emission and absorption properties and their excited states are susceptible to electron-transfer quenching. The lactone functionality in the coumarin ring system does limit the synthetic versatility of this lumophore compared to pyrene, but a successful synthetic route to an ethylene-bridged phosphine-ether with a 4-methylcoumarin substituent is shown below.

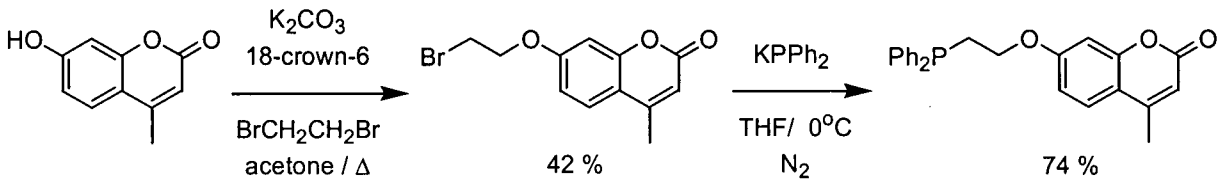

Scheme 7.13.

Studies of the coordination chemistry of this coumarin-derivatized phosphine-ether ligand have been initiated. Preliminary efforts to coordinate this ligand to Ru(II) have been unsuccessful; attempts to prepare both the bipyridyl complex $[cis\text{-}Ru(bpy)_2(POR)]^{2+}$ and bis(phosphine-ether) complex $RuCl_2(POR)_2$ led predominantly to unidentified Ru(III) species. Colleagues in the Wolf research group are continuing these efforts and have also begun investigation into the preparation of complexes with other open-shell metals such as cobalt.

References begin on page 256.

7.6 Experimental section

7.6.1 General details

General synthetic and instrumental details (NMR spectrometers, IR and UV/Vis spectrophotometers) are described in Chapter Two. Luminescence measurements for the compounds reported in this chapter were performed at room temperature on air-saturated solutions contained in suprasil quartz cells, using a Spex Fluorolog-Tau-3 spectrofluorometer located in the laboratory of Prof. Ian Clark-Lewis (UBC Biochemistry and Biomedical Research Centre).

Hydroxymethylpyrene (used in attempts to make methylpyrene phosphine-ether; not described here), 4-hydroxybutylpyrene, triphenylphosphine, imidazole (Aldrich) and $RuCl_3 \cdot xH_2O$ (Strem) were used as received from the suppliers. 2-Diphenylphosphinophenol was prepared using two different published routes, either from phenol[37,38] or from acid hydrolysis of POEt.[39] 2-Chloroethyldiphenylphosphine was prepared according to a modification of the published procedure, using $NaPPh_2$ (from $PPh_3/Na/NH_3$) in place of $KPPh_2$.[40] Spectroscopic grade cyclohexane (Aldrich) and reagent grade CH_2Cl_2 (distilled from CaH_2) were used for luminescence measurements; both solvents produced negligible background luminescence at the excitation wavelengths used.

7.6.2 Preparation of the phosphine pyrenyl-ether ligand

7.6.2.1 Preparation of 4-bromobutylpyrene

An alternate route to this compound was sought because of the low yield (~ 50 % before recrystallization) obtained using the literature procedure.[5] The route presented here is superior both in terms of reaction time (~ 4 h *vs.* 4 d) and yield, as it reduces formation of the side product, bis(4-(1-pyrenyl)butyl) ether (silica gel; CH_2Cl_2; $R_f = 0.05$).

An ice-cooled solution of PPh_3 (3.94 g, 15.0 mmol) and imidazole (2.04 g, 30.0 mmol) in dry CH_2Cl_2 (145 mL) was treated with Br_2 (0.77 mL, 15.0 mmol). The brown colour

References begin on page 256.

disappeared immediately upon contact with the PPh_3 solution; because a trace of yellow colour remained at the end of the addition, an additional small amount of PPh_3 was added to consume the excess Br_2. The mixture was stirred at 0 °C and a white solid gradually precipitated (Br_2PPh_3) over the course of 20 min. A yellow solution of 4-hydroxybutylpyrene (1.97 g, 7.16 mmol) in dry CH_2Cl_2 (20 mL) was added, then the mixture was stirred at 0°C for 30 min then warmed to RT and stirred for an additional 2 h (monitored by TLC). Saturated aqueous $NaHCO_3$ (50 mL) was added and the aqueous layer was extracted with CH_2Cl_2; the combined organic layers were dried over anhydrous Na_2SO_4, filtered and evaporated to yield a pale yellowish solid. Triphenylphosphine oxide and imidazole were removed by column chromatography (silica gel, CH_2Cl_2; collected 1st band, R_f = 0.82; yield 1.77 g of 4-bromobutylpyrene, 73 %). Recrystallization from hot cyclohexane yielded white crystals (56 %, 1st crop). The product was identical to that obtained using the literature procedure.

7.6.2.2 Preparation of 4-(2-(diphenylphosphino)phenoxy)butylpyrene, POC4Pyr

2-Diphenylphosphinophenol (2.5 g, 9.2 mmol) and 18-crown-6 (2.4 g, 9.2 mmol) were dissolved in dry THF (170 mL). The resulting clear pale yellow solution was treated at RT with potassium *tert*-butoxide (1.0 M in THF, 9.2 mL, 9.2 mmol) via a dropping funnel and stirred for 1.25 h to yield a slightly cloudy golden-brown mixture. To this mixture was dropwise added a solution of 4-bromobutylpyrene (3.1 g, 9.2 mmol) in THF (75 mL) and the reaction mixture was stirred for a total of 1.5 h, then the cloudy dirty yellow suspension was evaporated to dryness. The crude product was chromatographed (silica gel, CH_2Cl_2) to remove KBr and side products, then recrystallized from hot cyclohexane to yield white plates (m.p. 156 – 157 °C). Yield: 81 % after chromatography; 70 % after 3rd crop of crystals. Soluble in toluene, dichloromethane, chloroform; sparingly soluble in acetone, ether, THF, hot ethyl acetate, hot cyclohexane. Elemental analysis calcd. for $C_{38}H_{31}OP$ (%): C, 85.37; H, 5.84; found: C, 85.60; H, 5.95 after drying crystalline sample *in vacuo* at RT for 2 d. CV (200 mV/s, 25 °C, $CH_3CN/^nBu_4NPF_6$, V *vs.* SCE): E_{red} = - 2.18 V. $^{31}P\{^1H\}$ NMR (121.5 MHz, 25 °C, CD_2Cl_2): δ-14.2 (s). ^1H NMR (300.1 MHz, 25 °C, CD_2Cl_2): δ8.26 – 7.99 (m, 8H, pyrene), 7.80 (d, J = 7.68 Hz, 1H, pyrene), 7.33 – 7.21 (m, 11H, Ph), 6.90 – 6.82 (m, 2H, Ph), 6.69 – 6.64 (m, 1H, Ph), 3.95 (m, 2H, pyrene-$CH_2(CH_2)_2CH_2$-O), 3.23 (m, 2H, pyrene-$CH_2(CH_2)_2CH_2$-O), 1.69 (m, 4H, pyrene-$CH_2(CH_2)_2CH_2$-O). $^{13}C\{^1H\}$ NMR (75.0 MHz, 25

References begin on page 256.

°C, CD_2Cl_2): δ160.75 (d, $^2J_{CP}$ = 14.4 Hz, 4° *C*), 137.34 (d, $^1J_{CP}$ = 10.9 Hz, 2 × 4° *C*), 137.31 (2 × 4° *C*), 134.23 (d, $^2J_{CP}$ = 20.7 Hz, 4 × *C*H), 133.57 (d, $^2J_{CP}$ = 2.3 Hz, *C*H), 131.80 (4° *C*), 131.31 (4° *C*), 130.43 (*C*H), 130.07 (4° *C*), 128.96 (4° *C*), 128.83 (2 × *C*H), 128.66 (2 × *C*H), 128.56 (2 × *C*H), 127.87 (*C*H), 127.68 (*C*H), 127.37 (*C*H), 126.79 (*C*H), 126.56 (d, $^1J_{CP}$ = 13.2 Hz, 4° *C*), 126.17 (*C*H), 125.31 (4° *C*), 125.10 (2 × *C*H), 124.98 (*C*H), 123.98 (*C*H), 121.09 (*C*H), 111.34 (d, $^3J_{CP}$ = 1.2 Hz, *C*H), 68.46 (pyrene-$CH_2CH_2CH_2CH_2$-O), 33.36 (pyrene-$CH_2CH_2CH_2CH_2$-O), 29.47 (pyrene-$CH_2CH_2CH_2CH_2$-O), 28.29 (pyrene-$CH_2CH_2CH_2CH_2$-O); peak assignments are based on comparison to the calculated APT spectrum (ACD).

7.6.3 Preparation and characterization of Ru complexes

7.6.3.1 Preparation of trans,cis,cis-$RuCl_2$(POC4Pyr-P,O)$_2$, 10

Phosphine-ether 4-(2-(diphenylphosphino)phenoxy)butylpyrene, POC4Pyr, (1.54 g, 2.88 mmol) was dissolved in a boiling mixture of ethanol (140 mL) and toluene (80 mL). In a separate flask, $RuCl_3$•xH_2O (0.298 g, 1.43 mmol) was dissolved in water (20 mL), sonicated for 10 min with intermittent heating with a heat gun, then diluted with ethanol (20 mL). The prepared metal solution was added all at once to the boiling solution of POC4Pyr, and the opaque dark brown solution was heated to reflux for 3.25 h, over which time a gradual colour change to clear red occurred. The progress of the reaction was monitored by TLC (silica gel, CH_2Cl_2). The reaction mixture was cooled in the refrigerator (~ 5 °C) overnight to precipitate a dark red oil, which when dissolved in acetone/CH_2Cl_2 and concentrated yielded a flocculent pink solid. The solid was reprecipitated from CH_2Cl_2/hexanes, then washed well with boiling hexanes to remove unreacted ligand. Yield: 0.68 g (38 %) burgundy-pink powder. Soluble in aromatics, dichloromethane, THF. Elemental analysis calcd. for $C_{76}H_{62}Cl_2O_2P_2Ru$ (%): C, 73.54; H, 5.03; found: C, 73.49; H, 5.35 after drying sample *in vacuo* at RT for 3 d. CV (200 mV/s, 25 °C, CH_2Cl_2/^{n}Bu_4NPF_6, V *vs.* SCE): $E_{1/2}$ = 0.52, 1.18 V; E_{ox} = 1.33 V. $^{31}P\{^1H\}$ NMR (121.5 MHz, – 80 ° to 25 °C, CD_2Cl_2): δ63.7 (s). ^1H NMR (300.1 MHz, 25 °C, CD_2Cl_2): δ8.16 – 7.92 (m, 16H, pyrene), 7.74 (d, $^3J_{HH}$ = 8.0 Hz, 2H, pyrene), 7.38 – 7.07 (m, 26H, Ph),

References begin on page 256.

7.02 (m, 2H, Ph), 4.73 (m, 4H, pyrene-$CH_2(CH_2)_2CH_2$-O), 3.14 (m, 4H, pyrene-$CH_2(CH_2)_2CH_2$-O), 1.85 (m, 4H, pyrene-$CH_2CH_2CH_2CH_2$-O), 1.70 (m, 4H, pyrene-$CH_2CH_2CH_2CH_2$-O); assignments based on ^{1}H COSY spectrum in C_6D_6. $^{13}C\{^1H\}$ NMR (75.0 MHz, 25 °C, CD_2Cl_2): δ161.7 (t, $^2J_{CP}$ = 5.2 Hz, 4° *C*), 137.0 (s, 4° *C*), 134.5 (t, $^2J_{CP}$ = 4.9 Hz, *C*H), 134.1 (d, $^1J_{CP}$ = 25.3 Hz, 4° *C*), 133.1 (s, 4° *C*), 131.7 (s, *C*H), 131.2 (s, 4° *C*), 130.1 (s, 4° *C*), 129.8 (s, *C*H), 128.9 (s, 4° *C*), 127.8-127.4 (m, overlapped, *C*H), 126.8 (m, overlapped, *C*H), 126.1 (m, *C*H), 125.2 (d, $^2J_{CP}$ = 2.3 Hz, 4° *C*), 125.2 – 124.9 (m, overlapped, *C*H), 123.8 (m, *C*H), 122.4 (br m, *C*H), 116.6 (br m, *C*H), 74.3 (pyrene-$CH_2CH_2CH_2CH_2$-O), 33.4 (pyrene-$CH_2CH_2CH_2CH_2$-O), 29.0 (pyrene-$CH_2CH_2CH_2CH_2$-O), 27.2 (pyrene-$CH_2CH_2CH_2CH_2$-O).

7.6.3.2 Reaction of 10 with CO

Solutions of **10** ([**10**] ≈ 0.02 M) in (a) toluene-d_8 + 10 drops chlorobenzene, and (b) CD_2Cl_2 were sparged with CO until the colour changed from red to pale greenish-yellow. The samples were analyzed by $^{31}P\{^1H\}$ NMR spectroscopy immediately after the reaction:

(a) $^{31}P\{^1H\}$ NMR (121.5 MHz, 25 °C, toluene-d_8/chlorobenzene): δ27.0 (s).

(b) $^{31}P\{^1H\}$ NMR (121.5 MHz, 25 °C, CD_2Cl_2): δ27.1 (s).

This new complex, **11**, precipitates from toluene/chlorobenzene as a pale greenish-yellow solid but is more soluble in CD_2Cl_2. Samples in CD_2Cl_2 sparged with N_2 or degassed via freeze-pump-thaw after treatment with CO slowly underwent further conversion to form another complex, **12**, ($^{31}P\{^1H\}$ NMR (121.5 MHz, 25 °C, CD_2Cl_2): δ13.9 (s)), while those under CO atmosphere were more inert.

7.6.3.3 Reaction of 10 with ^{13}CO

Solutions of **10** ([**10**] ≈ 0.02 M) in (a) toluene-d_8 + 10 drops chlorobenzene, and (b) CD_2Cl_2 were introduced into NMR tubes sealed with gas-purgeable PTFE valves. The solutions were degassed by three freeze-pump-thaw cycles and the head space filled with 1 atm of ^{13}CO. The samples were sealed, mixed by inversion, and exposed again to ^{13}CO atmosphere repeatedly until the colour changed from red to pale greenish-yellow. Sample (a) was left

References begin on page 256.

under 1 atm ^{13}CO; sample (b) was degassed via three freeze-pump-thaw cycles. The samples were analyzed by $^{31}P\{^{1}H\}$ and $^{13}C\{^{1}H\}$ NMR spectroscopy. The $^{31}P\{^{1}H\}$ spectra of both the kinetic product **11** and thermodynamic product **12** contained triplet resonances, indicative of coupling of the two equivalent phosphines to two equivalent ^{13}CO moieties.

Sample (a) in toluene-d_8/chlorobenzene, under ^{13}CO. Immediately after treatment with ^{13}CO: $^{31}P\{^{1}H\}$ NMR (121.5 MHz, 25 °C, toluene-d_8/chlorobenzene): δ27.0 (t, $^{2}J_{PC}$ = 13.4 Hz). $^{13}C\{^{1}H\}$ NMR (75.0 MHz, 25 °C, toluene-d_8/chlorobenzene): δ198.3 (t, $^{2}J_{CP}$ = 13.5 Hz). After 1 d at RT: nearly complete precipitation of pale greenish-yellow solid; NMR spectra of supernatant essentially unchanged.

Sample (b) in CD_2Cl_2, degassed. Immediately after treatment with ^{13}CO: $^{31}P\{^{1}H\}$ NMR (121.5 MHz, 25 °C, CD_2Cl_2): δ27.1 (t, $^{2}J_{PC}$ = 13.4 Hz). $^{13}C\{^{1}H\}$ NMR (75.0 MHz, 25 °C, CD_2Cl_2): δ197.6 (t, $^{2}J_{CP}$ = 13.5 Hz). After 1 d at RT: $^{31}P\{^{1}H\}$ NMR (121.5 MHz, 25 °C, CD_2Cl_2): δ13.9 (t, $^{2}J_{PC}$ = 11.2 Hz). $^{13}C\{^{1}H\}$ NMR (75.0 MHz, 25 °C, CD_2Cl_2): δ193.8 (t, $^{2}J_{CP}$ = 10.9 Hz).

7.6.3.4 Dicarbonyl product 11: trans,trans,trans-$RuCl_2(CO)_2(POC4Pyr\text{-}P)_2$

Solutions of **10** treated with CO in dichloromethane or chloroform solution and maintained under CO atmosphere yield the greenish-yellow dicarbonyl product **11**. IR ($CHCl_3$): ν_{CO} = 2005 cm^{-1}. CV (200 mV/s, 25 °C, $CH_2Cl_2/^{n}Bu_4NPF_6$, V *vs.* SCE): $E_{1/2}$ = 1.18, 1.39 V; E_{ox} = 1.71 V. $^{31}P\{^{1}H\}$ NMR of ^{13}CO-labeled complex (121.5 MHz, 25 °C, CD_2Cl_2): δ27.1 (t, $^{2}J_{PC}$ = 13.4 Hz). ^{1}H NMR (300.1 MHz, 25 °C, CD_2Cl_2): δ8.19 – 7.95 (overlapping m, 14H, pyrenyl), 7.87 – 7.45 (overlapping m, 6H, pyrenyl), 7.65 (d, $^{3}J_{HH}$ = 8.0 Hz, 2H, pyrenyl), 7.43 (m, 2H), 7.28 – 7.10 (overlapping m, 12H), 7.02 – 6.79 (overlapping m, 6H), 3.77 (m, 4H, pyrene-CH_2CH$_2$CH$_2$CH$_2$-O), 3.06 (m, 4H, pyrene-CH$_2$CH$_2$CH$_2$CH_2-O), 1.52 (m, 4H, pyrene-CH$_2$CH$_2$CH_2CH$_2$-O), 1.31 (m, 4H, pyrene-CH$_2$CH_2CH$_2$CH$_2$-O). $^{13}C\{^{1}H\}$ NMR (75.0 MHz, 25 °C, CD_2Cl_2): δ197.6 (t, $^{2}J_{CP}$ = 13.5 Hz, CO), 160.5 (t, J_{CP} = 2.3 Hz, 4° *C*), 137,2 (s, 4° *C*), 135.3 (br m, *C*H), 135.0 (br m, *C*H), 132.8 (t, J_{CP} = 24.4 Hz, 4° *C*), 132.7 (s, *C*H), 131.8 (s, 4° *C*), 131.3 (s, 4° *C*), 130.2 (s, *C*H), 130.0 (s, 4° *C*), 128.9 (s, 4° *C*), 128.2 – 127.8 (overlapping m, *C*H), 127.3 (m, *C*H), 126.7 (m, *C*H), 126.1 (m, *C*H), 125.2 (d, J_{CP} = 5.8

References begin on page 256.

Hz, 4° *C*), 125.0 (m, *C*H), 124.0 (m, *C*H), 120.5 (br m, *C*H), 118.8 (t, J_{CP} = 23.9 Hz, 4° *C*), 111.2 (br m, *C*H), 68.4 (s, *C*H_2), 33.3 (s, *C*H_2), 29.0 (s, *C*H_2), 28.4 (s, *C*H_2).

7.6.3.5 Thermodynamic dicarbonyl product 12: cis,cis,trans-$RuCl_2(CO)_2(POC4Pyr\text{-}P)_2$

Solutions of **10** treated with CO in dichloromethane or chloroform solution and degassed after the colour change from red to greenish yellow undergo gradual conversion to the thermodynamic dicarbonyl product **12**. IR ($CHCl_3$): ν_{CO} = 2005, 2058 cm^{-1}. $^{31}P\{^1H\}$ NMR of ^{13}CO-labeled complex (121.5 MHz, 25 °C, CD_2Cl_2): δ13.9 (t, $^2J_{PC}$ = 11.2 Hz). ^1H NMR (300.1 MHz, 25 °C, CD_2Cl_2): δ8.24 – 7.94 (m, 24H, pyrenyl), 7.43 (d, $^3J_{HH}$ = 7.9 Hz, 2H, pyrenyl), 7.37 – 7.17 (overlapping m, 14H), 6.96 – 6.85 (overlapping m, 4H), 6.30 (br m, 2H), 3.10 (m, 4H, pyrene-CH_2CH$_2$CH$_2$CH$_2$-O), 2.92 (m, 4H, pyrene-CH$_2$CH$_2$CH$_2$CH_2-O), 1.05 (m, 8H, pyrene-CH$_2$CH_2CH_2CH$_2$-O). $^{13}C\{^1H\}$ NMR (75.0 MHz, 25 °C, CD_2Cl_2): δ193.7 (t, $^2J_{CP}$ = 10.9 Hz, CO), 159.0 (t, J_{CP} = 2.6 Hz, 4° *C*), 136.4 (s, 4° *C*), 135.5 (t, J_{CP} = 3.3 Hz, *C*H), 135.3 (br m, *C*H), 133.0 (s, *C*H), 131.8 (t, J_{CP} = 24 Hz, 4° *C*), 131.7 (s, 4° *C*), 131.2 (s, 4° *C*), 130.4 (br m, *C*H), 130.1 (s, 4° *C*), 128.8 (s, 4° *C*), 128.0 (br t, J_{CP} = 5.1 Hz, *C*H), 127.4 (m, *C*H), 126.9 (m, *C*H), 126.2 (m, *C*H), 125.2 (m, *C*H), 123.7 (t, J_{CP} = 5.2 Hz, *C*H), 121.0 (t, J_{CP} = 4.3 Hz, *C*H), 119.3 (t, J_{CP} = 23.5 Hz, 4° *C*), 111.3 (br s, *C*H), 68.1 (s, *C*H_2), 33.2 (s, *C*H_2), 28.4 (s, *C*H_2), 27.8 (s, *C*H_2).

7.6.4 Preparation and characterization of coumarin-containing phosphine ether

7.6.4.1 Synthesis of 7-(2-bromoethoxy)-4-methylcoumarin

A round-bottomed flask was charged with 7-hydroxy-4-methylcoumarin (5.12 g, 29.1 mmol), potassium carbonate (11.2 g, 80.8 mmol), 18-crown-6 (0.66 g, 2.5 mmol), 1,2-dibromoethane (100 mL, 1.160 mol) and acetone (300 mL). The mixture was heated to reflux for several days, during which time the yellowish mixture turned cloudy and creamy in appearance. After 4 days, the reaction mixture (which still contained unreacted starting material according to TLC) was filtered through Celite and evaporated to dryness to yield a brown oil. Unreacted 7-hydroxy-4-methylcoumarin was removed via extraction of a CH_2Cl_2

References begin on page 256.

solution of the crude product with 0.5 M $NaOH_{(aq)}$ until the washings were nearly free of luminescence under 366 nm light. The organic extracts were dried over anhydrous Na_2SO_4, filtered and the solvent removed *in vacuo* to yield a beige solid (4.9 g, 59 %). Pure 7-hydroxy-4-methylcoumarin was obtained as pale peach-coloured needles after recrystallization from hot methanol (3.5 g, 42 %, m.p. 109 – 110 °C). Soluble in polar organic solvents; decomposes on silica gel. Elemental analysis calcd. for $C_{12}H_{11}BrO_3$ (%): C, 50.91; H, 3.92; found: C, 51.09; H, 3.99 after drying sample *in vacuo* at RT for 16 h. ^{1}H NMR (300.1 MHz, 25 °C, $CDCl_3$): δ7.46 (d, $^3J_{HH}$ = 8.8 Hz, 1H), 6.85 (d, $^3J_{HH}$ = 2.6 Hz, 1H), 6.82 (d, $^3J_{HH}$ = 2.6 Hz, 1H), 6.75 (d, $^3J_{HH}$ = 2.6 Hz, 1H), 6.10 (d, $^4J_{HH}$ = 1.1 Hz, 1H), 4.31 (t, $^3J_{HH}$ = 6.0 Hz, 2H), 3.64 (t, $^3J_{HH}$ = 6.0 Hz, 2H), 2.36 (t, $^4J_{HH}$ = 1.1 Hz, 3H). ^{13}C{^{1}H} NMR (75.5 MHz, 25 °C, $CDCl_3$): δ160.94 (4° *C*), 160.90 (4° *C*), 155.10 (4° *C*), 155.29 (4° *C*), 125.66 (*C*H), 114.06 (4° *C*), 112.38 (*C*H), 112.26 (*C*H), 101.67 (*C*H), 68.13 (*C*H_2), 28.42 (*C*H_2), 18.53 (*C*H_3); assignments based on APT and comparison to simulated spectrum (ACD).

7.6.4.2 Synthesis of 7-(2-diphenylphosphino)ethoxy-4-methylcoumarin

A solution of potassium diphenylphosphide in THF (20 mL, 0.5 M, 10 mmol) was added dropwise under subdued lighting to a solution of 7-(2-bromoethoxy)-4-methylcoumarin (2.99 g, 10.6 mmol) in THF (160 mL) at 0 °C under nitrogen. The mixture was stirred for 45 min at 0 °C then warmed to room temperature over the course of 30 min. The solvent was removed *in vacuo* to yield a yellow solid, which was purified by column chromatography (silica gel; CH_2Cl_2 to elute first band containing $HPPh_2$ and $OPHPh_2$; 95 % CH_2Cl_2/5 % MeOH to elute product). The white solid (2.8 g, 74 %) was recrystallized with low recovery from hot methanol to yield white needles of pure 7-(2-diphenylphosphino)ethoxy-4-methylcoumarin (0.45 g, 12 %, m.p. 97 – 98 °C, decomp.). The phosphine is air-sensitive and must be stored under nitrogen. Elemental analysis calcd. for $C_{24}H_{21}O_3P$ (%): C, 74.22; H, 5.45; found: C, 74.02; H, 5.53 after drying *in vacuo* for 1 d. ^{31}P{^{1}H} NMR (121.5 MHz, 25 °C, $CDCl_3$): δ-21.2 (s). ^{1}H NMR (300.1 MHz, 25 °C, $CDCl_3$): δ7.46 – 7.33 (overlapping m, 11H), 6.71 (d, $^3J_{HH}$ = 8.8 Hz, 1H), 6.65 (s, 1H), 6.08 (s, 1H), 4.14 (apparent quartet, J = 7.7 Hz, 2H), 2.57 (t, $^3J_{HH}$ = 7.4 Hz, 2H), 2.34 (s, 3H). ^{13}C{^{1}H} NMR (75.5 MHz, 25 °C, $CDCl_3$): δ161.48 (4° *C*), 161.06 (4° *C*), 155.10 (4° *C*), 152.34 (4° *C*), 137.51 (d, $^1J_{CP}$ = 12.1 Hz, 4° *C*), 132.61 (d, $^2J_{CP}$ =

References begin on page 256.

19.0 Hz, *C*H), 128.88 (*C*H), 128.55 (d, $^{3}J_{CP}$ = 6.9 Hz, *C*H), 125.40 (*C*H), 113.56 (4° *C*), 112.33 (*C*H), 111.89 (*C*H), 101.50 (*C*H), 65.95 (d, $^{2}J_{CP}$ = 25.3 Hz, O-*C*H_2), 28.10 (d, $^{1}J_{CP}$ = 14.9 Hz, P-*C*H_2), 18.51 (*C*H_3); assignments based on APT and comparison to simulated spectrum (ACD).

References begin on page 256.

7.7 References

(1) Birks, J. B. *Photophysics of Aromatic Molecules*; Wiley-Interscience: London, 1970.

(2) Kalyanasundaram, K.; Thomas, J. K. *J. Am. Chem. Soc.* **1977**, *99*, 2039.

(3) Lewis, F. D.; Zhang, Y.; Letsinger, R. L. *J. Am. Chem. Soc.* **1997**, *119*, 5451.

(4) Winnik, F. M. *Chem. Rev.* **1993**, *93*, 587.

(5) Wielema, T. A.; Engberts, J. B. F. N. *Eur. Polym. J.* **1990**, *26*, 1065.

(6) Aoyagi, T.; Ikeda, H.; Ueno, A. *Bull. Chem. Soc. Jpn.* **2001**, *74*, 157.

(7) Bodenant, B.; Fages, F.; Delville, M.-H. *J. Am. Chem. Soc.* **1998**, *120*, 7511.

(8) Bodenant, B.; Weil, T.; Businelli-Pourcel, M.; Fages, F.; Barbe, B.; Pianet, I.; Laguerre, M. *J. Org. Chem.* **1999**, *64*, 7034.

(9) Fages, F.; Bodenant, B.; Weil, T. *J. Org. Chem.* **1996**, *61*, 3956.

(10) Hamada, F.; Narita, M.; Kinoshita, K.; Makabe, A.; Osa, T. *J. Chem. Soc., Perkin Trans. II.* **2001**, 388.

(11) Hossain, M. A.; Matsumura, S.; Kanai, T.; Hamasaki, K.; Mihara, H.; Ueno, A. *J. Chem. Soc., Perkin Trans. II.* **2000**, 1527.

(12) Matsumoto, H.; Shinkai, S. *Tet. Lett.* **1996**, *37*, 77.

(13) Monahan, C.; Bien, J. T.; Smith, B. D. *Chem. Commun.* **1998**, 431.

(14) Nishizawa, S.; Kato, Y.; Teramae, N. *J. Am. Chem. Soc.* **1999**, *121*, 9463.

(15) Sohna, J. E. S.; Jaumier, P.; Fages, F. *J. Chem. Res., Synop.* **1999**, 134.

(16) De Schryver, F. C.; Collart, P.; Vandendriessche, J.; Goedeweeck, R.; Swinnen, A.; Van der Auweraer, M. *Acc. Chem. Res.* **1987**, *20*, 159.

References begin on page 256.

(17) de Silva, A. P.; Gunaratne, H. Q. N.; Gunnlaugsson, T.; Huxley, A. J. M.; McCoy, C. P.; Rademacher, J. T.; Rice, T. E. *Chem. Rev.* **1997**, *97*, 1515.

(18) Yamauchi, A.; Hayashita, T.; Kato, A.; Nishizawa, S.; Watanabe, M.; Teramae, N. *Anal. Chem.* **2000**, *72*, 5841.

(19) Ji, H.-F.; Dabestani, r.; Brown, G. M.; Hettich, r. L. *Photochem. Photobiol.* **1999**, *69*, 513.

(20) Cairns, S. M.; McEwen, W. E. *Heteroatom. Chem.* **1990**, *1*, 9.

(21) Kaloun, E. B.; Merdes, R.; Genet, J.-P.; Uziel, J.; Juge, S. *J. Organomet. Chem.* **1997**, *529*, 455.

(22) Uziel, J.; Riegel, N.; Aka, B.; Figuiere, P.; Juge, S. *Tet. Lett.* **1997**, *38*, 3405.

(23) Shriver, D. F.; Atkins, P. W. *Inorganic Chemistry*; 3rd ed.; W. H. Freeman and Company: New York, 1999.

(24) Boyde, S.; Strouse, G. F.; Jones, W. E., Jr.; Meyer, T. J. *J. Am. Chem. Soc.* **1989**, *111*, 7448.

(25) Rauchfuss, T. B.; Patino, F. T.; Roundhill, D. M. *Inorg. Chem.* **1975**, *14*, 652.

(26) Lindner, E.; Scheytt, C.; Wegner, P. *Chem. Ber.* **1987**, *120*, 1621.

(27) Lindner, E.; Geprags, M.; Gierling, K.; Fawzi, R.; Steimann, M. *Inorg. Chem.* **1995**, *34*, 6106.

(28) Lindner, E.; Pautz, S.; Haustein, M. *Coord. Chem. Rev.* **1996**, *155*, 145.

(29) Jeffrey, J. C.; Rauchfuss, T. B. *Inorg. Chem.* **1979**, *18*, 2658.

(30) Lever, A. B. P. *Inorg. Chem.* **1990**, *29*, 1271.

(31) Mann, B. E.; Shaw, B. L.; Stainbank, R. E. *J. Chem. Soc., Chem. Comm.* **1972**, 151.

References begin on page 256.

(32) Wilkes, L. M.; Nelson, J. H.; Mitchener, J. P.; Babich, M. W.; Riley, W. C.; Helland, B. J.; Jacobson, R. A.; Cheng, M. Y.; Seff, K.; McCusker, L. B. *Inorg. Chem.* **1982**, *21*, 1376.

(33) Krassowski, D. W.; Nelson, J. H.; Brower, K. R.; Hauenstein, D.; Jacobson, R. A. *Inorg. Chem.* **1988**, *27*, 4294.

(34) Jessop, P. G.; Rettig, S. J.; Lee, C.-L.; James, B. R. *Inorg. Chem.* **1991**, *30*, 4617.

(35) Gill, D. F.; Mann, B. E.; Shaw, B. S. *J. Chem. Soc., Dalton Trans.* **1973**, 311.

(36) Barnard, C. F. J.; Daniels, J. A.; Jeffery, J.; Mawby, R. J. *J. Chem. Soc., Dalton Trans.* **1976**, 953.

(37) Rauchfuss, T. B. *Inorg. Chem.* **1977**, *16*, 2967.

(38) Yardley, J. P.; Fletcher, H., III. *Synthesis* **1976**, 244.

(39) Empsall, H. D.; Shaw, B. L.; Turtle, B. L. *J. Chem. Soc., Dalton Trans.* **1976**, 1500.

(40) Grim, S. D.; Barth, R. C. *J. Organomet. Chem.* **1975**, *94*, 327.

References begin on page 256.

Appendix 7.1 Comparison of the $^{13}C\{^1H\}$ NMR spectra of 10 and *trans,cis,cis*-$RuCl_2$(POMe-*P,O*)$_2$

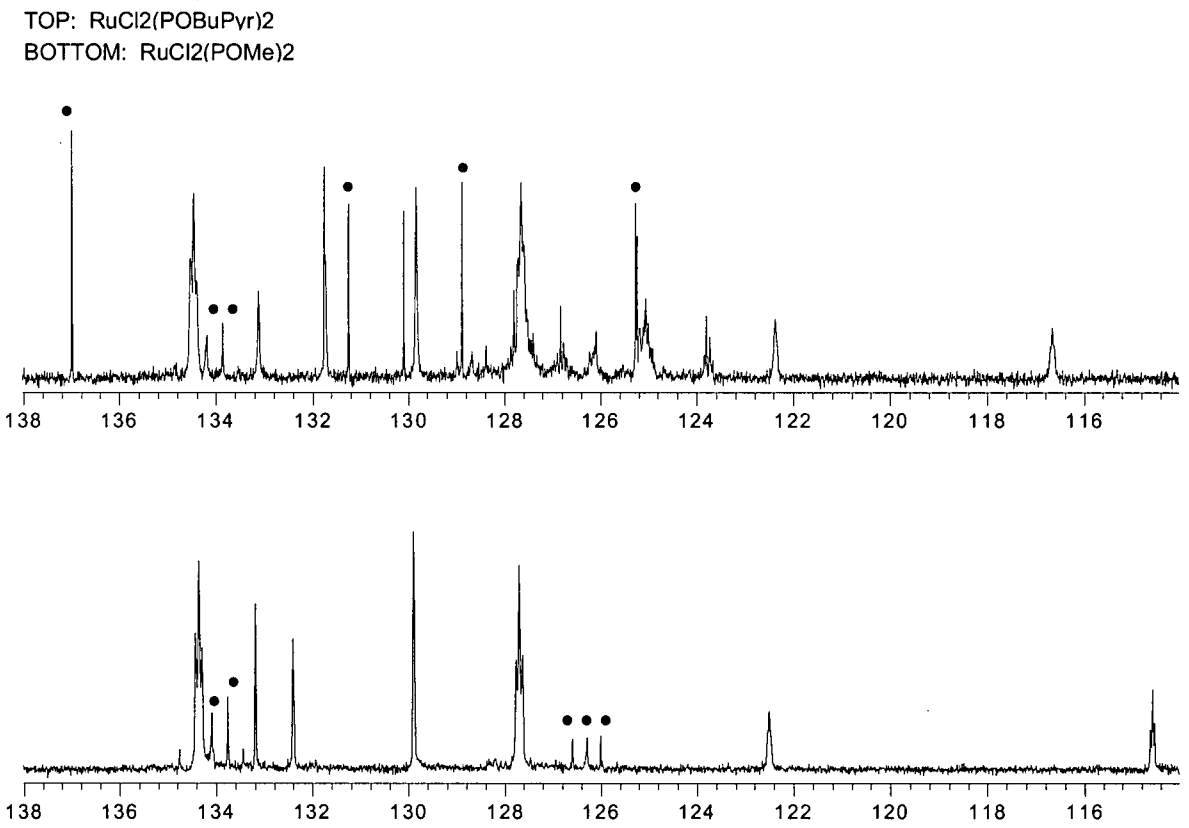

Figure A.7.1. Selected region of the $^{13}C\{^1H\}$ NMR spectra of **10** (top) and *trans,cis,cis*-$RuCl_2$(POMe-*P,O*)$_2$ (bottom). Data were acquired in CD_2Cl_2 solution and processed using Lorentz-Gaussian resolution enhancement (LB = -0.7, GB = 0.2). Resonances marked with a dot (•) correspond to quaternary carbons (assigned by APT); unmarked resonances correspond to methine (CH) carbons.

References begin on page 256.

Appendix 7.2 Cyclic voltammograms of *trans,cis,cis*-$RuCl_2(POC4\text{-}P,O)_2$, 10, and *trans,trans,trans*-$RuCl_2(CO)_2(POC4\text{-}P)_2$, 11

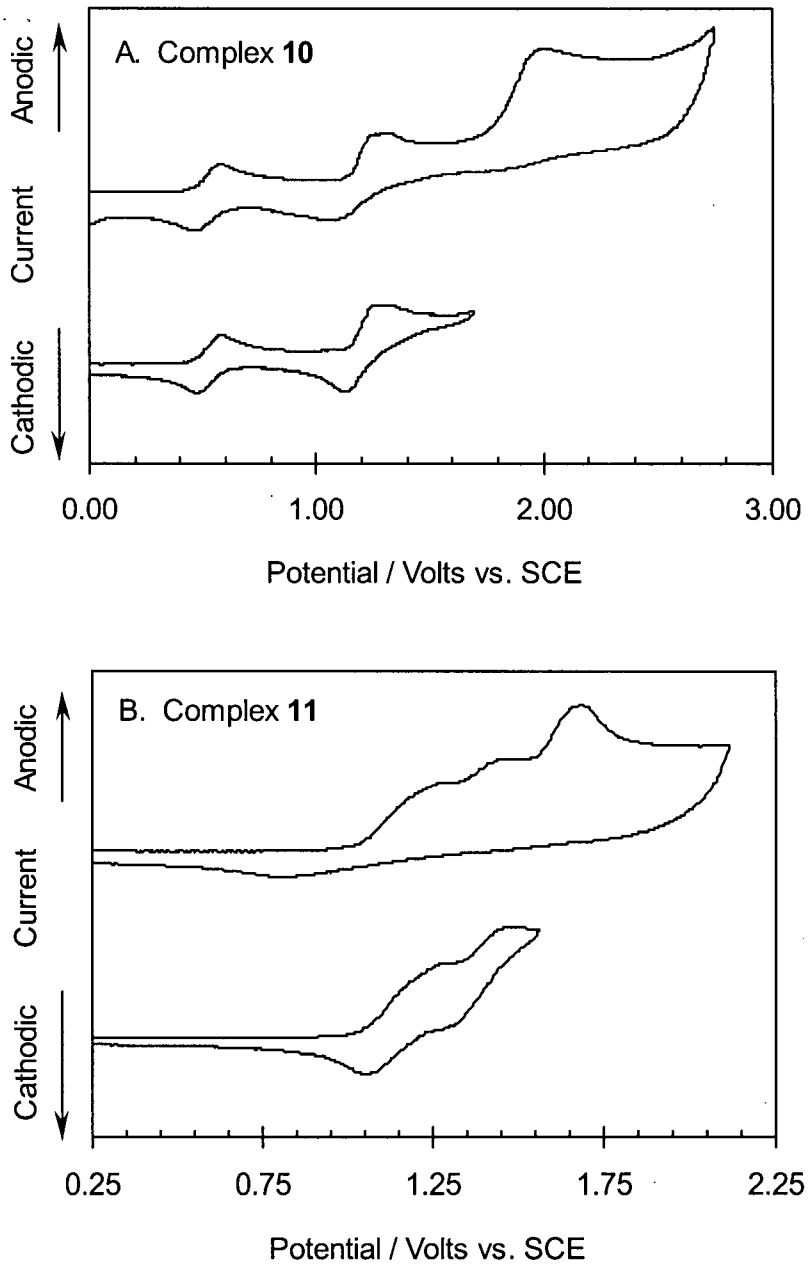

Figure A.7.2. Cyclic voltammograms of **10** (A) and **11** (B) in CH_2Cl_2 solution containing 0.1 M $^nBu_4NPF_6$ as supporting electrolyte; [**10**] ≈ [**11**] ≈ 10^{-3} M. The potential sweep program was: ~ 0 → ~ 1.5 – 3 → ~ 0 V. *vs.* SCE; subsequent scans were not significantly different in appearance from those shown.

References begin on page 256.